

AD-A041 484

WEST VIRGINIA UNIV MORGANTOWN DEPT OF ELECTRICAL ENG--ETC F/G 1/2
AIRCRAFT ANTENNA ANALYSIS AND MICROWAVE LANDING SYSTEM (MLS) AP--ETC(U)
JAN 76 C A BALANIS, Y CHENG DOT-OS-40013

UNCLASSIFIED

FAA-RD-76-37

NL

1 OF 3
ADA
041484



REPORT No. FAA-RD-76-37

7

AIRCRAFT ANTENNA ANALYSIS AND
MICROWAVE LANDING SYSTEM (MLS) APPLICATIONS

AD A 041 484

CONSTANTINE A. BALANIS
YUK-BUN CHENG



JANUARY 31, 1976

FINAL SUMMARY REPORT

DDC
JUL 11 1977
C

AD NO.
DDC FILE COPY

Document is available to the public through the
National Technical Information Service,
Springfield, Virginia 22161.

Prepared for

U.S. DEPARTMENT OF TRANSPORTATION
FEDERAL AVIATION ADMINISTRATION
Systems Research & Development Service
Washington, D.C. 20590

NOTICE

This document is disseminated under the sponsorship of the Department of Transportation in the interest of information exchange. The United States Government assumes no liability for its contents or use thereof.

Technical Report Documentation Page

1. Report No. 18 FAA-RD-76-37	2. Government Accession No. 11	3. Recipient's Catalog No. 31 Jan 76
4. Title and Subtitle 6 AIRCRAFT ANTENNA ANALYSIS AND MICROWAVE LANDING SYSTEM (MLS) APPLICATIONS	5. Report Date January 31, 1976	6. Performing Organization Code
7. Author(s) 10 Constantine A. Balanis, Yuk-Bun Cheng	8. Performing Organization Report No. 12 223p	9. Performing Organization Name and Address 410279
12. Sponsoring Agency Name and Address U.S. Department of Transportation Federal Aviation Administration Systems Research and Development Service Washington, D.C. 20590	10. Work Unit No. (TRAIS) 15	11. Contract or Grant No. DOT-OS-40013 new
13. Type of Report and Period Covered FINAL REPORT, Jan. 1, 1974 - Dec. 31, 1975	14. Sponsoring Agency Code ARD-722	15. Supplementary Notes 1-jan 74-31 Dec 75
16. Abstract The purpose of this investigation was to develop analytical methods for predicting the radiation characteristics of antennas on aircraft. Diffraction techniques in conjunction with other classical electromagnetic methods were used to take into account contributions from various structural features of an airframe (tail, nose, wings, and main fuselage). Computed values were compared with measured data of antennas on scaled model aircraft such as a 1/35 scale space shuttle, 1/11 scale Boeing 737, and 1/25 scale KC-135. A very good agreement between theory and experiment was indicated. With the availability and versatility of the analytical techniques, computations were made for antennas on full scale aircraft such as the Boeing 737, Boeing 747, and KC-135. The frequency of operation of the antennas on the full scale models was 5.1 GHz which is within the proposed band for the MLS. Of the antennas, locations, and aircraft examined in this investigation, a circumferential aperture, which is vertically polarized in the elevation plane, mounted below the nose (station 169) or above the cockpit (station 306) of a Boeing 747 provides the most attractive coverage for MLS application. A vertical monopole also demonstrates good coverage, but it is not as attractive as that of the circumferential aperture.		
17. Key Words Aircraft, Antennas, Microwave Landing System, Diffraction Techniques,	18. Distribution Statement Document is available to the public through the National Technical Information Service, Springfield, Virginia 22161.	
19. Security Classif. (of this report) UNCLASSIFIED	20. Security Classif. (of this page) UNCLASSIFIED	21. No. of Pages 224
		22. Price

Form DOT F 1700.7 (8-72)

Reproduction of completed page authorized

METRIC CONVERSION FACTORS

Approximate Conversions to Metric Measures

Symbol	When You Know	Multiply by	To Find	Symbol
LENGTH				
in	inches	2.5	centimeters	cm
ft	feet	30	meters	m
yd	yards	0.9	kilometers	km
mi	miles	1.6		
AREA				
in ²	square inches	6.5	square centimeters	cm ²
ft ²	square feet	0.09	square meters	m ²
yd ²	square yards	0.8	square meters	m ²
mi ²	square miles	2.6	square kilometers	km ²
	acres	0.4	hectares	ha
MASS (weight)				
oz	ounces	28	grams	g
lb	pounds	0.45	kilograms	kg
	short tons (2000 lb)	0.9	tonnes	t
VOLUME				
tsp	teaspoons	5	milliliters	ml
Tbsp	tablespoons	15	milliliters	ml
fl oz	fluid ounces	30	milliliters	ml
c	cups	0.24	liters	l
pt	pints	0.47	liters	l
qt	quarts	0.95	liters	l
gal	gallons	3.8	liters	l
ft ³	cubic feet	0.03	cubic meters	m ³
yd ³	cubic yards	0.76	cubic meters	m ³
TEMPERATURE (exact)				
°F	Fahrenheit temperature	5/9 (after subtracting 32)	Celsius temperature	°C

Approximate Conversions from Metric Measures

Symbol	When You Know	Multiply by	To Find	Symbol
LENGTH				
mm	millimeters	0.04	inches	in
cm	centimeters	0.4	inches	in
m	meters	3.3	feet	ft
km	kilometers	1.1	yards	yd
		0.6	miles	mi
AREA				
cm ²	square centimeters	0.16	square inches	in ²
m ²	square meters	1.2	square yards	yd ²
km ²	square kilometers	0.4	square miles	mi ²
ha	hectares (10,000 m ²)	2.5	acres	
MASS (weight)				
g	grams	0.035	ounces	oz
kg	kilograms	2.2	pounds	lb
t	tonnes (1000 kg)	1.1	short tons	
VOLUME				
ml	milliliters	0.03	fluid ounces	fl oz
l	liters	2.1	pints	pt
l	liters	1.06	quarts	qt
l	liters	0.26	gallons	gal
m ³	cubic meters	35	cubic feet	ft ³
m ³	cubic meters	1.3	cubic yards	yd ³

TEMPERATURE (exact)

°C	Celsius temperature	9/5 (then add 32)	Fahrenheit temperature	°F

*1 in = 2.54 in exactly. For other exact conversions and more details and tables, see NBS Mon. Publ. 286, *Units of Weights and Measures*, Price \$2.25, SO Catalog No. C13.112-86.

TABLE OF CONTENTS

	<u>Page</u>
I. INTRODUCTION	1
II. RADIATION MODELS	5
A. Two-Dimensional Wedge Model	5
B. Wedge Model With Curved Edge	22
C. Curved-Surface Model	42
1. Elevation Plane	42
2. Azimuth Plane	54
D. Mutual Coupling	66
III. COMPUTATIONS AND RESULTS	85
IV. CONCLUSIONS	184
V. ACKNOWLEDGEMENTS	185
VI. APPENDIX A: DIFFRACTION BY A PERFECTLY CONDUCTING WEDGE	186
VII. APPENDIX B: DYADIC DIFFRACTION FUNCTION BY A CONDUCTING WEDGE..	191
VIII. APPENDIX C: DIFFRACTION BY AN APERTURE ON A CURVED SURFACE	196
IX. REFERENCES	206

ACCESSION NO.	
MAIS	WIDE AREA
DOC	DATE
UNANNOUNCED	
JUSTIFICATION	
BY	
DISTRIBUTION/AVAILABILITY CODES	
Dist.	APPL. and/or SPECIAL
A	

LIST OF ILLUSTRATIONS

<u>Figure</u>	<u>Page</u>
1. Wedge modeling of airplane configuration in elevation plane	6
2. First order radiation mechanism for antenna at Position 1..	8
3. Pertinent dimensions for describing radiation from primary source and from wedges 3,4,5, and 6.....	9
4. Pertinent dimensions for describing radiation from wedges 1,2, and 3	13
5. Geometry for image source description for antenna at position 1.	16
6. Radiation mechanism and pertinent dimensions for antenna at position 2.....	18
7. Wedge surface model of elevation plane configuration	24
8. Conical cylinder modeling of elevation plane configuration.	25
9. Forward sector geometry of elevation plane.....	27
10. Rear sector geometry of elevation plane.....	28
11. Pertinent dimensions for radiation mechanism in the elevation plane from the forward sector	29
12. Pertinent dimensions for radiation mechanism in the elevation plane from the rear sector	34
13. Curved surface modeling of airplane configuration in elevation plane	44
14. Geometry for diffraction from wedge 3	45
15. Geometry for diffractions from the leading straight edges of the tail	47
16. Geometry for diffractions from the leading curved edge of the tail	48
17. Region separation toward the nose of the airplane	50
18. Geometry for diffractions in the lit transition region	51
19. Geometry for diffractions in the shadow transition and shadow regions	53

<u>Figure</u>	<u>Page</u>
20. Geometrical arrangement for antenna position at the nose of an aircraft	57
21. Geometrical arrangement for radiation in the shadow region above the nose	59
22. Geometrical arrangement for radiation in the shadow region below the nose	61
23. Geometrical arrangement for radiation in the lit transition region above the nose	62
24. Diffractions from fuselage/wing wedge (#3) and wing section	65
25. Geometrical arrangements of two apertures (1 and 2) on the nose of the airplane	67
26. Local geometry of nose and antenna positioning	68
27. Lit, transition, and shadow regions for antenna at position x_1, y_1	70
28. Expanded geometry for apertures 1 and 2 on the nose	71
29. Hard polarization geometry for two apertures on a cylinder. 73	
30. Soft polarization geometry for two apertures on a cylinder	74
31. Geometrical arrangement when slot 2 is in the transition region of slot 1	78
32. Expanded geometry when slot 2 is in the transition region of slot 1.....	79
33. Magnitude (modulus) distribution of hard polarization function $h(\xi)$	81
34. Phase (argument) distribution of hard polarization function $h(\xi)$	82
35. Magnitude (modulus) distribution of soft polarization function $\tilde{h}(\xi)$	83
36. Phase (argument) distribution of soft polarization function $\tilde{h}(\xi)$	84

<u>Figure</u>	<u>Page</u>
37. Circumferential and axial aperture orientations on the upper part of an airplane fuselage	86
38. Circumferential and axial aperture orientations on the lower part of an airplane fuselage	87
39. Computed and measured elevation plane amplitude patterns of a circumferential slot on position #1 of Figure 1	88
40. Computed and measured elevation plane amplitude patterns of a circumferential slot on position #2 of Figure 1	89
41. Space shuttle orbiter configuration with dimensions and antenna location on a 1/35 scale model	91
42. Computed and measured elevation plane amplitude patterns of a circumferential slot below the nose of 1/35 scale space shuttle	92
43. Computed and measured elevation plane amplitude patterns of an axial slot below the nose of 1/35 scale space shuttle ..	93
44. Computed and measured elevation plane amplitude patterns of a short monopole below the nose of 1/35 scale space shuttle	94
45. Boeing 737 airplane configuration with two antenna locations on a 1/11 scale model	95
46. Computed and measured elevation plane amplitude patterns of a circumferential waveguide below the nose (station 222) of 1/11 scale Boeing 737	96
47. Computed and measured elevation plane amplitude patterns of an axial waveguide below the nose (station 222) of 1/11 scale Boeing 737	97
48. Computed and measured elevation plane amplitude patterns of a short monopole below the nose (station 222) of 1/11 scale Boeing 737	98
49. Computed and measured elevation plane amplitude patterns of a quarter wavelength monopole below the nose (station 222) of 1/11 scale Boeing 737	99
50. Computed elevation plane relative phase pattern of a circumferential waveguide below the nose (station 222) of 1/11 scale Boeing 737	101

<u>Figure</u>	<u>Page</u>
51. Computed elevation plane relative phase pattern of an axial waveguide below the nose (station 222) of a 1/11 scale Boeing 737	102
52. Computed elevation plane relative phase pattern of a short monopole below the nose (station 222) of a 1/11 scale Boeing 737	103
53. Computed elevation plane relative phase pattern of a quarter wavelength monopole below the nose (station 222) of 1/11 scale Boeing 737	104
54. Computed and measured elevation plane amplitude patterns of a circumferential waveguide above the cockpit (station 220) of a 1/11 scale Boeing 737	105
55. Computed and measured elevation plane amplitude patterns of an axial waveguide above the cockpit (station 220) of 1/11 scale Boeing 737	106
56. Computed and measured elevation plane amplitude patterns of a short monopole above the cockpit (station 220) of 1/11 scale Boeing 737	107
57. Computed elevation plane relative phase pattern of a circumferential waveguide above the cockpit (station 220) of 1/11 scale Boeing 737	109
58. Computed elevation plane relative phase pattern of an axial waveguide above the cockpit (station 220) of 1/11 scale Boeing 737	110
59. Computed elevation plane relative phase pattern of a short monopole above the cockpit (station 220) of 1/11 scale Boeing 737	111
60. Measured azimuth plane amplitude pattern of a circumferential waveguide above the cockpit (station 220) of 1/11 scale Boeing 737	112
61. Measured azimuth plane amplitude pattern of an axial waveguide above the cockpit (station 220) of 1/11 scale Boeing 737	113
62. Measured azimuth plane amplitude pattern of a short monopole above the cockpit (station 220) of 1/11 scale Boeing 737	114
63. Computed elevation plane amplitude patterns of a circumferential and an axial waveguide below the nose (station 222) of a full scale Boeing 737	115

<u>Figure</u>		<u>Page</u>
64.	Computed elevation plane amplitude patterns of a circumferential and an axial waveguide above the cockpit (station 220) of a full scale Boeing 737	116
65.	Boeing 747 airplane configuration with two antenna locations	118
66.	Computed elevation plane amplitude patterns of a circumferential waveguide below the nose of full scale Boeing 737 (station 222) and full scale Boeing 747 (station 169)	119
67.	Computed elevation plane amplitude patterns of an axial waveguide below the nose of full scale Boeing 737 (station 222) and full scale Boeing 747 (station 169)	120
68.	Computed elevation plane amplitude patterns of a short monopole below the nose of full scale Boeing 737 (station 222) and full scale Boeing 747 (station 169)	121
69.	Computed elevation plane relative phase patterns of a circumferential waveguide below the nose of full scale Boeing 737 (station 222) and full scale Boeing 747 (station 169)	122
70.	Computed elevation plane relative phase patterns of an axial waveguide below the nose of full scale Boeing 737 (station 222) and full scale Boeing 747 (station 169).....	123
71.	Computed elevation plane relative phase patterns of a short monopole below the nose of full scale Boeing 737 (station 222) and full scale Boeing 747 (station 169).....	124
72.	Computed elevation plane amplitude patterns of a circumferential waveguide above the cockpit of full scale Boeing 737 (station 220) and full scale Boeing 747 (station 306)	125
73.	Computed elevation plane amplitude patterns of an axial waveguide above the cockpit of full scale Boeing 737 (station 220) and full scale Boeing 747 (station 306).....	126
74.	Computed elevation plane amplitude patterns of a short monopole above the cockpit of full scale Boeing 737 (station 220) and full scale Boeing 747 (station 306).....	127
75.	Computed elevation plane relative phase patterns of a circumferential waveguide above the cockpit of full scale Boeing 737 (station 220) and full scale Boeing 747 (station 306)	128

<u>Figure</u>	<u>Page</u>
76. Computed elevation plane relative phase patterns of an axial waveguide above the cockpit of full scale Boeing 737 (station 220) and full scale Boeing 747 (station 306)	129
77. Computed elevation plane relative phase patterns of a short monopole above the cockpit of full scale Boeing 737 (station 220) and full scale Boeing 747 (station 306)....	130
78. Computed elevation plane amplitude patterns of a circumferential waveguide below the nose (station 169) of a full scale Boeing 747 as a function of slant angle	132
79. Computed elevation plane amplitude patterns of an axial waveguide below the nose (station 169) of a full scale Boeing 747 as a function of slant angle	133
80. Computed elevation plane amplitude patterns of a circumferential waveguide above the cockpit (station 306) of a full scale Boeing 747 as a function of slant angle..	134
81. Computed elevation plane amplitude patterns of an axial waveguide above the cockpit (station 306) of a full scale Boeing 747 as a function of slant angle	135
82. Space shuttle orbiter configuration with dimensions and antenna location on a 1/35 scale model	136
83. Computed and measured elevation plane amplitude patterns of a circumferential waveguide below the nose of a 1/35 scale space shuttle	137
84. Computed and measured elevation plane amplitude patterns of an axial waveguide below the nose of a 1/35 scale space shuttle	138
85. Computed and measured elevation plane amplitude patterns of a quarter wavelength monopole below the nose of a 1/35 scale space shuttle	139
86. Elevation plane configuration and airplane dimensions of a 1/25 scale KC-135 model	141
87. Computed and measured elevation plane amplitude patterns of a circumferential waveguide above wings (location #2) of 1/25 scale KC-135	142
88. Computed and measured elevation plane amplitude patterns of an axial waveguide above wings (location #2) of 1/25 scale KC-135	143

<u>Figure</u>	<u>Page</u>
89. Computed and measured elevation plane amplitude patterns of a short monopole above wings (location #2) of 1/25 scale KC-135	144
90. Computed and measured elevation plane amplitude patterns of a circumferential waveguide forward of wings (location #1) of 1/25 scale KC-135	145
91. Computed and measured elevation plane amplitude patterns of an axial waveguide forward of wings (location #1) of 1/25 scale KC-135	146
92. Computed and measured elevation plane amplitude patterns of a short monopole forward of wings (location #1) of 1/25 scale KC-135	147
93. Computed elevation plane amplitude pattern of a circumferential waveguide above wings (location #2) of full scale KC-135	149
94. Computed elevation plane amplitude pattern of an axial waveguide above wings (location #2) of full scale KC-135..	150
95. Computed elevation plane amplitude pattern of a short monopole above wings (location #2) of full scale KC-135...	151
96. Computed elevation plane amplitude pattern of a circumferential waveguide forward of wings (location #1) of full scale KC-135	152
97. Computed elevation plane amplitude pattern of an axial waveguide forward of wings (location #1) of full scale KC-135	153
98. Computed elevation plane amplitude pattern of a short monopole forward of wings (location #1) of full scale KC-135	154
99. Azimuth plane airplane configuration with two antenna locations on the nose	155
100. Computed azimuth plane amplitude pattern of a circumferential waveguide on the nose (location #1) of a full scale KC-135	156
101. Computed azimuth plane amplitude pattern of an axial waveguide on the nose (location #1) of a full scale KC-135	157

<u>Figure</u>		<u>Page</u>
102.	Computed azimuth plane amplitude pattern of a short monopole on the nose (location #1) of a full scale KC-135.....	158
103.	Computed azimuth plane amplitude pattern of an axial waveguide on the nose (location #2) of a full scale KC-135	159
104.	Computed azimuth plane amplitude pattern of a circumferential waveguide on the nose (location #2) of a full scale KC-135	160
105.	Computed azimuth plane amplitude pattern of a short monopole on the nose (location #2) of a full scale KC-135....	161
106.	Mutual coupling between two axial apertures computed at West Virginia University (WVU) and compared with that reported in reference 29	163
107.	Mutual coupling between two axial apertures computed at West Virginia University (WVU) and compared with that reported in reference 29	164
108.	Antenna positioning along the nose of the aircraft	165
109.	Mutual coupling between two circumferential aperture antennas mounted as shown in Figure 108 (1/25 scale KC-135)	166
110.	Mutual coupling between two axial aperture antennas mounted as shown in Figure 108 (1/25 scale KC-135).....	167
111.	Mutual coupling between two circumferential aperture antennas mounted as shown in Figure 108 (full scale KC-135).....	168
112.	Mutual coupling between two axial aperture antennas mounted as shown in Figure 108 (full scale KC-135).....	169
113.	Mutual coupling for two circumferential aperture antennas mounted as shown in Figure 108 (full scale Boeing 737)...	170
114.	Mutual coupling for two axial aperture antennas mounted as shown in Figure 108 (full scale Boeing 737)	171
115.	Mutual coupling for two circumferential aperture antennas mounted as shown in Figure 108 (full scale Boeing 747)...	172

<u>Figure</u>		<u>Page</u>
116.	Mutual coupling for two axial aperture antennas mounted as shown in Figure 108 (full scale Boeing 747)	173
117.	Antenna positioning along the nose of the aircraft	174
118.	Mutual coupling for two circumferential aperture antennas mounted as shown in Figure 117 (1/25 scale KC-135)	176
119.	Mutual coupling for two axial aperture antennas mounted as shown in Figure 117 (1/25 scale KC-135).....	177
120.	Mutual coupling for two circumferential aperture antennas mounted as shown in Figure 117 (full scale KC-135).....	178
121.	Mutual coupling for two axial aperture antennas mounted as shown in Figure 117 (full scale KC-135)	179
122.	Mutual coupling for two circumferential aperture antennas mounted as shown in Figure 117 (full scale Boeing 737)... ..	180
123.	Mutual coupling for two axial aperture antennas mounted as shown in Figure 117 (full scale Boeing 737)	181
124.	Mutual coupling for two circumferential aperture antennas mounted as shown in Figure 117 (full scale Boeing 747)	182
125.	Mutual coupling for two axial aperture antennas mounted as shown in Figure 117 (full scale Boeing 747)	183
A.1.	Two-dimensional wedge and region separation	187
B.1.	Oblique wave incidence diffraction by a two-dimensional wedge	192
B.2.	Oblique wave incidence diffraction by a two-dimensional wedge with curved edge	195
C.1.	Region separation for wave diffraction of an aperture on a curved surface	197
C.2.	Geometry for illuminated region radiation by an aperture on a curved surface	198
C.3.	Geometry for illuminated transition region radiation by an aperture on a curved surface	198
C.4.	Path of integration for Fock functions	200

<u>Figure</u>	<u>Page</u>
C.5. Magnitude (modulus) distributions of hard $[g(\xi)]$ and soft $[\hat{g}(\xi)]$ Fock functions	202
C.6. Phase (argument) distributions of hard $[g(\xi)]$ and soft $[\hat{g}(\xi)]$ Fock functions	203
C.7. Geometry for shadow transition region radiation by an aperture on a curved surface	204
C.8. Geometry for shadow region radiation by an aperture on a curved surface	204

LIST OF TABLES

<u>Table</u>		<u>Page</u>
1.	FIELD REGIONS FOR POSITION 1	17
2.	FIELD REGIONS FOR POSITION 2	23
3.	DIFFRACTION COEFFICIENTS AND ATTENUATION CONSTANTS FOR CIRCULAR CYLINDERS AND SPHERES	55
4.	GENERALIZED DIFFRACTION COEFFICIENTS AND ATTENUATION CONSTANTS	56

I. INTRODUCTION

The problems associated with our Transportation Systems, especially those of congestion, system saturation, and safety are well documented and have been the subject of several intensive studies during the past several years. The result was a number of recommendations addressed primarily toward solution of transportation problems, and the need to examine new concepts and new technologies, for near-term as well as longer-term improvements. It was decided that increased effort is needed in the analysis of advance systems concepts and the related research performance studies and evaluation of technology which might be applied in the future. In defining this effort, the total transportation system must be considered.

Increased efforts have been undertaken in upgrading the aircraft safety by installing more sophisticated ground approach and landing systems at more airports around this country especially at locations with mountainous terrains. However, such facilities cannot function to their maximum capability unless the airborne systems are also upgraded and optimized. In 1971 a major research and development program was initiated by FAA and supported by international participation to develop a new approach and landing system known as the Microwave Landing System (MLS).¹⁻³ This system, which is to be operated at microwave frequencies is intended as an improvement over the existing lower frequency Instrument Landing System (ILS), now in operation at many airports around the country. The introduction of the MLS will enhance the safety of the approach and landing of an aircraft. This will improve the accuracy of landing during times of poor visibility and reduce one of the leading causes of accidents and fatalities. The operation of the MLS, however, will require new designs of airborne antenna systems.

In modern aircraft the electromagnetic/avionic environment becomes extremely complex and due to inter-relationships and interaction between the various systems, they become vulnerable to malfunction and erratic behavior. One of the principal problems in the design of a safe airborne communication, navigation, or approach and landing system is the location of the antennas for desired radiation characteristics. Because of the complicated geometry of the airframe, the antenna designer is usually required to approve new antenna systems on the basis of scale model patterns or accept a particular structural location since the cost of running extensive experimental studies for alternate structural locations has become prohibitive in time and dollars. Experience has shown that due to various compromises required in the manufacture of small-scale antennas and aircraft models, flight radiation measurements are required as a final check on the validity of the model patterns on each new type of antenna system and aircraft.⁴ It would then be extremely important from the viewpoint of economy and safety to be able to analyze and assess the performance of an antenna system on an aircraft (or on any other mode of transportation) prior to installation to avoid costly development of systems which are incompatible with the structural configuration and the existing onboard systems.

Improved antenna design methods can now be realized including determination of optimum locations for coupling or interference between systems, with the development of a mathematical radiation model of an aircraft. This type of investigation has much been needed in the past, and it will eliminate the need of running extensive and costly experimental pattern studies for alternate structural locations. In the past, many antenna designers and researchers avoided tackling such a problem, because of the mathematical intractability of the complex aircraft frame. Recent developments of

geometrical diffraction techniques and their application to many previously intractable problems,⁵⁻¹⁶ now give us the necessary tools to embark on the development of analytical radiation models of antennas on aircraft. The models will provide analytical design methods essential in the continued efforts by our scientific community for the improvement of aircraft communication and navigation systems and for the design of a new generation of air traffic control systems. The implementation of these techniques will lead to safer airborne systems.

In this document an investigation is reported which led to the development of analytical radiation models for predicting the principal plane patterns and coupling of antennas on an aircraft using geometrical diffraction methods. Initially the modeling of the aircraft structure is simplified, to reduce the mathematical complexities, and progresses to more realistic representations. In all cases, the computed results are checked with measurements on scale models and/or other available data.

In this report computed and measured amplitude antenna patterns are included for

- a. 1/35 scale space shuttle at 35 GHz
- b. 1/11 scale Boeing 737 at 35 GHz
- c. 1/25 scale KC-135 at 35 GHz

In addition, computed data at the proposed MLS frequency of 5.1 GHz are considered for

- d. full scale Boeing 737
- e. full scale Boeing 747
- f. full scale KC-135

In almost all cases radiation patterns have been examined for infinitesimal dipoles and circumferential and axial slots at locations which look promising

for positioning antennas to provide the required coverage for the MLS.
Computed phase patterns are also included which provide information on the
movement of the phase center of the system.

II. RADIATION MODELS

In this section the development of the analytical radiation model for antennas on aircraft will be outlined. It begins with simplified models, to reduce the mathematical details, and is followed by more complicated and realistic representations.

A. Two-Dimensional Wedge Model

As an initial step, the elevation plane of an aircraft structure, modeled as shown in Figure 1, is considered. Two antenna positions are chosen to be analyzed, one on the fuselage (1) and the other on the tail section (2). A two-dimensional configuration is assumed and the various structural features of the airframe are modeled with wedges of sharp edges each one with different included angle and each designated as #1, #2, #3, etc. Although this may not be an accurate representation of the aircraft, it is convenient for mathematical tractability. Curved surfaces will replace the sharp edges in other modeling configurations. The analysis begins by assuming that each antenna, whether in position 1 or 2, is mounted on an infinite structure. This geometry determines the major contribution to the overall radiation pattern,^{17,18} and it will be referred to as the "primary" component. In order to accurately predict the overall radiation pattern, perturbations introduced by the various wedges which are used to approximate the structure of the aircraft must be included. This can be done by assuming that the currents introduced on the surface by the "primary" radiation are the same for the infinite and finite structures. Such an approximation is quite valid and has been used previously in simpler problems

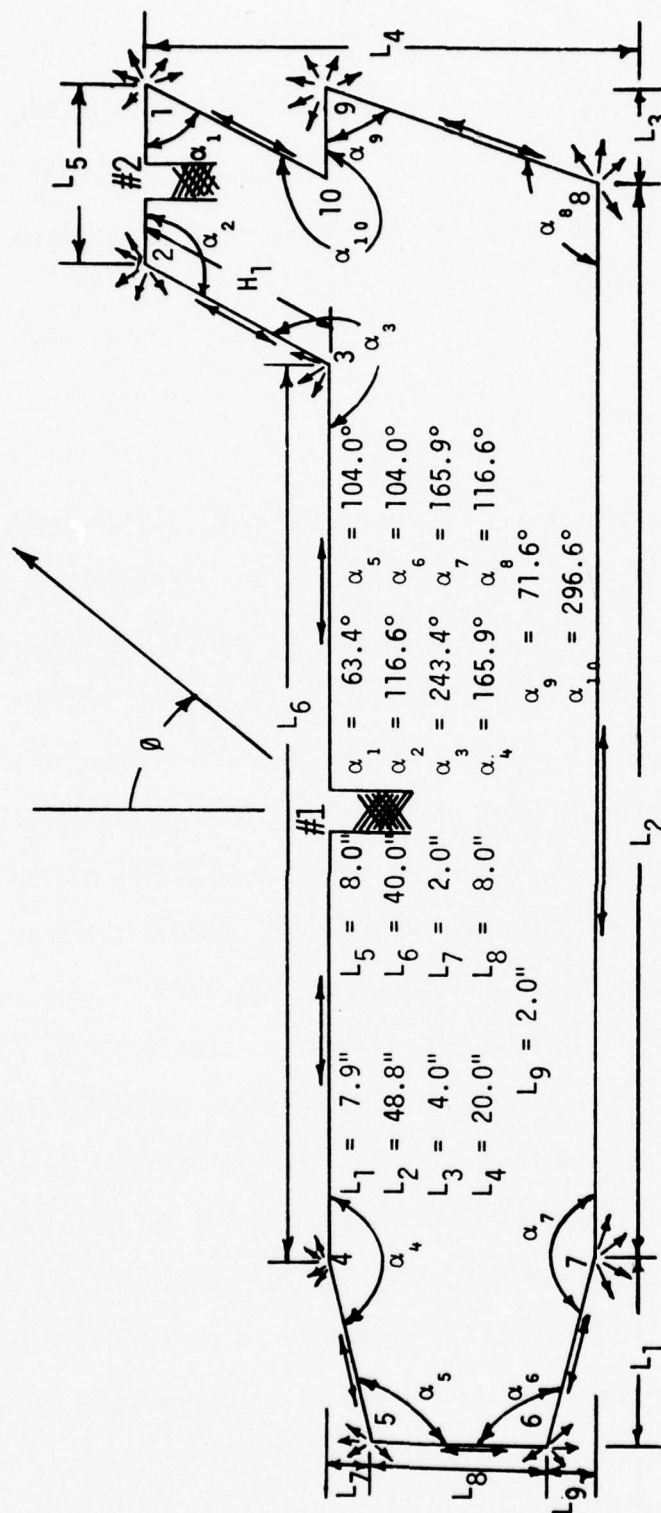


Figure 1. Wedge modeling of airplane configuration in elevation plane.

with good results.⁶⁻¹⁰ This permits the approximation of the fields on the finite structure which are used as the source for determining the contribution from each of the wedges, and they will be referred to as the "secondary" components.

The manner by which the contributions from each wedge are determined will be outlined when the primary source is located on the fuselage (position 1). Similar steps are followed for position 2 or any other location. The field from the primary source in the direction of wedges 2,3, and 4 will be the incident ray on the respective wedges. The amount diffracted by each wedge will be determined by the application of the diffraction coefficient of a plane or cylindrical wave by a two-dimensional wedge.¹⁹⁻²² Now the field from wedges 2,3, and 4 in the direction of the adjacent wedges will be diffracted again. This process continues to higher order diffractions. For structures large compared to wavelength, higher order diffractions can usually be neglected, because their contribution is small compared to that of the "primary" component and of lower order diffractions. Some diffraction mechanisms have been indicated graphically in Figure 2.

Another radiation mechanism that must be included is the reflection of the "primary" field by the tail structure. The distribution of the reflected field will be introduced using image theory.^{7,9} It should be pointed out that the diffracted field from each wedge and the reflected components from the different sides will not be applicable in all space about the airframe. The regions where each will be introduced will be determined by the laws of classical geometrical optics²³ and the laws of geometrical diffraction.^{16,24,25}

The primary source contribution is given, referring to Figure 3, by

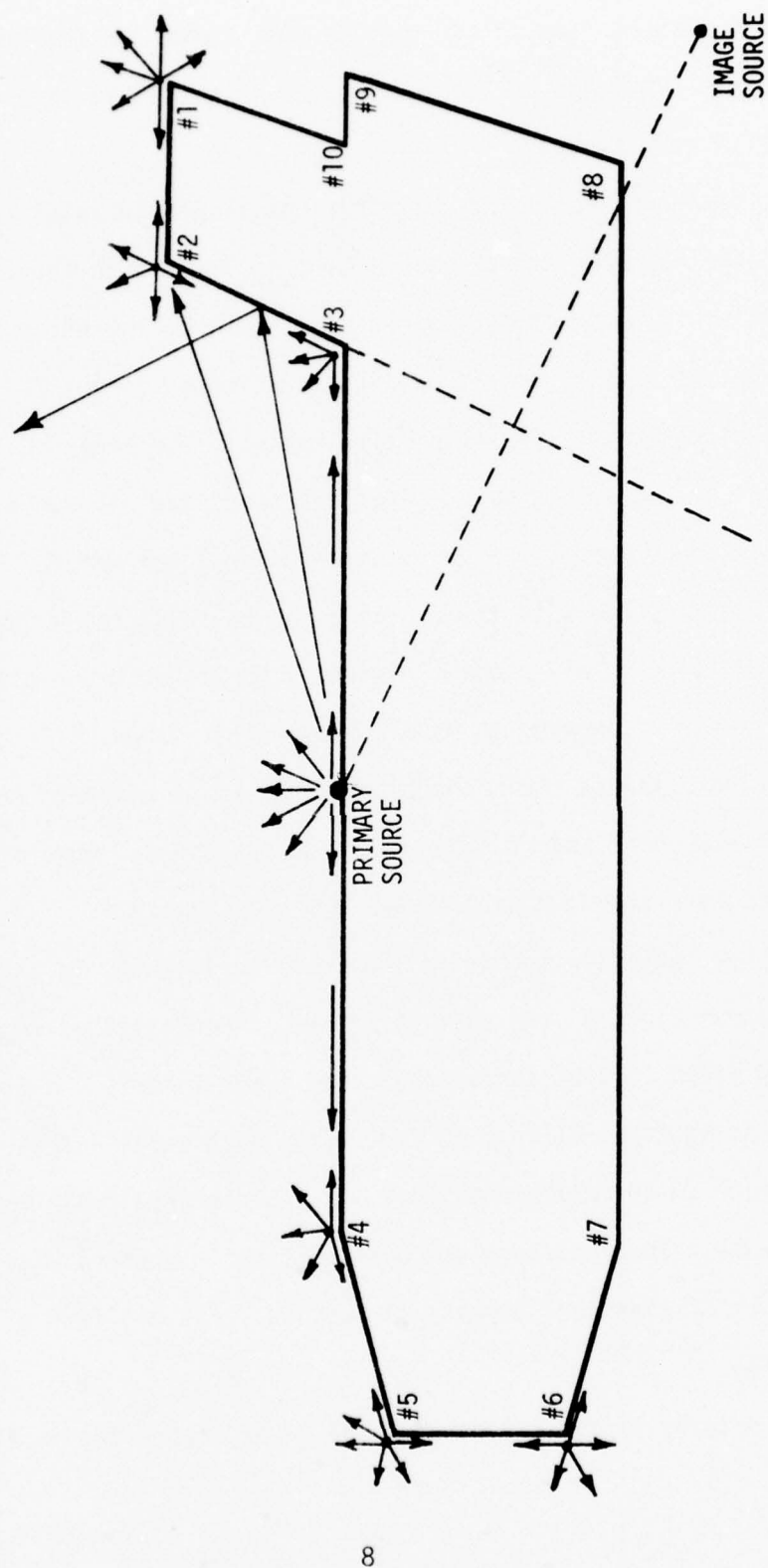


Figure 2. First order radiation mechanism for antenna at position 1.

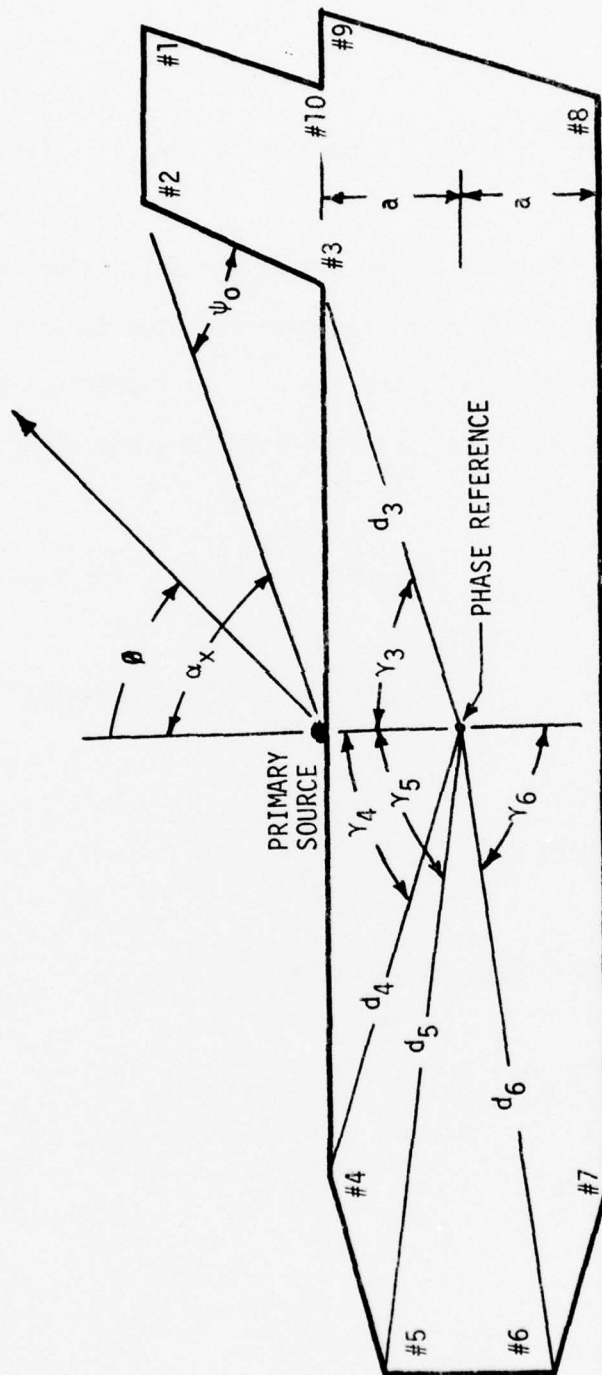


Figure 3. Pertinent dimensions for describing radiation from primary source and from wedges 3,4,5, and 6.

$$E_D(\theta) = e^{jk a \cos \theta} R_D(\theta) \quad 3\pi/2 < \theta < 2\pi \text{ and } 0 < \theta < \alpha_x \quad (1)$$

$$\text{where } \alpha_x = 3\pi/2 - \alpha_3 + \psi_0 \quad (1a)$$

$$\psi_0 = \tan^{-1} \left\{ \left[\frac{L_6}{2} - H_1 \cos \alpha_3 \right] / (-H_1 \sin \alpha_3) \right\} - (3\pi/2 - \alpha_3) \quad (1b)$$

$R_D(\theta)$ is the angular field distribution of the antenna on an infinite ground plane. The phase reference point has been selected to be the center of the fuselage, as shown in Figure 3, and the e^{-jkr}/r factor has been suppressed.

The diffraction contributions from wedge # 4 are given, referring to Figure 3, by

$$E_{D4}(\theta) = e^{jkd_4 \cos(\gamma_4 + \theta)} \cdot \begin{cases} R_{D4}(\theta) & \pi/2 + \alpha_4 < \theta < 2\pi \\ R'_{D4}(\theta) & 0 < \theta < \pi/2 - \beta \end{cases} \quad (2)$$

where

$$R_{D4}(\theta) = R_D(3\pi/2) V_B[L_6/2, 5\pi/2 - \theta, n_4] \quad (2a)$$

$$R'_{D4}(\theta) = R_D(3\pi/2) V_B[L_6/2, \pi/2 - \theta, n_4] \quad (2b)$$

$$d_4 = [(L_6/2)^2 + a^2]^{\frac{1}{2}} \quad (2c)$$

$$\gamma_4 = \tan^{-1}[L_6/2a] \quad (2d)$$

$$n_4 = 2 - \alpha_4/\pi \quad (2e)$$

$$\beta = \tan^{-1}[(L_4 - 2a)/(L_6 - H_1 \cos \alpha_3)] \quad (2f)$$

$V_B(r, \psi, n)$ is the wedge diffraction function¹⁹⁻²¹ (see Appendix A).

The diffractions from wedge #5 are given by

$$E_{D5}(\vartheta) = e^{jkd_5 \cos(\gamma_5 + \vartheta)} \cdot \begin{cases} R_{D5}(\vartheta) & \pi < \vartheta < 2\pi \\ R'_{D5}(\vartheta) & 0 < \vartheta < \pi - \alpha_5 \end{cases} \quad (3)$$

where

$$R_{D5}(\vartheta) = R_{D4}(\pi/2 + \alpha_4) V_B[-L_1/\cos\alpha_4, 3\pi/2 + \alpha_4 - \vartheta, n_5] \quad (3a)$$

$$R'_{D5}(\vartheta) = R_{D4}(\pi/2 + \alpha_4) V_B[-L_1/\cos\alpha_4, \pi - \alpha_5 - \vartheta, n_5] \quad (3b)$$

$$d_5 = [(L_1 + L_6/2)^2 + (L_8/2)^2]^{1/2} \quad (3c)$$

$$\gamma_5 = \tan^{-1}[(2L_1 + L_6)/L_8] \quad (3d)$$

$$n_5 = 2 - \alpha_5/\pi \quad (3e)$$

and from wedge # 6 by

$$E_{D6}(\vartheta) = e^{-jkd_6 \cos(\gamma_6 - \vartheta)} R_{D6}(\vartheta) \quad \alpha_6 < \vartheta < 2\pi \quad (4)$$

where

$$R_{D6}(\vartheta) = R_{D5}(\pi) V_B[L_8, 2\pi - \vartheta, n_6] \quad (4a)$$

$$d_6 = [(L_1 + L_6/2)^2 + (L_8/2)^2]^{1/2} \quad (4b)$$

$$\gamma_6 = \tan^{-1}[(2L_1 + L_6)/L_8] \quad (4c)$$

$$n_6 = 2 - \alpha_6/\pi \quad (4d)$$

In a similar fashion the fields diffracted from wedge # 3 can be written, and they are given by

$$E_{D3}(\vartheta) = e^{jkd_3 \cos(\gamma_3 - \vartheta)} \cdot \begin{cases} R_{D3}(\vartheta) & 3\pi/2 < \vartheta < 2\pi \\ R'_{D3}(\vartheta) & 0 < \vartheta < 3\pi/2 - \alpha_3 \end{cases} \quad (5)$$

where

$$R_{D3}(\vartheta) = R_D(\pi/2) V_B[L_6/2, \vartheta - 3\pi/2, n_3] \quad (5a)$$

$$R'_{D3}(\vartheta) = R_D(\pi/2) V_B[L_6/2, \vartheta + \pi/2, n_3] \quad (5b)$$

$$d_3 = [(L_6/2)^2 + a^2]^{\frac{1}{2}} \quad (5c)$$

$$\gamma_3 = \tan^{-1}[L_6/2a] \quad (5d)$$

$$n_3 = 2 - \alpha_3/\pi \quad (5e)$$

Diffracted energy from wedge #3 directed toward #2 will be diffracted again. In addition energy from the main source directed toward wedge # 2 will also be diffracted. The two-term diffraction contribution from wedge # 2 is then given, referring to Figure 4, by

$$E_{D2}(\vartheta) = e^{jkd_2 \cos(\gamma_2 - \vartheta)} \cdot \begin{cases} R_{D2}(\vartheta) & 3\pi/2 - \beta < \vartheta < 2\pi \\ R'_{D2}(\vartheta) & 0 < \vartheta < \pi/2 \end{cases} \quad (6)$$

where

$$R_{D2}(\vartheta) = R_D(\alpha_x) [V_B(R, \alpha_3 + \vartheta - 5\pi/2 - \psi_0, n_2) + V_B(R, \alpha_3 + \vartheta - 5\pi/2 + \psi_0, n_2)] \\ + R'_{D3}(3\pi/2 - \alpha_3) V_B(H_1, \vartheta + \alpha_3 - 5\pi/2, n_2) \quad (6a)$$

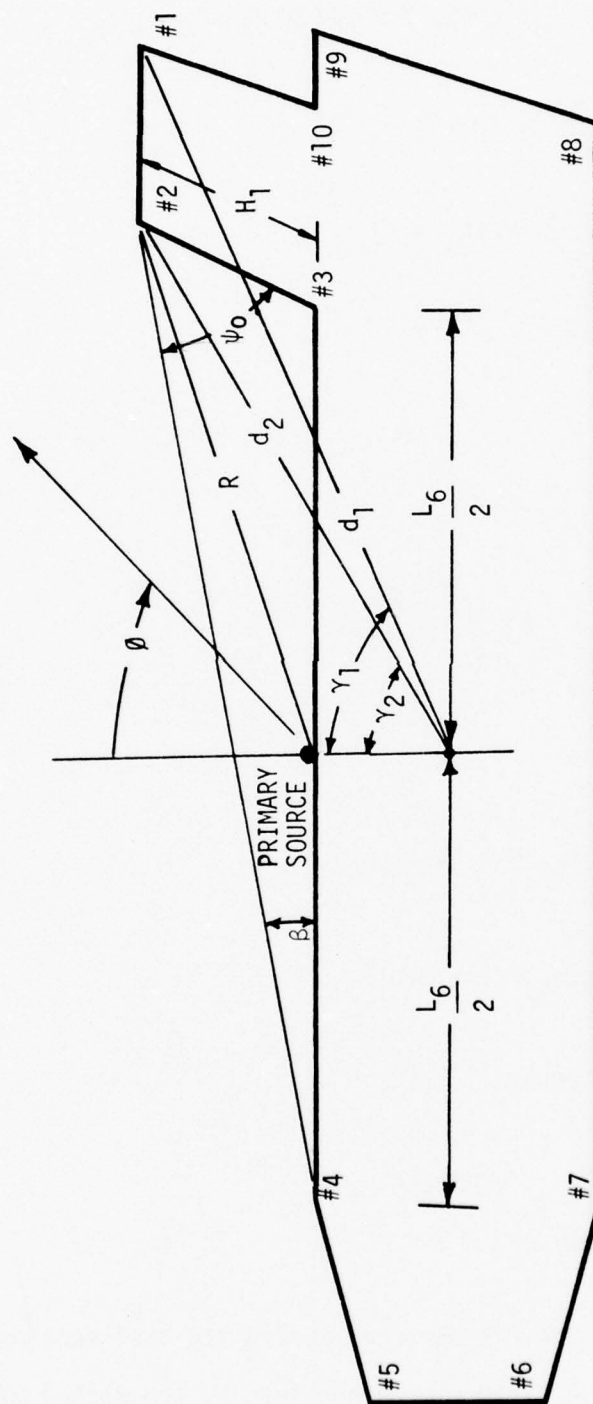


Figure 4. Pertinent dimensions for describing radiation from wedges 1, 2, and 3.

$$R_{D2}'(\vartheta) = R_D(\alpha_x) [V_B(R, \vartheta - \pi/2 + \alpha_3 - \psi_0, n_2) + V_B(R, \vartheta - \pi/2 + \alpha_3 + \psi_0, n_2)] \\ + R_{D3}'(3\pi/2 - \alpha_3) V_B(H_1, \vartheta - \pi/2 + \alpha_3, n_2) \quad (6b)$$

$$R = [(L_6/2 - H_1 \cos \alpha_3)^2 + (H_1 \sin \alpha_3)^2]^{\frac{1}{2}} \quad (6c)$$

$$d_2 = [(L_6/2 - H_1 \cos \alpha_3)^2 + (L_4 - a)^2]^{\frac{1}{2}} \quad (6d)$$

$$\gamma_2 = \tan^{-1} [(L_6/2 - H_1 \cos \alpha_3) / (L_4 - a)] \quad (6e)$$

$$n_2 = 2 - \alpha_2/\pi \quad (6f)$$

and by wedge # 1 by

$$E_{D1}(\vartheta) = e^{jkd_1 \cos(\gamma_1 - \vartheta)} \begin{cases} R_{D1}(\vartheta) & 3\pi/2 < \vartheta < 2\pi \\ R_{D1}'(\vartheta) & 0 < \vartheta < \pi \end{cases} \quad (7)$$

where

$$R_{D1}(\vartheta) = R_{D2}'(\pi/2) V_B[L_5, \vartheta - 3\pi/2, n_1] \quad (7a)$$

$$R_{D1}'(\vartheta) = R_{D2}'(\pi/2) V_B[L_5, \pi/2 + \vartheta, n_1] \quad (7b)$$

$$d_1 = [(L_6/2 + L_5 - H_1 \cos \alpha_3)^2 + (L_4 - a)^2]^{\frac{1}{2}} \quad (7c)$$

$$\gamma_1 = \tan^{-1} [(L_6/2 + L_5 - H_1 \cos \alpha_3) / (L_4 - a)] \quad (7d)$$

$$n_1 = 2 - \alpha_1/\pi \quad (7e)$$

Energy from the main source directed toward the tail section will be reflected. This reflected field may be obtained by the method of images.

Assuming that the tail section is an infinite, perfectly conducting ground plane and a source of known field distribution $R_D(\theta)$ is located at position 1, then the field distribution due to the image source is given, referring to Figure 5, as

$$E_{\text{DIMAGE}}(\theta) = e^{-jkd_i \cos(\gamma_i + \theta)} R_{\text{DIMAGE}}(\theta) \quad 5\pi/2 - 2\alpha_1 < \theta < 3\pi/2 + \alpha_2 - \psi_0 \quad (8)$$

where

$$R_{\text{DIMAGE}}(\theta) = R_D(\theta + \alpha_3 - 2\pi) \quad (8a)$$

$$d_i = [L_6^2 \sin^2 \alpha_1 - 2aL_6 \sin \alpha_1 \cos \alpha_1 + a^2]^{1/2} \quad (8b)$$

$$\gamma_i = \tan^{-1} [L_6 \sin^2 \alpha_1 / (L_6 \sin \alpha_1 \cos \alpha_1 - a)] \quad (8c)$$

Since each field component does not contribute in all space, a summary has been prepared which indicates the different field components and the region where each one contributes. This is shown in Table 1.

The analysis procedure for the case where the antenna is located in position 2 is similar to the one above. The "primary" field in the direction of wedges 1 and 2 will serve as the incident ray, and the amount diffracted will be determined by the diffraction coefficients of wedges 1 and 2, respectively. Now the field from wedges 1 and 2 in the direction of 10 and 9 and 3 and 4, respectively, will be diffracted again. This process will continue to higher order diffractions as in the previous case. Also part of the diffracted field from wedge 2 will be reflected by the surface of the fuselage. Figure 6 shows the diffraction mechanism for an antenna mounted on the tail section of the airplane. The image field contribution due to the reflections from the fuselage is also indicated.

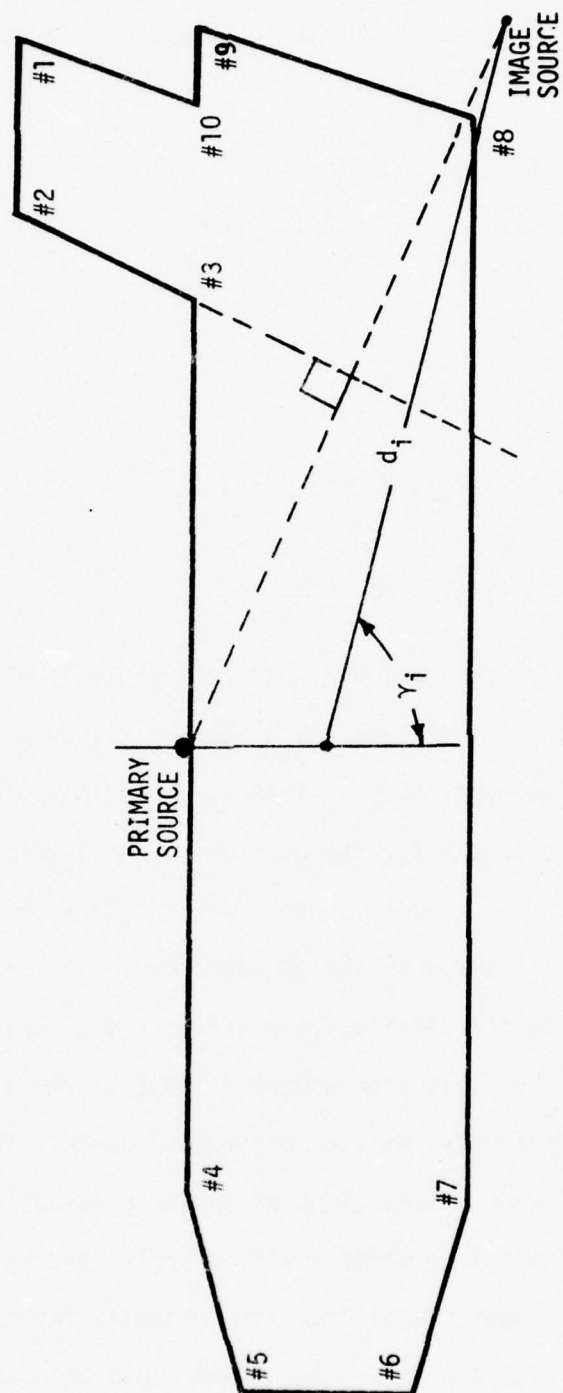


Figure 5. Geometry for image source description for antenna at position 1.

TABLE 1
FIELD REGIONS FOR POSITION 1

REGION	TOTAL FIELD	BOUNDARY
I	$E_D + E_{D1}' + E_{D2}' + E_{D3}' + E_{D4}' + E_{D5}'$	$0 < \theta < 3\pi/2 - \alpha_3$
II	$E_D + E_{D1}' + E_{D2}' + E_{D4}' + E_{D5}'$	$3\pi/2 - \alpha_3 < \theta < \alpha_x$
III	$E_{D1}' + E_{D2}' + E_{D4}' + E_{D5}'$	$\alpha_x < \theta < \pi/2 - \alpha_5$
IV	$E_{D1}' + E_{D2}' + E_{D4}'$	$\pi/2 - \alpha_5 < \theta < \pi/2 - \beta$
V	$E_{D1}' + E_{D2}'$	$\pi/2 - \beta < \theta < \pi/2$
VI	E_{D1}'	$\pi/2 < \theta < \alpha_6$
VII	$E_{D1}' + E_{D6}$	$\alpha_6 < \theta < \pi$
VIII	$E_{D5} + E_{D6}$	$\pi < \theta < \pi/2 + \alpha_4$
IX	$E_{D4} + E_{D5} + E_{D6}$	$\pi/2 + \alpha_4 < \theta < 3\pi/2 - \beta$
X	$E_{D2} + E_{D4} + E_{D5} + E_{D6}$	$3\pi/2 - \beta < \theta < 3\pi/2$
XI	$E_D + E_{D1}' + E_{D2}' + E_{D3}' + E_{D4}' + E_{D5}' + E_{D6}$	$3\pi/2 < \theta < 5\pi/2 - 2\alpha_7$
XII	$E_D + E_{D1}' + E_{D1}' + E_{D2}' + E_{D3}' + E_{D4}' + E_{D5}' + E_{D6}$	$5\pi/2 - 2\alpha_7 < \theta < 3\pi/2 + \alpha_2 - \psi_0$
XIII	$E_D + E_{D1}' + E_{D2}' + E_{D3}' + E_{D4}' + E_{D5}' + E_{D6}$	$3\pi/2 + \alpha_2 - \psi_0 < \theta < 2\pi$

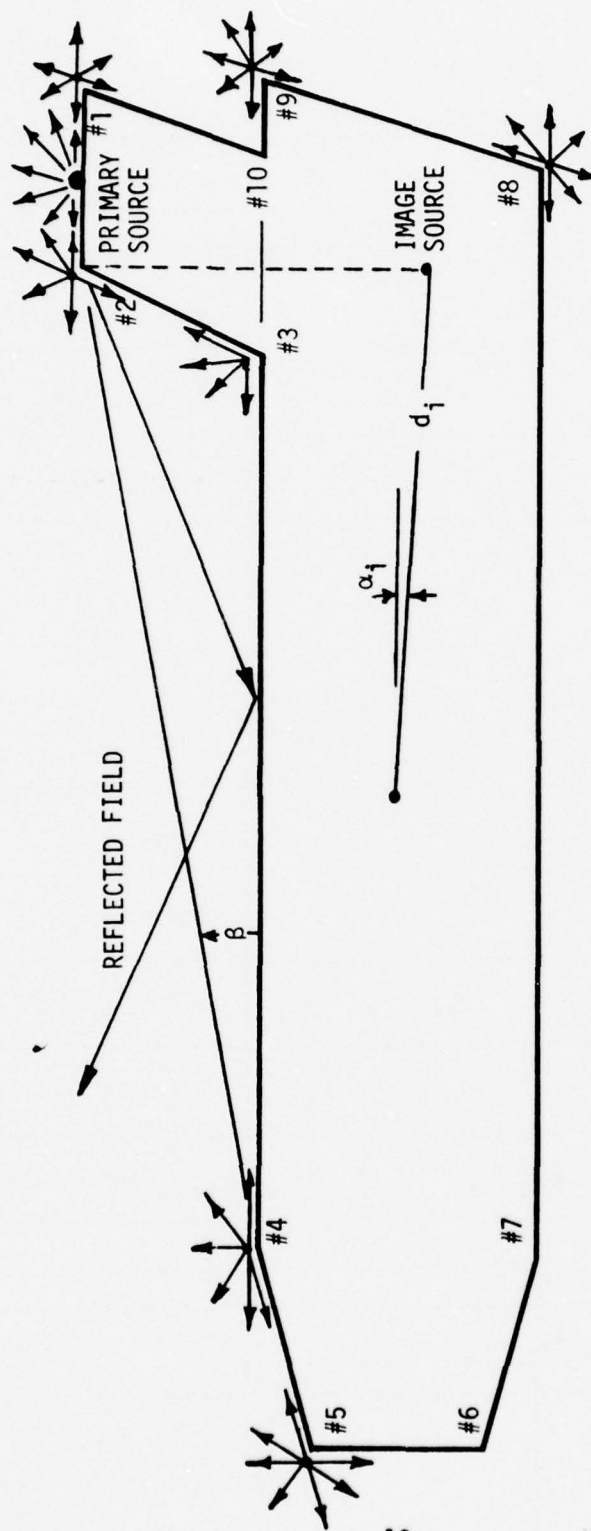


Figure 6. Radiation mechanism and pertinent dimensions for antenna at position 2.

The primary source contribution, when the antenna is mounted in position 2 as shown in Figure 6, is given by

$$E_D(\theta) = e^{+jkd_0 \sin(\gamma_0 + \theta)} R_D(\theta) \quad (9)$$

where

$$d_0 = [(L_6/2 + L_5/2 - H_1 \cos \alpha_3)^2 + (L_4 - a)^2]^{1/2} \quad (9a)$$

$$\gamma_0 = \tan^{-1}[(L_4 - a)/(L_6/2 + L_5/2 - H_1 \cos \alpha_3)] \quad (9b)$$

$R_D(\theta)$ is the angular field distribution when the antenna is mounted on an infinite ground plane.

The field diffractions from wedge #2 are given, referring to Figure 4, by

$$E_{D2}(\theta) = e^{+jkd_2 \cos(\gamma_2 - \theta)} \cdot \begin{cases} R_{D2}(\theta) & 3\pi/2 - \beta < \theta < 2\pi \\ R'_{D2}(\theta) & 0 < \theta < \pi/2 \end{cases} \quad (10)$$

where

$$R_{D2}(\theta) = R_D(3\pi/2) V_B[L_5/2, 5\pi/2 - \theta, n_2] \quad (10a)$$

$$R'_{D2}(\theta) = R_D(3\pi/2) V_B[L_5/2, \pi/2 - \theta, n_2] \quad (10b)$$

The quantities d_2, γ_2 , and n_2 are defined by Equations (6d) - (6f).

Similarly the contributions from wedge # 3 are given by

$$E_{D3}(\theta) = e^{jkd_3 \cos(\gamma_3 - \theta)} \cdot \begin{cases} R_{D3}(\theta) & 3\pi/2 < \theta < 2\pi \\ R'_{D3}(\theta) & 0 < \theta < 3\pi/2 - \alpha_3 \end{cases} \quad (11)$$

where

$$R_{D3}(\vartheta) = R_{D2}(\pi/2 + \alpha_2) V_B[H_1, 7\pi/2 - \alpha_3 - \vartheta, n_3] \quad (11a)$$

$$R'_{D3}(\vartheta) = R_{D2}(\pi/2 + \alpha_2) V_B[H_1, 3\pi/2 - \alpha_3 - \vartheta, n_3] \quad (11b)$$

with d_3 , γ_3 , and n_3 defined by Equations (5c) - (5e).

The diffractions from wedge # 4 are given, referring to Figure 3, by

$$E_{D4}(\vartheta) = e^{jkd_4 \cos(\gamma_4 + \vartheta)} \cdot \begin{cases} R_{D4}(\vartheta) & \pi/2 + \alpha_4 < \vartheta < 2\pi \\ R'_{D4}(\vartheta) & 0 < \vartheta < \pi/2 - \psi_0 \end{cases} \quad (12)$$

where

$$\begin{aligned} R_{D4}(\vartheta) &= R_{D3}(3\pi/2) V_B[L_6, 5\pi/2 - \vartheta, n_4] \\ &+ R_{D2}(3\pi/2 - \psi_0) [V_B(R, 5\pi/2 - \vartheta - \psi_0, n_4) + V_B(R, 5\pi/2 - \vartheta + \psi_0, n_4)] \end{aligned} \quad (12a)$$

$$\begin{aligned} R'_{D4}(\vartheta) &= R_{D3}(3\pi/2) V_B[L_6, \pi/2 - \vartheta, n_4] \\ &+ R_{D2}(3\pi/2 - \psi_0) [V_B(R, \pi/2 - \vartheta - \psi_0, n_4) + V_B(R, \pi/2 - \vartheta + \psi_0, n_4)] \end{aligned} \quad (12b)$$

which are attributed to diffractions from wedges # 3 and # 2. The quantities d_4 , γ_4 , and n_4 are defined by Equations (2c) - (2e).

The contributions from wedge #5 are given by

$$E_{D5}(\vartheta) = e^{jkd_5 \cos(\gamma_5 + \vartheta)} \cdot \begin{cases} R_{D5}(\vartheta) & \pi < \vartheta < 2\pi \\ R'_{D5}(\vartheta) & 0 < \vartheta < \pi - \alpha_5 \end{cases} \quad (13)$$

where

$$R_{D5}(\vartheta) = R_{D4}(\pi/2 + \alpha_4) V_B[-L_1/\cos\alpha_4, 3\pi/2 + \alpha_4 - \vartheta, n_5] \quad (13a)$$

$$R'_{D5}(\theta) = R_{D4}(\pi/2 + \alpha_4) V_B[-L_1/\cos\alpha_4, \alpha_4 - \pi/2 - \theta, n_5] \quad (13b)$$

where d_5 , γ_5 , and n_5 are defined by Equations (3c) - (3e).

Finally the diffractions from wedge # 1 are given, referring to Figure 4, by

$$E_{D1}(\theta) = e^{jkd_1 \cos(\gamma_1 - \theta)} \cdot \begin{cases} R_{D1}(\theta) & 3\pi/2 < \theta < 2\pi \\ R'_{D1}(\theta) & 0 < \theta < \pi \end{cases} \quad (14)$$

where

$$R_{D1}(\theta) = R_D(\pi/2) V_B[L_5/2, \theta - 3\pi/2, n_1] \quad (14a)$$

$$R'_{D1}(\theta) = R_D(\pi/2) V_B[L_5/2, \pi/2 + \theta, n_1] \quad (14b)$$

with the quantities d_1 , γ_1 , and n_1 defined by Equations (7c) - (7e).

As was shown in Figure 6, part of the energy diffracted by wedge # 2 is directed toward the fuselage where it undergoes a reflection. To account for this reflection, an image source is introduced and its contribution is given by

$$E_{DIMAGE}(\theta) = e^{jkd_i \sin(3\pi - \alpha_i)} R_{DIMAGE}(\theta) \quad 3\pi/2 + \beta < \theta < \pi/2 + \alpha_3 \quad (15)$$

where

$$R_{DIMAGE}(\theta) = R_{D2}(3\pi - \theta) \quad (15a)$$

$$d_i = [(L_6/2 - H_1 \cos\alpha_3)^2 + (L_4 - 3a)^2]^{1/2} \quad (15b)$$

$$\alpha_i = \cos^{-1}[(L_6/2 - H_1 \cos\alpha_3)/d_i] \quad (15c)$$

Additional diffractions occur at wedges # 10, # 9, and # 8 but their mathematical forms will not be reported here to preserve some space. Their contribution is of secondary order and will not contribute significantly. However they have been included in the computer program and all the components and the regions where they contribute are shown in Table 2.

B. Wedge Model With Curved Edge

A more advanced modeling of the elevation plane of an aircraft will be to represent the surface with sharp wedges, as was done in the previous section and indicated now in Figure 7, but with a curved geometry in the transverse plane, as shown in Figure 8. In other words the aircraft structure is modeled with a number of truncated conical cylinders. For this geometry, two antenna positions are examined, one below the nose and designated as #1 and the other above the cockpit and designated as #2. These two positions were selected because they represent locations which are available for placing antennas and are near the forward (nose) region where coverage is of primary concern for the MLS. The nose was also modeled by a truncated cylinder because it was assumed that the radome cover was absent. Such a simplification was necessary to reduce the mathematical details, and, as will be shown later by comparing computed values with measured data, it does adequately represent the radiation mechanism in the forward sector of the aircraft structure.

The radiation mechanism for each antenna position is similar to the one described in the previous section with the exception of an additional factor which is used to represent the curvature in the transverse plane. The phase reference is chosen again to be the center of the fuselage as shown in Figure 7. Before presenting the mathematical equations for the contributions from the

TABLE 2
FIELD REGIONS FOR POSITION 2

REGION	TOTAL FIELD	BOUNDARY
I	$E_D + E_{D1}' + E_{D2}' + E_{D3}' + E_{D4}' + E_{D5}' + E_{D9}'$	$0 < \theta < \alpha_8 - \pi/2$
II	$E_D + E_{D1}' + E_{D2}' + E_{D3}' + E_{D4}' + E_{D5}' + E_{D8}' + E_{D9}'$	$\alpha_8 - \pi/2 < \theta < 3\pi/2 - \alpha_3$
III	$E_D + E_{D1}' + E_{D2}' + E_{D4}' + E_{D5}' + E_{D8}' + E_{D9}'$	$3\pi/2 - \alpha_3 < \theta < \pi - \alpha_5$
IV	$E_D + E_{D1}' + E_{D2}' + E_{D4}' + E_{D8}' + E_{D9}'$	$\pi - \alpha_5 < \theta < \pi/2 - \beta$
V	$E_D + E_{D1}' + E_{D2}' + E_{D8}' + E_{D9}'$	$\pi/2 - \beta < \theta < \pi/2$
VI	$E_{D1}' + E_{D8}' + E_{D9}'$	$\pi/2 < \theta < \pi$
VII	$E_{D5}' + E_{D8}' + E_{D9}'$	$\pi < \theta < 3\pi/2 - \alpha_7$
VIII	$E_{D5}' + E_{D8}'$	$3\pi/2 - \alpha_7 < \theta < \pi/2 + \alpha_4$
IX	$E_{D4}' + E_{D5}' + E_{D8}'$	$\pi/2 + \alpha_4 < \theta < 3\pi/2 - \beta$
X	$E_{D2}' + E_{D4}' + E_{D5}' + E_{D8}'$	$3\pi/2 - \beta < \theta < 3\pi/2$
XI	$E_D + E_{D1}' + E_{D2}' + E_{D3}' + E_{D4}' + E_{D5}'$	$3\pi/2 < \theta < 3\pi/2 + \beta$
XII	$E_D + E_{D1}' + E_{D1}' + E_{D2}' + E_{D3}' + E_{D4}' + E_{D5}'$	$3\pi/2 + \beta < \theta < \pi/2 + \alpha_3$
XIII	$E_D + E_{D1}' + E_{D2}' + E_{D3}' + E_{D4}' + E_{D5}'$	$\pi/2 + \alpha_3 < \theta < 2\pi$

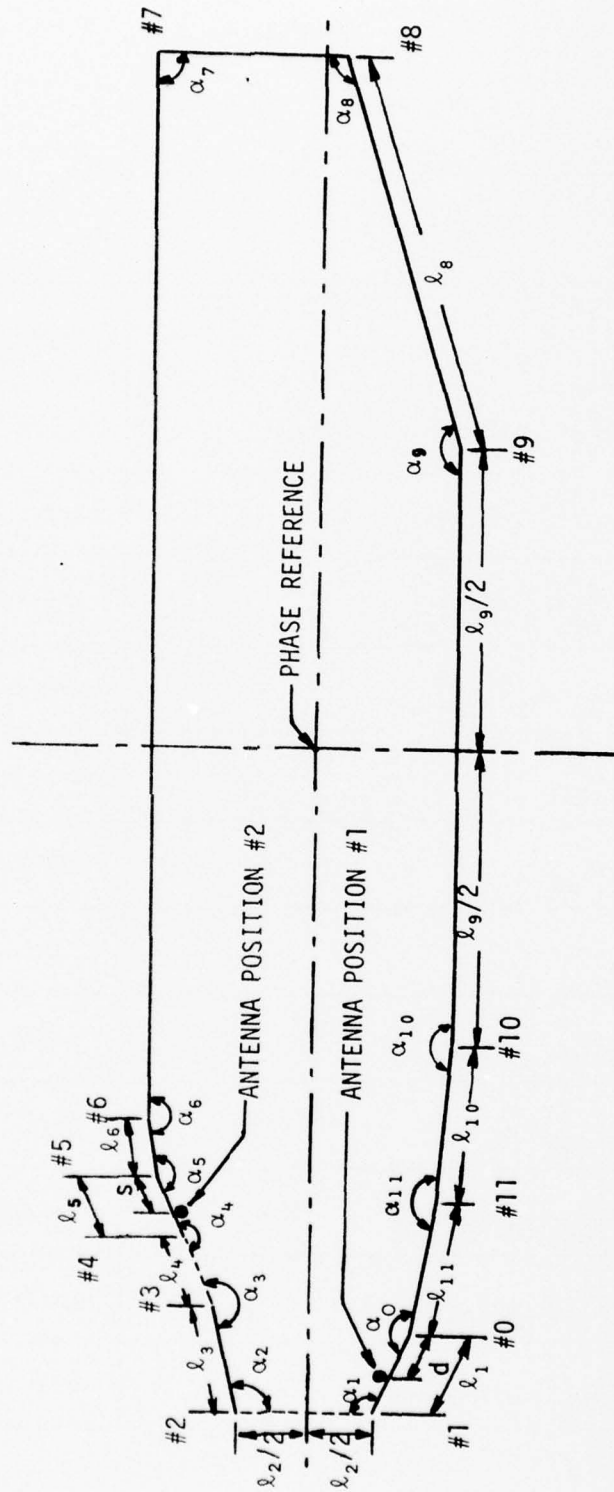


Figure 7. Wedge surface model of elevation plane configuration.

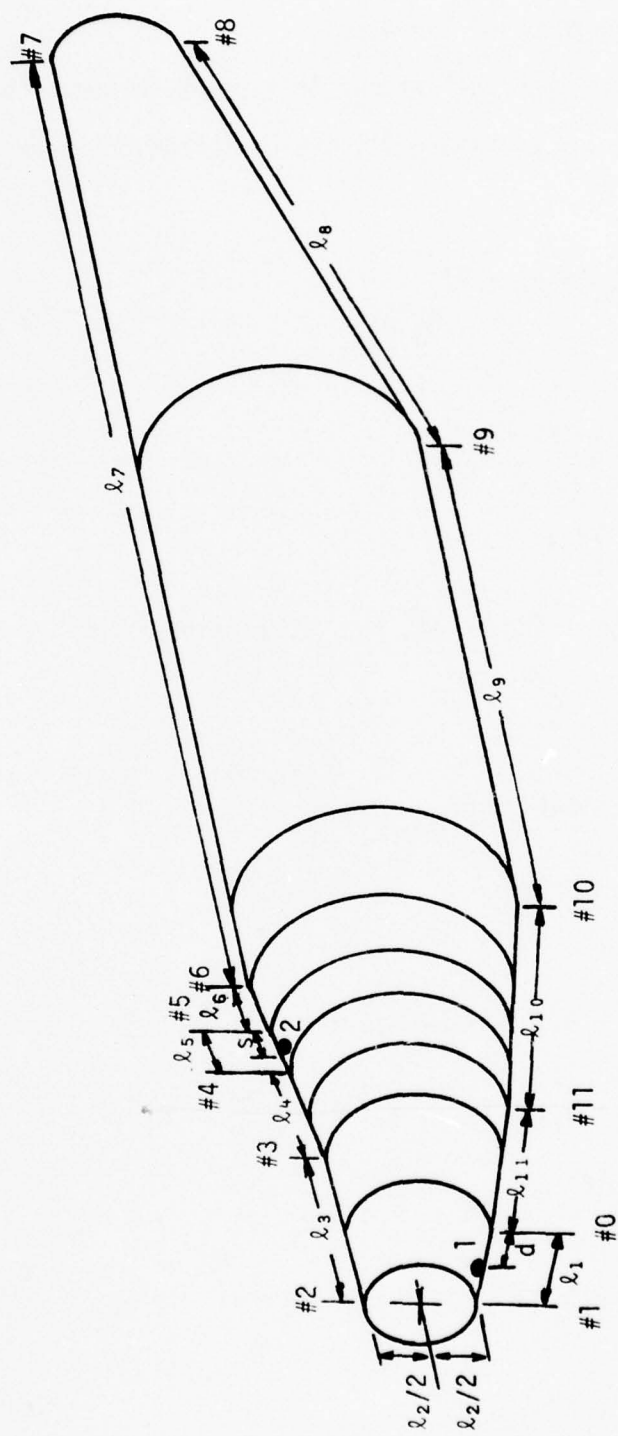


Figure 8. Conical cylinder modeling of elevation plane configuration.

main source and from each wedge, some pertinent dimensions are shown in Figures 9 and 10. The structure is split into two to more clearly illustrate the main features of the model.

The radiation when the antenna is located in position #1 will first be examined. Referring to Figure 11, the contributions from the main source are given by

$$E_D(\theta) = e^{jkd_{s_1} \cos(\beta_{s_1} - \theta)} R_D(\theta) \quad 0 < \theta < \alpha_1, \pi + \alpha_1 < \theta < 2\pi \quad (16)$$

where

$$d_{s_1} = [f_{s_1}^2 + g_{s_1}^2]^{1/2} \quad (16a)$$

$$\beta_{s_1} = \tan^{-1}[f_{s_1}/g_{s_1}] \quad (16b)$$

From the geometry of Figure 11, the diffractions from wedge # 1 can be written as

$$E_{D1}(\theta) = e^{jkd_1 \cos(\beta_1 - \theta)} DF_1(\theta) \cdot \begin{cases} R_{D1}(\theta) & 0 < \theta < \pi \\ R'_{D1}(\theta) & \pi + \alpha_1 < \theta < 2\pi \end{cases} \quad (17)$$

where

$$R_{D1}(\theta) = R_D(\theta = \alpha_1) V_B[\ell_1 - d_1, \pi - \alpha_1 + \theta, n_1] \quad (17a)$$

$$R'_{D1}(\theta) = R_D(\theta = \alpha_1) V_B[\ell_1 - d_1, \theta - \alpha_1 - \pi, n_1] \quad (17b)$$

$$d_1 = [f_1^2 + g_1^2]^{1/2} \quad (17c)$$

$$\beta_1 = \tan^{-1}[f_1/g_1] \quad (17d)$$

$$n_1 = 2 \quad (17e)$$

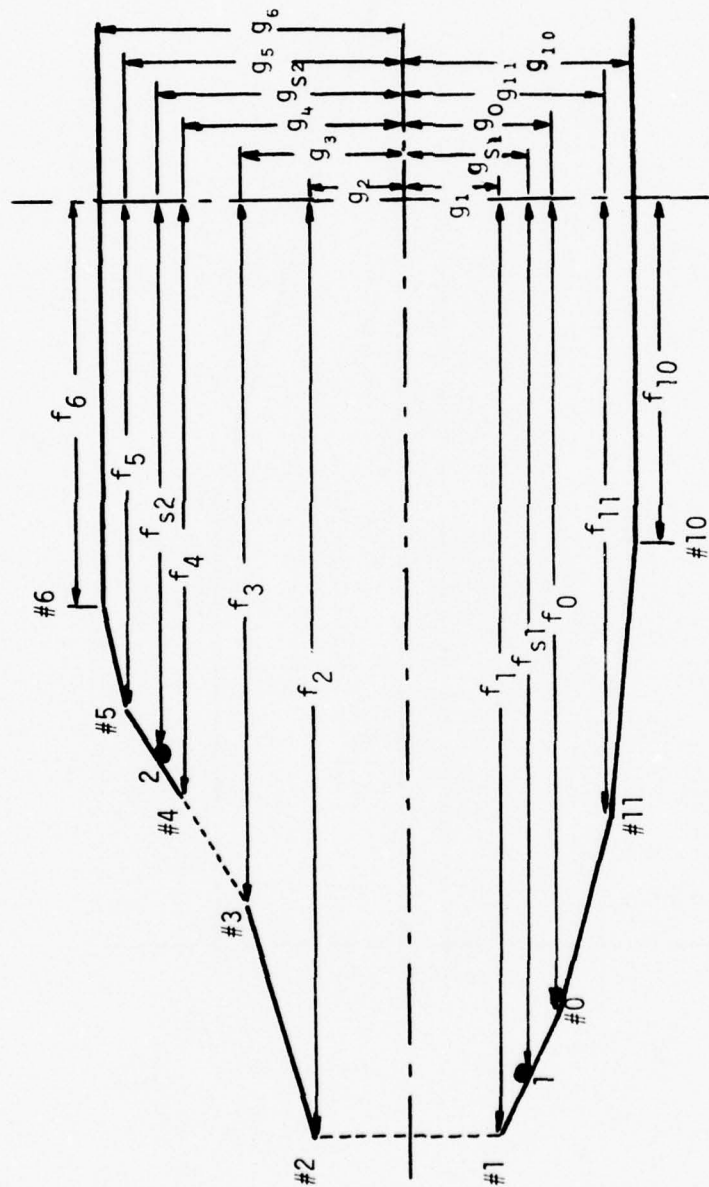


Figure 9. Forward sector geometry of elevation plane.

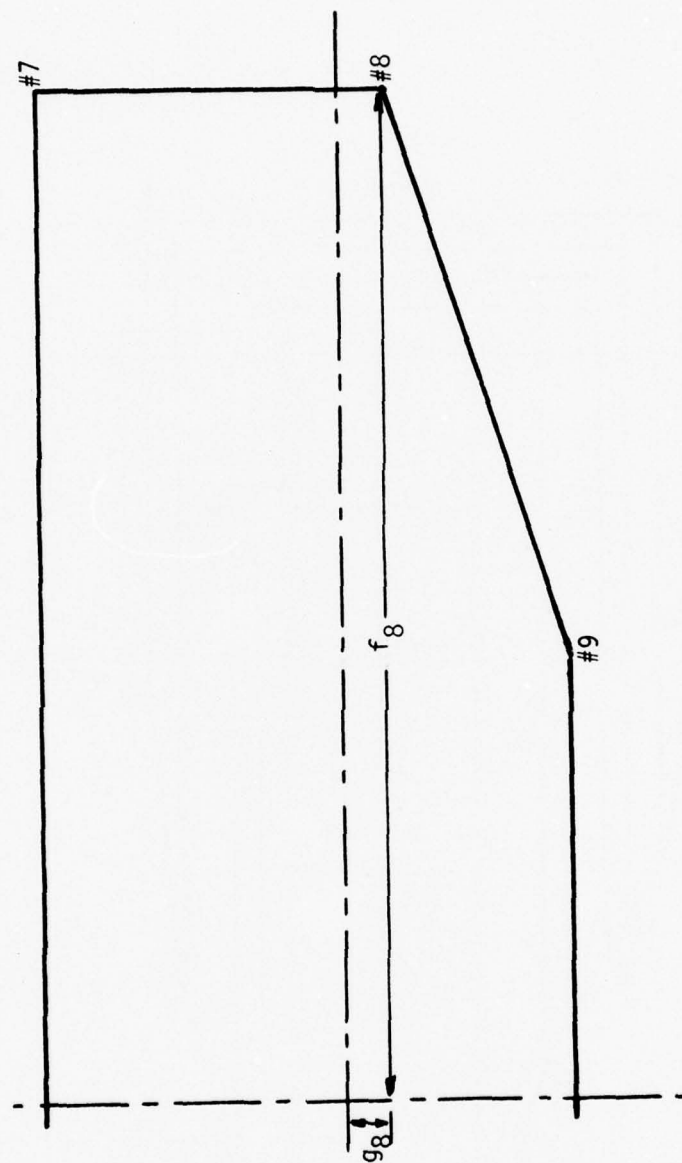


Figure 10. Rear sector geometry of elevation plane.

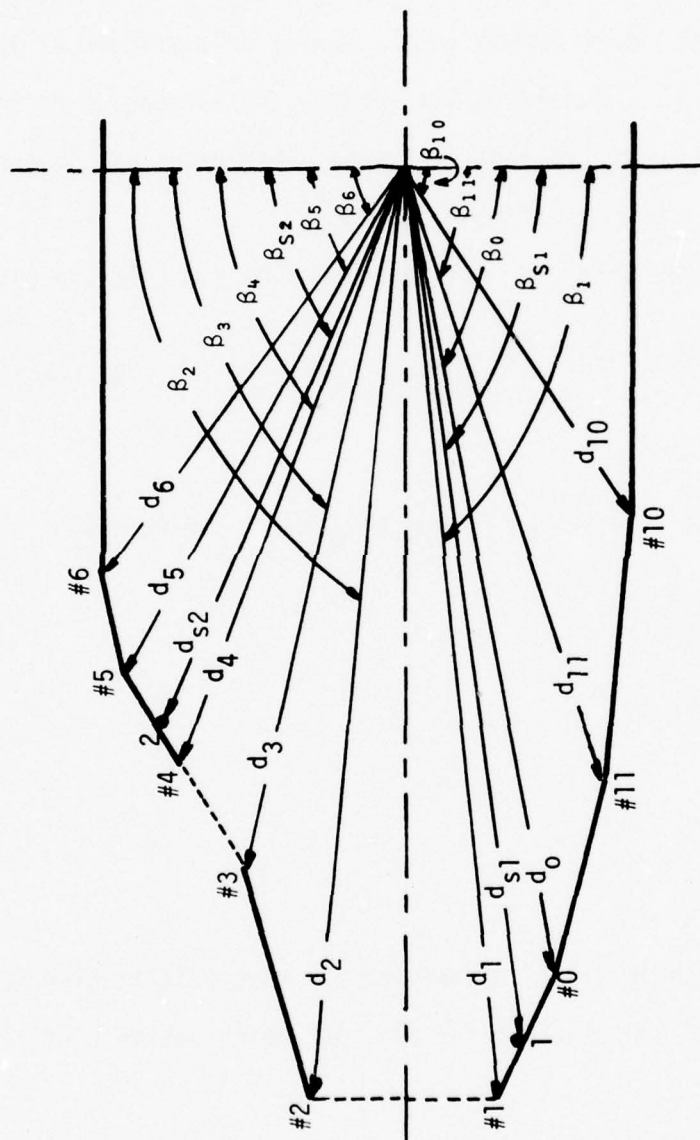


Figure 11. Pertinent dimensions for radiation mechanism in the elevation plane from the forward sector.

$$DF_1(\theta) = \begin{cases} \left[\frac{g_1}{g_1 + (\ell_1 - d)[\sin(\alpha_1 - \pi/2) + \cos\theta]} \right]^{1/2} & 0 < \theta < \alpha_1 \\ & \pi + \alpha_1 < \theta < 2\pi \\ 1 & \text{elsewhere} \end{cases} \quad (17f)$$

The ray divergence factor given by (17f) is used to take into account the spreading of the energy caused by the radius of curvature of the edge¹⁶ (see Appendix B). Outside the lit region, the divergence factor has been approximated by unity since it approaches that value and it avoids the pole indicating the presence of the caustic.

In a similar manner the diffractions from wedge #2 are given by

$$E_{D2}(\theta) = e^{-jkd_2 \cos(\beta_2 + \theta)} DF_2(\theta) R_{D2}(\theta) \quad 0 < \theta < 2\pi - \alpha_2 \quad (18)$$

where

$$R_{D2}(\theta) = R_{D1}(\theta = \pi)[V_B(\ell_2, \theta, n_2) \pm V_B(\ell_2, 2\alpha_2 + \theta, n_2)] \quad (18a)$$

$$d_2 = [f_1^2 + g_1^2]^{1/2} \quad (18b)$$

$$\beta_2 = \tan^{-1}[f_1/g_1] \quad (18c)$$

$$n_2 = 2 \quad (18d)$$

$$DF_2(\theta) = 1 \quad (18e)$$

The plus (+) sign in (18a) is used for the hard polarization (E-field normal to the edge) and the minus(-) for the soft polarization (E-field parallel to the edge).

The diffractions from wedge # 3 can be written as

$$E_{D3}(\theta) = e^{-jkd_3 \cos(\beta_3 + \theta)} DF_3(\theta) R_{D3}(\theta) \quad \pi - \alpha_2 < \theta < 3\pi - \alpha_3 - \alpha_2 \quad (19)$$

where

$$R_{D3}(\theta) = R_{D2}(\theta = 2\pi - \alpha_2) V_B[\lambda_3, \theta + \alpha_2 - \pi, n_3] \quad (19a)$$

$$d_3 = [f_3^2 + g_3^2]^{1/2} \quad (19b)$$

$$\beta_3 = \tan^{-1}[f_3/g_3] \quad (19c)$$

$$n_3 = 2 - \alpha_3/\pi \quad (19d)$$

$$DF_3(\theta) = 1 \quad (19e)$$

Diffractions from wedges #4, #5, #6, and #7 are far removed from the primary source and are considered of secondary order. They are not included in the computations.

The diffractions from the wedges nearest to the source in the counter-clockwise direction will now be considered. From the geometry of Figure 11, the contributions from wedge #0 can be written as

$$E_{D0}(\theta) = e^{jkd_0 \cos(\beta_0 - \theta)} DF_0(\theta) \cdot \begin{cases} R_{D0}(\theta) & 0 < \theta < \alpha_1 \\ R'_{D0}(\theta) & \alpha_1 + \alpha_0 < \theta < 2\pi \end{cases} \quad (20)$$

where

$$R_{D0}(\theta) = R_D(\theta = \pi + \alpha_1) V_B[d, \alpha_1 - \theta, n_0] \quad (20a)$$

$$R'_{D0}(\theta) = R_D(\theta = \pi + \alpha_1) V_B[d, 2\pi + \alpha_1 - \theta, n_0] \quad (20b)$$

$$d_0 = [f_0^2 + g_0^2]^{1/2} \quad (20c)$$

$$\beta_0 = \tan^{-1}[f_0/g_0] \quad (20d)$$

$$n_0 = 2 - \alpha_0/\pi \quad (20e)$$

$$DF_0(\theta) = \begin{cases} \left[\frac{g_0}{g_0 - d[\sin(\alpha_1 - \pi/2) - \cos\theta]} \right]^{1/2} & \begin{array}{l} 0 < \theta < \alpha_1 \\ \pi + \alpha_1 < \theta < 2\pi \end{array} \\ 1 & \text{elsewhere} \end{cases} \quad (20f)$$

The contributions from wedge #11 are given by

$$E_{D11}(\theta) = e^{jkd_{11}\cos(\beta_{11} - \theta)} DF_{11}(\theta) \cdot \begin{cases} R_{D11}(\theta) & 0 < \theta < \alpha_0 + \alpha_1 - \pi \\ R'_{D11}(\theta) & \alpha_0 + \alpha_1 + \alpha_{11} - \pi < \theta < 2\pi \end{cases} \quad (21)$$

where

$$R_{D11}(\theta) = R'_{D0}(\theta = \alpha_0 + \alpha_1) V_B[l_{11}, \alpha_0 + \alpha_1 - \theta - \pi, n_{11}] \quad (21a)$$

$$R'_{D11}(\theta) = R'_{D0}(\theta = \alpha_0 + \alpha_1) V_B[l_{11}, \alpha_0 + \alpha_1 - \theta + \pi, n_{11}] \quad (21b)$$

$$d_{11} = [f_{11}^2 + g_{11}^2]^{1/2} \quad (21c)$$

$$\beta_{11} = \tan^{-1}[f_{11}/g_{11}] \quad (21d)$$

$$n_{11} = 2 - \alpha_{11}/\pi \quad (21e)$$

$$DF_{11}(\theta) = 1 \quad (21f)$$

Continuing in the counterclockwise direction, the contribution from wedge # 10 can be written as

$$E_{10}(\theta) = e^{jkd_{10}\cos(\beta_{10} - \theta)} DF_{10}(\theta) \cdot \begin{cases} R_{D10}(\theta) & 0 < \theta < 3\pi/2 - \alpha_{10} \\ R'_{D10}(\theta) & 3\pi/2 < \theta < 2\pi \end{cases} \quad (22)$$

where

$$R_{D10}(\theta) = R_{D11}'(\theta = \alpha_0 + \alpha_1 + \alpha_{11} - \pi) V_B[\ell_{10}, 3\pi/2 - \alpha_{10} - \theta, n_{10}] \quad (22a)$$

$$R_{D10}'(\theta) = R_{D11}'(\theta = \alpha_0 + \alpha_1 + \alpha_{11} - \pi) V_B[\ell_{10}, 7\pi/2 - \alpha_{10} - \theta, n_{10}] \quad (22b)$$

$$d_{10} = [f_{10}^2 + g_{10}^2]^{1/2} \quad (22c)$$

$$\beta_{10} = \tan^{-1}[f_{10}/g_{10}] \quad (22d)$$

$$n_{10} = 2 - \alpha_{10}/\pi \quad (22e)$$

$$DF_{10}(\theta) = 1 \quad (22f)$$

Referring to Figure 12 the contributions from wedge # 9 are given by

$$E_{D9}(\theta) = e^{jkd_9 \cos(\beta_9 + \theta)} DF_9(\theta) \cdot \begin{cases} R_{D9}(\theta) & 0 < \theta < \pi/2 \\ R_{D9}'(\theta) & \pi/2 + \alpha_9 < \theta < 2\pi \end{cases} \quad (23)$$

where

$$R_{D9}(\theta) = R_{D10}'(\theta = 3\pi/2) V_B[\ell_9, \pi/2 - \theta, n_9] \quad (23a)$$

$$R_{D9}'(\theta) = R_{D10}'(\theta = 3\pi/2) V_B[\ell_9, 5\pi/2 - \theta, n_9] \quad (23b)$$

$$d_9 = [f_{10}^2 + g_{10}^2]^{1/2} = d_{10} \quad (23c)$$

$$\beta_9 = \tan^{-1}[f_{10}/g_{10}] = \beta_{10} \quad (23d)$$

$$n_9 = 2 - \alpha_9/\pi \quad (23e)$$

$$DF_9(\theta) = 1 \quad (23f)$$

and finally from wedge # 8 by

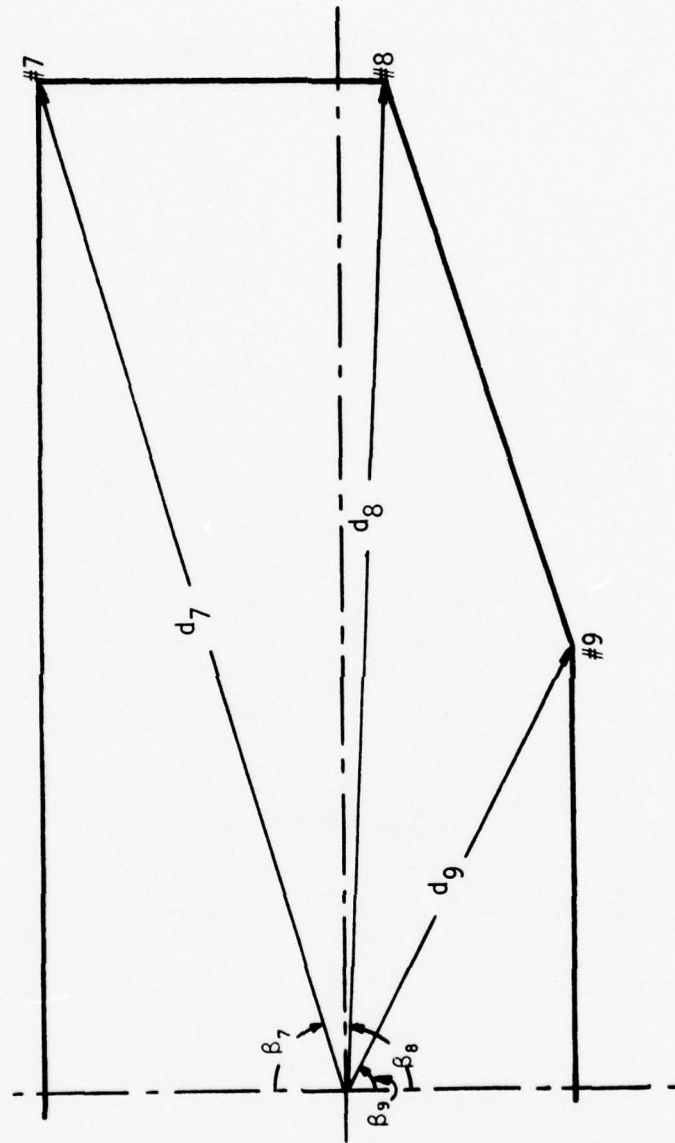


Figure 12. Pertinent dimensions for radiation mechanism in the elevation plane from the rear sector.

$$E_{D8}(\theta) = e^{-jkd_8 \cos(\theta + \beta_8)} DF_8(\theta) \cdot \begin{cases} R_{D8}(\theta) & 0 < \theta < \pi - \alpha_8 \\ R'_{D8}(\theta) & \pi < \theta < 2\pi \end{cases} \quad (24)$$

where

$$R_{D8}(\theta) = R'_{D9}(\theta = \pi/2 + \alpha_9) V_B[\ell_8, \pi - \alpha_8 - \theta, n_8] \quad (24a)$$

$$R'_{D8}(\theta) = R'_{D9}(\theta = \pi/2 + \alpha_9) V_B[\ell_8, 3\pi - \alpha_8 - \theta, n_8] \quad (24b)$$

$$d_8 = [f_8^2 + g_8^2]^{1/2} \quad (24c)$$

$$\beta_8 = \tan^{-1}[f_8/g_8] \quad (24d)$$

$$n_8 = 2 - \alpha_8/\pi \quad (24e)$$

$$DF_8(\theta) = 1 \quad (24f)$$

The analysis when the antenna is placed above the cockpit (#2 position in Figure 7) is similar to the one outlined for position # 1. The only difference will be that for position #2 a reflected component will be included to take into account the energy scattered by the forward sector of the nose (section ℓ_3 of Figure 7). Referring to Figures 11 and 12, the contributions from the main source and diffractions from each wedge will be outlined when the antenna is positioned above the cockpit.

The radiation from the main source is given by

$$E_D(\theta) = e^{-jkd_{s2} \cos(\beta_{s2} + \theta)} R_D(\theta) \quad \alpha_3 + \alpha_5 + \alpha_6 - \sigma - 5\pi/2 < \theta < 3\pi - \alpha_3 - \alpha_2 \quad (25)$$

$$\text{where } \sigma = \sin^{-1}[-(\ell_4 - \ell_5 - s) \sin \alpha_3 / h] \quad (25a)$$

$$h = [\ell_3^2 + (\ell_4 + \ell_5 - s)^2 - 2\ell_3(\ell_4 + \ell_5 - s)\cos\alpha_3]^{1/2} \quad (25b)$$

$$d_{s2} = [f_{s2}^2 + g_{s2}^2]^{1/2} \quad (25c)$$

$$\beta_{s2} = \tan^{-1}[f_{s2}/g_{s2}] \quad (25d)$$

As before, $R_D(\theta)$ is the angular far-field distribution when the source is mounted on an infinite ground plane.

The diffraction contributions from wedge #5 are given by

$$E_{D5}(\theta) = e^{-jkd_5 \cos(\theta + \beta_5)} DF_5(\theta) R_{D5}(\theta) \quad \delta_5 < \theta < \pi/2 + \alpha_6 \quad (26)$$

where

$$\delta_5 = \tan^{-1}[(f_2 - f_5)/(g_5 - g_2)] \quad (26a)$$

$$R_{D5}(\theta) = R_D(\theta = 3\pi - \alpha_3 - \alpha_2) V_B[s, \theta + \alpha_3 + \alpha_2 - 2\pi, n_5] \quad (26b)$$

$$d_5 = [f_5^2 + g_5^2]^{1/2} \quad (26c)$$

$$\beta_5 = \tan^{-1}[f_5/g_5] \quad (26d)$$

$$n_5 = 2 - \alpha_5/\pi \quad (26e)$$

$$DF_5(\theta) = \begin{cases} \left[\frac{g_5}{g_5 - s[\cos(\alpha_3 + \alpha_2) + \cos\theta]} \right]^{1/2} & \alpha_3 + \alpha_5 + \alpha_6 - \sigma - 5\pi/2 < \theta < 3\pi - \alpha_3 - \alpha_2 \\ 1 & \text{elsewhere} \end{cases} \quad (26f)$$

from wedge # 6 by

$$E_{D6}(\theta) = e^{-jkd_6 \cos(\beta_6 + \theta)} DF_6(\theta) R_{D6}(\theta) \quad \alpha_6 - \pi/2 < \theta < 3\pi/2 \quad (27)$$

where

$$R_{D6}(\vartheta) = R_{D5}(\vartheta = \pi/2 + \alpha_6) V_B[\lambda_6, \vartheta - \alpha_6 + \pi/2, n_6] \quad (27a)$$

$$d_6 = [f_6 + g_6]^{1/2} \quad (27b)$$

$$\beta_6 = \tan^{-1}[f_6/g_6] \quad (27c)$$

$$n_6 = 2 - \alpha_6/\pi \quad (27d)$$

$$DF_6(\vartheta) = 1 \quad (27e)$$

and from wedge # 7 by

$$E_{D7}(\vartheta) = e^{-jkd_7 \cos(\beta_7 - \vartheta)} DF_7(\vartheta) R_{D7}(\vartheta) \quad \pi/2 < \vartheta < 2\pi \quad (28)$$

where

$$R_{D7}(\vartheta) = R_{D6}(\vartheta = 3\pi/2) V_B[\lambda_7, \vartheta - \pi/2, n_7] \quad (28a)$$

$$\lambda_7 = f_6 + f_8 \quad (28b)$$

$$d_7 = [f_8^2 + g_6^2]^{1/2} \quad (28c)$$

$$\beta_7 = \tan^{-1}[f_8/g_6] \quad (28d)$$

$$n_7 = 2 - \alpha_7/\pi \quad (28e)$$

$$DF_7(\vartheta) = 1 \quad (28f)$$

Considering the wedges in the counterclockwise direction relative to the source, their contributions can be written in the same form as for the previous wedges. The diffractions from wedge # 4 are written as

$$E_{D4}(\vartheta) = e^{-jkd_4 \cos(\beta_4 + \vartheta)} DF_4(\vartheta) R_{D4}(\vartheta) \quad \delta_4 < \vartheta < 3\pi - \alpha_3 - \alpha_2 \quad (29)$$

where

$$\delta_4 = \tan^{-1}[(f_2 - f_4)/(g_4 - g_2)] \quad (29a)$$

$$R_{D4}(\theta) = R_D(\theta = 2\pi - \alpha_3 - \alpha_2) V_B[\ell_5 - s, 3\pi - \theta - \alpha_3 - \alpha_2, n_4] \quad (29b)$$

$$d_4 = [f_4^2 + g_4^2]^{1/2} \quad (29c)$$

$$\beta_4 = \tan^{-1}[f_4/g_4] \quad (29d)$$

$$n_4 = 2 \quad (29e)$$

$$DF_4(\theta) = \begin{cases} \left[\frac{g_4}{g_4 + (\ell_5 - s)[\cos(\alpha_3 + \alpha_2) - \cos\theta]} \right]^{1/2} & \alpha_3 + \alpha_5 + \alpha_6 - \sigma - 5\pi/2 < \theta < 3\pi - \alpha_3 - \alpha_2 \\ 1 & \text{elsewhere} \end{cases} \quad (29f)$$

and from wedge # 3 by

$$E_{D3}(\theta) = e^{-jkd_3 \cos(\beta_3 + \theta)} DF_3(\theta) R_{D3}(\theta) \quad \pi - \alpha_2 < \theta < 3\pi - \alpha_3 - \alpha_2 \quad (30)$$

where

$$R_{D3}(\theta) = R_{D4}(\theta = 2\pi - \alpha_3 - \alpha_2) [V_B(\ell_4, 3\pi - \theta - \alpha_2 - \alpha_3, n_3) \pm V_B(\ell_4, 3\pi - \theta - \alpha_2 + \alpha_3, n_3)] \quad (30a)$$

$$d_3 = [f_3^2 + g_3^2]^{1/2} \quad (30b)$$

$$\beta_3 = \tan^{-1}[f_3/g_3] \quad (30c)$$

$$n_3 = 2 \quad (30d)$$

$$DF_3(\theta) = \begin{cases} \left[\frac{g_3}{g_3 + \ell_4[\cos(\alpha_3 + \alpha_2) - \cos\theta]} \right]^{1/2} & \alpha_3 + \alpha_5 + \alpha_6 - \sigma - 5\pi/2 < \theta < 3\pi - \alpha_3 - \alpha_2 \\ 1 & \text{elsewhere} \end{cases} \quad (30e)$$

It should be pointed out that the dashed section shown between wedges #3 and #4 in Figure 7 represents an opening to model the window in the aircraft. The plus(+) sign between the two terms within the brackets in (30a) is used for the hard polarization (E-field normal to the edge) and the minus(-) for the soft polarization (E-field parallel to the edge).

Now the diffractions from wedge #2 will be outlined. There will be three waves which will be incident upon wedge #2 that will be diffracted; namely, radiation from the main source directed toward wedge #2 and diffractions from wedges 4 and 3. The total contributions from wedge #2 are then given by

$$E_{D2}(\theta) = e^{-jkd_2 \cos(\beta_2 + \theta)} [DF_{21}(\theta) R_{D21}(\theta) + DF_{22}(\theta) R_{D22}(\theta) + DF_{23}(\theta) R_{D23}(\theta)]$$

$$0 < \theta < \pi + \delta_5 \quad (31)$$

where

$$R_{D21}(\theta) = R_D(\theta = \pi - \alpha_2 - \sigma) [V_B(h, 2\pi - \alpha_2 - \theta - \sigma, n_2) \pm V_B(h, 2\pi - \alpha_2 - \theta + \sigma, n_2)] \quad (31a)$$

$$R_{D22}(\theta) = R_{D3}(\theta = \pi - \alpha_2) V_B[\ell_3, 2\pi - \alpha_2 - \theta, n_2] \quad (31b)$$

$$R_{D23}(\theta) = R_{D4}(\theta = \delta_4) [V_B(q, \pi - \theta + \delta_4, n_2) \pm V_B(q, 3\pi - 2\alpha_2 - \theta - \delta_4, n_2)] \quad (31c)$$

$$q = [(f_2 - f_4)^2 + (g_4 - g_2)^2]^{1/2} \quad (31d)$$

$$d_2 = [f_2^2 + g_2^2]^{1/2} \quad (31e)$$

$$\beta_2 = \tan^{-1}[f_2/g_2] \quad (31f)$$

$$n_2 = 2 \quad (31g)$$

$$DF_{21}(\vartheta) = \begin{cases} \left[\frac{g_2}{g_2 - h[\cos(\sigma + \alpha_2) + \cos\vartheta]} \right]^{1/2} & \alpha_3 + \alpha_5 + \alpha_6 - \sigma - 5\pi/2 < \vartheta < 3\pi - \alpha_3 - \alpha_2 \\ 1 & \text{elsewhere} \end{cases} \quad (31h)$$

$$DF_{22}(\vartheta) = \begin{cases} \left[\frac{g_2}{g_2 - \ell_3[\cos\alpha_2 + \cos\vartheta]} \right]^{1/2} & \alpha_3 + \alpha_5 + \alpha_6 - \sigma - 5\pi/2 < \vartheta < 3\pi - \alpha_3 - \alpha_2 \\ 1 & \text{elsewhere} \end{cases} \quad (31i)$$

$$DF_{23}(\vartheta) = \begin{cases} \left[\frac{g_2}{g_2 + q[\cos\delta_4 - \cos\vartheta]} \right]^{1/2} & \alpha_3 + \alpha_5 + \alpha_6 - \sigma - 5\pi/2 < \vartheta < 3\pi - \alpha_3 - \alpha_2 \\ 1 & \text{elsewhere} \end{cases} \quad (31j)$$

In continuation, the diffractions from wedge #1 are written as

$$E_{D1}(\vartheta) = e^{jkd_1 \cos(\beta_1 - \vartheta)} DF_1(\vartheta) \cdot \begin{cases} R_{D1}(\vartheta) & 0 < \vartheta < \pi \\ R'_{D1}(\vartheta) & \pi + \alpha_1 < \vartheta < 2\pi \end{cases} \quad (32)$$

where

$$R_{D1}(\vartheta) = R_{D2}(\vartheta=0)[V_B(\ell_2, \pi - \vartheta, n_1) \pm V_B(\ell_2, \pi - \vartheta + 2\alpha_1, n_1)] \quad (32a)$$

$$R'_{D1}(\theta) = R_{D2}(\theta=0)[V_B(\ell_2, 3\pi-\theta, n_1) \pm V_B(\ell_2, 3\pi-\theta + 2\alpha_1, n_1)] \quad (32b)$$

$$d_1 = [f_1^2 + g_1^2]^{1/2} \quad (32c)$$

$$\beta_1 = \tan^{-1}[f_1/g_1] \quad (32d)$$

$$n_1 = 2 \quad (32e)$$

$$DF_1(\theta) = 1 \quad (32f)$$

and from wedge # 0 by

$$E_{D0}(\theta) = e^{jkd_0 \cos(\beta_0 - \theta)} DF_0(\theta) \cdot \begin{cases} R_{D0}(\theta) & 0 < \theta < \alpha_1 \\ R'_{D0}(\theta) & \alpha_0 + \alpha_{11} < \theta < 2\pi \end{cases} \quad (33)$$

where

$$R_{D0}(\theta) = R'_{D1}(\theta = \pi + \alpha_1) V_B[\ell_1, 5\pi/2 - \theta - \alpha_0 - \alpha_{11}, n_0] \quad (33a)$$

$$R'_{D0}(\theta) = R'_{D1}(\theta = \pi + \alpha_1) V_B[\ell_1, 9\pi/2 - \theta - \alpha_0 - \alpha_{11}, n_0] \quad (33b)$$

$$d_0 = [f_0^2 + g_0^2]^{1/2} \quad (33c)$$

$$\beta_0 = \tan^{-1}[f_0/g_0] \quad (33d)$$

$$n_0 = 2 - \alpha_0/\pi \quad (33e)$$

Contributions from the remaining wedges (11, 10, 9, and 8) will not be included because they are of secondary order when the antenna is placed above the cockpit.

Finally the reflections from the forward sector of the nose (section ℓ_3 of Figure 7) are taken into account by using image theory and are given by

$$E_{DI}(\theta) = e^{-jkd_i \cos(\beta_i + \theta)} R_{DI}(\theta) \quad \pi - \alpha_2 + \sigma < \theta < \alpha_3 - \alpha_2 \quad (34)$$

where

$$d_i = [d_3^2 + w^2 + 2d_3 w \cos(\beta_3 - \alpha_2)]^{1/2} \quad (34a)$$

$$\beta_i = \beta_3 + \sigma_i \quad (34b)$$

$$w = [(\ell_4 + \ell_5 - s) \sin(\alpha_3 - \alpha_2 - \theta) / \sin \delta_i] \quad (34c)$$

$$\sigma_i = \sin^{-1}[w \sin(\alpha_2 + \beta_3) / d_i] \quad (34d)$$

$$\delta_i = \theta + \alpha_2 - \pi \quad (34e)$$

C. Curved-Surface Model

To reduce some of the restrictions placed by the two-dimensional wedge surface model, curved-surface models in the elevation and azimuth planes will now be considered. The nose part of the plane is modeled by a smooth curved surface to better simulate actual operating conditions. The contributions from the nose part of the structure can be accounted by considering mathematical expressions in terms of Fock functions¹⁵ in the transition region and creeping wave functions^{15,26-28} in the shadow region.

1. Elevation Plane

The elevation plane configuration of a curved-surface model of an aircraft

is shown in Figure 13. The tail section in this case has been modeled by an inclined wedge. Actual measurements do indicate that the presence of the tail section does contribute significantly and can be easily identified.

The main contributions to the total radiation field will now be outlined with the corresponding mathematical expressions indicated. The main source contribution is given, according to Figure 14, by

$$E_D(\theta) = 2R_D(\theta)e^{+jk\alpha\cos\theta} \frac{e^{-jkr}}{r} \quad (35)$$

where $R_D(\theta)$ is the normalized far-field angular distribution of the source. The expression for $R_D(\theta)$ will depend largely upon the type of antenna, physical orientation, and electrical dimensions.

Some of the energy from the main source is directed toward wedge # 3 where it is diffracted and its distribution is given by

$$E_{D3R}(\theta) = 2R_D\left(\frac{\pi}{2}\right) [V_B\left(\frac{\theta}{2}, \theta + \frac{\pi}{2}, n_3\right)] e^{jkd_3\cos(\gamma_3+\theta)} \frac{e^{-jkr}}{r}, \quad (36)$$

$$\frac{3\pi}{2} - \alpha_3 > \theta > 0$$

$$E_{D3L}(\theta) = 2R_D\left(\frac{\pi}{2}\right) [V_B\left(\frac{\theta}{2}, \theta - \frac{3\pi}{2}, n_3\right)] e^{+jkd_3\cos(\gamma_3-\theta)} \frac{e^{-jkr}}{r},$$

$$2\pi > \theta > \frac{3\pi}{2} \quad (37)$$

where $V_B(r, \psi, n)$ is the wedge diffraction coefficient.¹⁹⁻²² The appropriate geometry is shown in Figure 14.

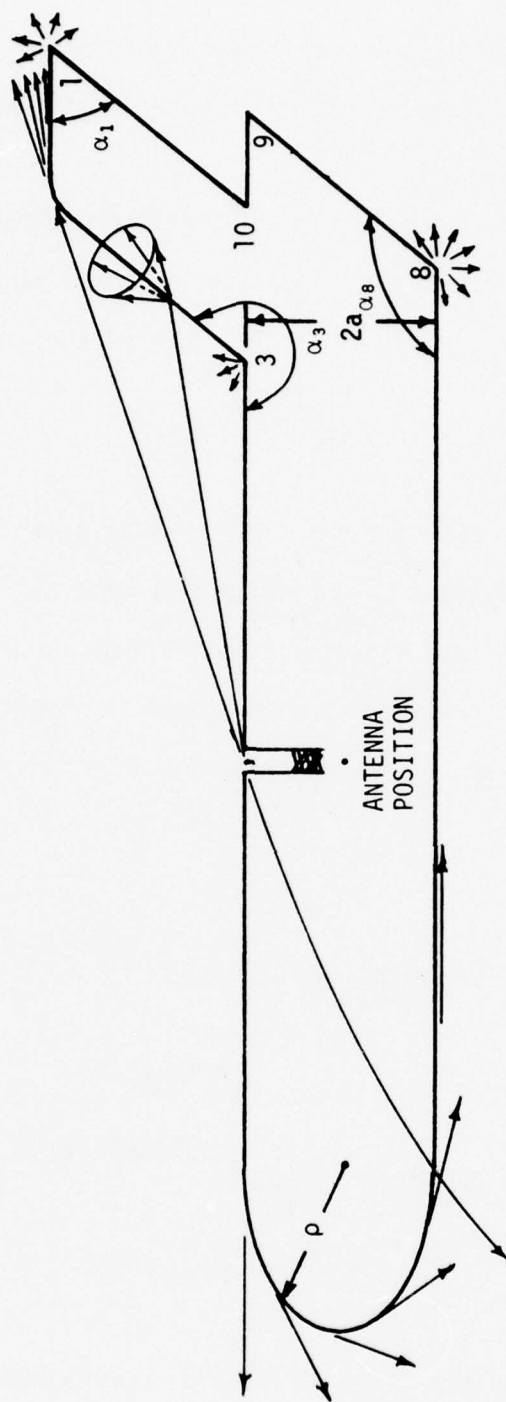


Figure 13. Curved surface modeling of airplane configuration in elevation plane.

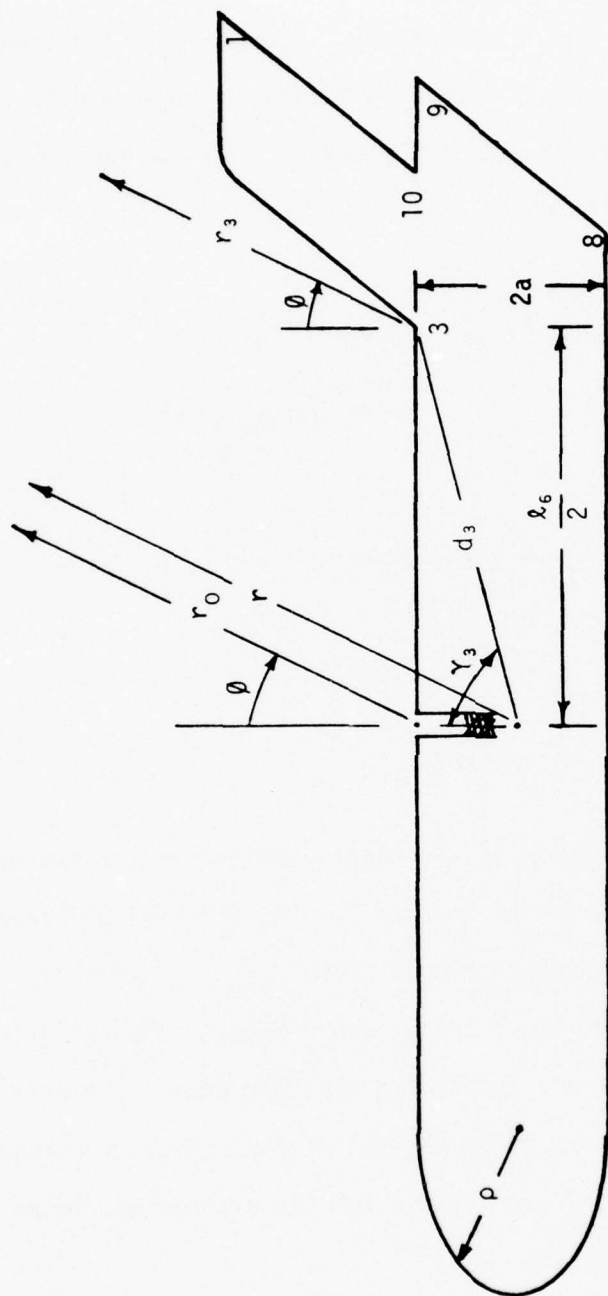


Figure 14. Geometry for diffraction from wedge 3.

The energy from the main source directed toward the tail section undergoes a diffraction and is distributed, according to the laws of diffraction,^{5,16} in a conical surface as indicated in Figure 13. Referring to the geometry of Figure 15, the diffractions from the leading straight edge of the tail are written as

$$E_{DTS}(\theta) = -2R_D(\theta') [V_B(L_t, 0, n_t) + V_B(L_t, 2\pi - \alpha_t, n_t)] e^{+jkd_s \cos(\gamma_t - \theta)} \cdot e^{-jks' \cos^2 \beta_0} \frac{e^{-jkr}}{r} \quad (38)$$

where

$$L_t = s' \sin^2 \beta_0 \quad (38a)$$

$$\beta_0 = \frac{5\pi}{2} - \alpha_t - \theta \quad (38b)$$

$$n_t = 2 - \frac{\alpha_t}{\pi} \quad (38c)$$

where α_t is the included angle of the wedge forming the leading edge of the tail section, the minus (-) sign is used for the vertical polarization, and the plus (+) for the horizontal polarization.

The diffractions from the leading curved edge of the tail can be accounted in a similar manner as for the straight edge. The only difference is a divergence factor which is a function of the radius of curvature. Referring to Figure 16, the expressions for the diffracted fields from the curved section of the tail are

$$E_{DTC}(\theta) = -2R_D(\theta') [V_B(L_c, 0, n_t) - V_B(L_c, 2\pi - \alpha_t, n_t)] \cdot D_{IV}(\theta_i) e^{-jks' \cos^2 \beta_{0c}} \frac{e^{-jkr_c}}{r_c} \quad (39)$$

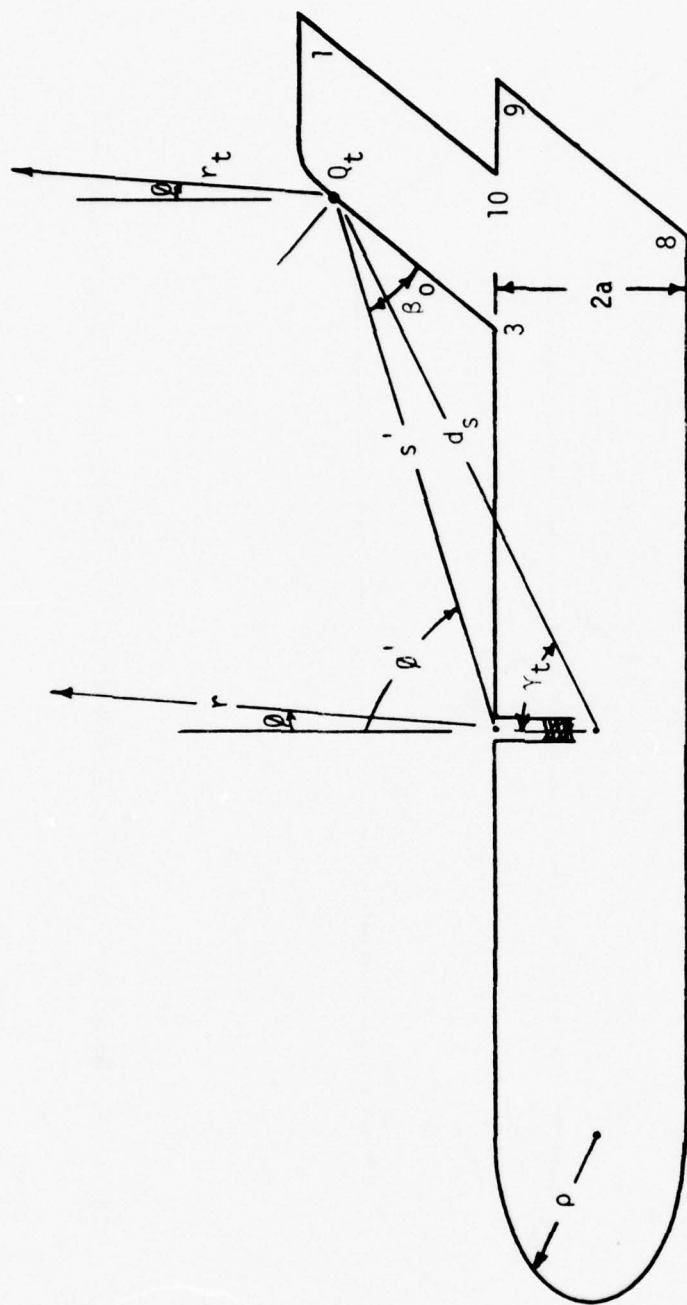


Figure 15. Geometry for diffractions from the leading straight edges of the tail.

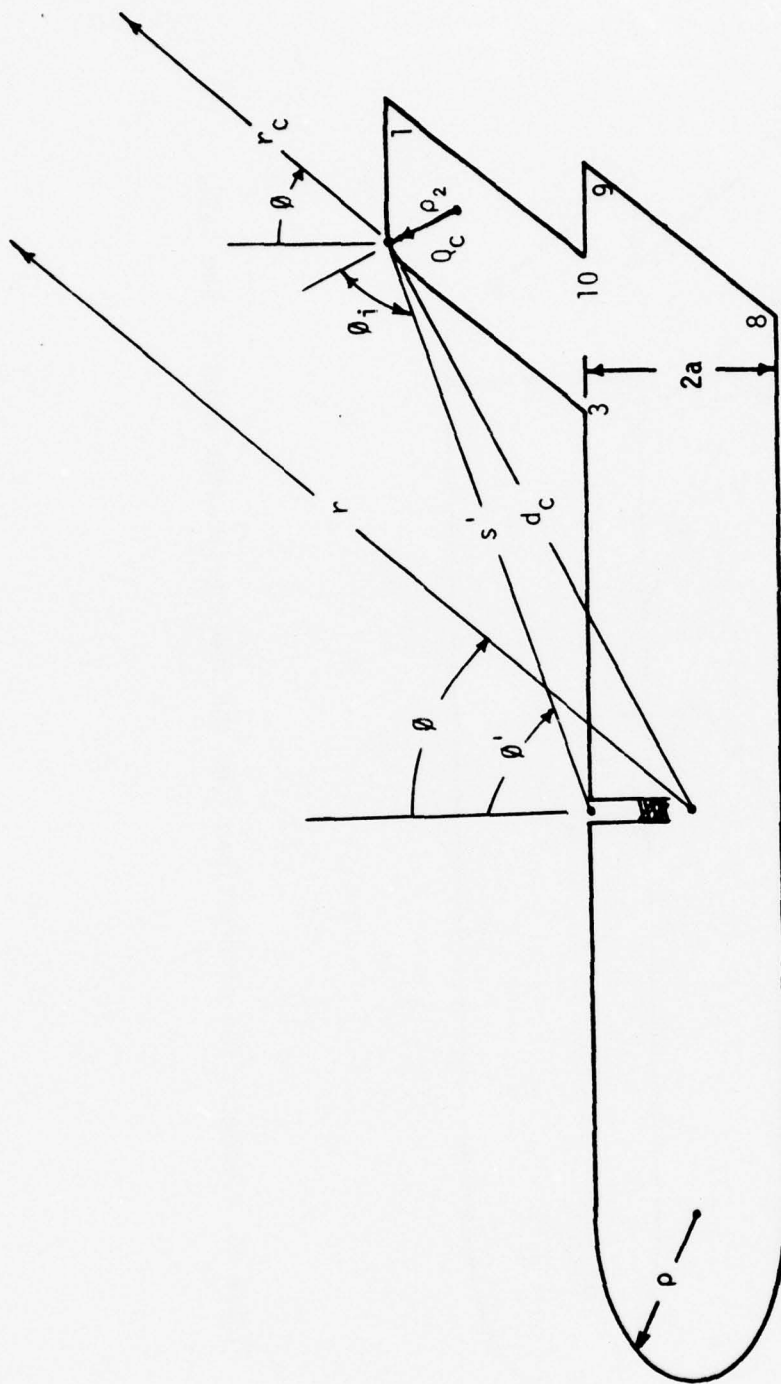


Figure 16. Geometry for diffractions from the leading curved edge of the tail.

where

$$L_c = s' \sin^2 \theta_{oc} \quad (39a)$$

$$D_{IV}(\theta') = \sqrt{\frac{\rho_2^2 \cos \theta_i}{s'(2s' + \rho_2 \cos \theta_i)}} \quad (39b)$$

To accurately model the radiation mechanism in the forward (nose) direction, creeping wave contributions in the deep shadow region and Fock functions in the transition region will be introduced. The transition region itself is divided into two parts to provide smooth transitions between the lit and shadow regions. The part of the transition region neighboring the lit region is referred to as "lit transition" and the one neighboring the shadow region as "shadow transition". The lit, lit transition, shadow transition, and shadow regions are all demonstrated in Figure 17. The boundaries separating the different regions are determined by the radius of curvature at point Q_1 of Figure 17. Referring to Figure 18, the contributions in the lit transition region ($3\pi/2 < \theta < 3\pi/2 + \Delta_4$) are given for the hard and soft boundary conditions by

$$E_{CNh}(\theta) = R_D(\theta) e^{-jk\ell_6/2} g(\xi) e^{-jks_1} \frac{e^{-jkr_n}}{r_n} \quad (40a)$$

$$E_{CNs}(\theta) = R_D\left(\frac{3\pi}{2} + \Delta_4\right) e^{-jk\ell_6/2} \left[-j\left(\frac{2}{k\rho_1}\right)^{1/3} \frac{\sin \psi_1}{\psi_1}\right] g(\xi) e^{-jks_1} \frac{e^{-jkr_n}}{r_n} \quad (40b)$$

where

$$\xi = - \int_0^{s_1} \frac{1}{\rho} \left(\frac{k\rho}{2}\right)^{1/3} ds' \quad (40c)$$

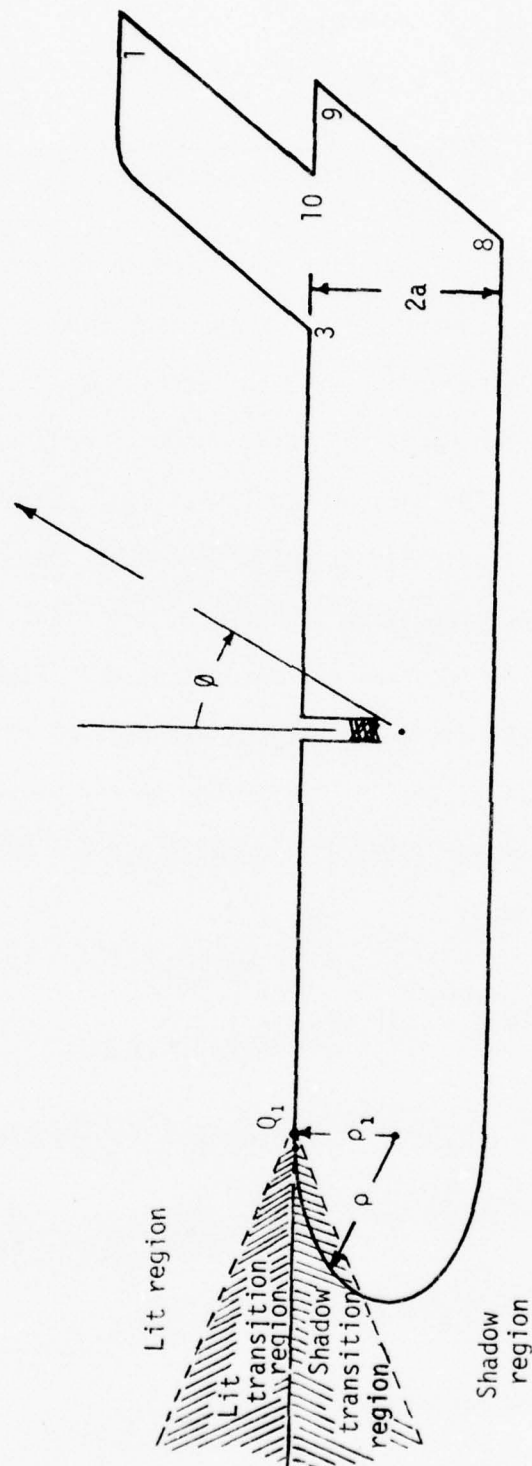


Figure 17. Region separation toward the nose of the airplane.

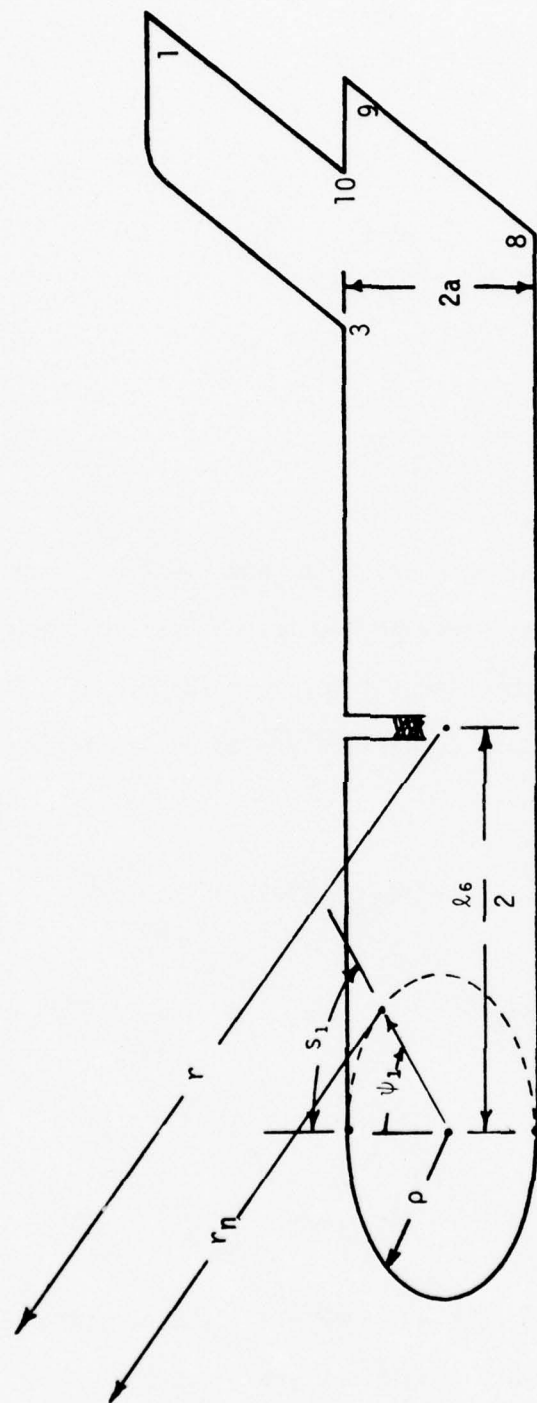


Figure 18. Geometry for diffractions in the lit transition region.

$$g(\xi) = \frac{1}{\sqrt{\pi}} \int_{\Gamma_1} \frac{e^{-j\tau\xi}}{w_2(\tau)} d\tau \quad (40d)$$

$$\tilde{g}(\xi) = \frac{1}{\sqrt{\pi}} \int_{\Gamma_1} \frac{e^{-j\tau\xi}}{w_2'(\tau)} d\tau \quad (40e)$$

$$\Delta_4 = \frac{1}{(k\rho_1)^{1/3}} \quad (40f)$$

where $g(\xi)$ and $\tilde{g}(\xi)$ are the hard and soft Fock functions¹⁵ and $w_2(\tau)$ and $w_2'(\tau)$ are the Fock-type Airy function and its derivative, respectively.

The contributions in the shadow transition ($3\pi/2 - \Delta_4 < \theta < 3\pi/2$) region for the hard and soft boundary conditions are given, referring to Figure 19, by

$$E_{CNh}(\theta) = R_D(3\pi/2) e^{-jk\ell_6/2} g(\xi) e^{-jks_2} \left[\frac{\rho_g(Q_2)}{\rho_g(Q_1)} \right]^{1/6} \frac{e^{-jkr_n}}{r_n} \quad (41a)$$

$$E_{CNs}(\theta) = R_D(3\pi/2 + \Delta_4) e^{-jk\ell_6/2} \left[-j \left(\frac{2}{k\rho_1} \right)^{1/3} \right] \tilde{g}(\xi) e^{-jks_2} \left[\frac{\rho_g(Q_2)}{\rho_g(Q_1)} \right]^{1/6} \frac{e^{-jkr_n}}{r_n} \quad (41b)$$

where

$$\xi = \int_0^{s_2} \frac{1}{\rho} \left(\frac{k\rho}{2} \right)^{1/3} ds' \quad (41c)$$

In the shadow region ($\pi/2 < \theta < 3\pi/2 - \Delta_4$) the creeping wave contributions for the hard and soft boundary conditions are given by

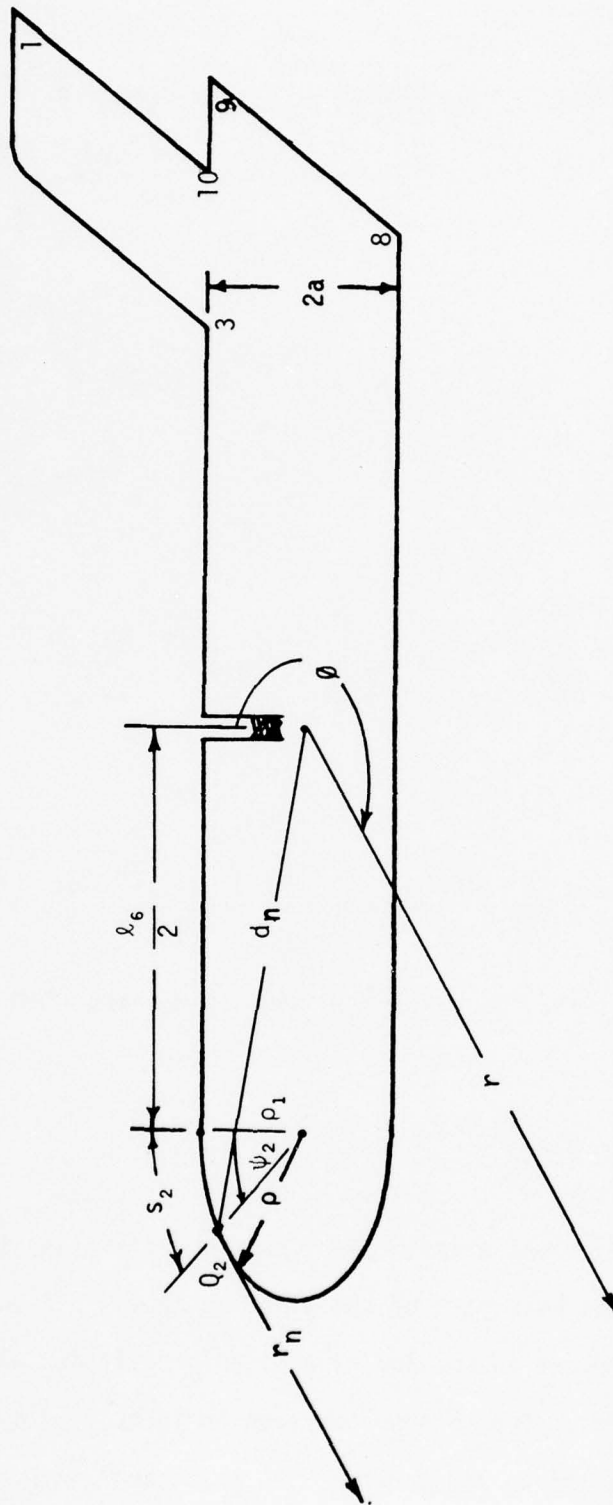


Figure 19. Geometry for diffractions in the shadow transition and shadow regions.

$$E_{CWh}(\theta) = R_D(3\pi/2)e^{-jk\ell_6/2} D_{oh}(Q) L_{oh} e^{-\int_0^{s_2} \alpha_{os}(s') ds'} \cdot e^{-jks_2} \frac{e^{-jkr_n}}{r_n} \quad (42a)$$

$$E_{Cws}(\theta) = R_D(3\pi/2 + \Delta_4)e^{-jk\ell_6/2} D_{os}(Q_2) L_{os} e^{-\int_0^{s_2} \alpha_{os}(s') ds'} \cdot e^{-jks_2} \frac{e^{-jkr_n}}{r_n} \quad (42b)$$

$$L_{oh} = e^{j\frac{\pi}{12}} \sqrt{2\pi k} \left(\frac{2}{k\rho_1}\right)^{1/3} A_i(-\bar{q}_0) \left[1 + \left(\frac{2}{k\rho_1}\right)^{2/3} \frac{\bar{q}_0}{15} e^{j\frac{2\pi}{3}}\right] D_{oh}(Q_2) \quad (42c)$$

$$L_{os} = e^{-j\frac{\pi}{12}} \sqrt{2\pi k} \left(\frac{2}{k\rho_1}\right)^{2/3} A'_i(-q_0) \left[1 - \left(\frac{2}{k\rho_1}\right)^{2/3} \frac{q_0}{15} e^{j\frac{2\pi}{3}}\right] D_{os}(Q_2) \quad (42d)$$

where D_{oh} , D_{os} , α_{oh} , α_{os} , $A_i(-\bar{q}_0)$, and $A'_i(-q_0)$ are listed in Tables 3 and 4[15].

2. Azimuth Plane

For the principal azimuth plane configuration, the antenna is assumed to be mounted on the nose part of the plane as shown in Figure 20. The fuselage part of the airplane is modeled by a circular cylinder with the wings represented by a wedge. The antenna location is identified by coordinates (x_0, y_0) with 2a and 2b representing the major and minor axes. The space about

TABLE 3

DIFFRACTION COEFFICIENTS AND ATTENUATION CONSTANTS FOR CIRCULAR CYLINDERS AND SPHERES

Surface	SQUARE OF DIFFRACTION COEFFICIENT $D_p^2 = (\text{Column A}) \cdot (\text{Column B})$		ATTENUATION CONSTANT $\alpha_p = (\text{Column C}) \cdot (\text{Column D})$		ZERGES OF THE AIRY FUNCTION
	A. Keller's Result	B. Correction Terms	C. Keller's Result	D. Correction Terms	
Soft Cylinder	$\frac{-1/2 - 5/6 \frac{1}{3} e^{-j\pi/12}}{k^{1/6} (A_1'(-q_p))^2}$	$1 + \left(\frac{2}{ka}\right)^{2/3} q_p \frac{1}{30} e^{-j\pi/3}$	$\frac{q_p}{6} e^{j\pi/6} \left(\frac{ka}{2}\right)^{1/3}$	$1 + \left(\frac{2}{ka}\right)^{2/3} \frac{q_p}{60} e^{-j\pi/3}$	ZERGES OF THE AIRY FUNCTION $A_1'(-q_p) = 0$ $q_0 = 2.33811$ $q_1 = 4.08795$ $A_1'(-q_0) = .70121$ $A_1'(-q_1) = -.80311$
Soft Acoustic and Soft EM Sphere		$1 + \left(\frac{2}{ka}\right)^{2/3} q_p \left(\frac{1}{30} + \frac{1}{4}\right) e^{-j\pi/3}$			
Hard Cylinder	$\frac{-1/2 - 5/6 \frac{1}{3} e^{-j\pi/12}}{k^{1/6} q_p (A_1'(-q_p))^2}$	$1 + \left(\frac{2}{ka}\right)^{2/3} \left(\frac{q_p}{30} - \frac{1}{2} \frac{1}{10} \right) e^{-j\pi/3}$	$\frac{q_p}{6} e^{j\pi/6} \left(\frac{ka}{2}\right)^{1/3}$	$1 + \left(\frac{2}{ka}\right)^{2/3} \left(\frac{q_p}{60} + \frac{1}{2} \frac{1}{10} \right) e^{-j\pi/3}$	ZERGES OF THE DERIVATIVE OF THE AIRY FUNCTION $A_1'(-q_p) = 0$ $q_0 = 1.01879$ $q_1 = 3.24820$ $A_1'(-q_0) = .53565$ $A_1'(-q_1) = -.41902$
Hard Acoustic Sphere		$1 + \left(\frac{2}{ka}\right)^{2/3} \left(\frac{q_p}{30} \left(\frac{1}{30} + \frac{1}{4} \right) - \frac{1}{2} \frac{1}{10} \left(\frac{1}{10} + \frac{1}{4} \right) \right) e^{-j\pi/3}$		$1 + \left(\frac{2}{ka}\right)^{2/3} \left(\frac{q_p}{60} + \frac{1}{2} \frac{1}{10} \left(\frac{1}{10} + \frac{1}{4} \right) \right) e^{-j\pi/3}$	
Hard EM Sphere		$1 + \left(\frac{2}{ka}\right)^{2/3} \left(\frac{q_p}{30} \left(\frac{1}{30} + \frac{1}{4} \right) - \frac{1}{2} \frac{1}{q_p} \left(\frac{1}{10} - \frac{1}{2} \right) \right) e^{-j\pi/3}$		$1 + \left(\frac{2}{ka}\right)^{2/3} \left(\frac{q_p}{60} + \frac{1}{2} \frac{1}{q_p} \left(\frac{1}{10} - \frac{1}{2} \right) \right) e^{-j\pi/3}$	

TABLE 4

GENERALIZED DIFFRACTION COEFFICIENTS AND ATTENUATION CONSTANTS

Surface	SQUARE OF DIFFRACTION COEFFICIENT $D_p^2 = (\text{Column A}) \cdot (\text{Column B})$		ATTENUATION CONSTANT $a_p = (\text{Column C}) \cdot (\text{Column D})$	
	A. Keller's Result	B. Correction Terms	C. Keller's Result	D. Correction Terms
Soft Acoustic and Soft EM	$\frac{-1/2 - 5/6 \rho_g^{1/3} e^{-j\pi/12}}{k^{1/6} (A_1'(-\rho_p))^{1/2}}$	$1 + \left(\frac{2}{k\rho_g}\right)^{2/3} \rho_p \left(\frac{1}{30} + \frac{\rho_g}{4\rho_p \tan} + \dots \right) e^{-j\pi/3}$	$\frac{\rho_p}{\rho_g} e^{j\pi/6} \left(\frac{k\rho_g}{2}\right)^{1/3}$	$1 + \left(\frac{2}{k\rho_g}\right)^{2/3} \rho_p \left(\frac{1}{60} - \frac{2}{45} \rho_g^2 + \frac{4}{135} \rho_g^2 \right) e^{-j\pi/3}$
Hard Acoustic	$\frac{-1/2 - 5/6 \rho_g^{1/3} e^{-j\pi/12}}{k^{1/6} \rho_p (A_1'(-\rho_p))^{1/2}}$	$1 + \left(\frac{2}{k\rho_g}\right)^{2/3} \rho_p \left(\frac{1}{30} + \frac{\rho_g}{4\rho_p \tan} + \dots \right) e^{-j\pi/3}$	$\frac{\rho_p}{\rho_g} e^{j\pi/6} \left(\frac{k\rho_g}{2}\right)^{1/3}$	$1 + \left(\frac{2}{k\rho_g}\right)^{2/3} \rho_p \left(\frac{1}{60} - \frac{2}{45} \rho_g^2 + \frac{4}{135} \rho_g^2 \right) e^{-j\pi/3}$ $+ \frac{1}{\rho_p} \left(\frac{1}{10} + \frac{\rho_g}{4\rho_p \tan} - \frac{\rho_g^2}{60} + \frac{\rho_g^2}{90} \right) e^{-j\pi/3}$
		$1 + \left(\frac{2}{k\rho_g}\right)^{2/3} \rho_p \left(\frac{1}{30} + \frac{\rho_g}{4\rho_p \tan} + \dots \right) e^{-j\pi/3}$ $- \frac{1}{\rho_p} \left(\frac{1}{10} + \frac{\rho_g}{4\rho_p \tan} + \dots \right) e^{-j\pi/3}$		$1 + \left(\frac{2}{k\rho_g}\right)^{2/3} \rho_p \left(\frac{1}{60} - \frac{2}{45} \rho_g^2 + \frac{4}{135} \rho_g^2 \right) e^{-j\pi/3}$ $+ \frac{1}{\rho_p} \left(\frac{1}{10} - \frac{\rho_g}{4\rho_p \tan} - \frac{\rho_g^2}{60} + \frac{\rho_g^2}{90} \right) e^{-j\pi/3}$

 ρ_g = radius of curvature along the geodesic ρ_p = radius of curvature perpendicular to the geodesic (transverse curve)

dots(.) indicate differentiation with respect to arc length variable

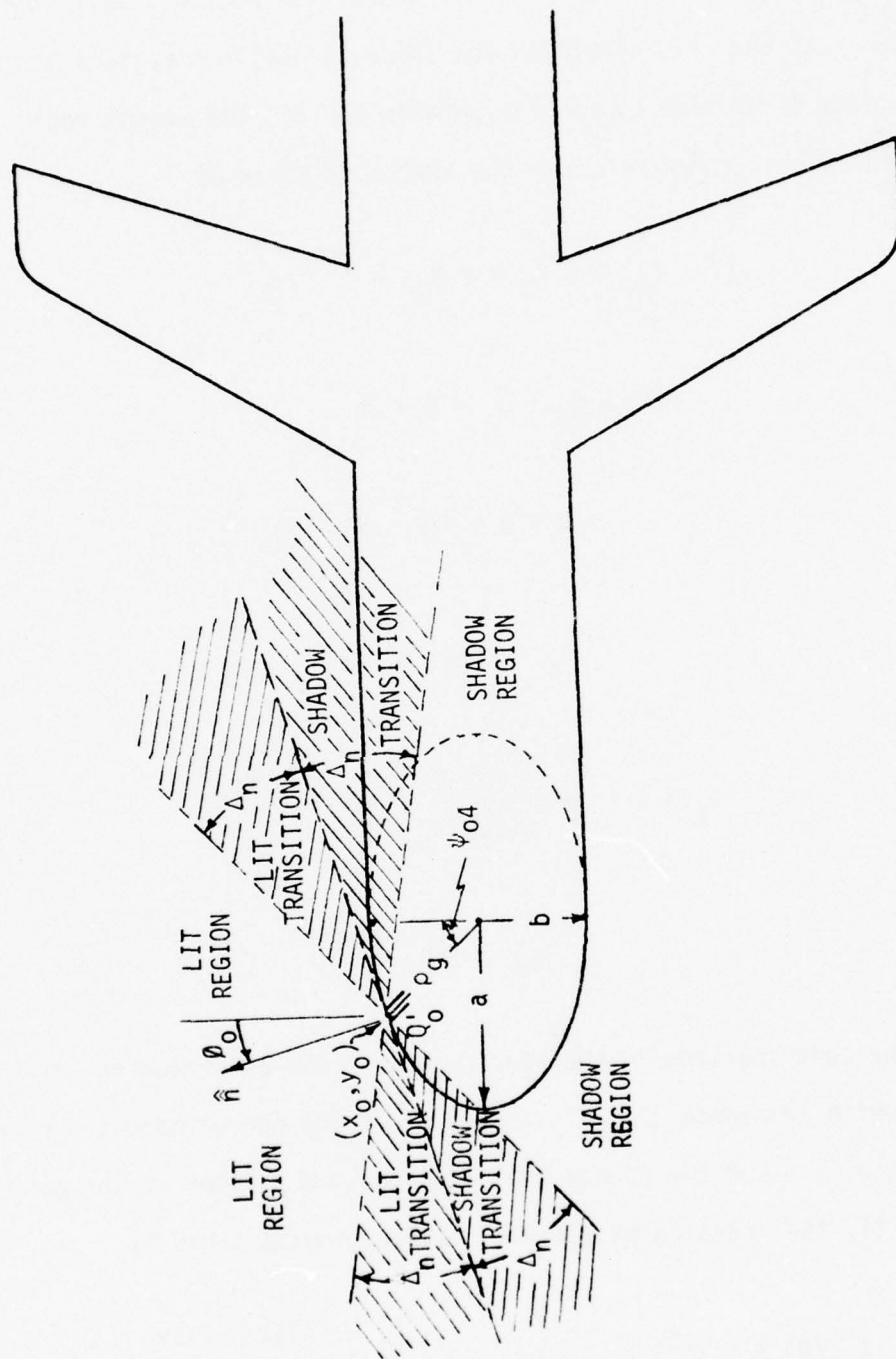


Figure 20. Geometrical arrangement for antenna position at the nose of an aircraft.

the antenna is divided into three distinct regions; namely, the lit, transition, and shadow regions. The transition region itself is subdivided into the lit transition and shadow transition regions and has been introduced to provide continuity between the lit and shadow region fields.

The direct radiation from the source is given by

$$E_D(\theta + \theta_0) = 2 R_D(\theta + \theta_0) e^{-jkr_0/r_0} \quad (43)$$

for

$$3\pi/2 - \theta_0 + \Delta_n < \theta < 2\pi \quad (43a)$$

$$0 < \theta < \pi/2 - \theta_0 - \Delta_n \quad (43b)$$

$$\Delta_n = [1/k\rho_g(Q')]^{\frac{1}{3}} \quad (43c)$$

$$\rho_g(Q') = \frac{1}{ab} \left[\frac{a^4 \cos^2 \theta_0 + b^4 \sin^2 \theta_0}{a^2 \cos^2 \theta_0 + b^2 \sin^2 \theta_0} \right]^{\frac{1}{2}} \quad (43d)$$

$$\psi_{04} = \tan^{-1} \left(\frac{x_0}{y_0} \right) \quad (43e)$$

The contributions in the shadow regions can be accounted for by creeping waves which propagate around the surface of the curved nose and reradiate tangentially. For the shadow region in the top portion of the nose, shown in Figure 21, the creeping wave field contribution is given by

$$E_{ct}(\theta) = E_i(Q'_0) D_{ob}(Q_0) L_{ob}(Q'_0) T(t) e^{-jkt} e^{-jkr_n/r_n} \quad (44)$$

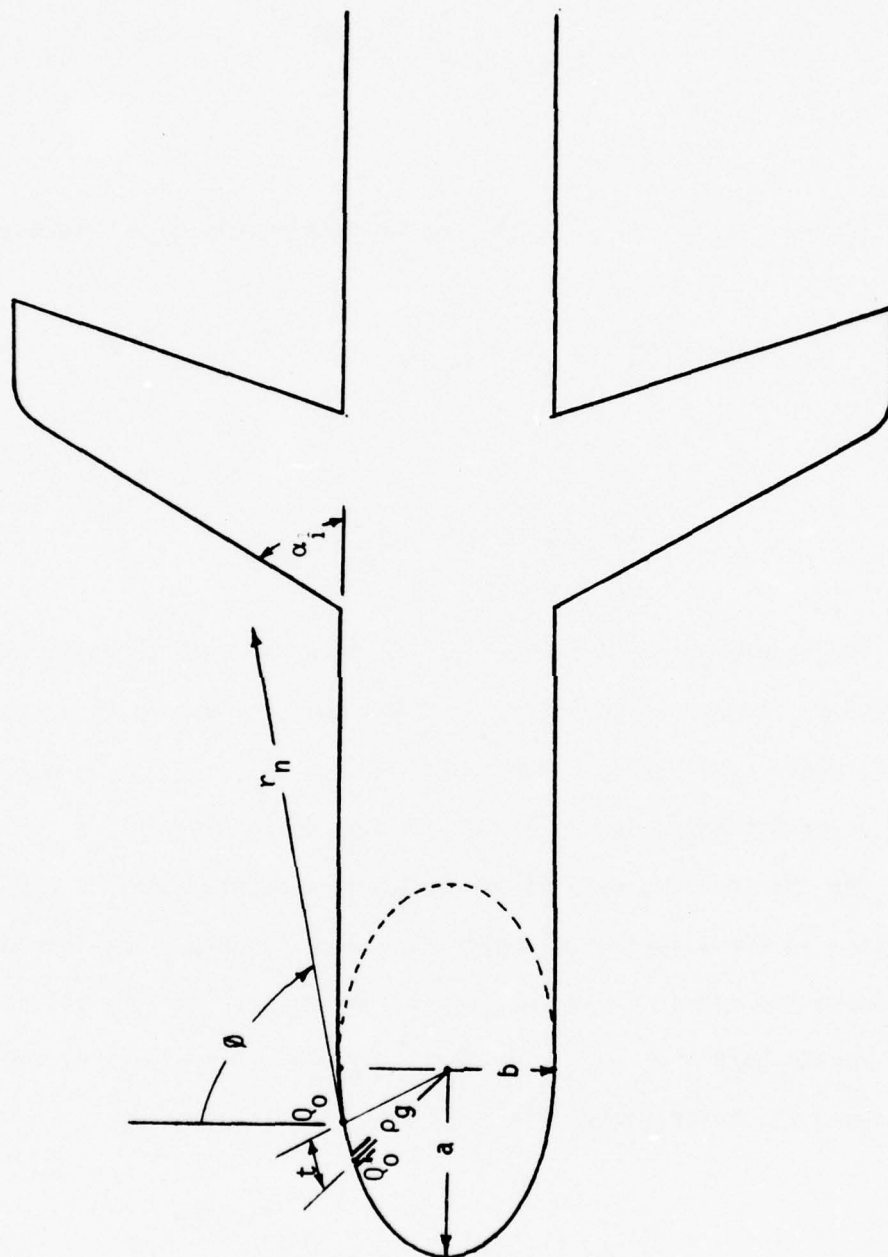


Figure 21. Geometrical arrangement for radiation in the shadow region above the nose.

for

$$\pi/2 - \theta_0 + \Delta_n < \theta < \pi/2 - \alpha_1 + \delta_m - \Delta_n \quad (44a)$$

$$T(t) = e^{-\int_0^t \alpha_{oh}(\rho_g) dt} \quad (44b)$$

and for the shadow region in the bottom part of the nose, shown in Figure 22, as

$$E_{cb}(\theta) = E_i(Q'_0) D_{oh}(Q_0) L_{oh}(Q'_0) T(t) e^{-jkt} e^{-jkr_n/r_n} \quad (45)$$

for

$$\pi/2 < \theta < 3\pi/2 - \theta_0 - \Delta_n \quad (45a)$$

The launching coefficients for the hard and soft boundary conditions are related to the corresponding diffraction coefficients by Equations (42c) and (42d), where $\rho_1 = \rho_g(Q'_0)$. The functions D_{oh} , D_{os} , α_{oh} , α_{os} , $A_i(-\bar{q}_0)$, and $A'_i(q_0)$ are listed in Tables 3 and 4 shown previously.

For the creeping wave fields to blend smoothly with the geometrical optics solution in the illuminated region, the Fock functions are introduced to represent the radiation in the transition region. For the illuminated transition region ($\pi/2 - \theta_0 - \Delta_n < \theta < \pi/2 - \theta_0$) in the top part of the nose, shown in Figure 23, the radiated field distribution is given by

$$E_t^-(\theta) = E_i(Q'_0) [F(Q_0, Q'_0) + G(Q_0, Q'_0)] e^{-jkr_n/r_n} \quad (46)$$

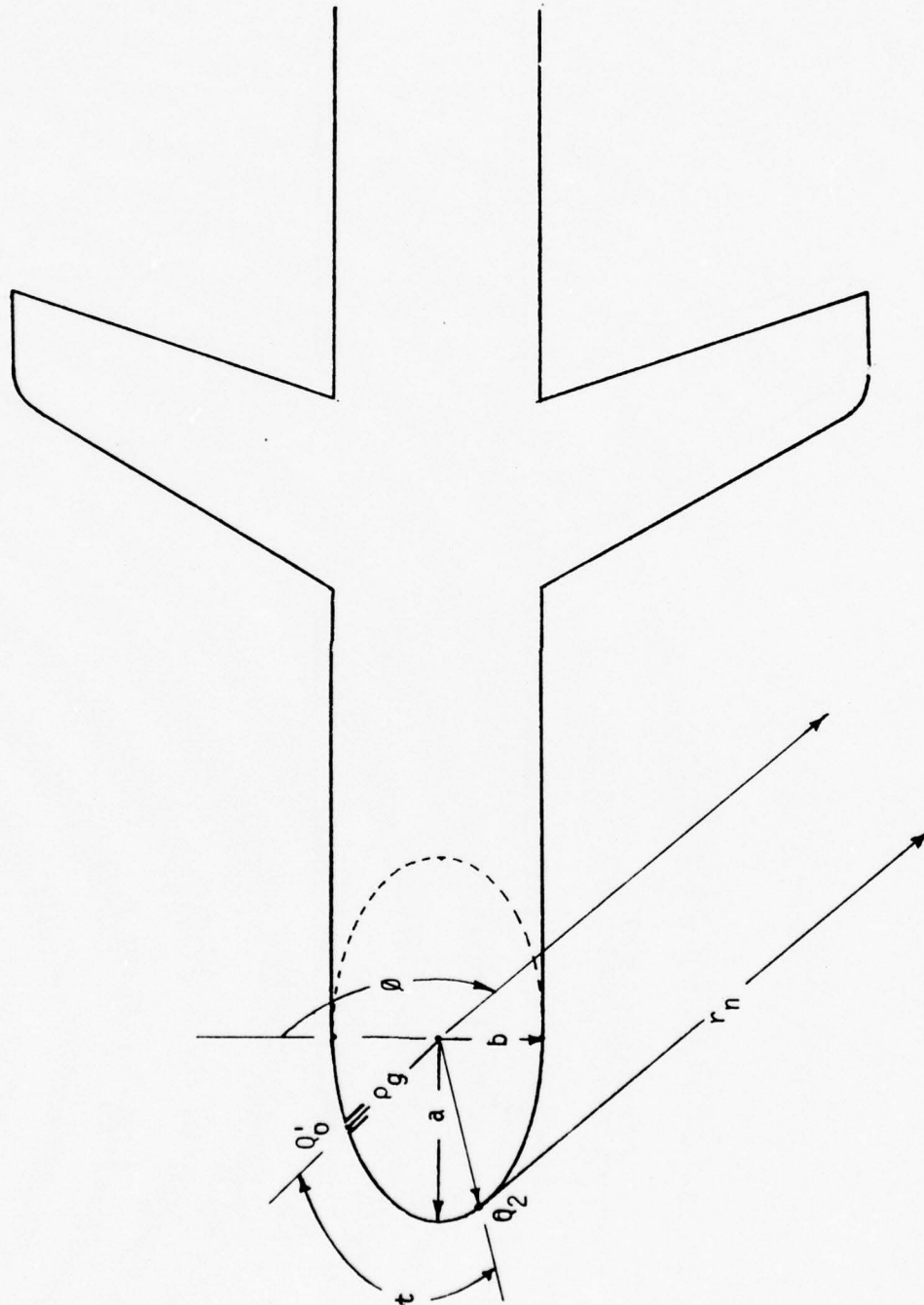


Figure 22. Geometrical arrangement for radiation in the shadow region below the nose.

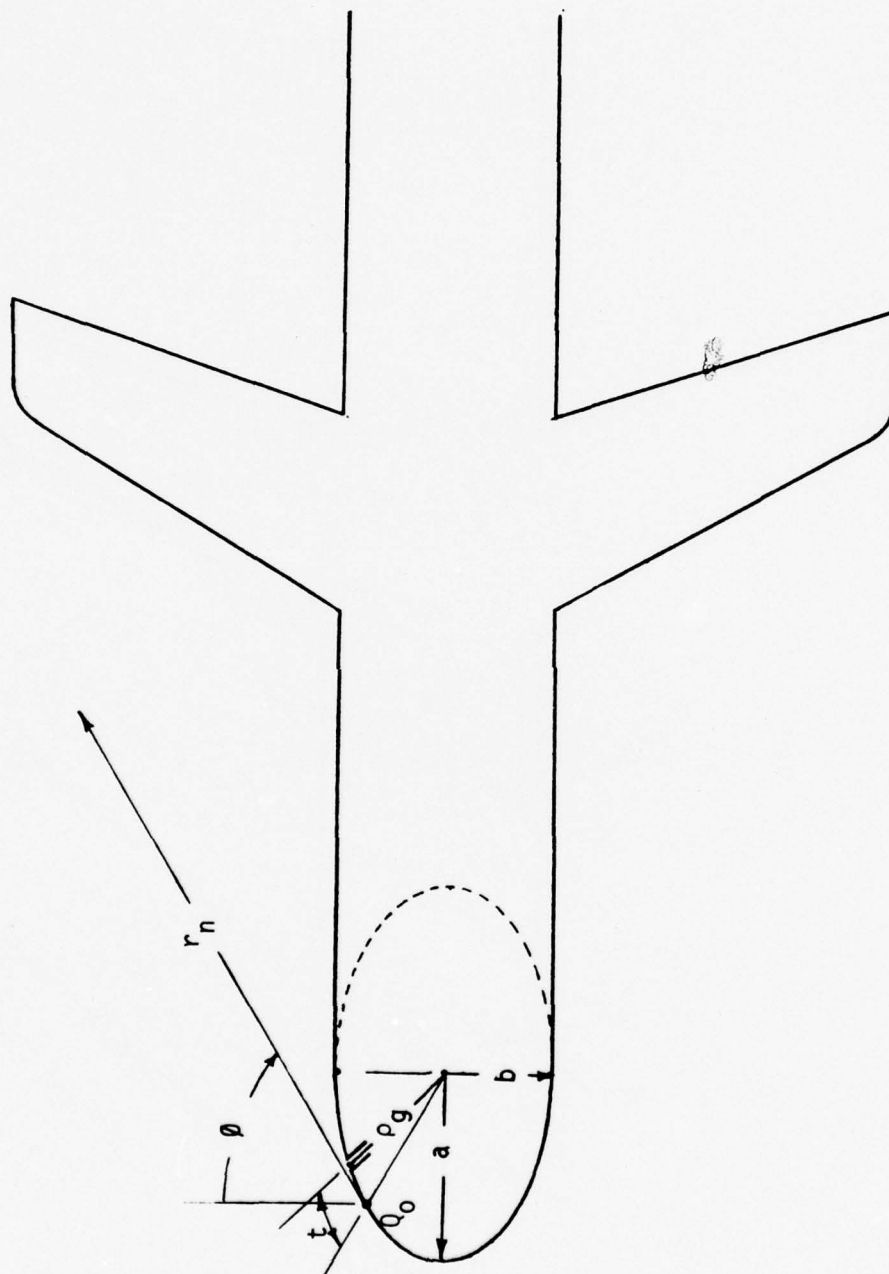


Figure 23. Geometrical arrangement for radiation in the lit transition region above the nose.

where

$$F(Q_0, Q_0') = g(\xi) e^{+jkt} \quad (46a)$$

$$G(Q_0, Q_0') = 0 \quad (46b)$$

for vertical polarization and

$$F(Q_0, Q_0') = 0 \quad (46c)$$

$$G(Q_0', Q_0) = -j \left[\frac{2}{k \rho_g(Q_0')} \right]^{\frac{1}{3}} \tilde{g}(\xi) f(t) e^{+jkt} \quad (46d)$$

for horizontal polarization. The functions $g(\xi)$ and $\tilde{g}(\xi)$ are the hard and soft Fock functions defined by Equations (40d) and (40e). The function $f(t)$ is a function which is introduced to join smoothly the field across the boundary.

For the portion extending into the shadow transition region $(\pi/2 - \theta_0 < \theta < \pi/2 - \theta_0 + \Delta_n)$, the field contribution is given by

$$E_t^+(\theta) = E_i(Q_0') [F(Q_0, Q_0') + G(Q_0, Q_0')] e^{-jkr_n/r_n} \quad (47)$$

where

$$F(Q_0, Q_0') = g(\xi) e^{-jkt} \left[\frac{\rho_g(Q_0)}{\rho_g(Q_0')} \right]^{\frac{1}{6}} \quad (47a)$$

$$G(Q_0, Q_0') = 0 \quad (47b)$$

for vertical polarization and

$$F(Q_0, Q_0') = 0 \quad (47c)$$

$$G(Q_0, Q_0') = -j \left[\frac{2}{k \rho_g(Q_0')} \right]^{1/3} \tilde{g}(\xi) e^{-jkt \left[\frac{\rho_g(Q_0)}{\rho_g(Q_0')} \right]^{1/6}} \quad (47d)$$

for horizontal polarization.

For the transition region below the nose, the field distribution is represented by Fock functions as outlined by equations (46) - (47d) for the transition region in the top part.

The energy from the source propagating around the upper portion of the nose is directed along the wing section where it undergoes diffractions. The energy is diffracted by the wedge formed by the fuselage and wing section and indicated in Figure 24 as wedge #3. In addition energy is diffracted from the wing section which has been modeled by a wedge whose leading edge is straight and curves near its tip. The diffractions from wedge #3 and the contributions from the wing section are similar to those outlined for the tail section by Equations (36) - (39b). It should, however, be pointed out that the diffractions from the wing section are initiated by radiation which may come from the lit, lit transition, the shadow transition, or the shadow region. This will depend upon the antenna location on the nose (coordinates x_0, y_0 of Figure 20) and radius of curvature of the nose at that point $[\rho(Q_0')]$.

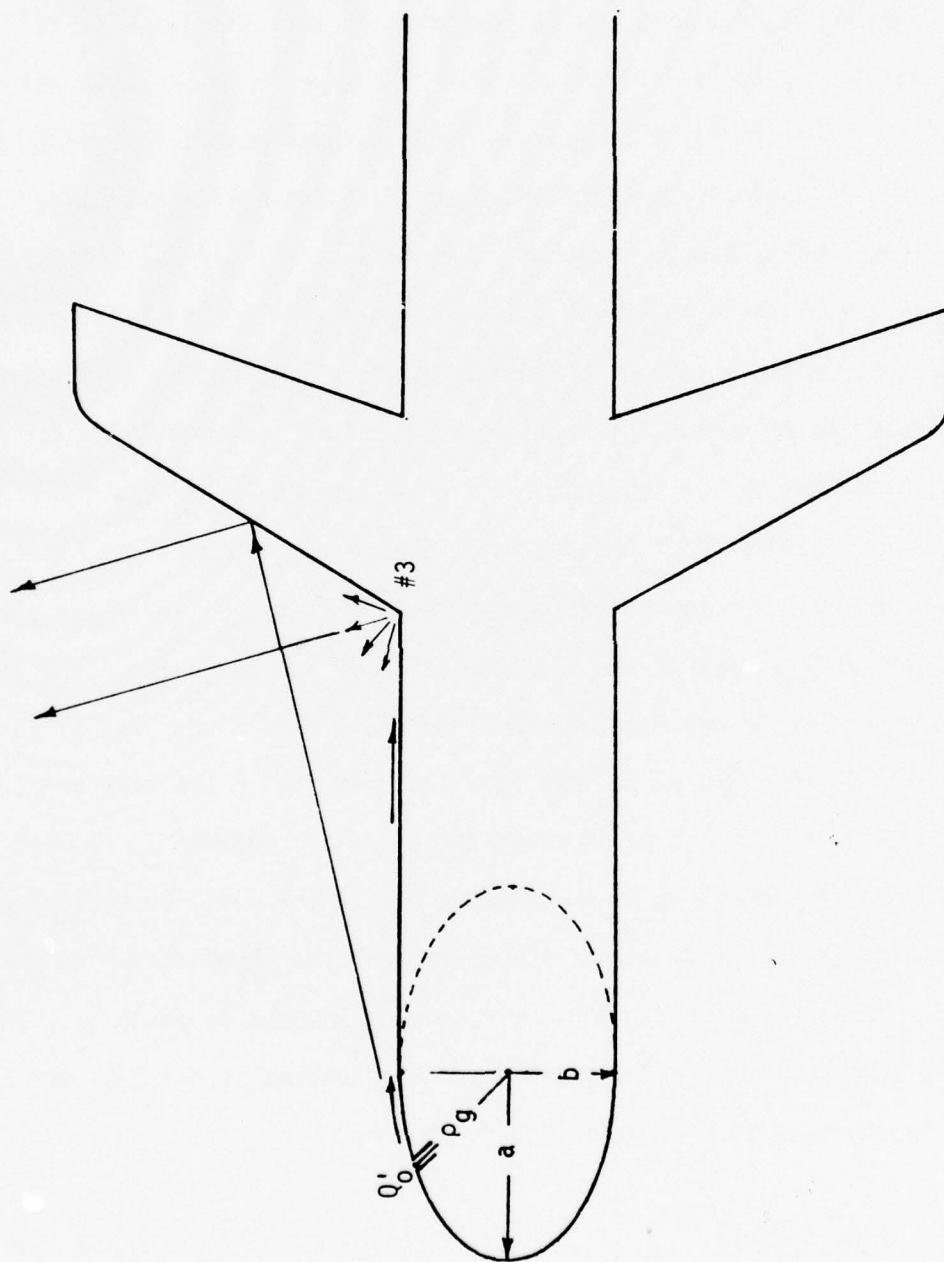


Figure 24. Diffractions from fuselage/wing wedge (#3) and wing section.

D. Mutual Coupling

The mutual coupling between two aperture antennas mounted on a convex perfectly conducting cylinder will be examined in this section. It is assumed that the tangential electric field in the aperture is known which allows the formulation of an equivalent infinitesimal magnetic current moment, which is used to represent the aperture. The equivalent magnetic moment is then multiplied by launching coefficients to initiate surface ray modes which travel along ray paths which are geodesics of the surface. When the surface ray modes arrive at the other aperture, attachment coefficients are introduced to determine the modal current induced in the slot which is then used to determine the coupling. It is assumed here that the two slots are positioned so that the one is in the shadow region of the other.

The geometry under investigation is shown in Figure 25 where two slots are indicated in the nose of the airplane. The dimensions a and b are used to represent the major and minor axes of the elliptical nose. The slots are separated by an angle ψ . A more detailed geometry of the nose and antenna positioning is shown in Figure 26 where the energized antenna is assumed to be at point Q_1 and the coupling to the antenna at point Q_2 will be determined. By reciprocity the obtained values also represent the coupling for an energized antenna at point Q_2 with the receiving antenna at point Q_1 . The parameters used to identify the position of the antenna at point Q_1 and the geometry of the nose at that point are defined by

$$\Delta_1 = (k\rho_1)^{-1/3} \quad (48a)$$

$$\rho_1 = [(a^4 \cos^2 \theta_1 + b^4 \sin^2 \theta_1) / (a^2 \cos^2 \theta_1 + b^2 \sin^2 \theta_1)]^{3/2} / ab \quad (48b)$$

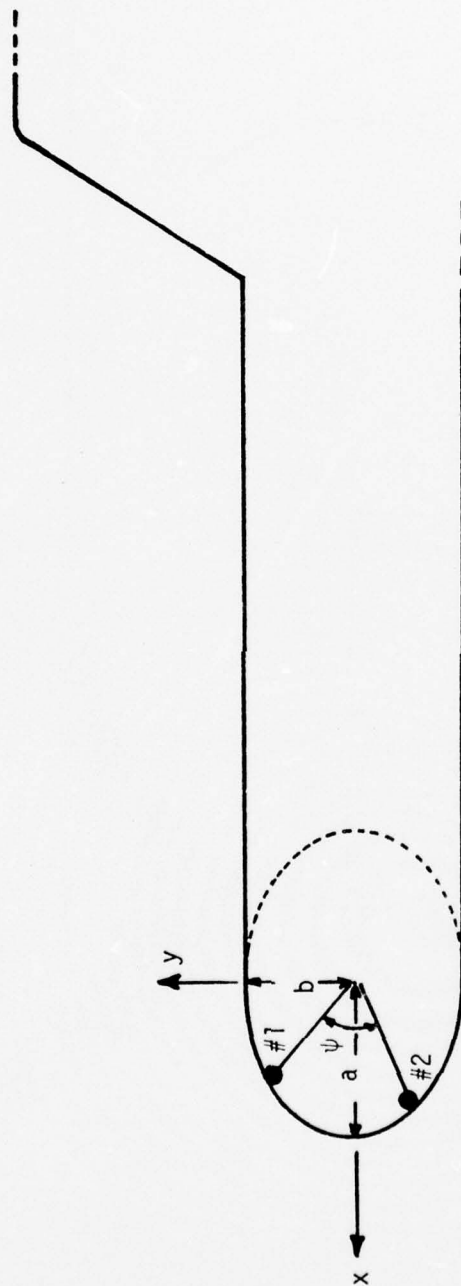


Figure 25. Geometrical arrangements of two apertures (1 and 2) on the nose of the airplane.

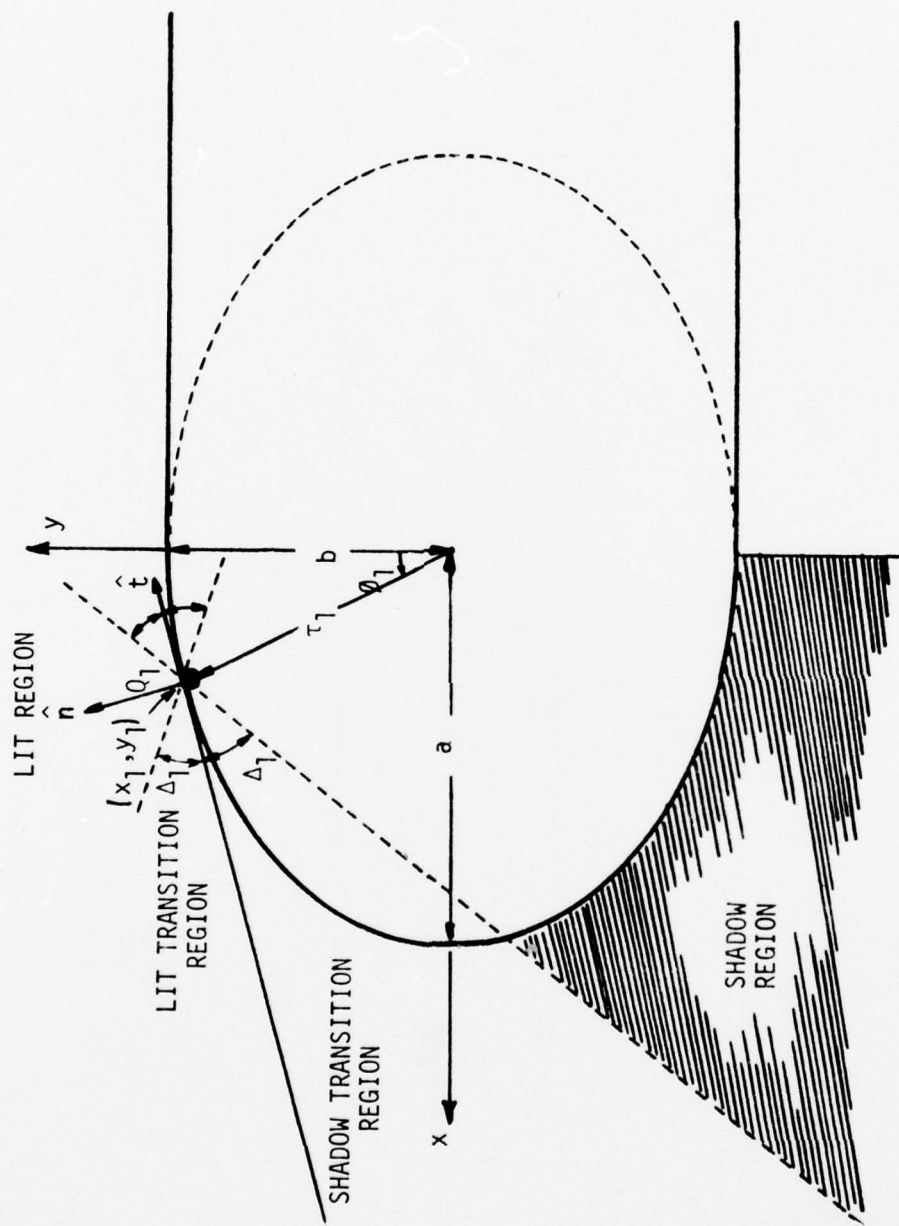


Figure 26. Local geometry of nose and antenna positioning.

$$\rho_{tn1} = b^2 \sqrt{(x_1/a^2)^2 + (y_1/b^2)^2} \quad (48c)$$

$$x_1 = ab \sin \theta_1 / (a^2 \cos^2 \theta_1 + b^2 \sin^2 \theta_1)^{1/2} \quad (48d)$$

$$y_1 = ab \cos \theta_1 / (a^2 \cos^2 \theta_1 + b^2 \sin^2 \theta_1)^{1/2} \quad (48e)$$

$$\theta_1 = \tan^{-1}(x_1/y_1) \quad (48f)$$

where

Δ_1 = angle to determine transition region

ρ_1 = radius of curvature at point Q_1

ρ_{tn1} = transverse radius of curvature at point Q_1

x_1, y_1 = rectangular coordinates of point Q_1

θ_1 = angle indicating point Q_1

Referring to the geometries shown in Figures 27,28, the coupling coefficient between the two slots is calculated by²⁹

$$S_{12} = -2Y_{12}Y_{g2} / [(Y_{g1} + Y_{11})(Y_{g2} + Y_{22}) - Y_{12}^2] \quad (49)$$

where Y_{ii} and Y_{gi} are the self-admittance and the waveguide characteristic admittance for aperture i . The mutual admittance Y_{12} is given by

$$Y_{12} = \iint_{S_2} \underline{M}(2) \cdot \underline{H}(2,1) ds' / V_1 V_2 \quad (50)$$

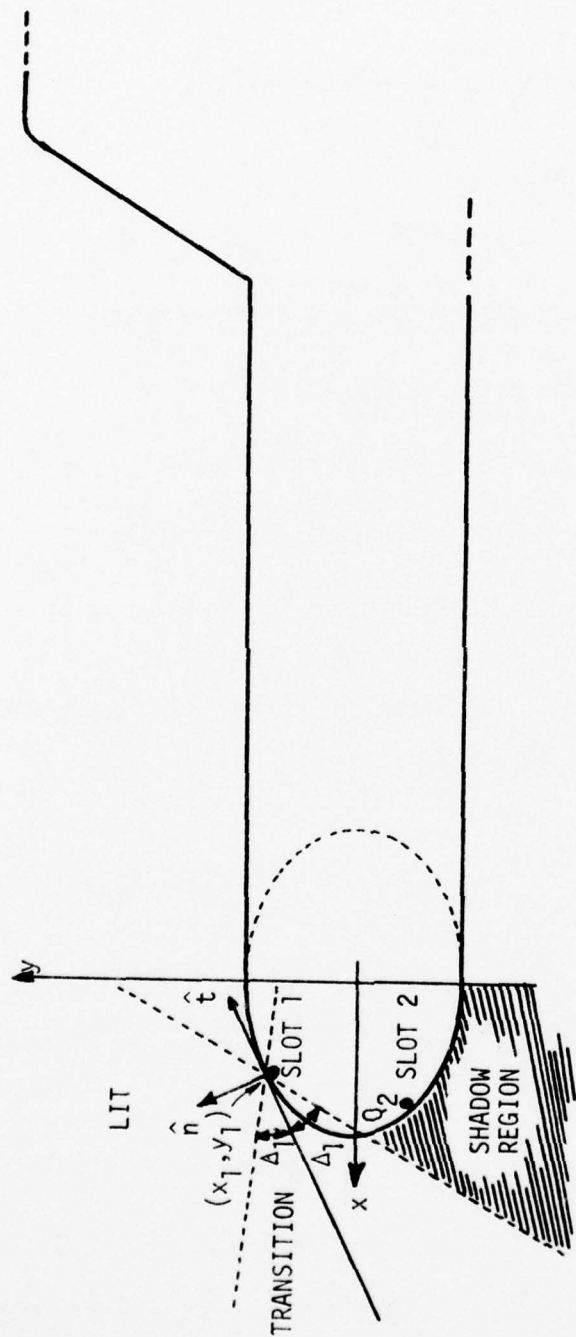


Figure 27. Lit, transition, and shadow regions for antenna at position x_1, y_1 .

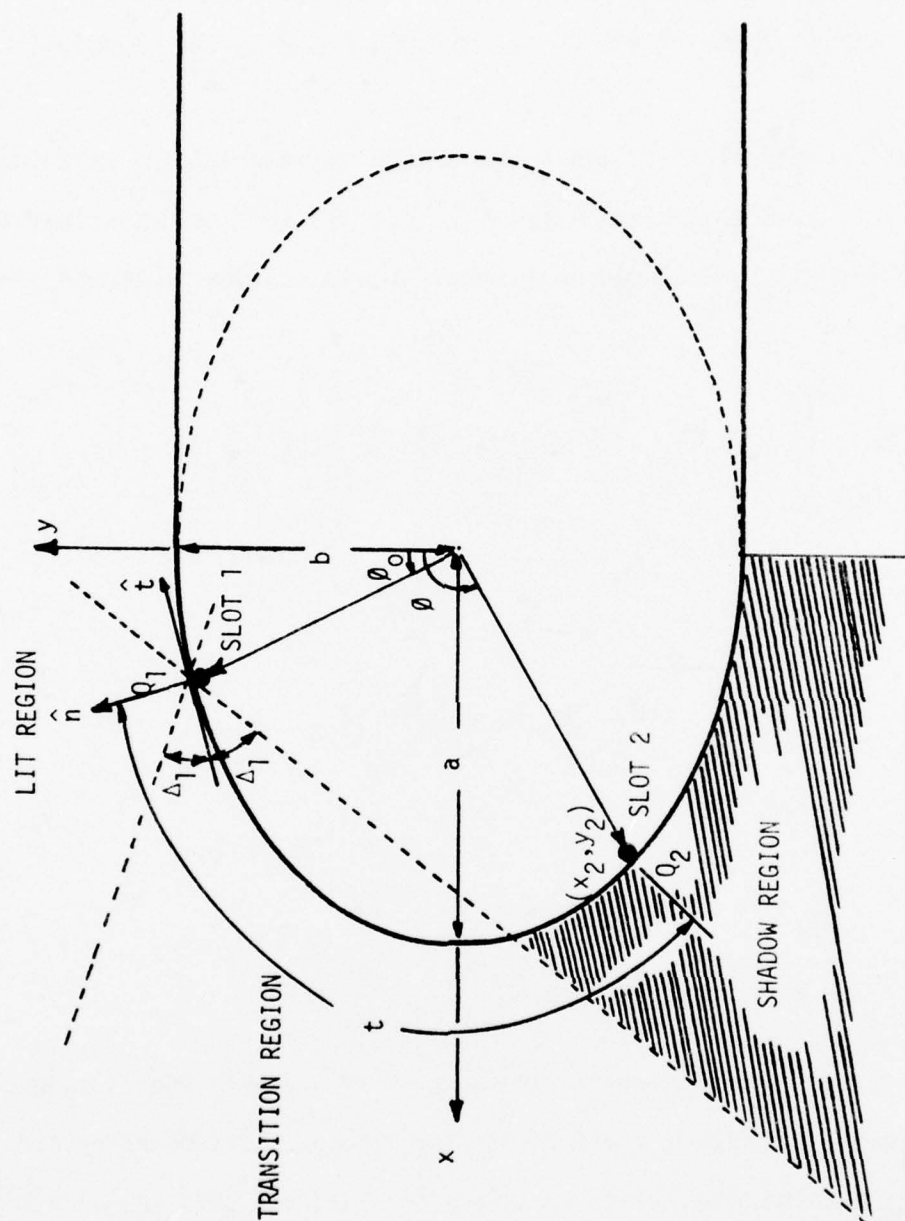


Figure 28. Expanded geometry for apertures 1 and 2 on the nose.

where $\underline{M}(2)$ is the equivalent magnetic current produced by the voltage V_2 at aperture 2, and $\underline{H}(2,1)$ is the magnetic field produced by a voltage V_1 at aperture 1, if aperture 2 is short circuited. In writing (50) it is assumed that the electric aperture fields can be represented by the principal waveguide modes.³⁰

For two identical slots and dominant mode representation, as shown in Figure 29 for hard polarization and Figure 30 for soft polarization, the magnetic field $\underline{H}(2,1)$ produced at aperture 2 by a voltage V_1 at aperture 1 is given by

$$\underline{H}(2,1) = \iint_{S_1} d\underline{H}(Q_1) = Y_0 \iint_{S_1} d\underline{M}(Q_1) \cdot [\hat{b}_1 \hat{b}_2^{\sim} \underline{F}_s + \hat{t}_1 \hat{t}_2^{\sim} \underline{G}_s] \quad (51)$$

where

$$\underline{F}_s^{\sim} = - \frac{jke^{-jkt}}{4\pi} \sqrt{\frac{1}{\rho} \frac{d\psi_0}{d\psi}} \sum_{p=0}^{\infty} L_{ph}(Q_1) A_{ph}(Q_2) T_{ph} \quad (52a)$$

$$\underline{G}_s^{\sim} = - \frac{jke^{-jkt}}{4\pi} \sqrt{\frac{1}{\rho} \frac{d\psi_0}{d\psi}} \sum_{p=0}^{\infty} L_{ps}(Q_1) A_{ps}(Q_2) T_{ps} \quad (52b)$$

L_{ph}, L_{ps} are the launching coefficients for hard and soft boundary conditions, A_{ph}, A_{ps} are the attachment coefficients for hard and soft boundary conditions, and T_{ph}, T_{ps} are the propagation functions for hard and soft boundary conditions. The launching coefficients L_{oh}, L_{os} are defined by Equations (42c) and (42d), the attachment coefficients are given by

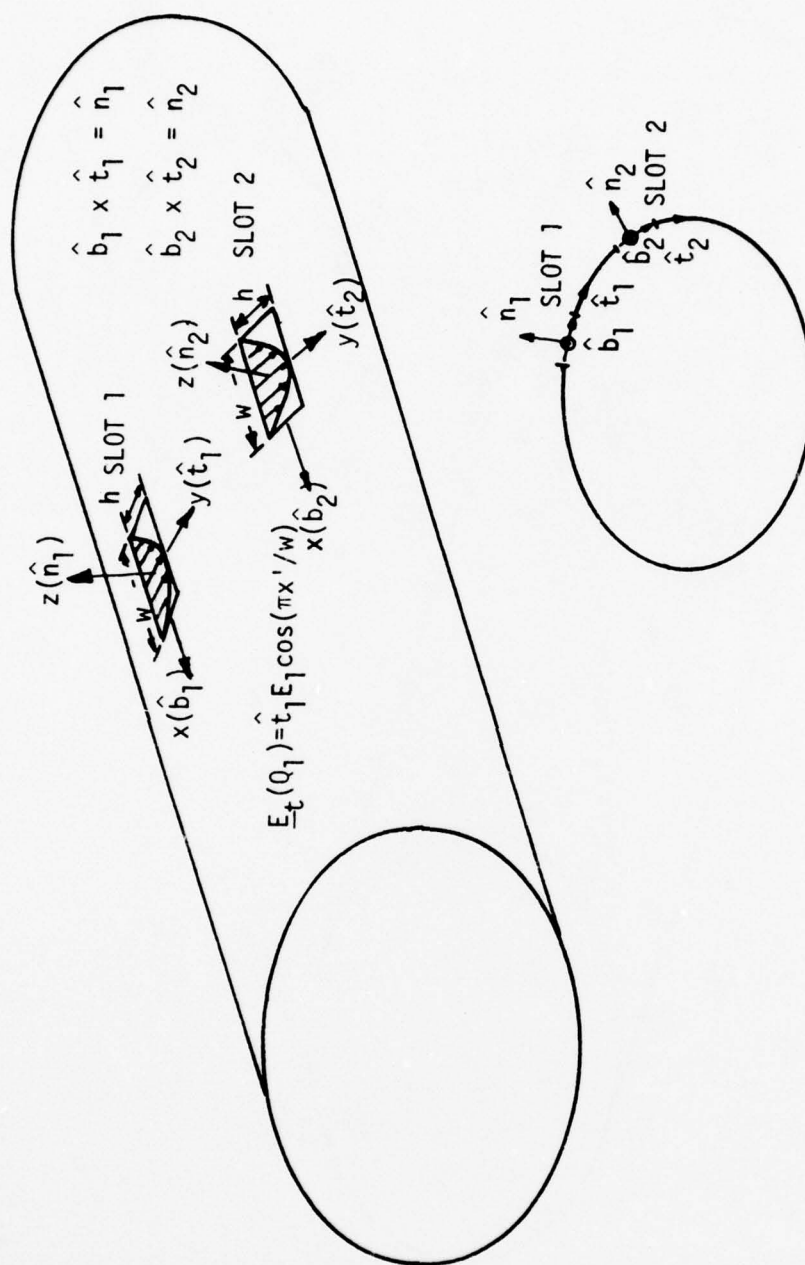


Figure 29. Hard polarization geometry for two apertures on a cylinder.

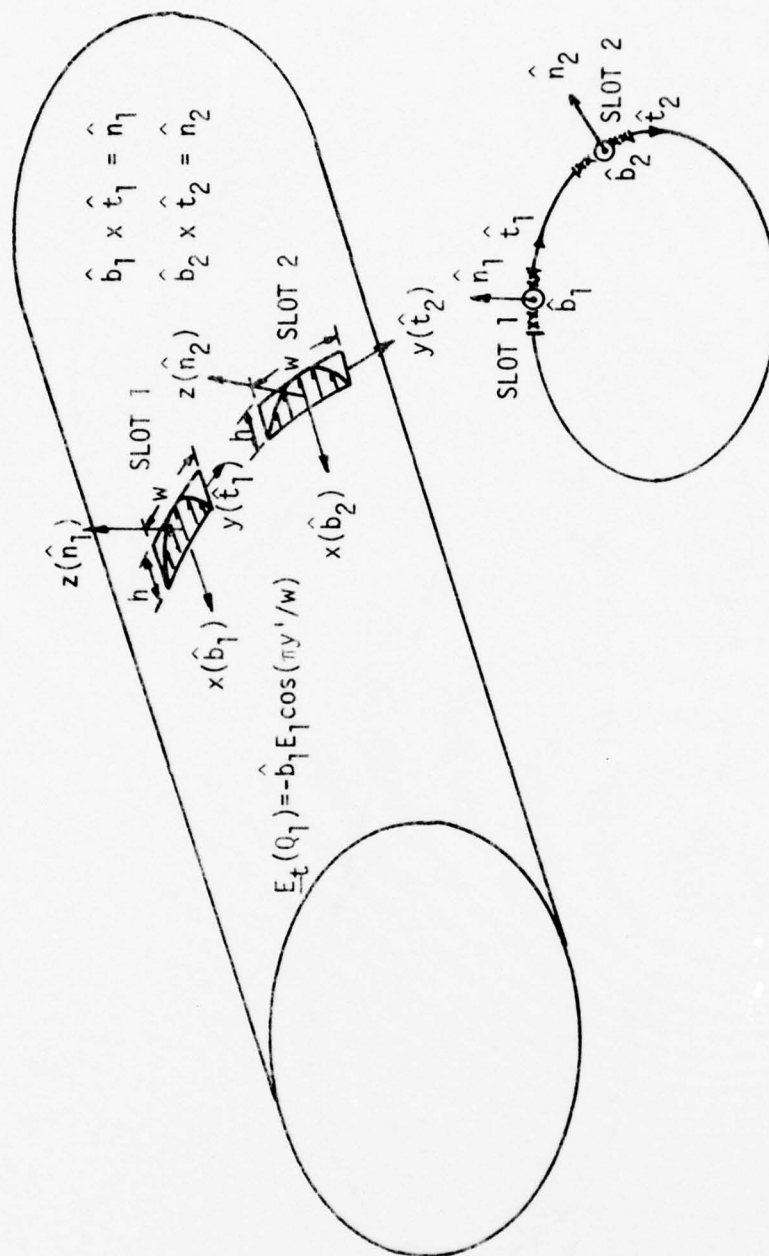


Figure 30. Soft polarization geometry for two apertures on a cylinder.

$$A_{ph} = + L_{ph} \quad (53a)$$

$$A_{ps} = - L_{ps} \quad (53b)$$

and the propagations functions by

$$T_{ph} = e^{-\int_0^t \alpha_{ph}(t') dt'} \quad (54a)$$

$$T_{ps} = e^{-\int_0^t \alpha_{ps}(t') dt'} \quad (54b)$$

where $\alpha_{ph}(t')$ and $\alpha_{ps}(t')$ are the attenuation coefficients for hard and soft boundary conditions and are listed in Tables 3 and 4.

For an arrangement of apertures as shown in Figure 29 (hard polarization) and with a dominant mode field distribution given by

$$\underline{E}_t(Q_1) = \hat{t}_1 E_1 \cos(\pi x'/w) \quad (55)$$

where h is the smallest dimension of the aperture, the magnetic current density can be written as

$$\underline{M}(1) = -\hat{n}_1 \times \underline{E}_t(Q_1) = \hat{b}_1 E_1 \cos(\pi x'/w) \quad (56)$$

$\underline{H}(2,1)$ by

$$\underline{H}(2,1) = \iint_{S_1} \underline{M}(1) \cdot [\hat{b}_1 \hat{b}_2 \tilde{F}_s + \hat{t}_1 \hat{t}_2 \tilde{G}_s] ds' = \hat{b}_2 Y_0 \tilde{F}_s E_1 (2wh/\pi) \quad (57)$$

where w is the largest dimension of the aperture, and

$$\iint_{S_2} \underline{M}(2) \cdot \underline{H}(2,1) \, ds' = Y_0 \tilde{F}_S (2w/\pi)^2 V_1 V_2 \quad (58)$$

V_1 and V_2 are the voltages at apertures 1 and 2, respectively. Finally the mutual admittance of Equation (50) reduces to

$$Y_{12} = Y_0 \tilde{F}_S (2w/\pi)^2 \quad (59)$$

and the coupling coefficient of (49) assuming

$$Y_{11} = Y_{22} = Y_0 \quad (60a)$$

$$Y_{g1} = Y_{g2} = Y_0 \sqrt{1 - (\lambda/2w)^2} \quad (60b)$$

to

$$S_{12} = - \frac{\tilde{F}_S (2w/\pi)^2 \sqrt{1 - (\lambda/2w)^2}}{[\sqrt{1 - (\lambda/2w)^2} + 1]^2 - \tilde{F}_S^2 (2w/\pi)^4} \quad (61)$$

In a similar manner the coupling for the aperture arrangement shown in Figure 30 (soft polarization) can be derived. The aperture field distribution is given by

$$\underline{E}_t(Q_1) = -b_1 \underline{E}_1 \cos(\pi y'/w) \quad (62)$$

the magnetic density by

$$\underline{M}(1) = -\hat{n}_1 \times \underline{E}_t(Q_1) = \hat{t}_1 \cos(\pi y'/w) \quad (63)$$

the magnetic field of Equation (57) by

$$\underline{H}(2,1) = \hat{t}_2 \tilde{Y}_0 \tilde{G}_S E_1(2wh/\pi) \quad (64)$$

and

$$\iint_{S_2} \underline{M}(2) \cdot \underline{H}(2,1) ds' = \tilde{Y}_0 \tilde{G}_S (2w/\pi)^2 V_1 V_2 \quad (65)$$

Finally the coupling coefficient for the soft polarization arrangement, assuming dominant mode field distribution, reduces to

$$S_{12} = - \frac{\tilde{G}_S (2w/\pi)^2 \sqrt{1 - (\lambda/2w)^2}}{[\sqrt{1 - (\lambda/2w)^2} + 1]^2 - \tilde{G}_S^2 (2w/\pi)^4} \quad (66)$$

As antenna 2 leaves the shadow region and enters the transition region, as shown in Figures 31, 32, the series representations of the \tilde{F}_S and \tilde{G}_S in (52a) and (52b) become poorly convergent and must be replaced by integral formulations.²⁹ In other words, the \tilde{F}_S and \tilde{G}_S of (52a) and (52b) when antenna 2 is in the transition region of antenna 1 reduce to²⁹

$$\tilde{F}_S = - \frac{jke^{-jkt}}{4\pi} \sqrt{\frac{1}{\rho} \frac{d\psi_0}{d\psi}} \left[\left(\frac{jk}{2}\right)^{1/2} (m\chi)^{-1} h(\xi) \right] \quad (67)$$

$$\tilde{G}_S = - \frac{jke^{-jkt}}{4\pi} \sqrt{\frac{1}{\rho} \frac{d\psi_0}{d\psi}} \left[-\left(\frac{jk}{2}\right)^{1/2} (m\chi)^{-1} \tilde{h}(\xi) \right] \quad (68)$$

where

$$m = (k\rho_1/2)^{1/3} \quad (69)$$

$$\chi = (\rho_2/\rho_1)^{1/6} \quad (70)$$

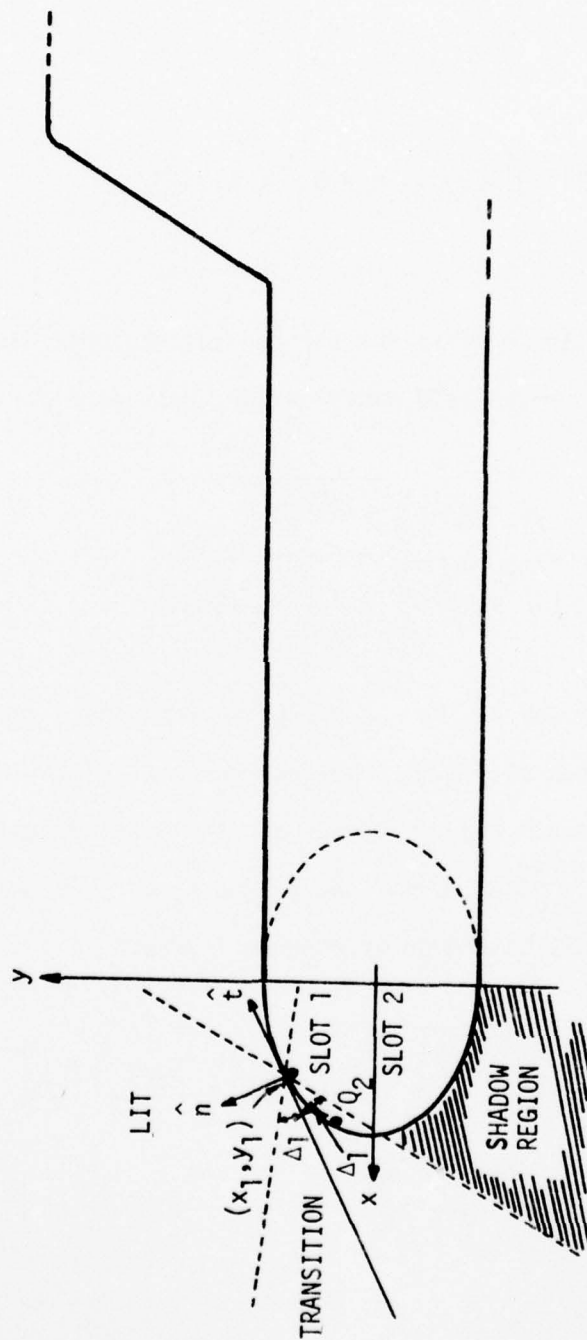


Figure 31. Geometrical arrangement when slot 2 is in the transition region of slot 1.

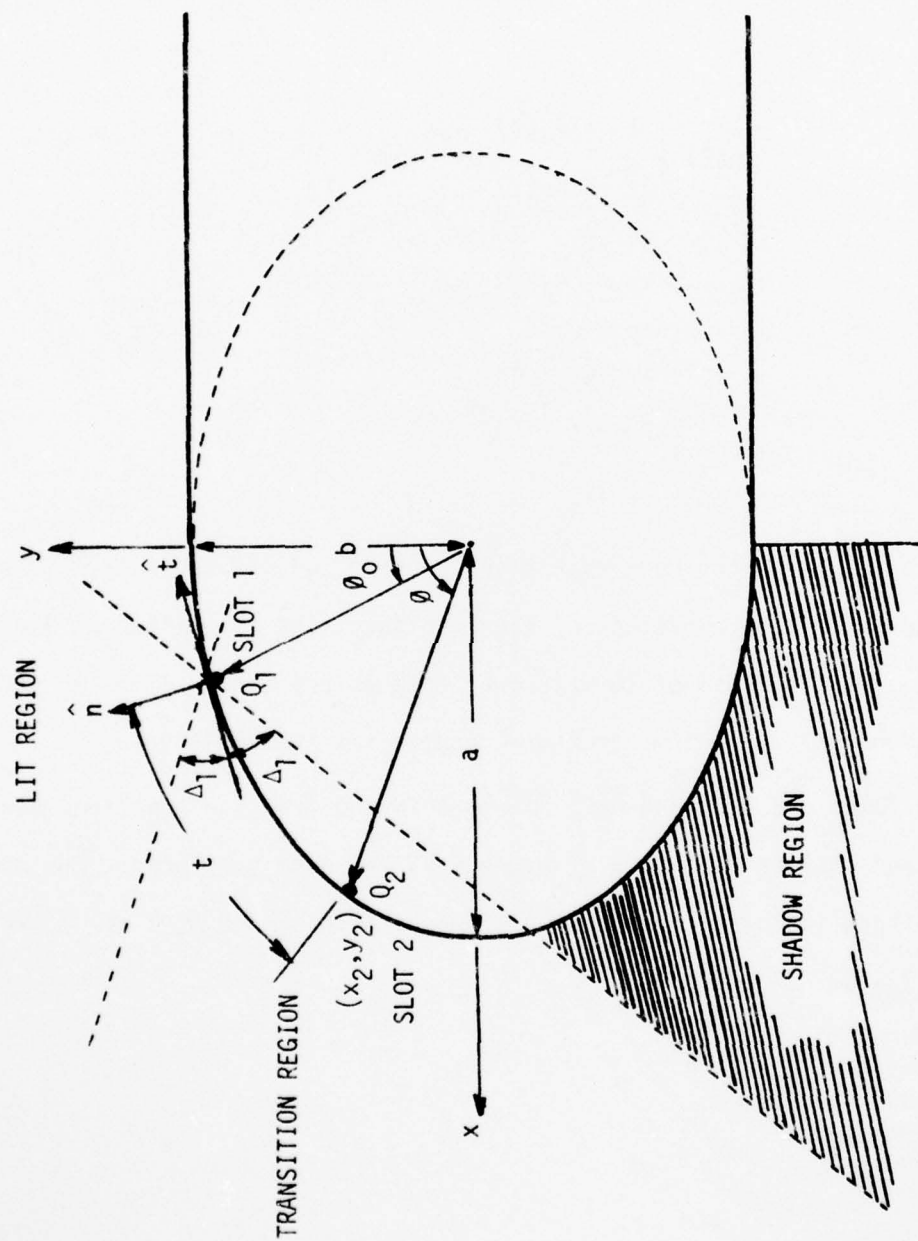


Figure 32. Expanded geometry when slot 2 is in the transition region of slot 1.

$$h(\xi) = \frac{i}{\sqrt{\pi}} \int_{\Gamma_1} \frac{w_2(\tau)}{w_2'(\tau)} e^{-j\xi\tau} d\tau \quad (71)$$

$$\tilde{h}(\xi) = \frac{1}{\sqrt{\pi}} \int_{\Gamma_1} \frac{w_2'(\tau)}{w_2(\tau)} e^{-j\xi\tau} d\tau \quad (72)$$

$$\xi = \int_0^t \frac{1}{\rho_g} \left(\frac{k\rho_g}{2} \right)^{1/3} dt \quad (73)$$

$w_2(\tau)$ and $w_2'(\tau)$ are the Fock-type Airy function and its derivative, respectively, Γ_1 is the path of integration for the Fock functions (see Figure C.4 of Appendix C), ρ_1 and ρ_2 are the radii of curvature at antenna positions 1 and 2, and ρ_g is the radius of curvature of the structure between the two positions.

The functions $h(\xi)$ and $\tilde{h}(\xi)$ can be obtained from the functions designated as $V(\xi)$ and $U(\xi)$ in Reference 31 where they are also tabulated. For completeness, the magnitude (modulus) and phase (argument) of $h(\xi)$ and $\tilde{h}(\xi)$ are shown plotted in Figures 33-36.

AD-A041 484

WEST VIRGINIA UNIV MORGANTOWN DEPT OF ELECTRICAL ENG--ETC F/G 1/2
AIRCRAFT ANTENNA ANALYSIS AND MICROWAVE LANDING SYSTEM (MLS) AP--ETC(U)
JAN 76 C A BALANIS, Y CHENG

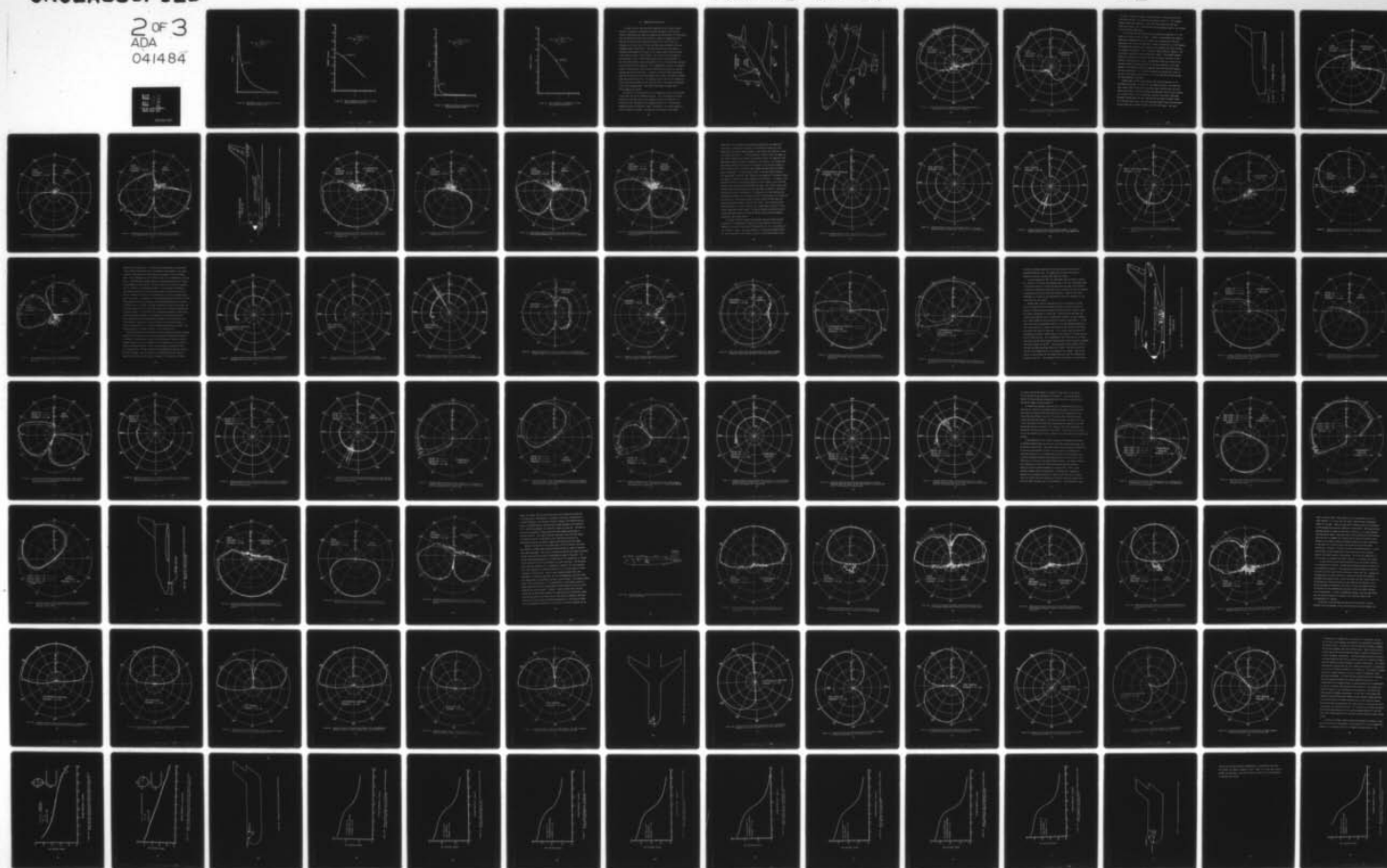
DOT-OS-40013

UNCLASSIFIED

FAA-RD-76-37

NL

2 OF 3
ADA
041484



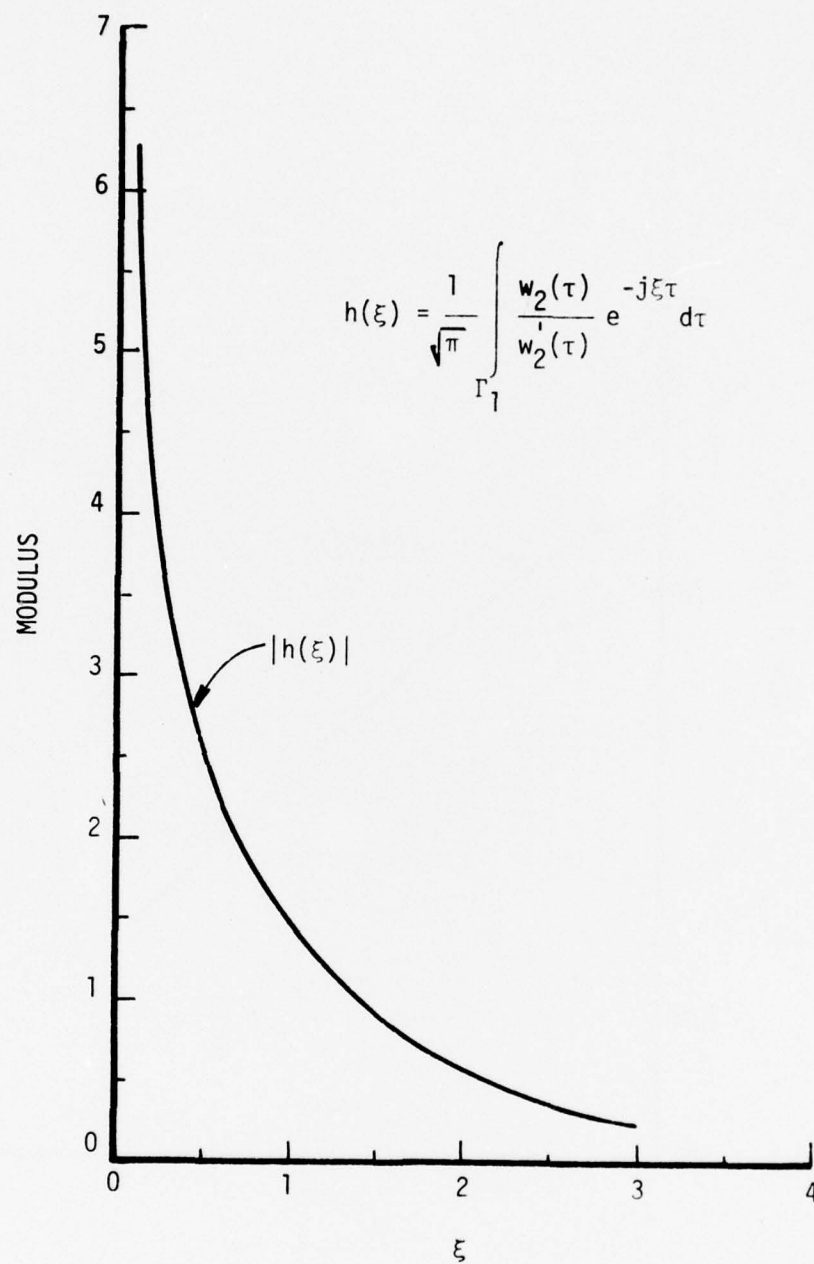


Figure 33. Magnitude (modulus) distribution of hard polarization function $h(\xi)$.

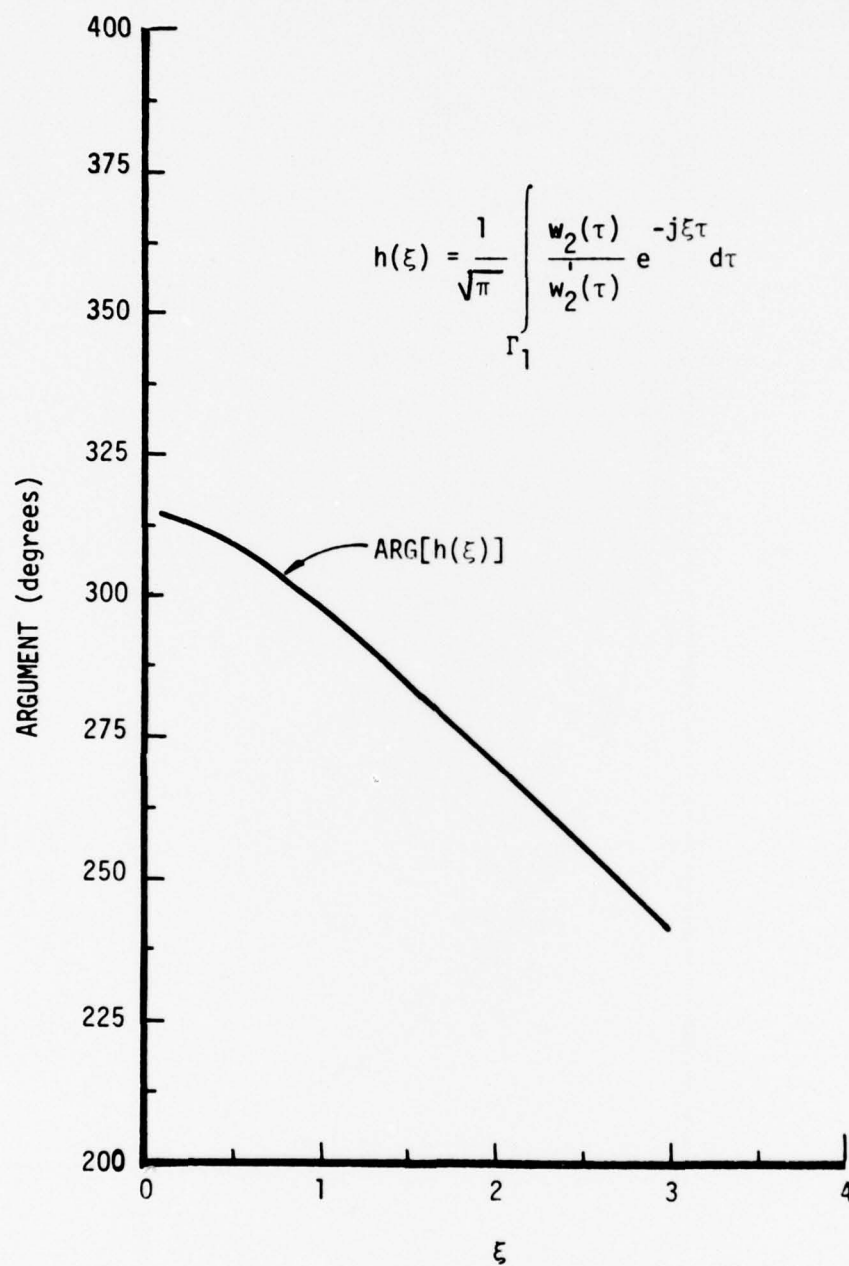


Figure 34. Phase (argument) distribution of hard polarization function $h(\xi)$.

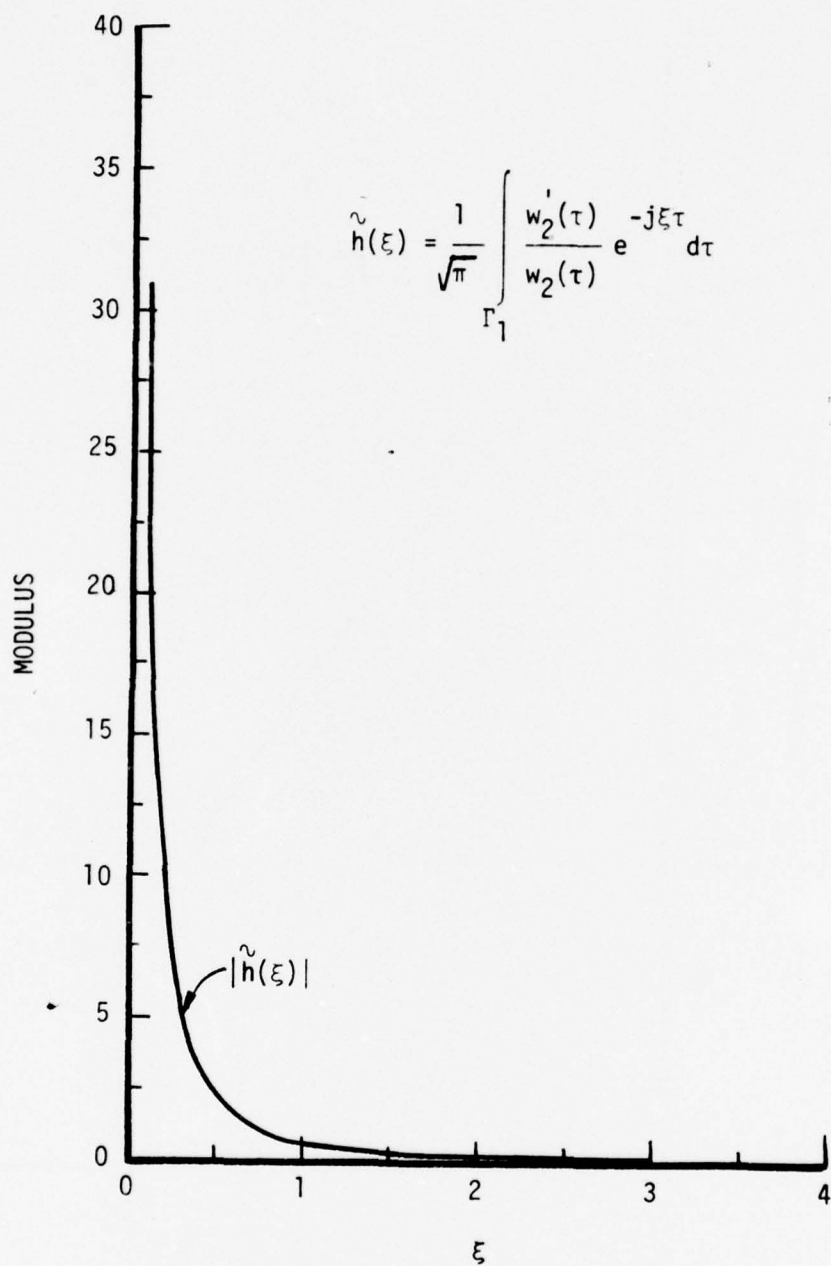


Figure 35. Magnitude (modulus) distribution of soft polarization function $\tilde{h}(\xi)$.

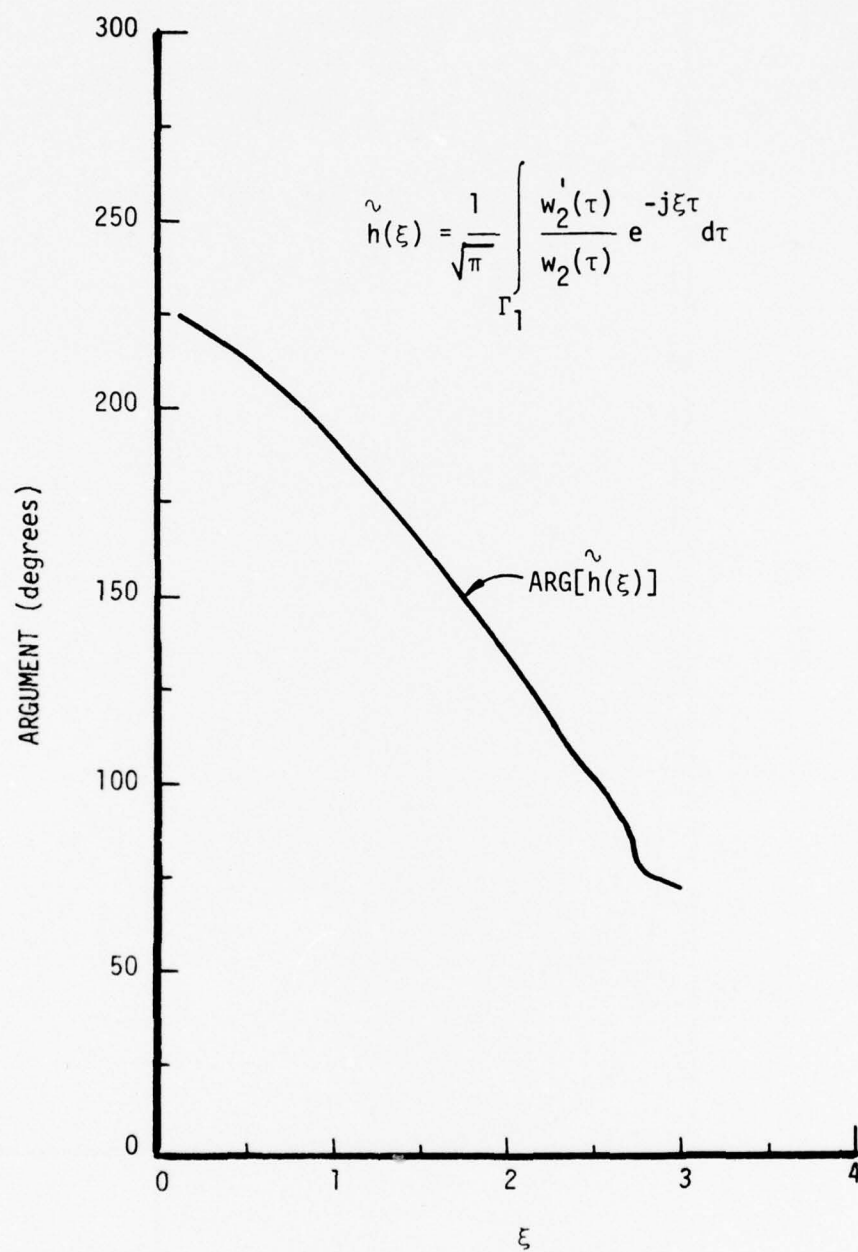


Figure 36. Phase (argument) distribution of soft polarization function $\tilde{h}(\xi)$.

III. COMPUTATIONS AND RESULTS

In order to verify the analytical modelings of the radiation characteristics of antennas on airplanes which were developed in the previous section, computations were made and compared with measurements on scaled models. Once the theoretical models were verified, a number of computations were made on full scale aircraft (Boeing 737, Boeing 747, and KC-135) at a frequency of 5.1 GHz, which is within the band under consideration for the Microwave Landing System (MLS). Locations were examined which seemed to provide the most promising coverage in the forward (nose) direction, which is the space of concern during landing. The results will be presented in the same order as that in which the analytical models were developed. In most cases the antennas under consideration will be a circumferential aperture, an axial aperture, and a monopole. The circumferential aperture and monopole provide in the elevation plane vertical polarization and the axial aperture provides horizontal polarization. A number of coverage comparisons between vertical and horizontal polarized antennas will be made at different locations along the aircraft structure. The coverage criteria used for the comparisons will be 20° above the nose and 30° below the nose in the elevation plane and $\pm 60^\circ$ in the azimuth plane. These define the primary coverage sector during landing for the MLS.

In Figure 37 the orientations of a circumferential and an axial aperture on the upper part of the fuselage are shown. The orientations of the same apertures on the lower part of the fuselage are shown in Figure 38. In Figures 39 and 40 the measured and computed patterns of a circumferential waveguide mounted at locations 1 and 2, respectively, on a scaled model aircraft of Figure 1 are shown. The model was constructed of flat plates

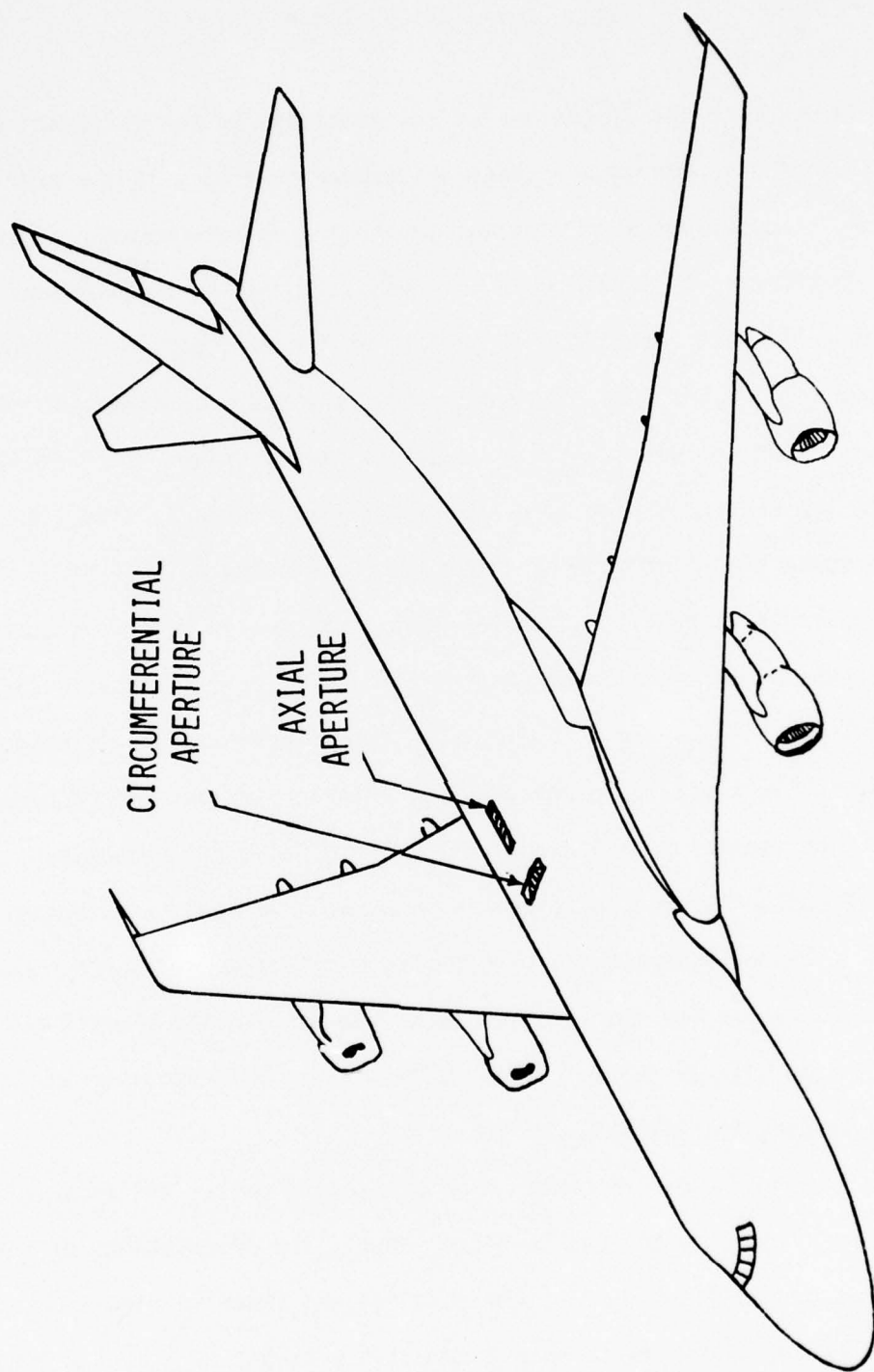


Figure 37. Circumferential and axial aperture orientations on the upper part of an airplane fuselage.

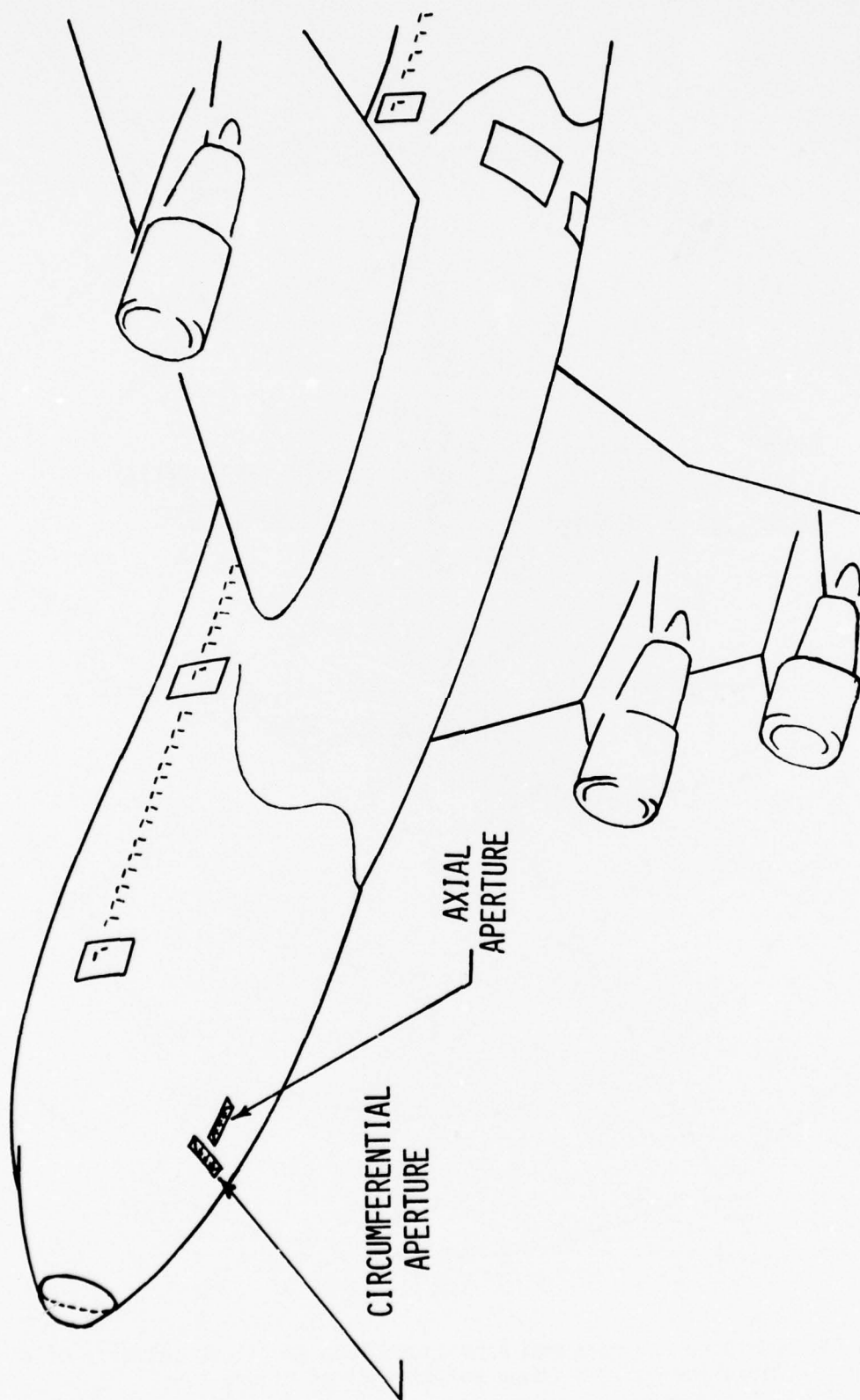


Figure 38. Circumferential and axial aperture orientations on the lower part of an airplane fuselage.

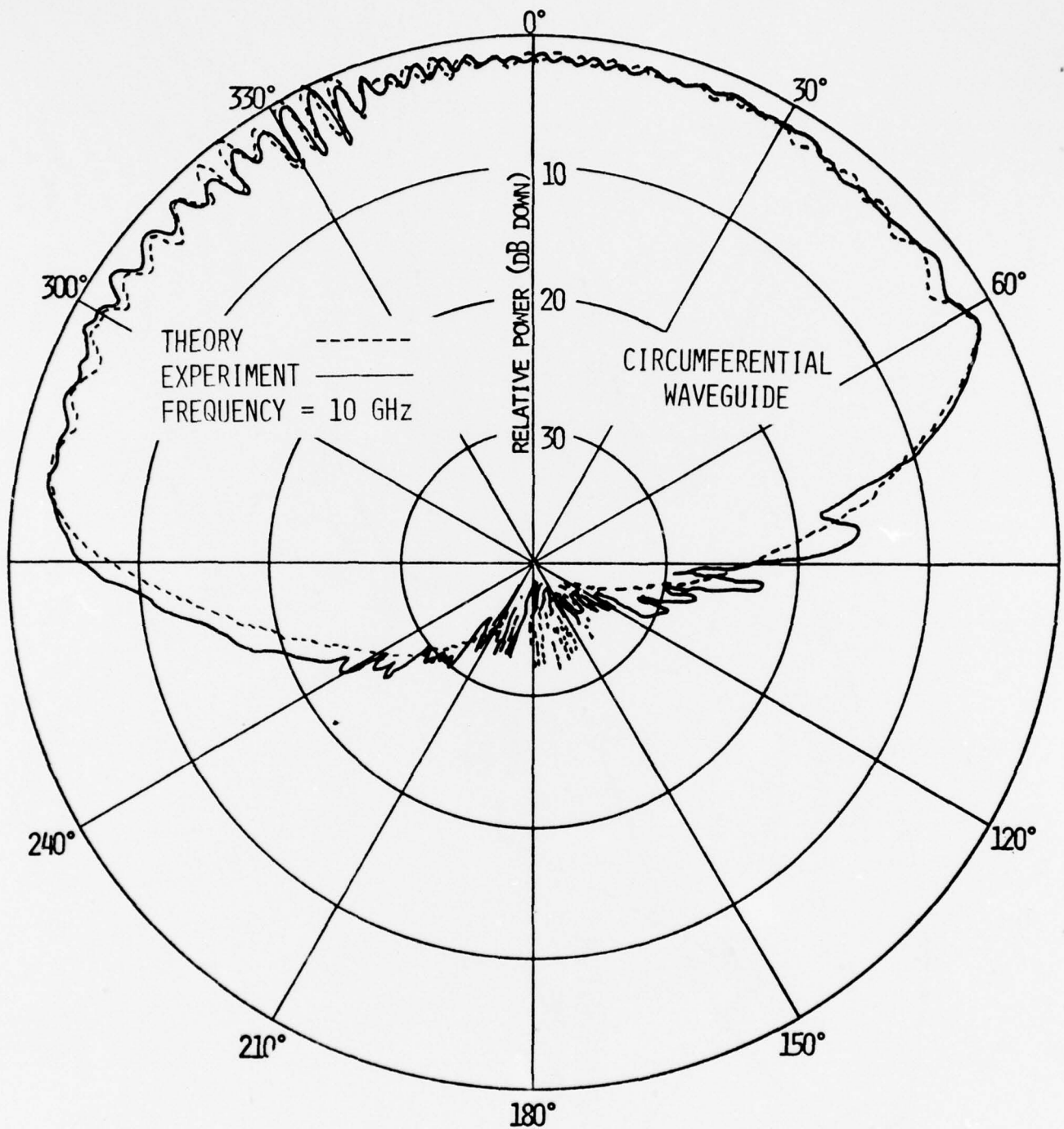


Figure 39. Computed and measured elevation plane amplitude patterns of a circumferential slot on position #1 of Figure 1.

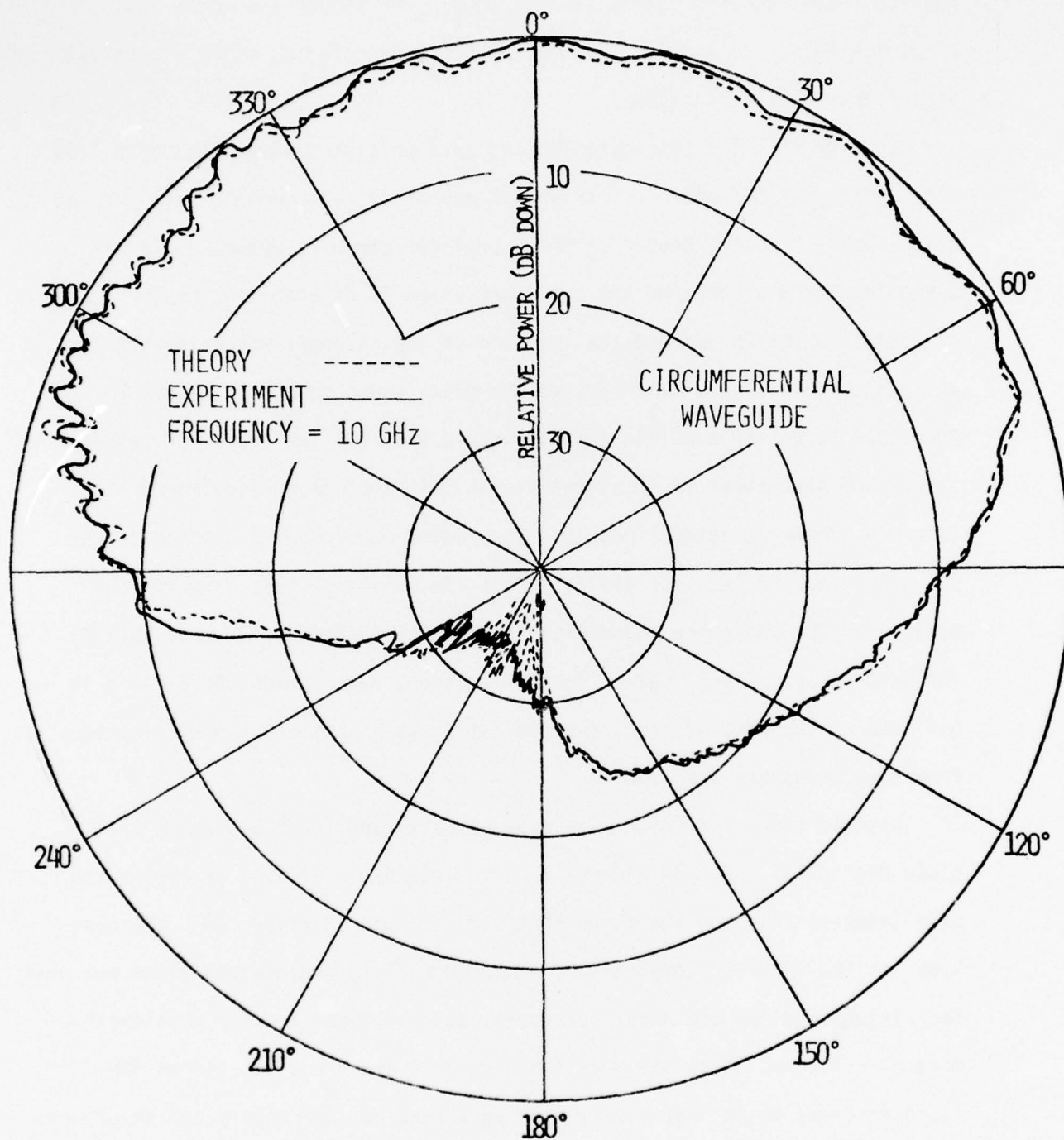


Figure 40. Computed and measured elevation plane amplitude patterns of a circumferential slot on position #2 of Figure 1.

12" wide. Although a somewhat simplified model, it was the initial configuration examined. The dimensions are shown in Figure 1. The agreement between theory and experiment is very good, even though the model was electrically small, and it provided the first encouraging signs of the validity of the analytical techniques.

In Figure 41 the configuration and some pertinent dimensions of a 1/35 scale space shuttle model are shown. A number of measurements were made at NASA Langley Research Center on this model for circumferential and axial waveguides, and a short monopole and are shown in Figures 42 - 44. The frequency of operation was 35 GHz and the location of the antennas was below the nose, as indicated in Figure 41. Part of the nose, shown dashed in Figure 41, was truncated to better simulate the dielectric radome. The agreement between theory and experiment is excellent and that is another indication of the accuracy of the analytical models. The radiation along the surface of the structure (toward the nose and tail) for the axial aperture is very weak because of the vanishing boundary conditions that the E-field must satisfy for this polarization. For a finite structure, even though the E-field is not zero at the edge of the structure, it is very weak and the diffractions from that wedge are very small.

Another model for which measurements were made available was a 1/11 scale Boeing 737 shown in Figure 45. Two antenna locations, are below the nose (station 222) and the other above the cockpit (station 220), are also shown in the figure. Computed and measured amplitude elevation plane patterns for circumferential and axial apertures, and short and quarter wavelength monopoles located below the nose (station 222) are shown in Figures 46-49. It is observed again that a very good agreement between theory and experiment has been obtained everywhere except in the 120° - 180° region. The small

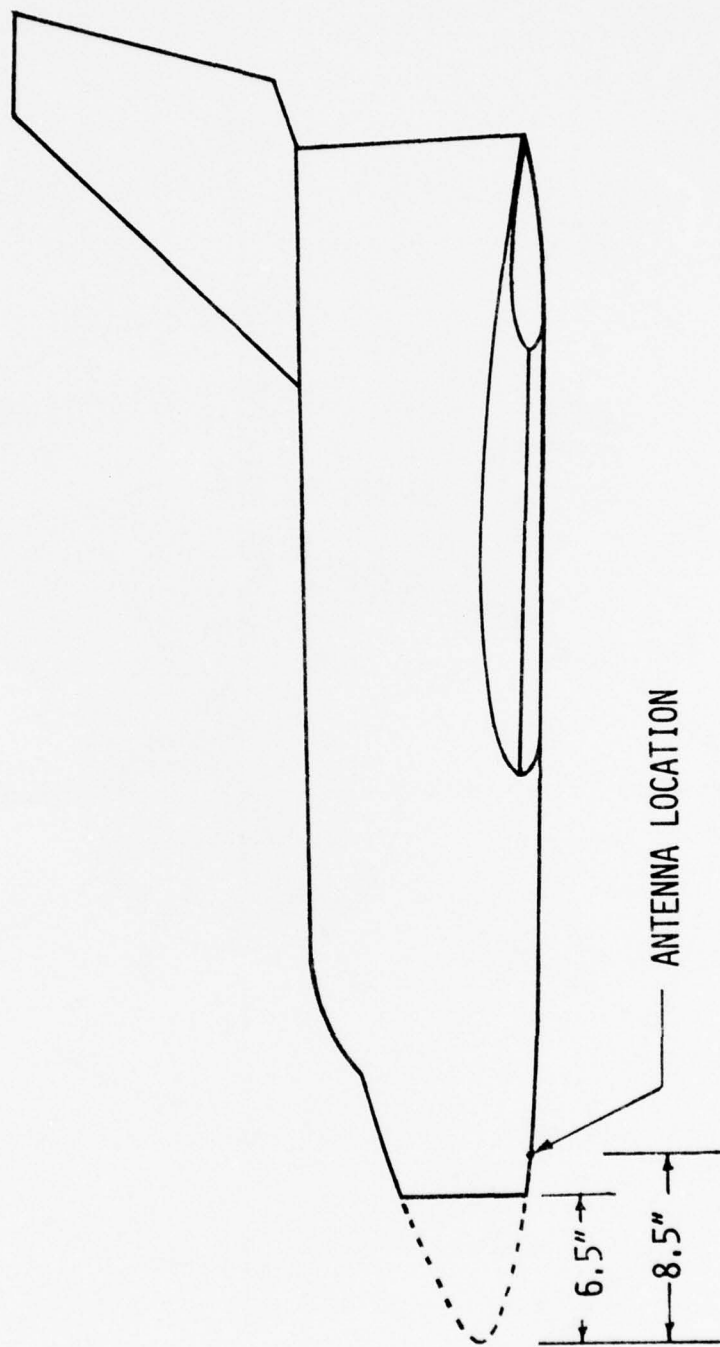


Figure 41. Space shuttle orbiter configuration with dimensions and antenna location on a 1/35 scale model.

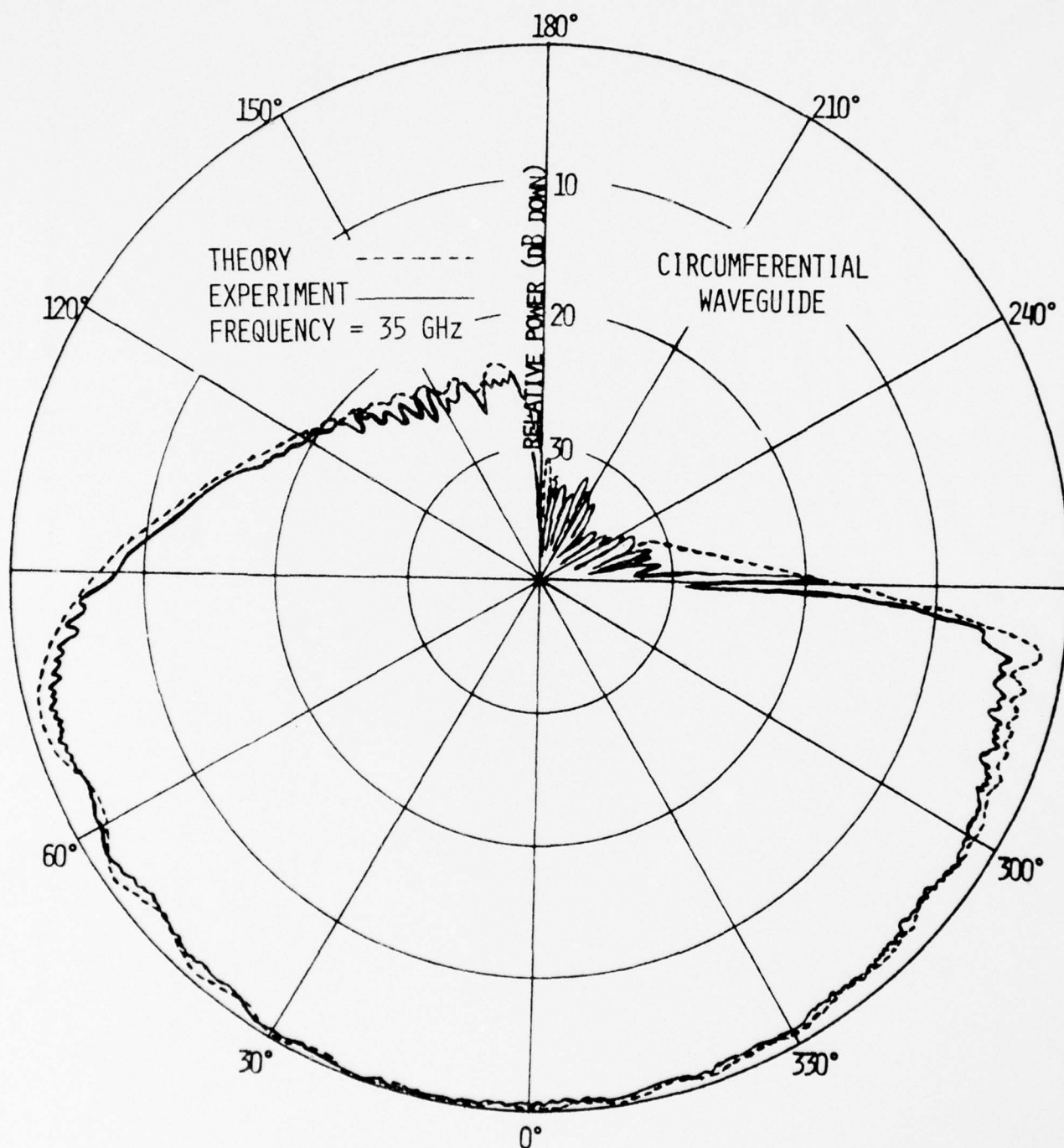


Figure 42. Computed and measured elevation plane amplitude patterns of a circumferential slot below the nose of 1/35 scale space shuttle.

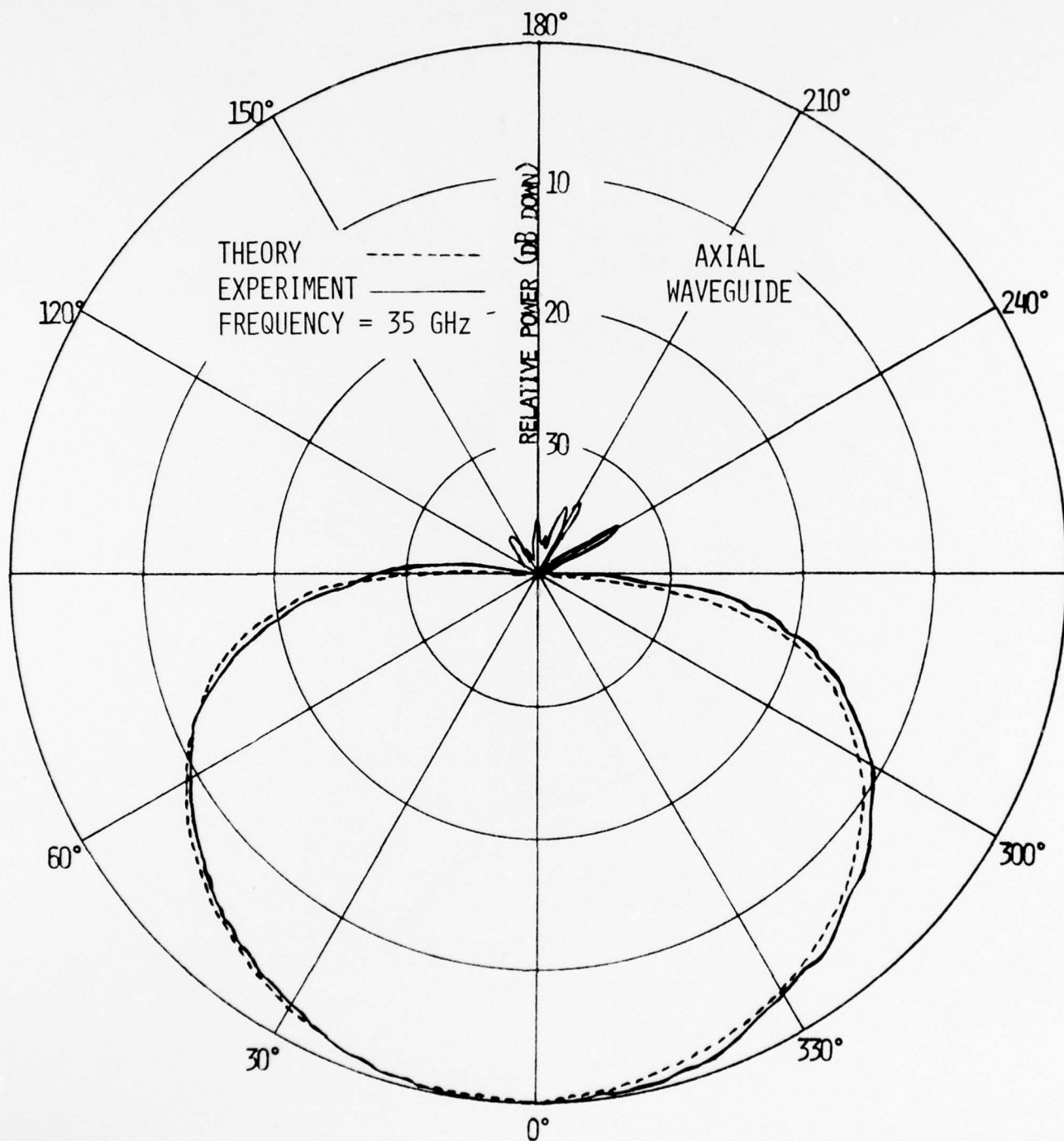


Figure 43. Computed and measured elevation plane amplitude patterns of an axial slot below the nose of 1/35 scale space shuttle.

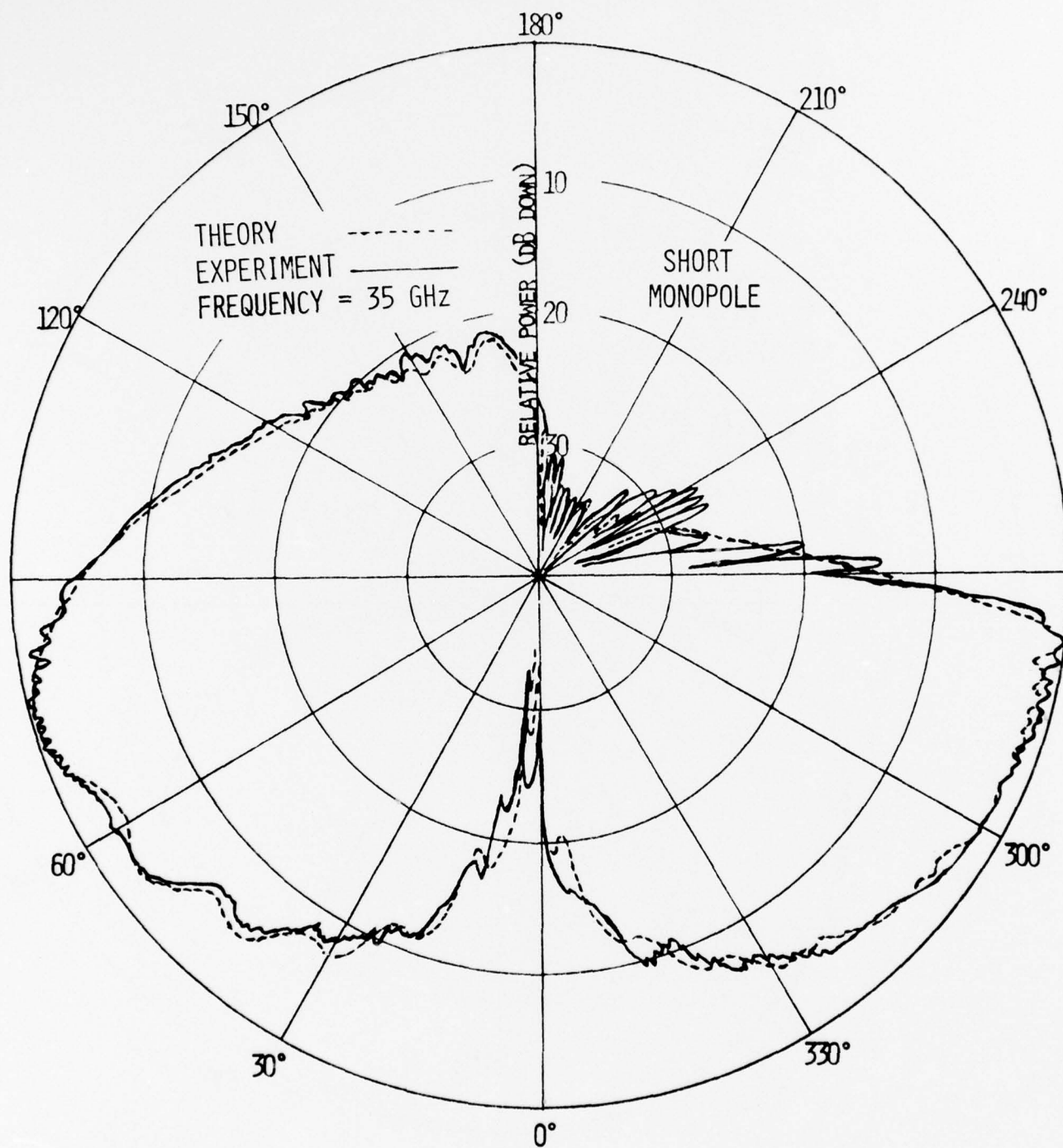


Figure 44. Computed and measured elevation plane amplitude patterns of a short monopole below the nose of 1/35 scale space shuttle.

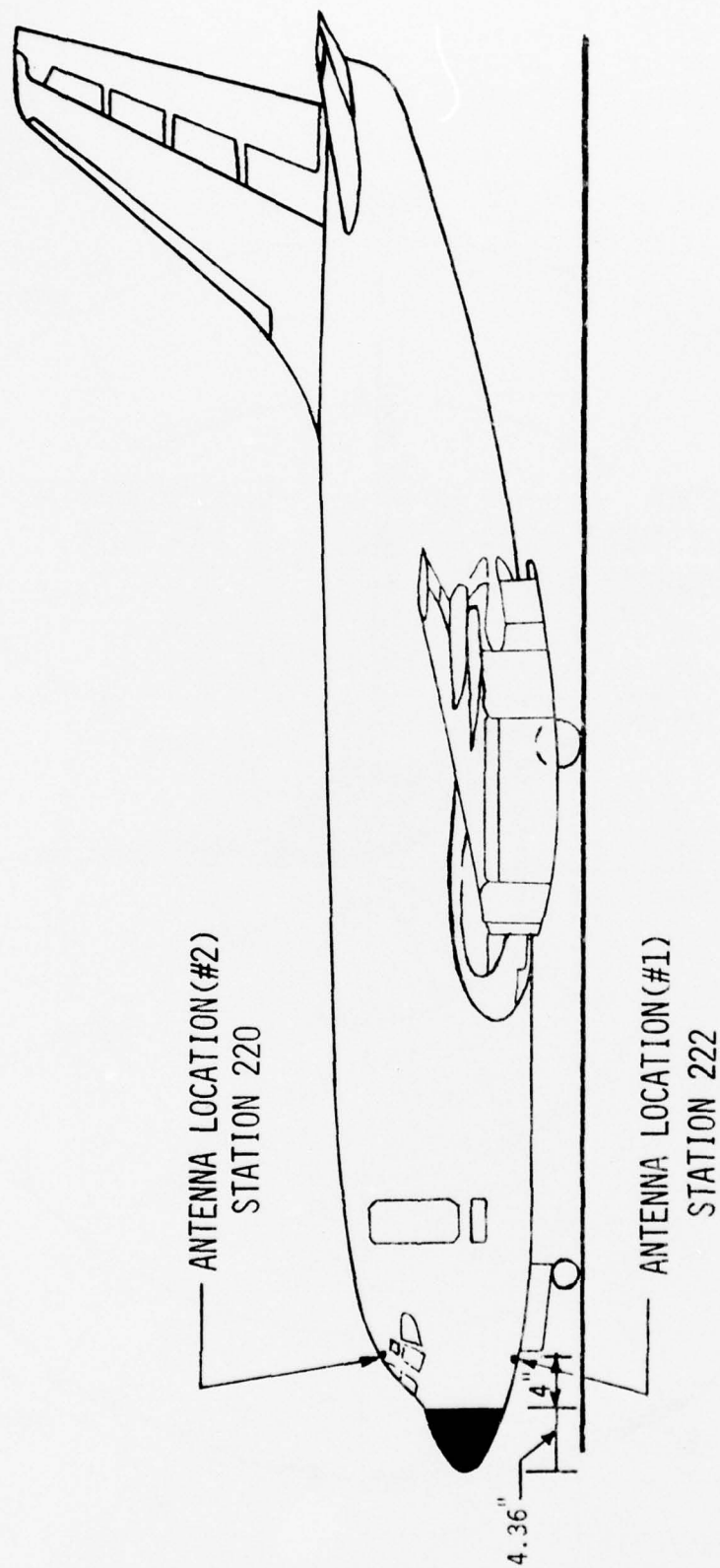


Figure 45. Boeing 737 airplane configuration with two antenna locations on a 1/11 scale model.

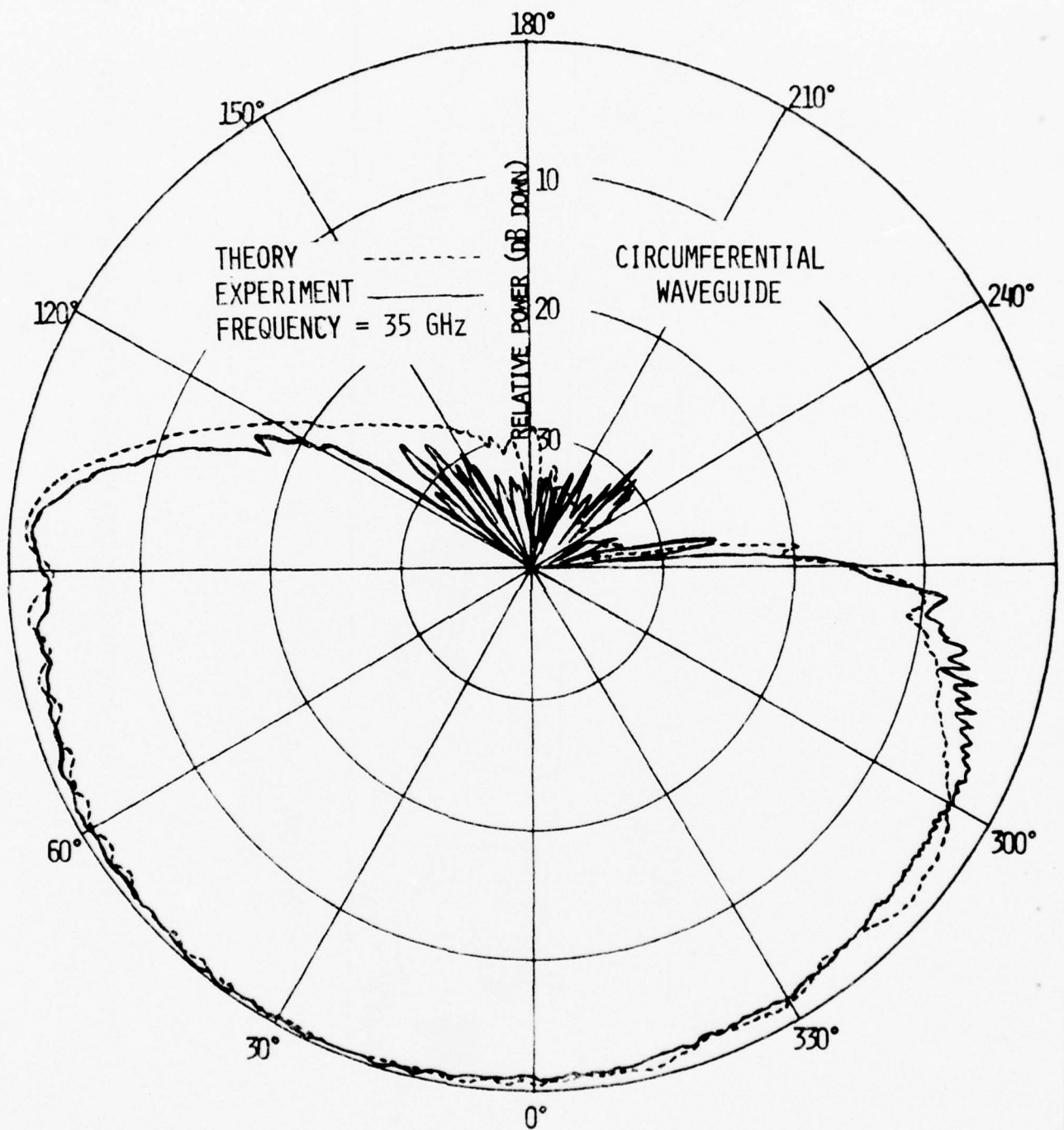


Figure 46. Computed and measured elevation plane amplitude patterns of a circumferential waveguide below the nose (station 222) of 1/11 scale Boeing 737.

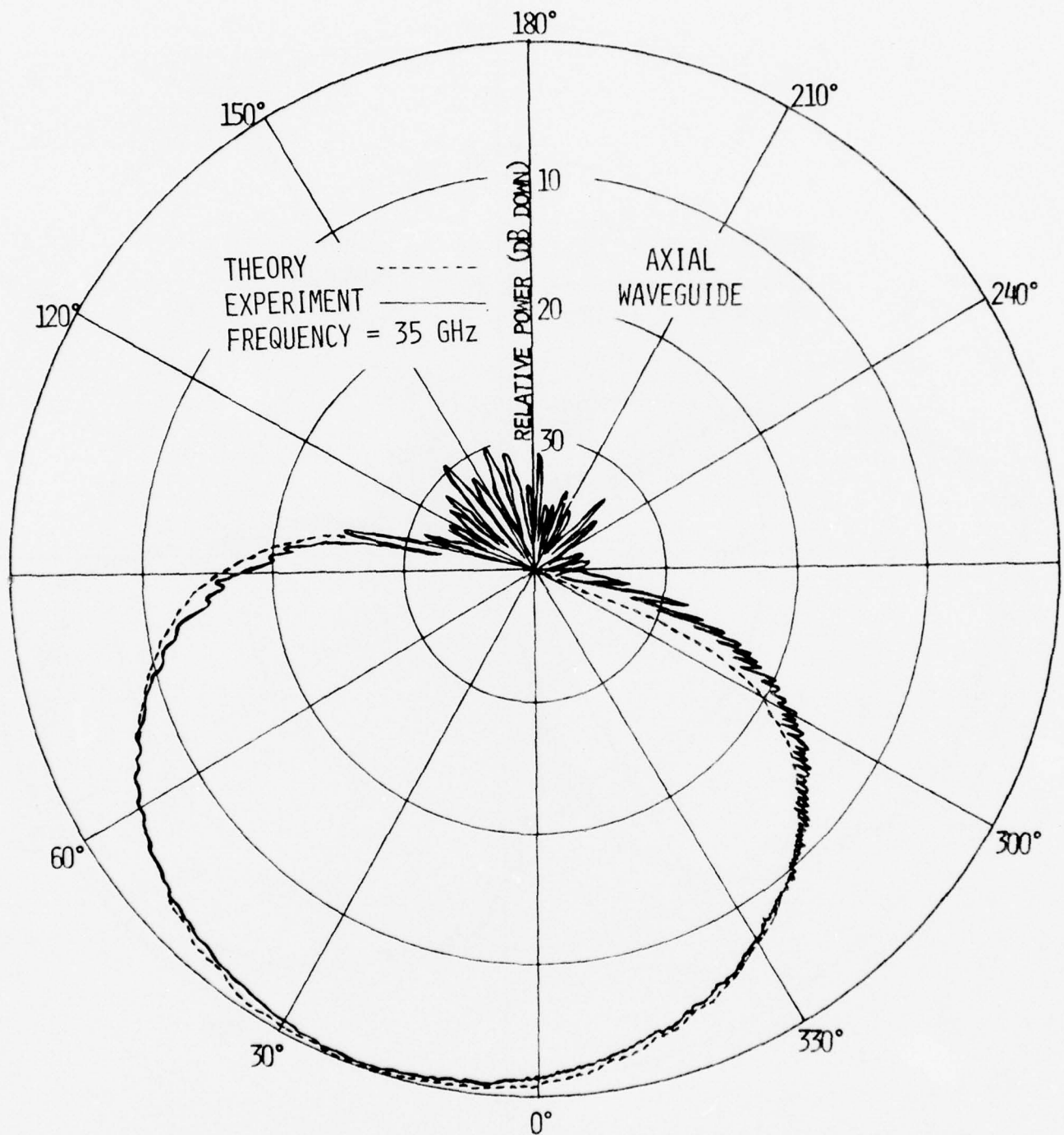


Figure 47. Computed and measured elevation plane amplitude patterns of an axial waveguide below the nose (station 222) of 1/11 scale Boeing 737.

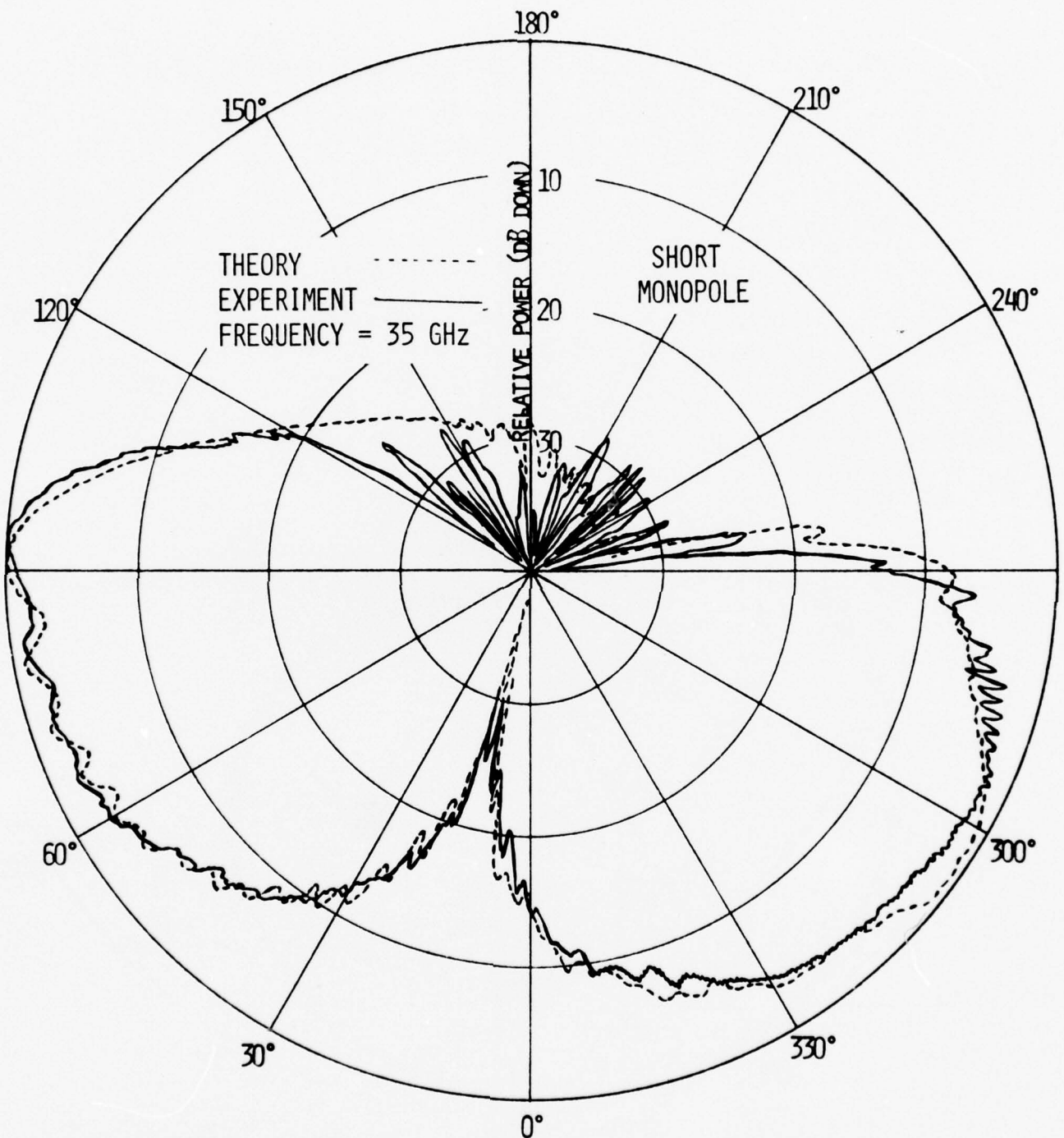


Figure 48. Computed and measured elevation plane amplitude patterns of a short monopole below the nose (station 222) of 1/11 scale Boeing 737.

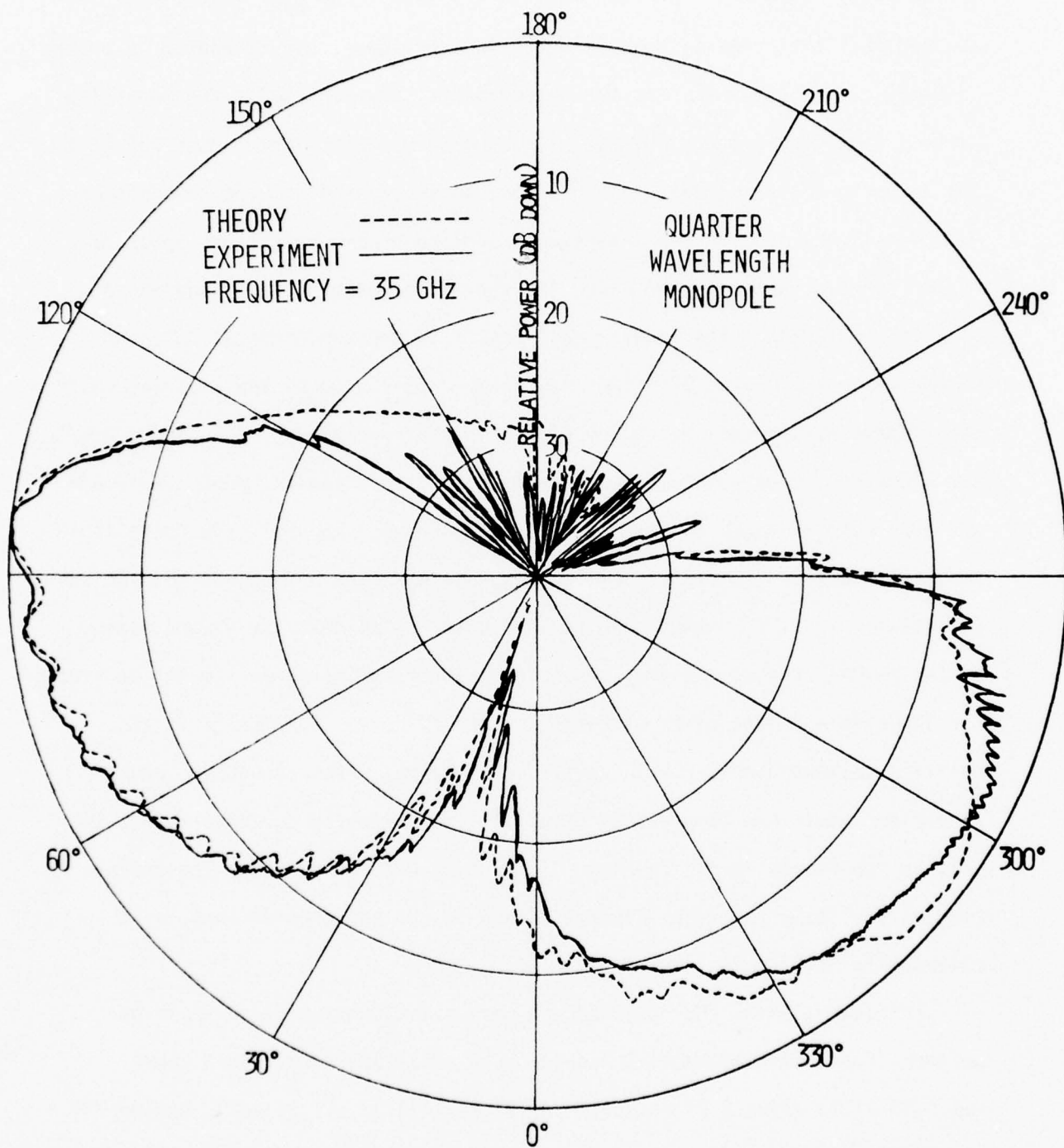


Figure 49. Computed and measured elevation plane amplitude patterns of a quarter wavelength monopole below the nose (station 222) of 1/11 scale Boeing 737.

differences are attributed to the analytical modeling of the radome part of the nose. Referring to Figure 45, in the analytical modeling it was assumed that the radome, shown darkened in the figure, was truncated in order to simplify the analysis. In the measurements, however, while the remaining part of the structure was covered with conductive paint, the radome was left unpainted to better simulate its presence in an aircraft. Even though there were simplifications in the analytical modeling of the radiation mechanism of the forward sector of the nose, the agreement between theory and experiment is remarkable. The lower signal levels in the experimental patterns of Figures 46-49 in the 120° - 180° region are attributed to the trapping, within the radome, of some of the energy headed in that direction. In Figures 50-53 the elevation plane relative phase patterns of the antennas, whose amplitude patterns were included in Figures 46-49, are shown. The relative phase shown in each figure is the difference in the phase when the antenna is mounted on the actual aircraft to that when it is mounted on an infinite ground plane. So the phase patterns are only shown for $\pm 90^{\circ}$ from the normal to the aperture. The variations in the phase patterns are small, except for the short and quarter wavelength monopole in the 15° - 25° region. Even though the phase variations there are large, they occur in a region where coverage is not of primary importance during landing. It must be pointed out that the corresponding amplitude patterns, Figures 48 and 49, do not provide acceptable coverage in this region either.

In Figures 54-56 the computed and measured elevation plane amplitude patterns for a circumferential aperture, an axial aperture, and a short monopole at location 2 (station 220 of Figure 45) of a 1/11 scale Boeing 737 are displayed. Again a very good agreement is indicated everywhere except for some differences in the pattern structure in the forward (nose) and in

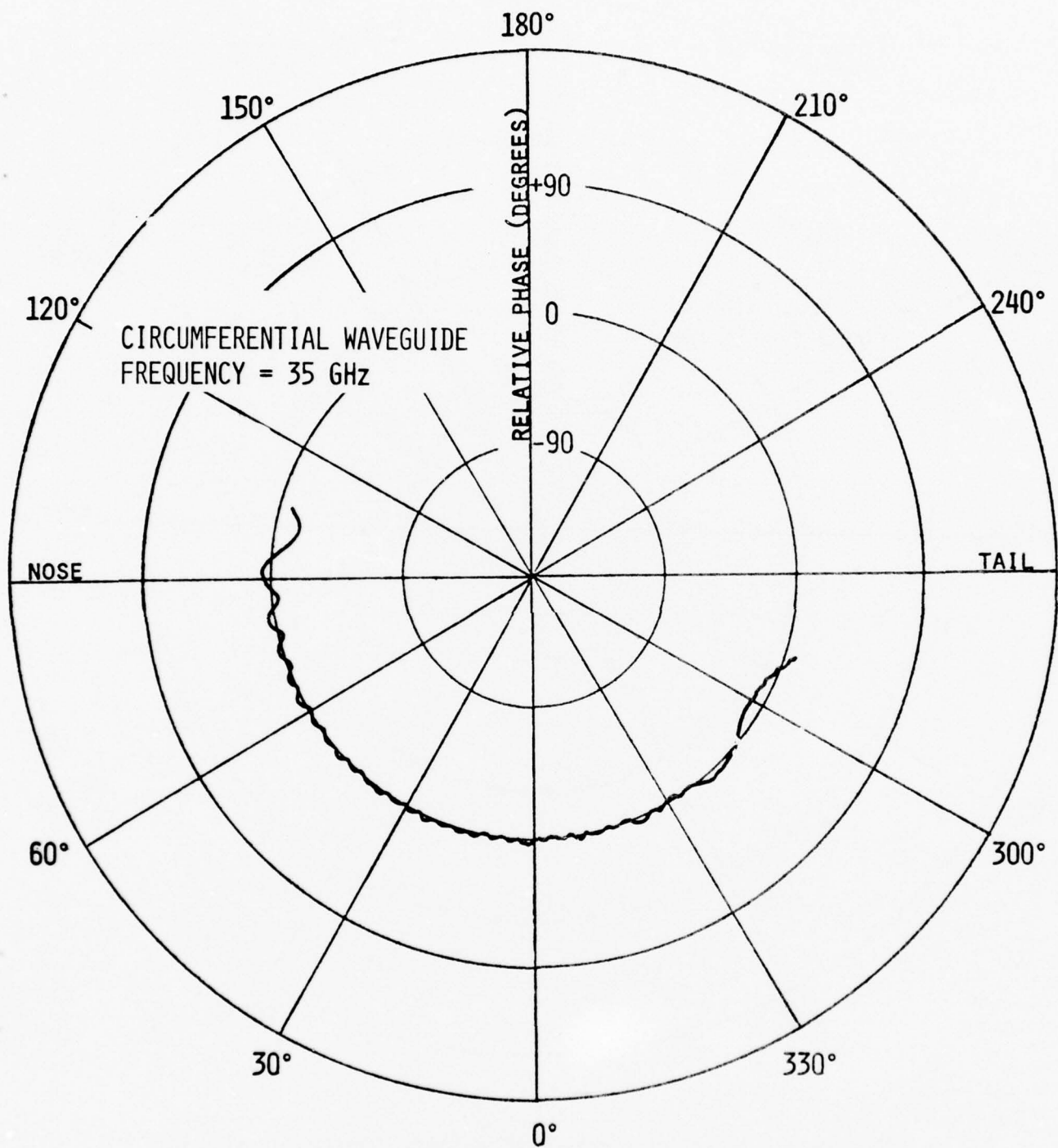


Figure 50. Computed elevation plane relative phase pattern of a circumferential waveguide below the nose (station 222) of 1/11 scale Boeing 737.

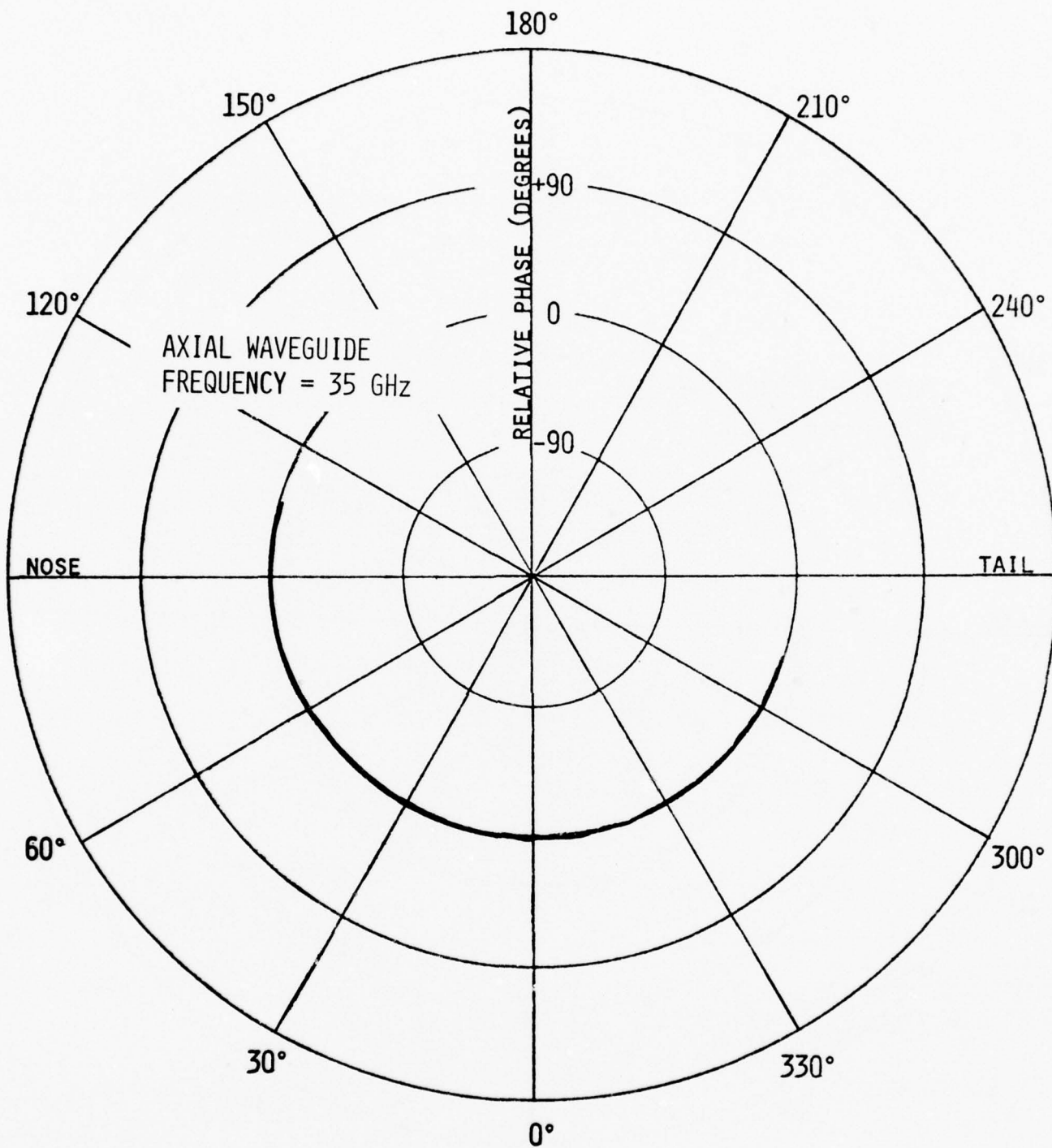


Figure 51. Computed elevation plane relative phase pattern of an axial waveguide below the nose(station 222) of a 1/11 scale Boeing 737.

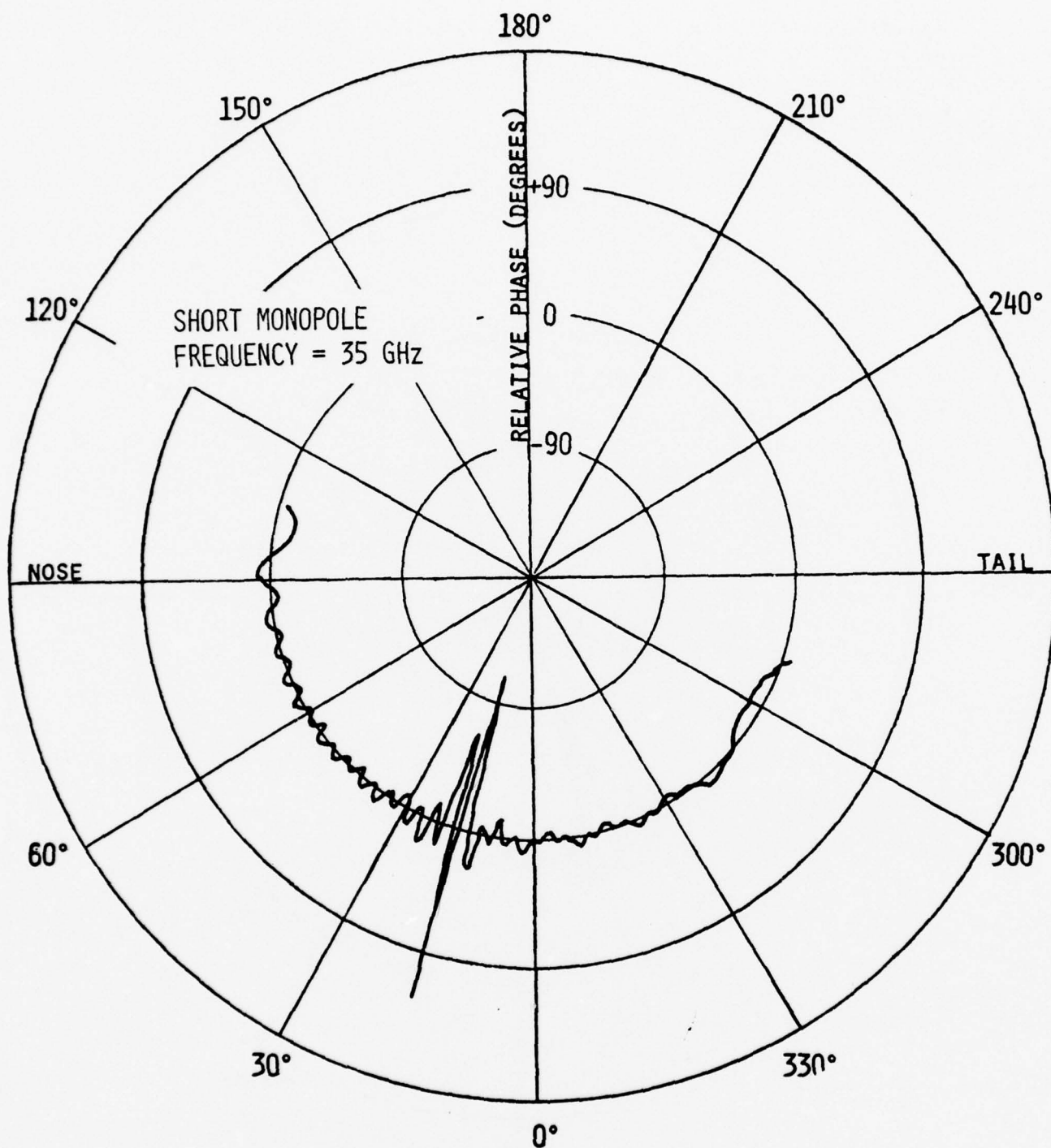


Figure 52. Computed elevation plane relative phase pattern of a short monopole below the nose (station 222) of 1/11 scale Boeing 737.

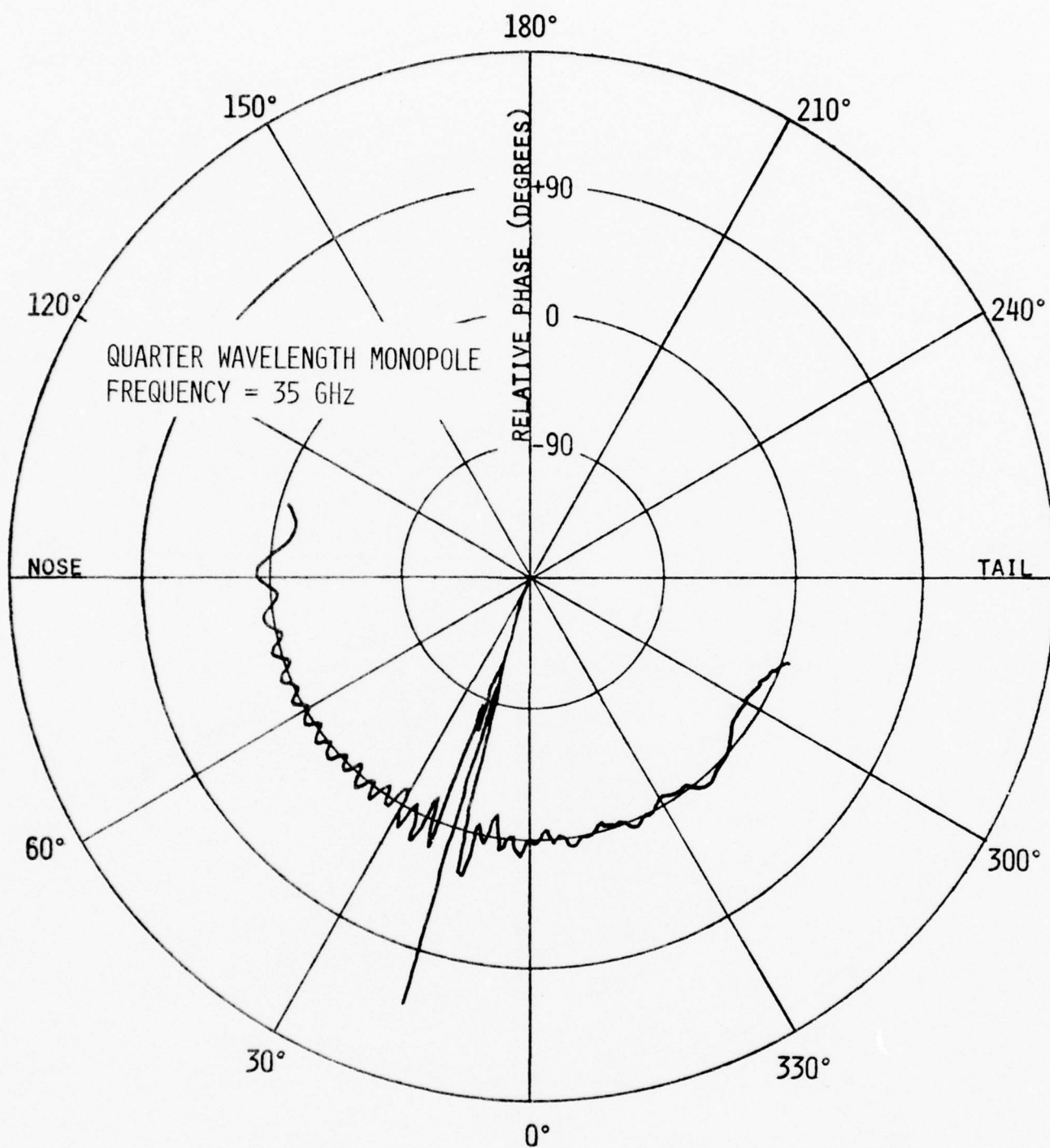


Figure 53. Computed elevation plane relative phase pattern of a quarter wavelength monopole below the nose (station 222) of 1/11 scale Boeing 737.

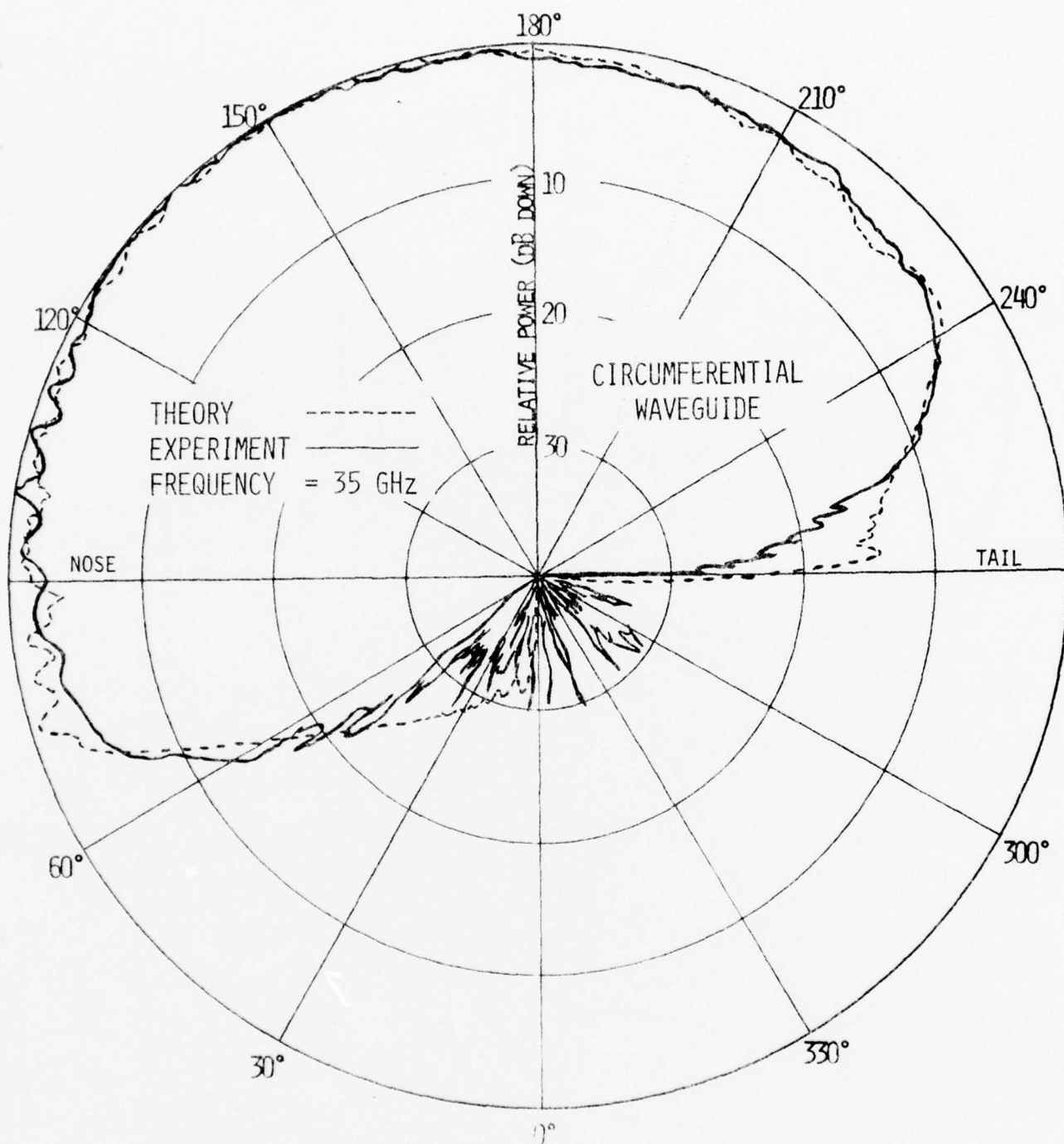


Figure 54. Computed and measured elevation plane amplitude patterns of a circumferential waveguide above the cockpit (station 220) of 1/11 scale Boeing 737.

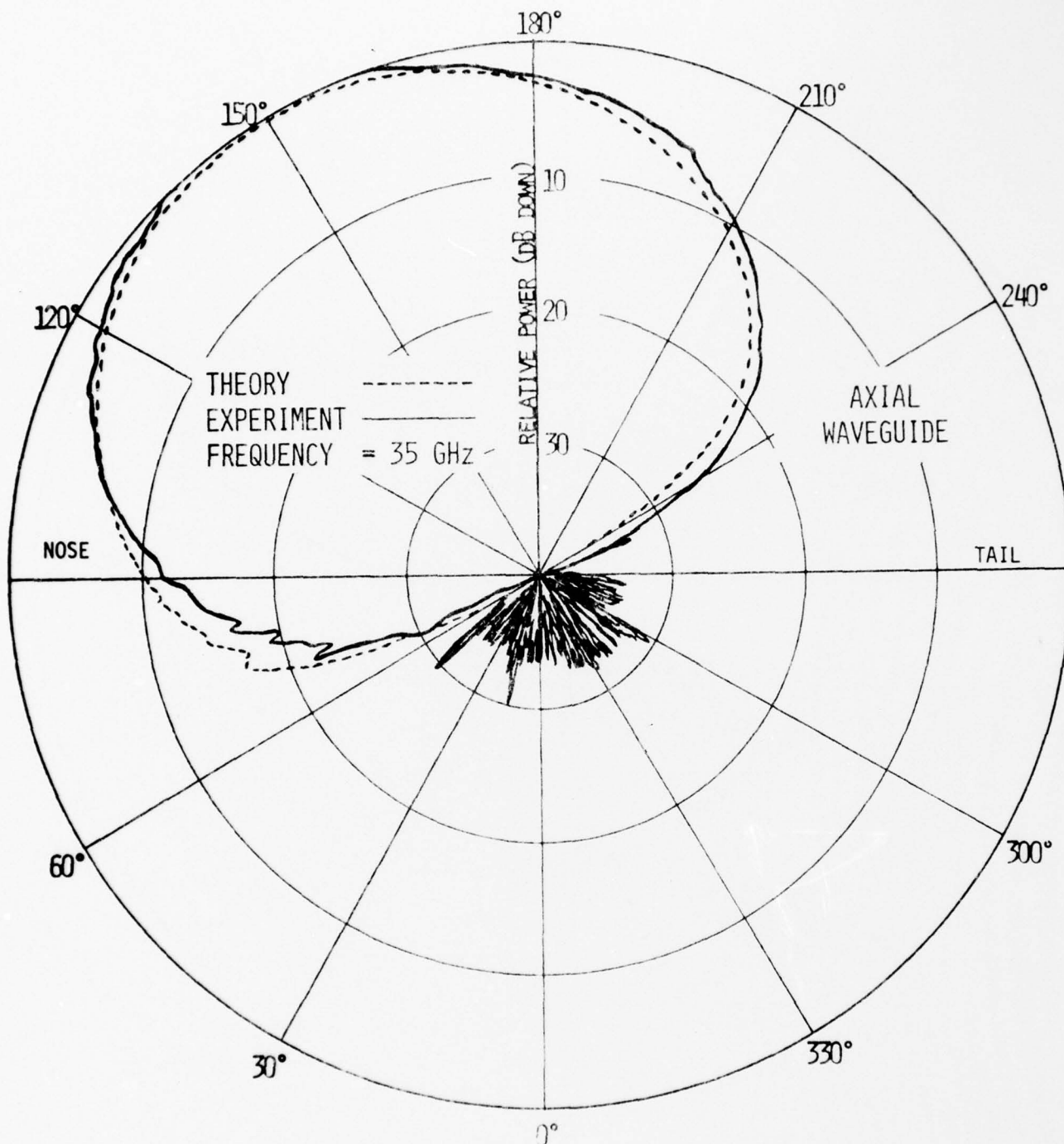


Figure 55. Computed and measured elevation plane amplitude patterns of an axial waveguide above the cockpit (station 220) of 1/11 scale Boeing 737.

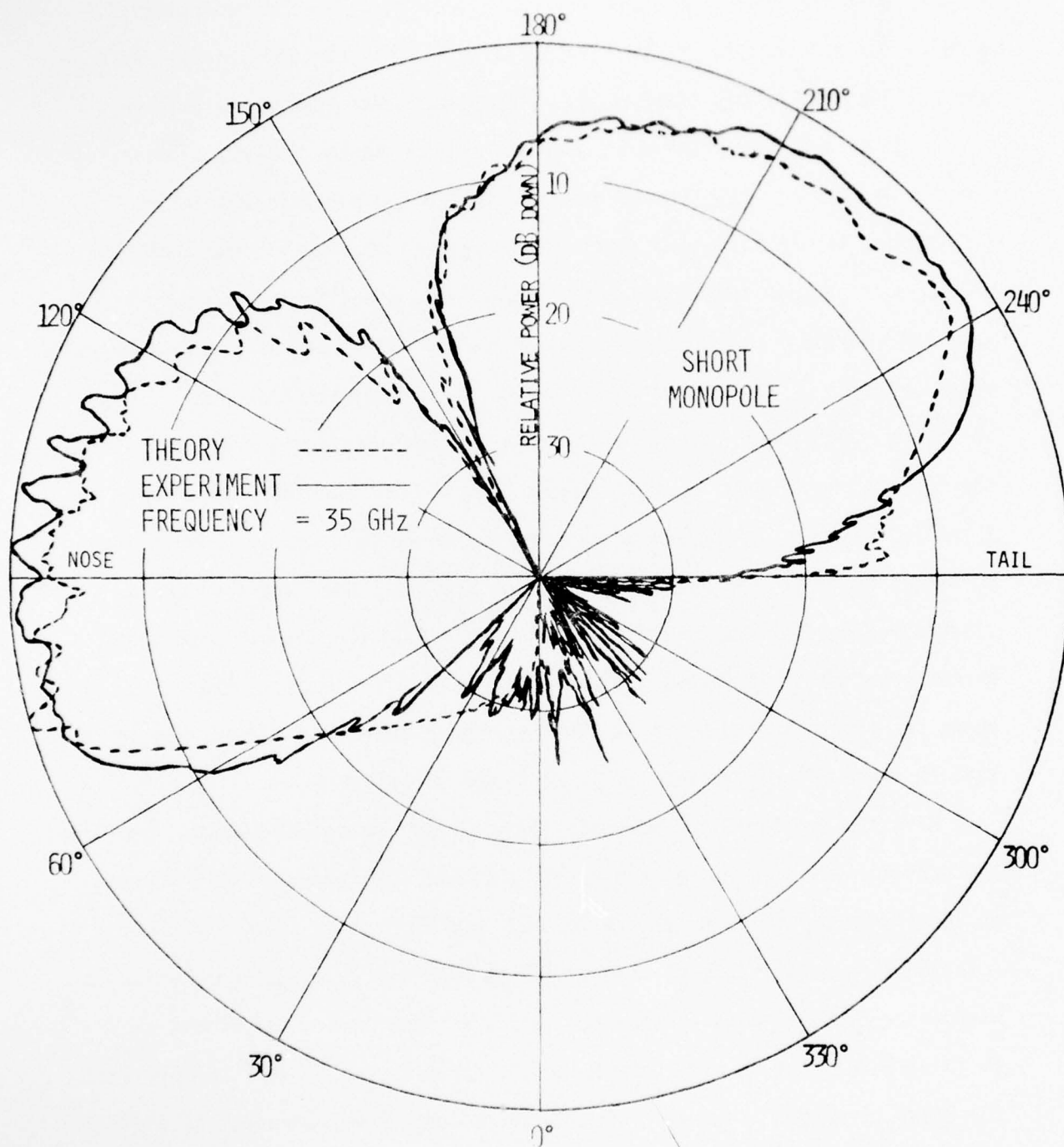


Figure 56. Computed and measured elevation plane amplitude patterns of a short monopole above the cockpit (station 220) of 1/11 scale Boeing 737.

the back (tail) directions. The differences between theory and experiment in the forward (nose) direction are attributed to the absence of the radome structure in the analytical modeling and its presence in the experimental model. The differences are small especially for the circumferential and axial slots. The differences between theory and experiment toward the tail region are attributed to the absence of the tail section in the analytical modeling and its presence in the experimental model. In the analytical modeling it was assumed that the tail section was not present to simplify the analysis and any differences that would occur would be in a region of secondary importance for landing. In Figures 57-59 the corresponding elevation plane relative phase patterns of the same antennas, whose amplitude patterns were included in Figures 54-56, are shown. The phase variations are again small except for the short monopole near the 150° region, which is of secondary importance for a landing system. In Figures 60-62 the corresponding measured azimuth plane amplitude patterns are shown. Even though the axial aperture provides a wider coverage than the circumferential aperture in the azimuth plane, the circumferential aperture has a wider coverage in the elevation plane, as shown in Figures 54 and 55. The short monopole provides good coverage in the azimuth plane but is somewhat marginal in the elevation plane.

With the availability and versatility of the analytical methods, amplitude patterns for circumferential and axial apertures were computed when mounted at location 1 below the nose (station 222) and location 2 above the cockpit (station 220) on a full scale Boeing 737 at a frequency of 5.1 GHz, which is within the proposed band for the MLS, and are shown in Figures 63 and 64. It is observed that in either location the circumferential aperture provides the wider coverage. When the antenna is located below the nose, the proposed elevation plane primary sector coverage, of 20° above and 30° below

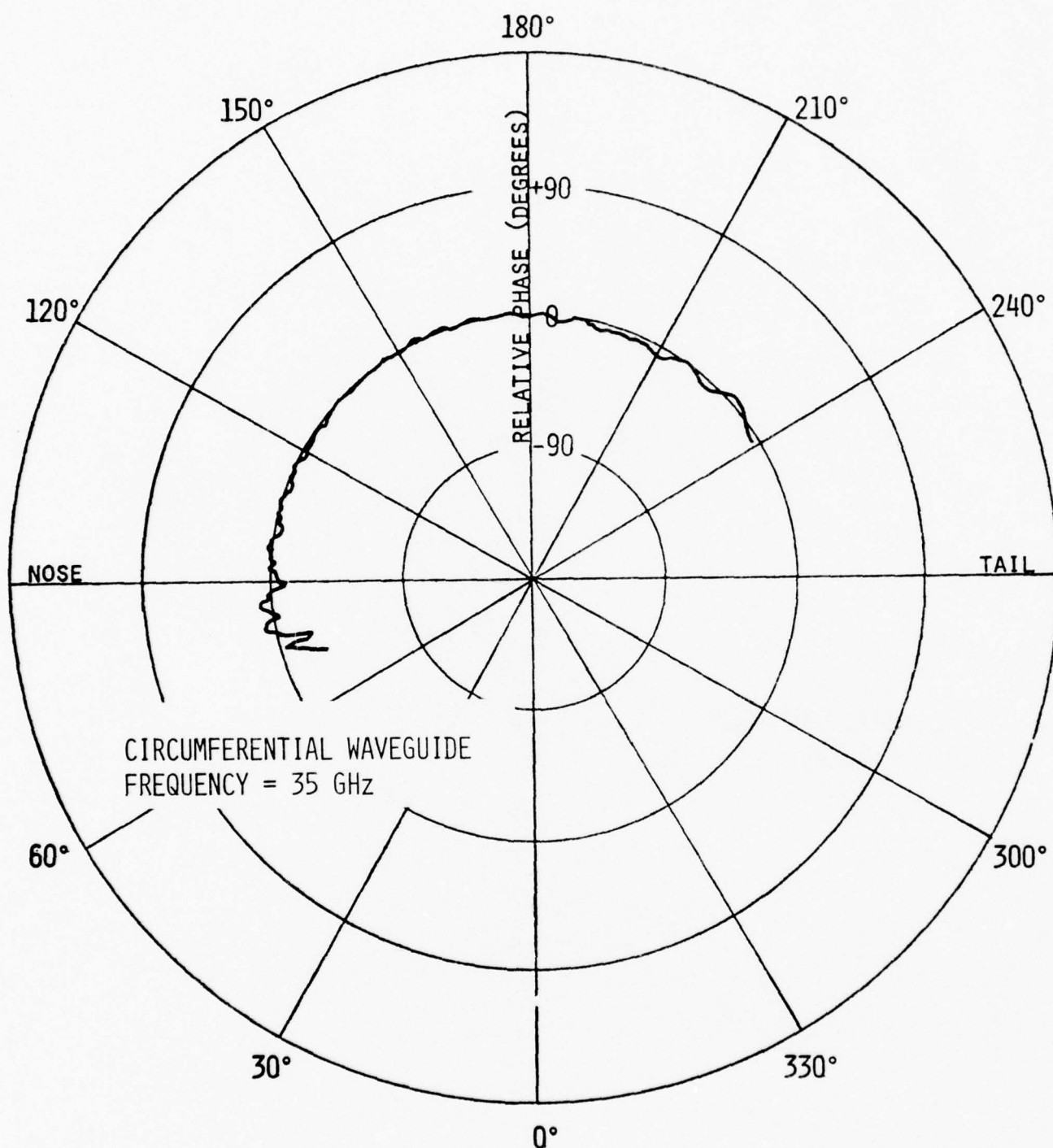


Figure 57. Computed elevation plane relative phase pattern of a circumferential waveguide above the cockpit (station 220) of 1/11 scale Boeing 737.

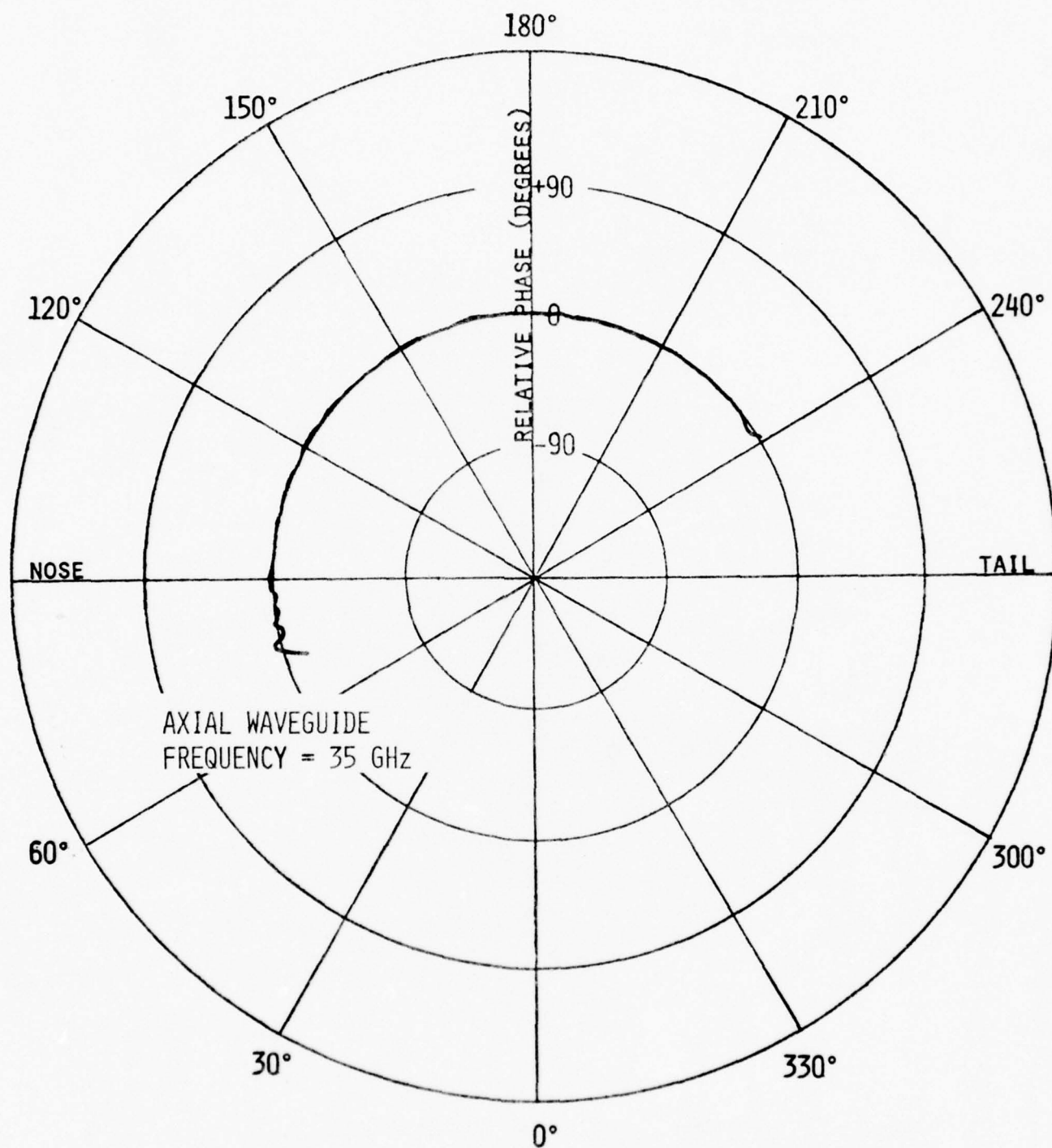


Figure 58. Computed elevation plane relative phase pattern of an axial waveguide above the cockpit (station 220) of 1/11 scale Boeing 737.

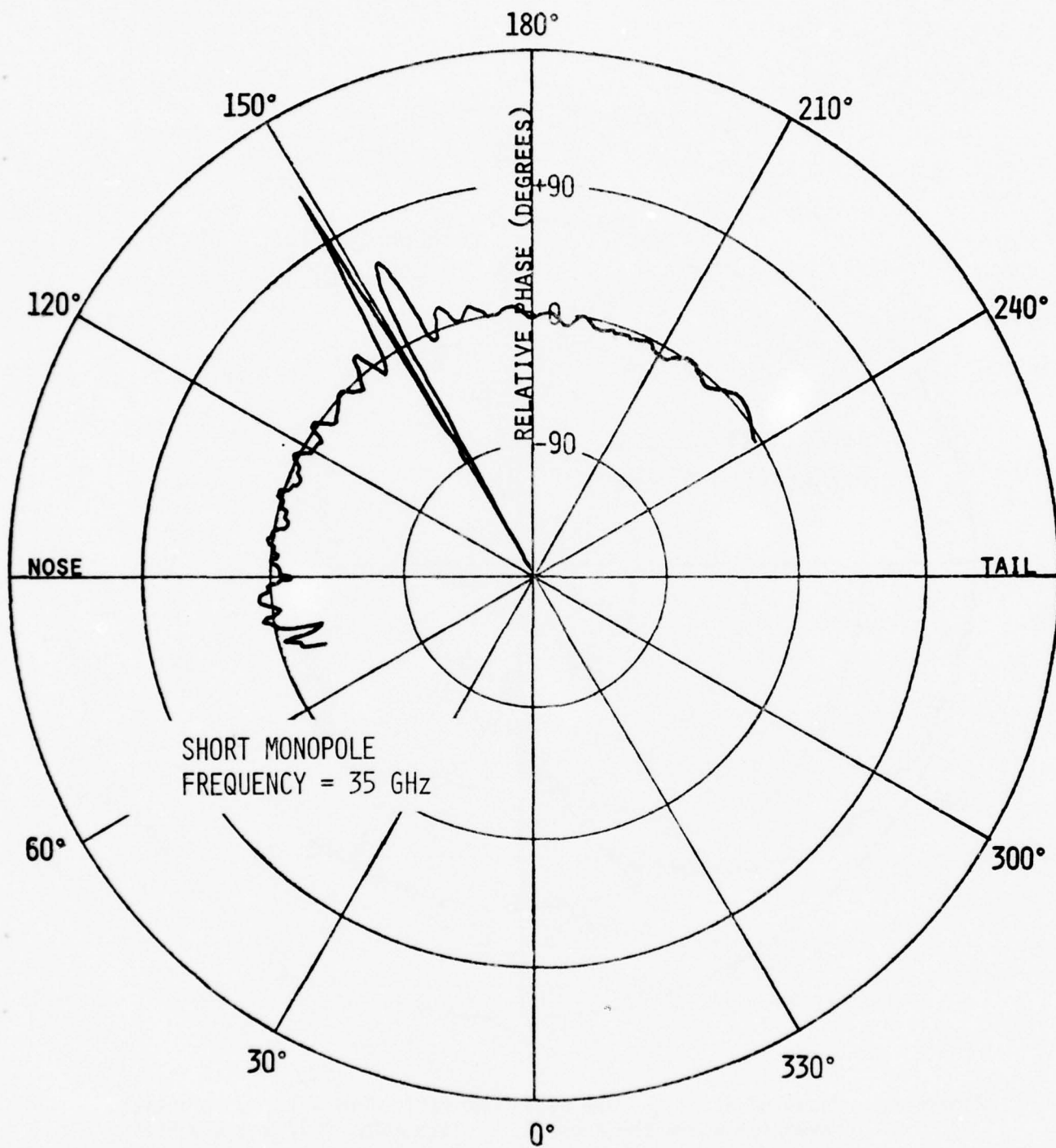


Figure 59. Computed elevation plane relative phase pattern of a short monopole above the cockpit (station 220) of 1/11 scale Boeing 737.

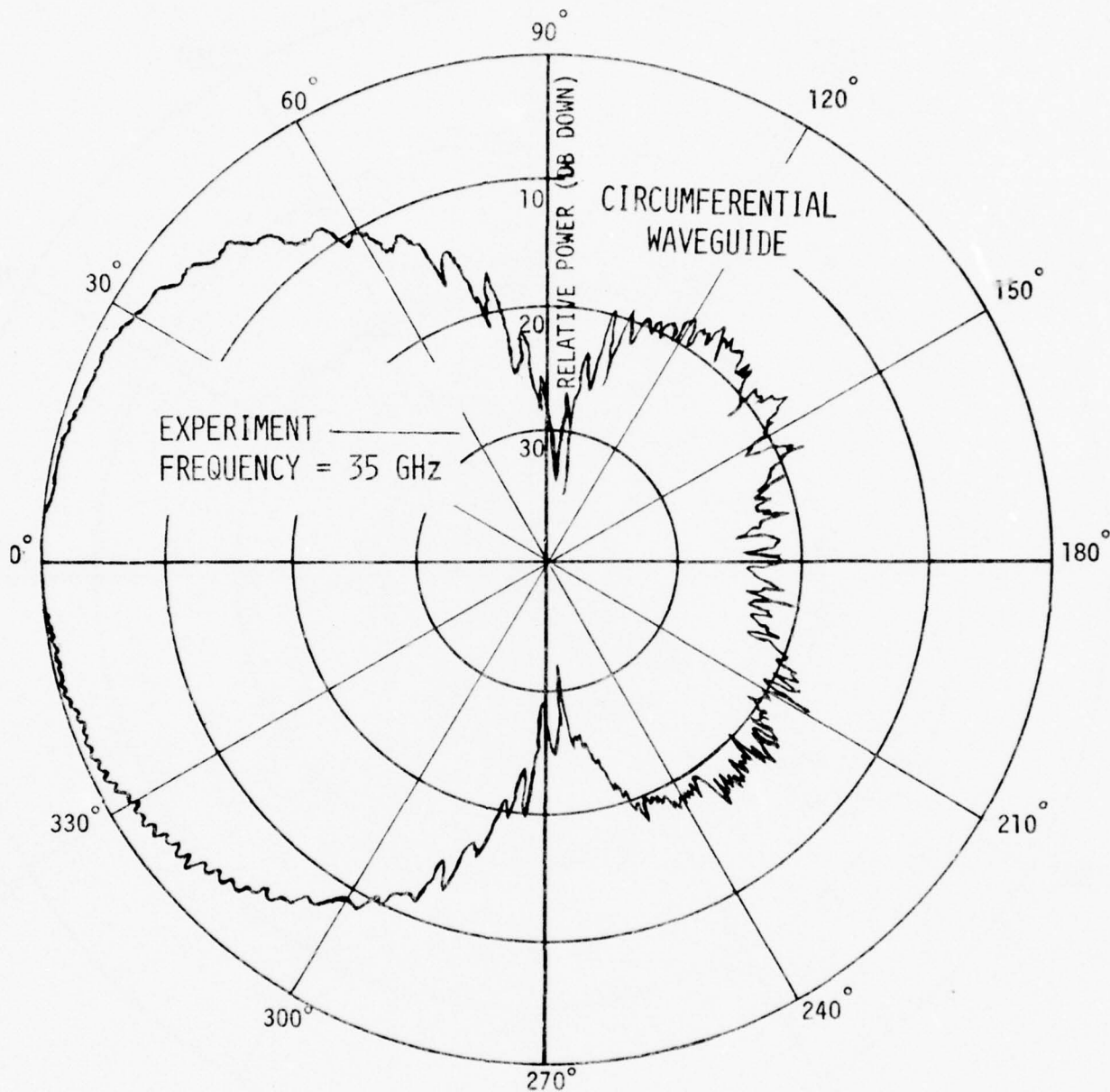


Figure 60. Measured azimuth plane amplitude pattern of a circumferential waveguide above the cockpit (station 220) of 1/11 scale Boeing 737.

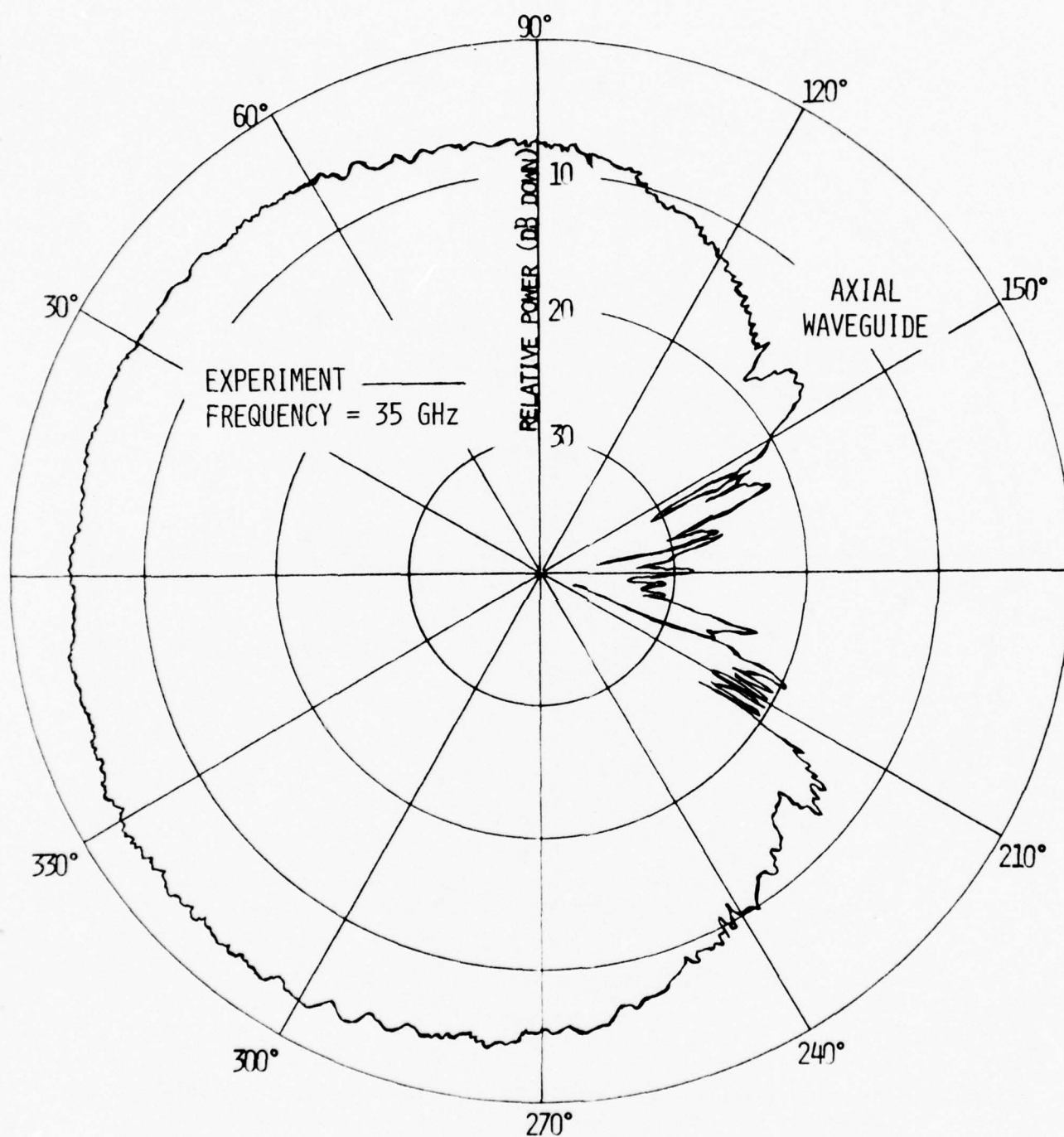


Figure 61. Measured azimuth plane amplitude pattern of an axial waveguide above the cockpit (station 220) of 1/11 scale Boeing 737.

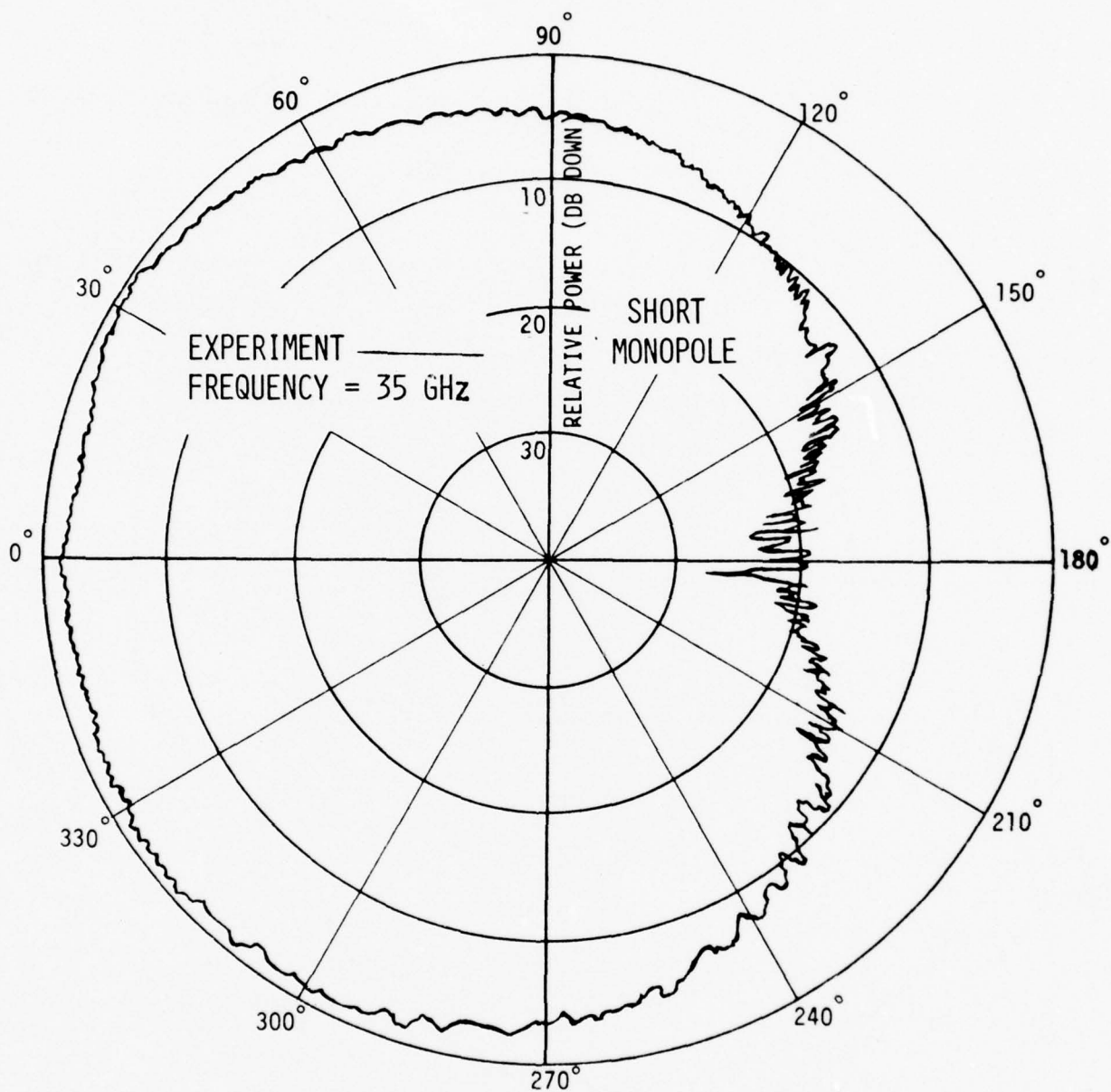


Figure 62. Measured azimuth plane amplitude pattern of a short monopole above the cockpit (station 220) of 1/11 scale Boeing 737.

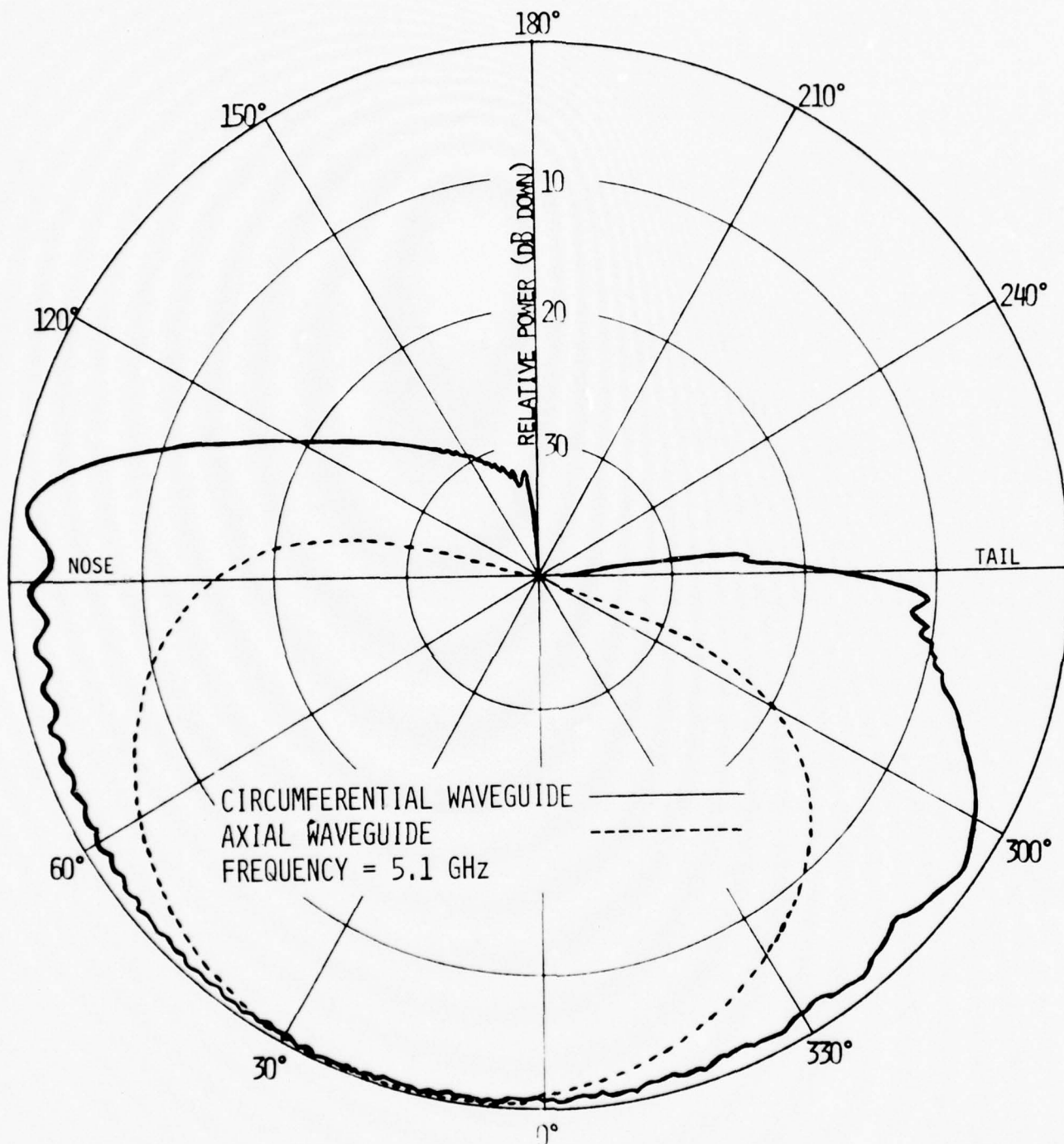


Figure 63. Computed elevation plane amplitude patterns of a circumferential and an axial waveguide below the nose (station 222) of a full scale Boeing 737.

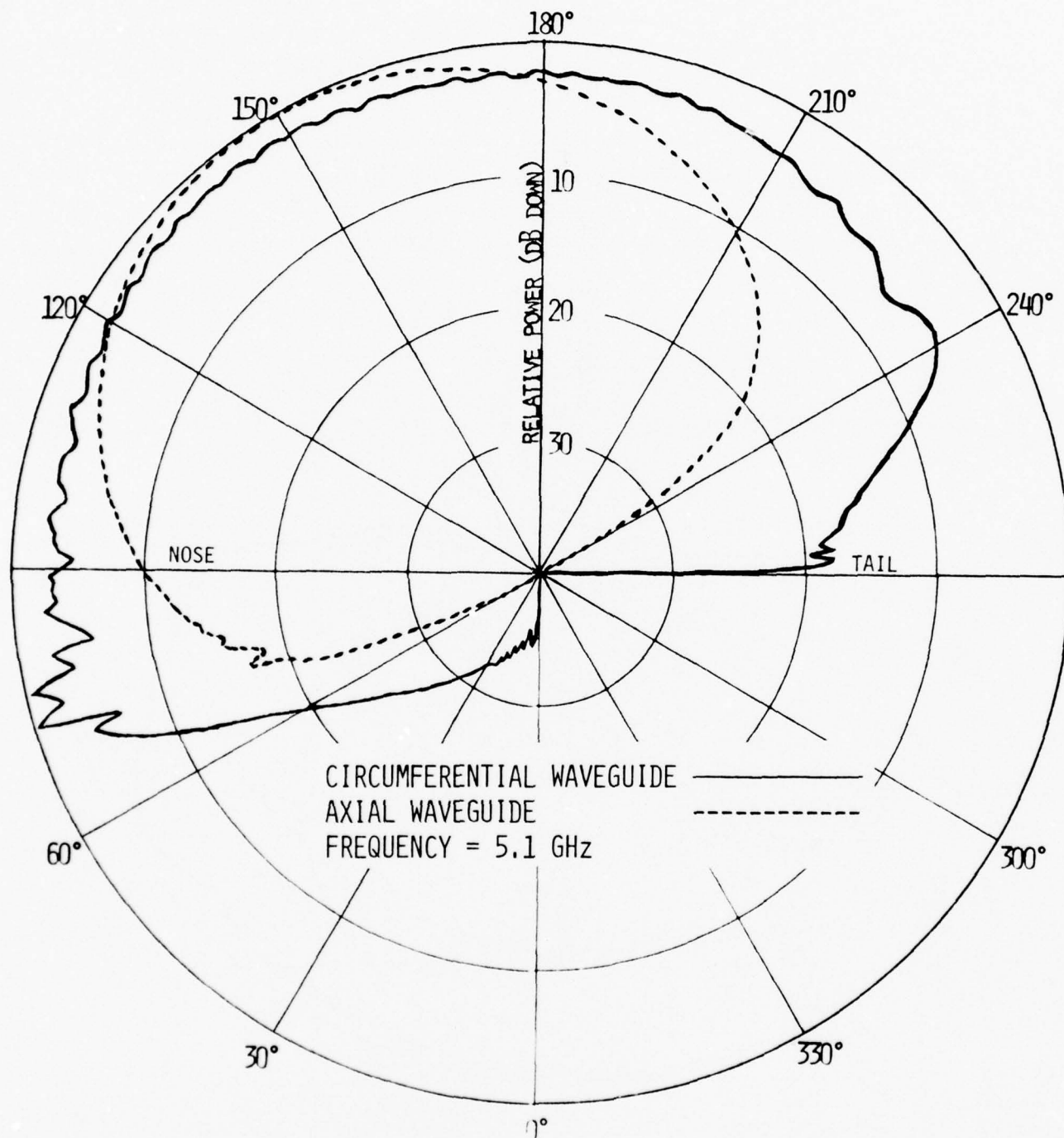


Figure 64. Computed elevation plane amplitude patterns of a circumferential and an axial waveguide above the cockpit (station 220) of a full scale Boeing 737.

the nose is somewhat marginal for the region above the nose and very acceptable below the nose. The opposite occurs when the antenna is mounted at location 2 (station 220) above the cockpit.

A close comparison of the 1/11 scale model patterns shown in Figures 46, 47 and 54, 55 with the corresponding ones of the full scale model shown in Figures 63 and 64 will reveal that basically the shape of the patterns is primarily controlled by the profile of the structure to which the antenna is mounted and not by the electrical dimensions. There are some small differences as a result of the nonidentical electrical dimensions of the scaled and full scale models.

Another model that was examined was a full scale Boeing 747 whose overall configuration and two antenna locations are shown in Figure 65. Location 1 below the nose corresponds to station 169 and location 2 above the cockpit corresponds to station 306. Elevation plane amplitude and relative phase patterns for a circumferential aperture, an axial aperture, and a short monopole at both locations are shown in Figures 66-77. In the same figures the corresponding patterns for the same antennas mounted on a full scale Boeing 737 at station 222 below the nose and station 220 above the cockpit are shown for comparison. It is obvious that the Boeing 747 configuration provides a wider coverage in the region of 20° above the nose and 30° below the nose. The circumferential slot below the nose or above the cockpit and the short monopole below the nose provide the most acceptable radiation coverage for the MLS. The corresponding phase patterns also do not show any large deviations within this region. The wider coverage by the 747 in the forward sector is attributed to the steeper slope in the profile of the structure at the antenna locations than the corresponding profile for the 737. For the Boeing 747 the slant angle of the structure

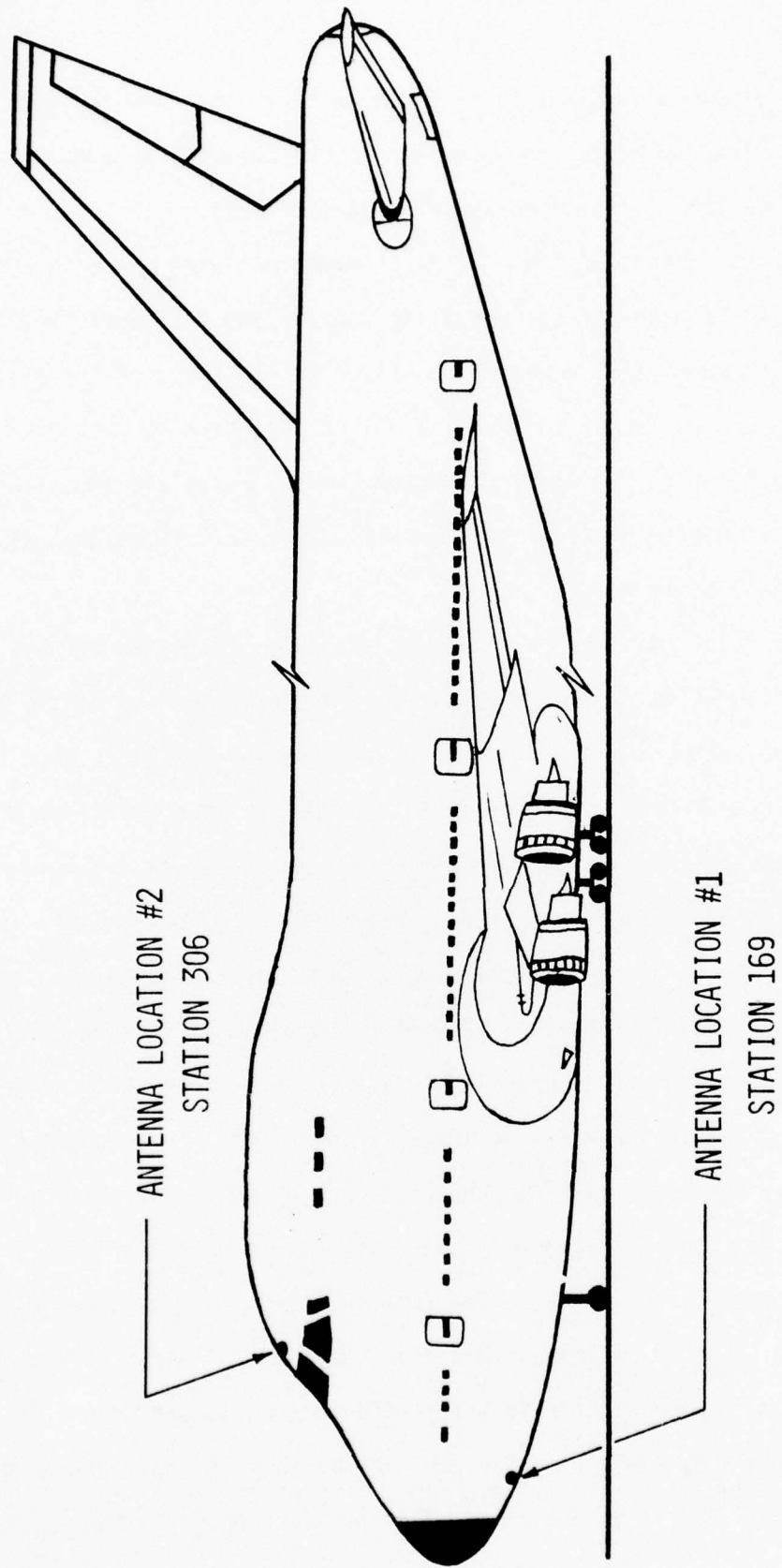


Figure 65, Boeing 747 airplane configuration with two antenna locations.

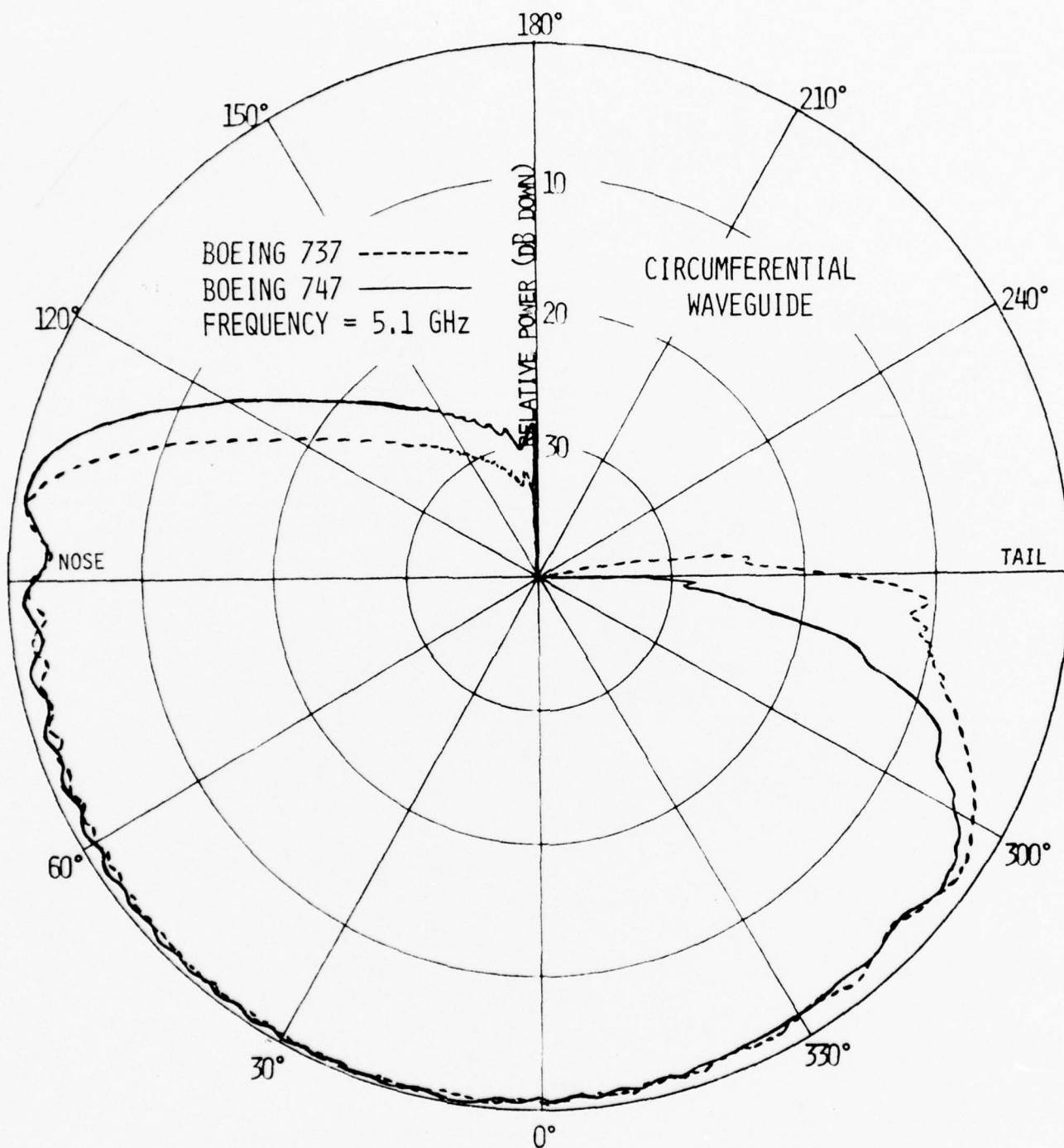


Figure 66. Computed elevation plane amplitude patterns of a circumferential waveguide below the nose of full scale Boeing 737 (station 222) and full scale Boeing 747 (station 169).

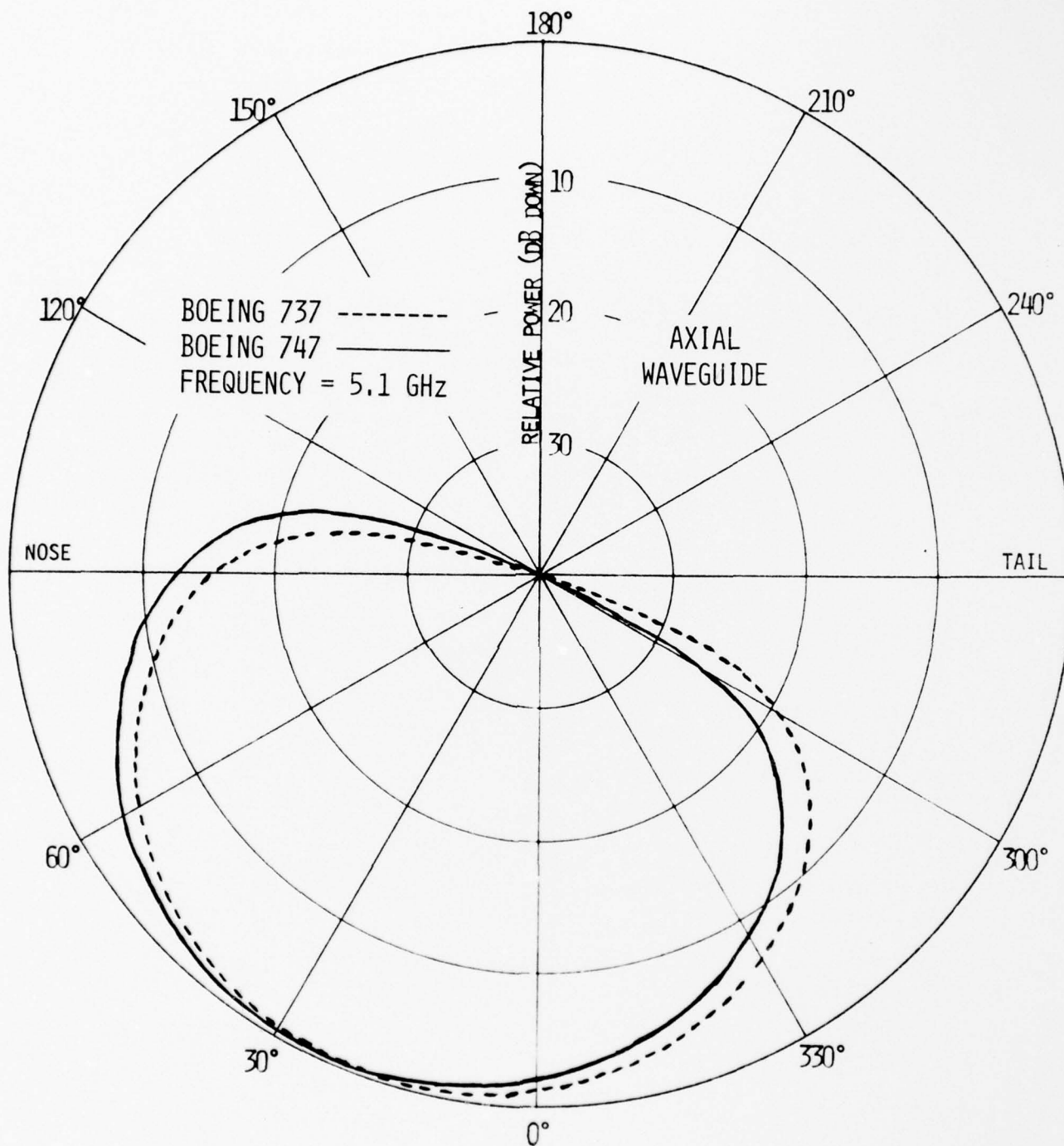


Figure 67. Computed elevation plane amplitude patterns of an axial waveguide below the nose of full scale Boeing 737 (station 222) and full scale Boeing 747 (station 169).

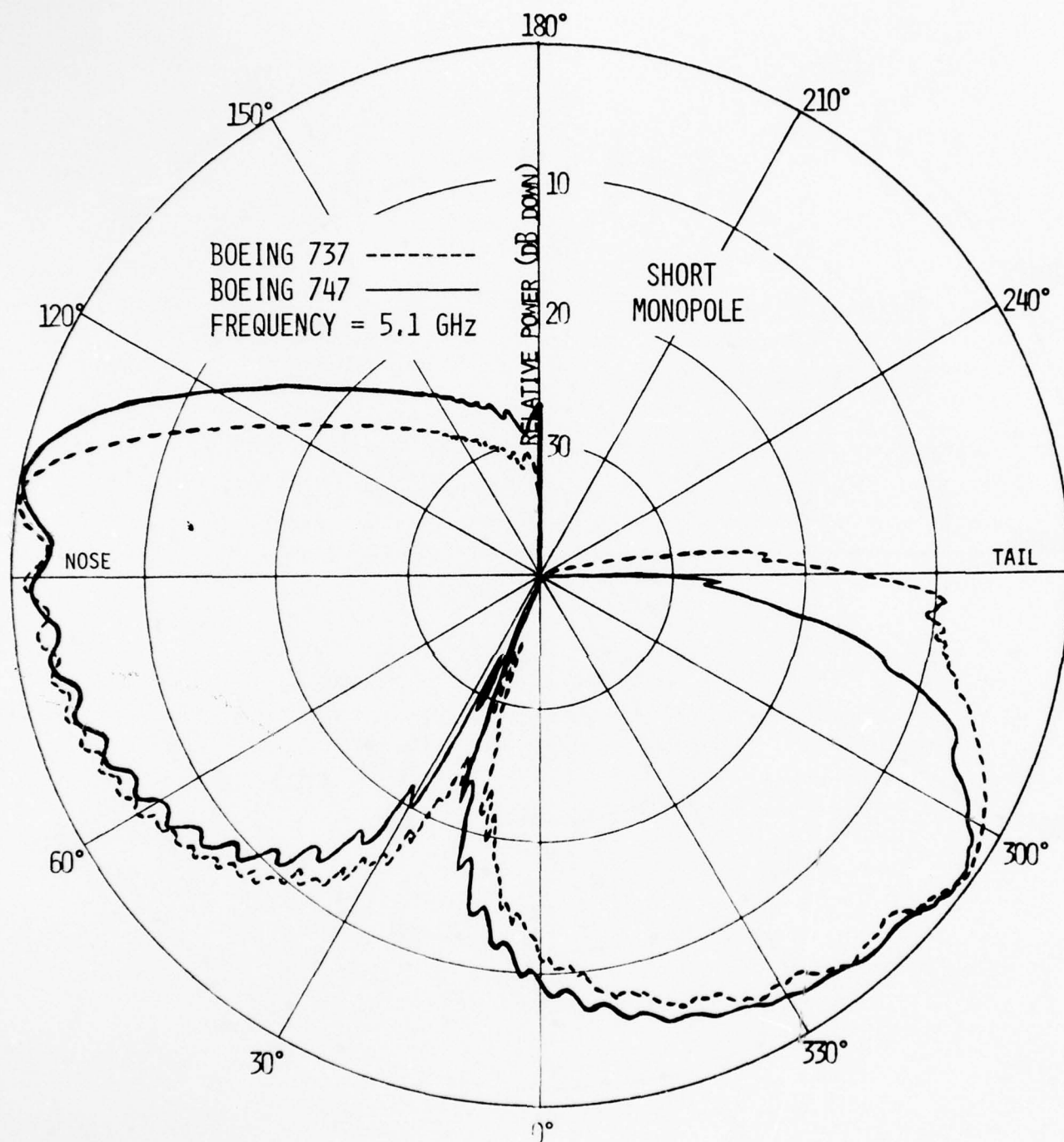


Figure 68. Computed elevation plane amplitude patterns of a short monopole below the nose of full scale Boeing 737 (station 222) and full scale Boeing 747 (station 169).

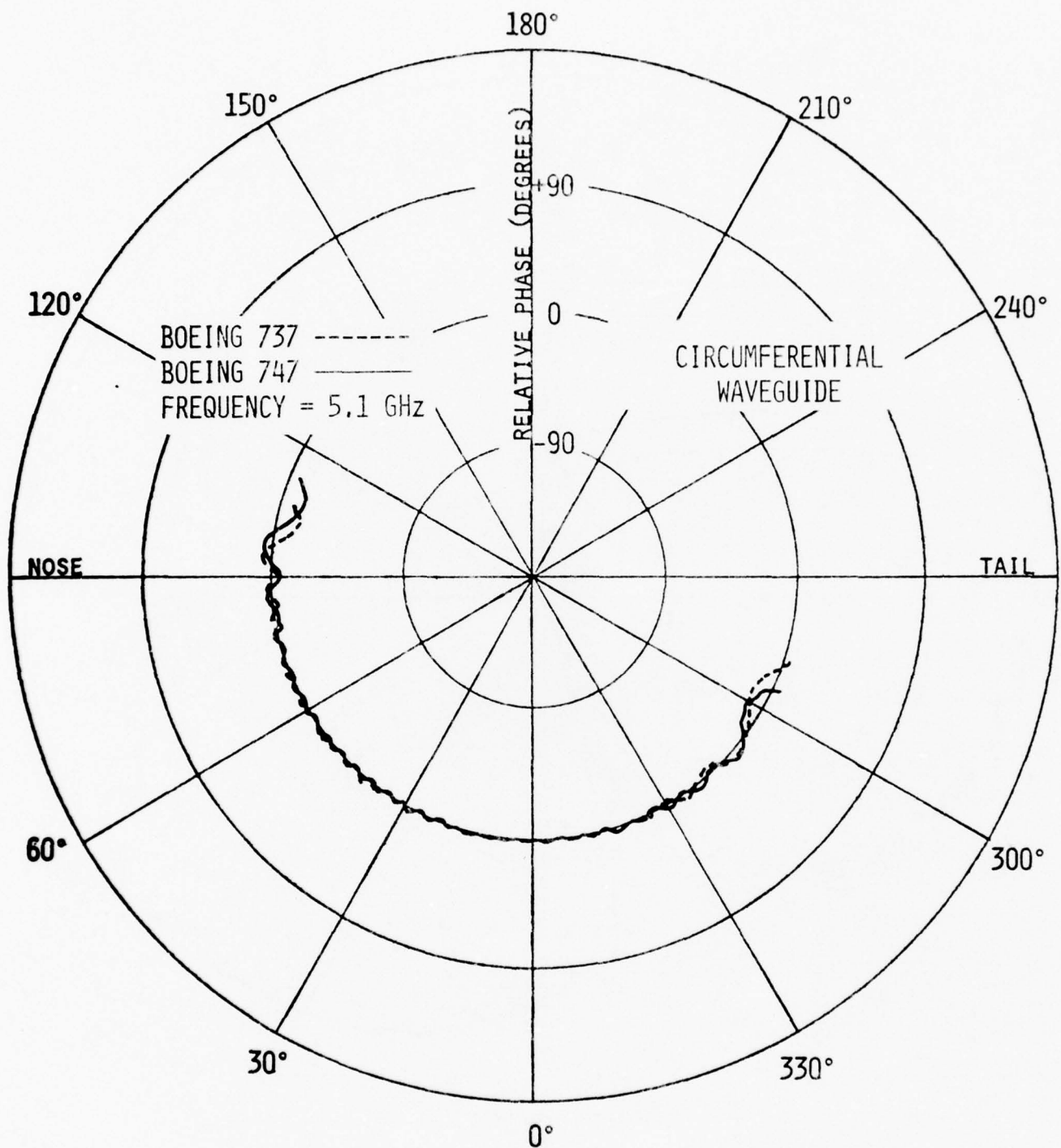


Figure 69. Computed elevation plane relative phase patterns of a circumferential waveguide below the nose of full scale Boeing 737 (station 222) and full scale Boeing 747 (station 169).

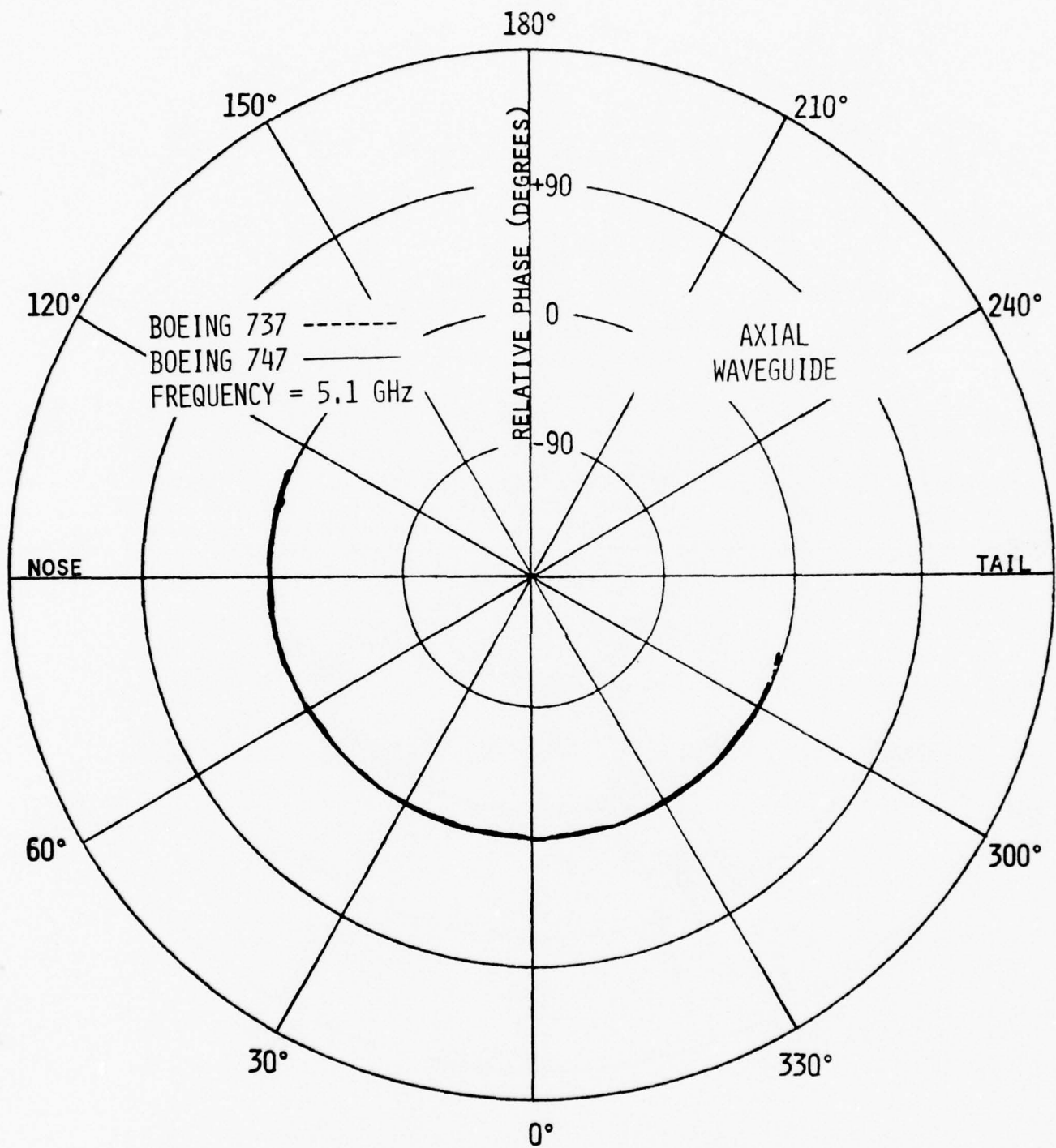


Figure 70. Computed elevation plane relative phase patterns of an axial waveguide below the nose of full scale Boeing 737 (station 222) and full scale Boeing 747 (station 169)

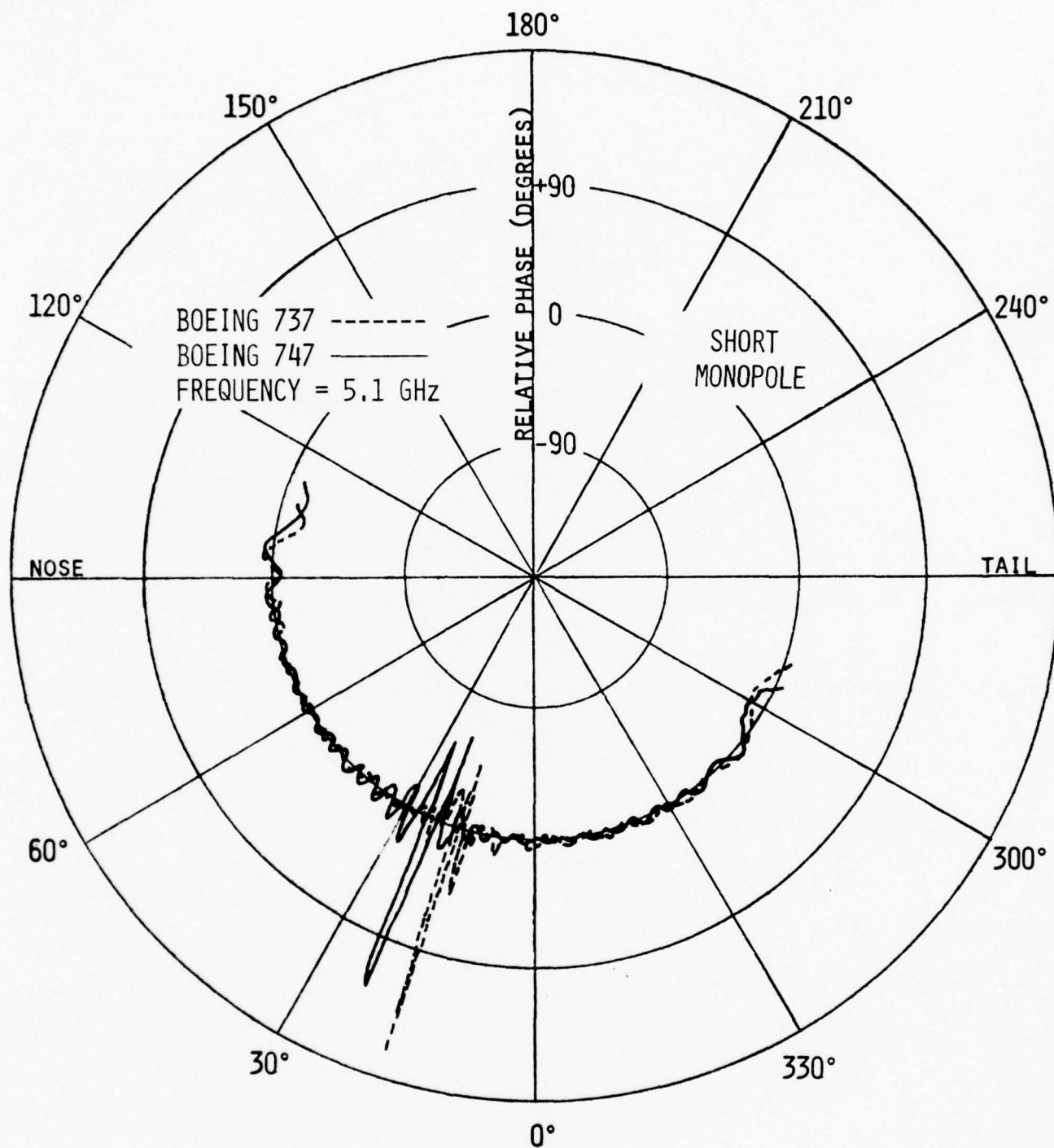


Figure 71. Computed elevation plane relative phase patterns of a short monopole below the nose of full scale Boeing 737 (station 222) and full scale Boeing 747 (station 169).

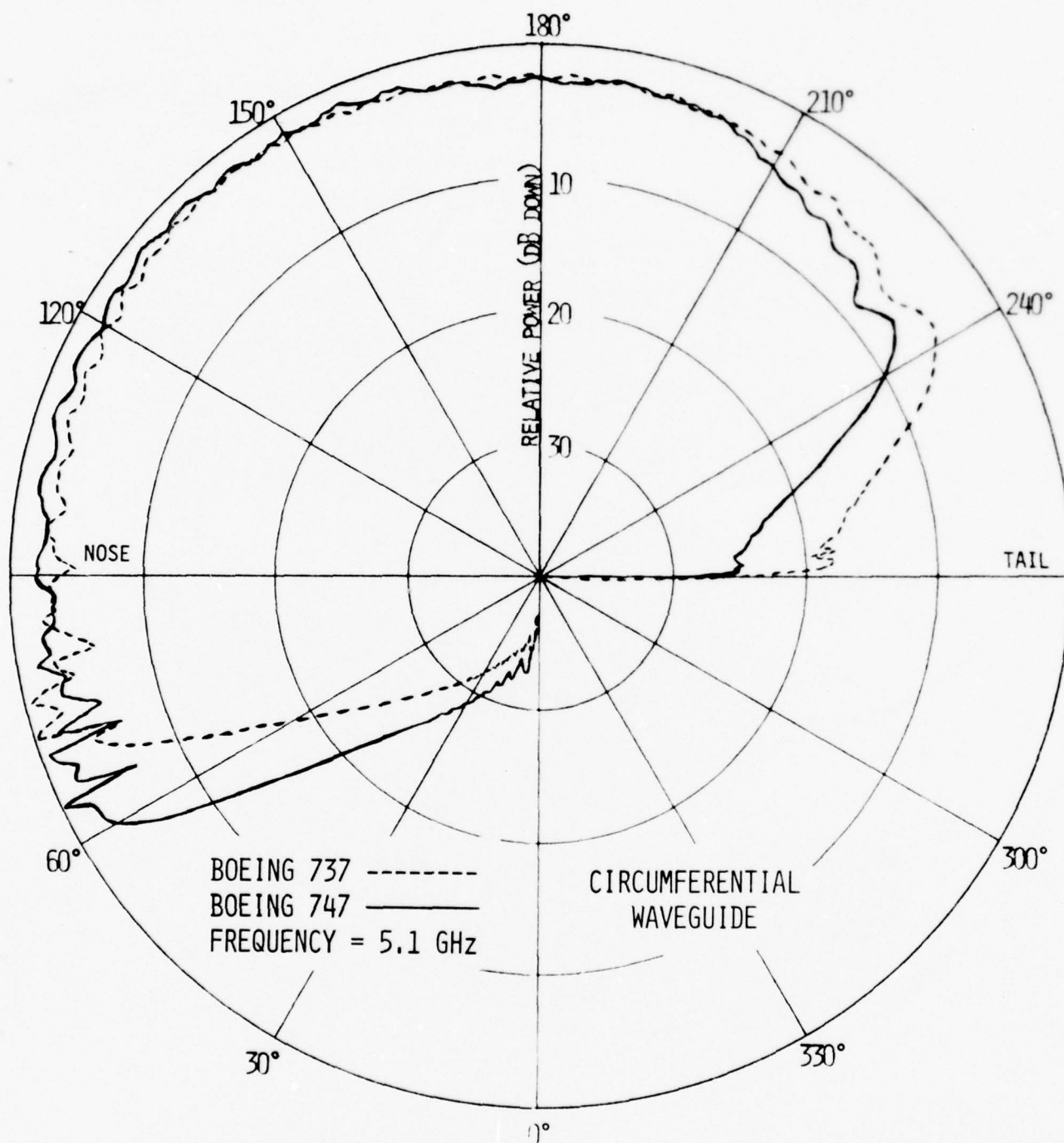


Figure 72. Computed elevation plane amplitude patterns of a circumferential waveguide above the cockpit of full scale Boeing 737 (station 220) and full scale Boeing 747 (station 306).

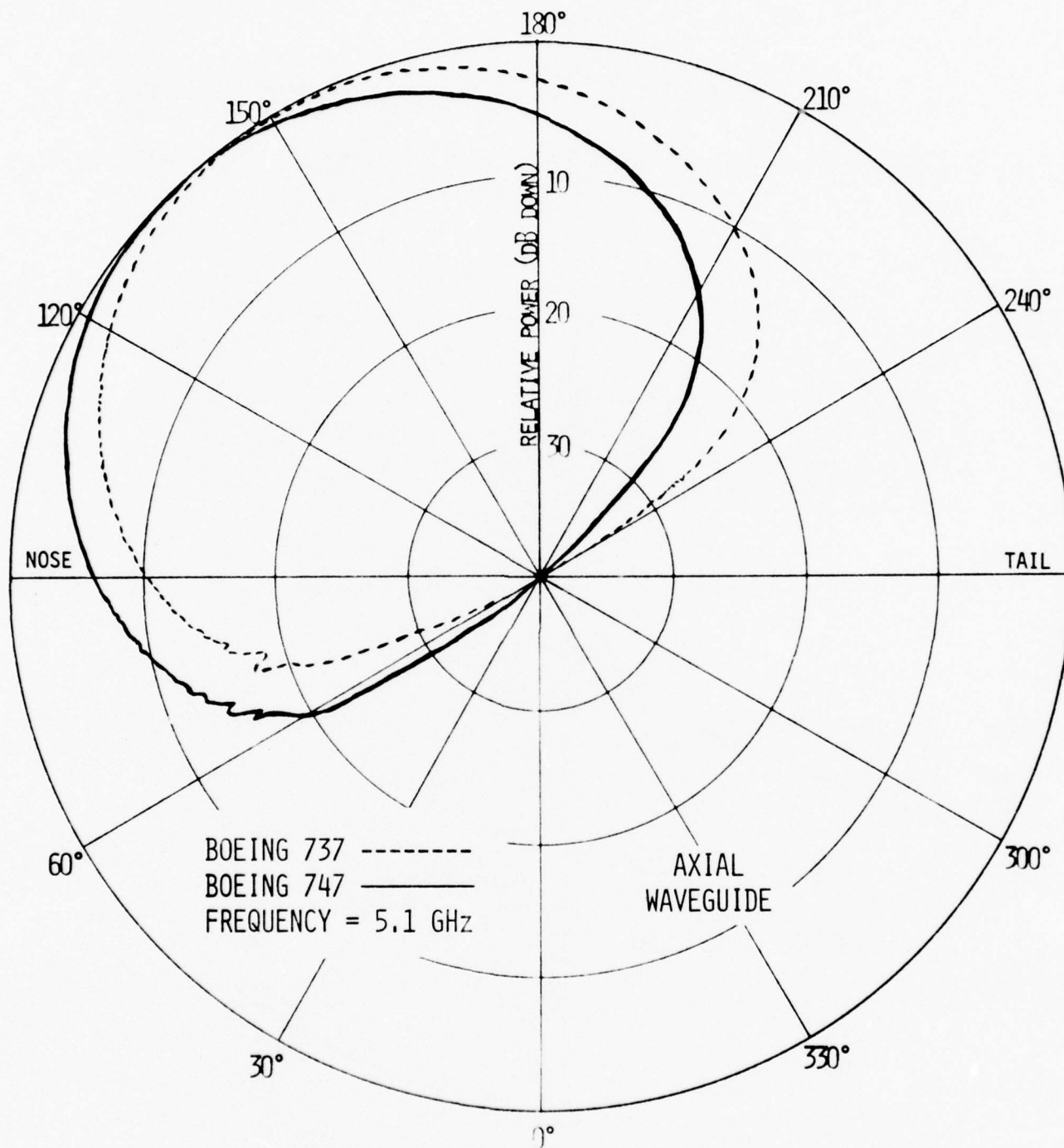


Figure 73. Computed elevation plane amplitude patterns of an axial waveguide above the cockpit of full scale Boeing 737 (station 220) and full scale Boeing 747 (station 306).

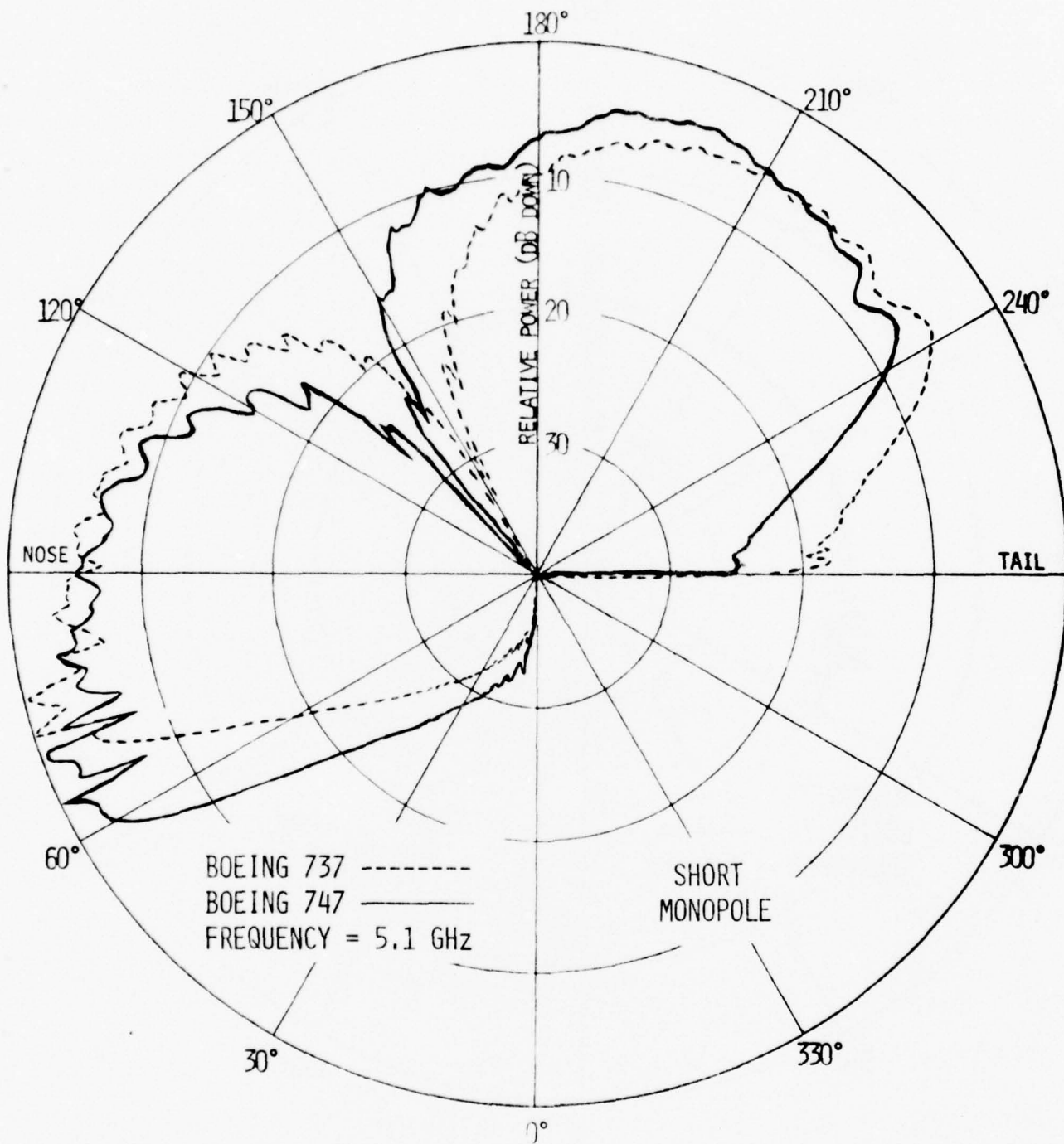


Figure 74. Computed elevation plane amplitude patterns of a short monopole above the cockpit of full scale Boeing 737 (station 220) and full scale Boeing 747 (station 306).

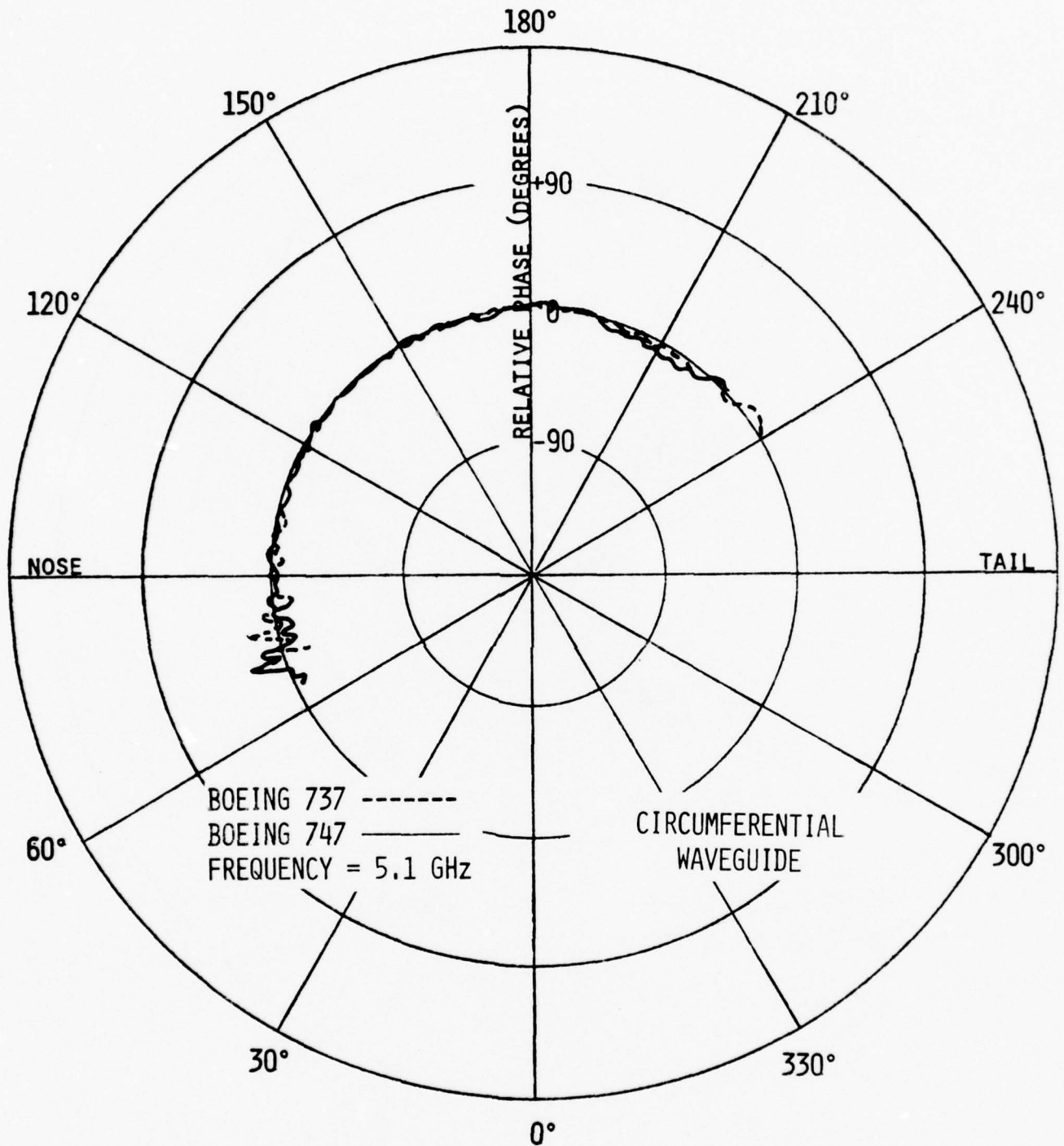


Figure 75. Computed elevation plane relative phase patterns of a circumferential waveguide above the cockpit of full scale Boeing 737 (station 220) and full scale Boeing 747 (station 306).

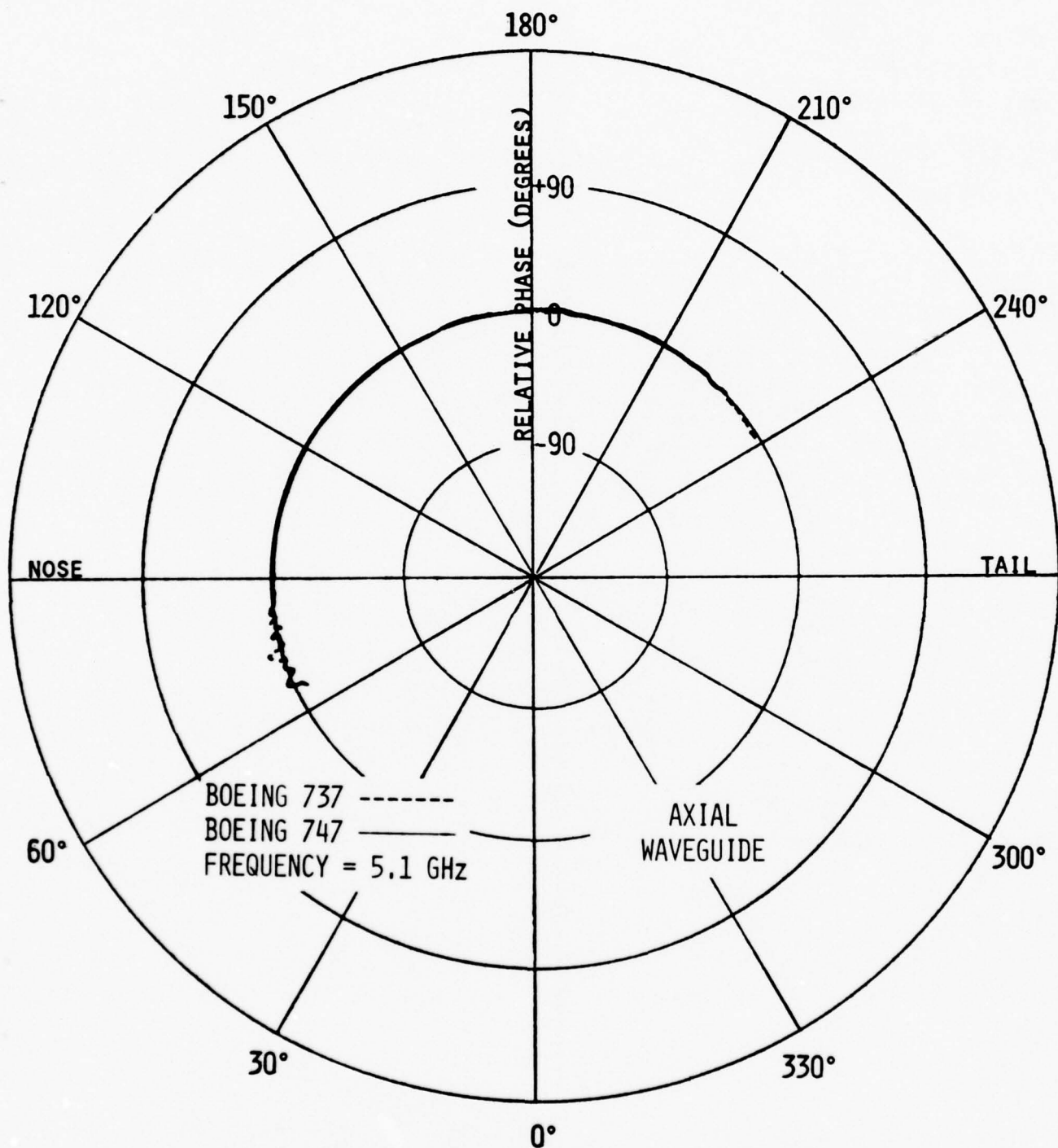


Figure 76. Computed elevation plane relative phase patterns of an axial waveguide above the cockpit of full scale Boeing 737 (station 220) and full scale Boeing 747 (station 306).

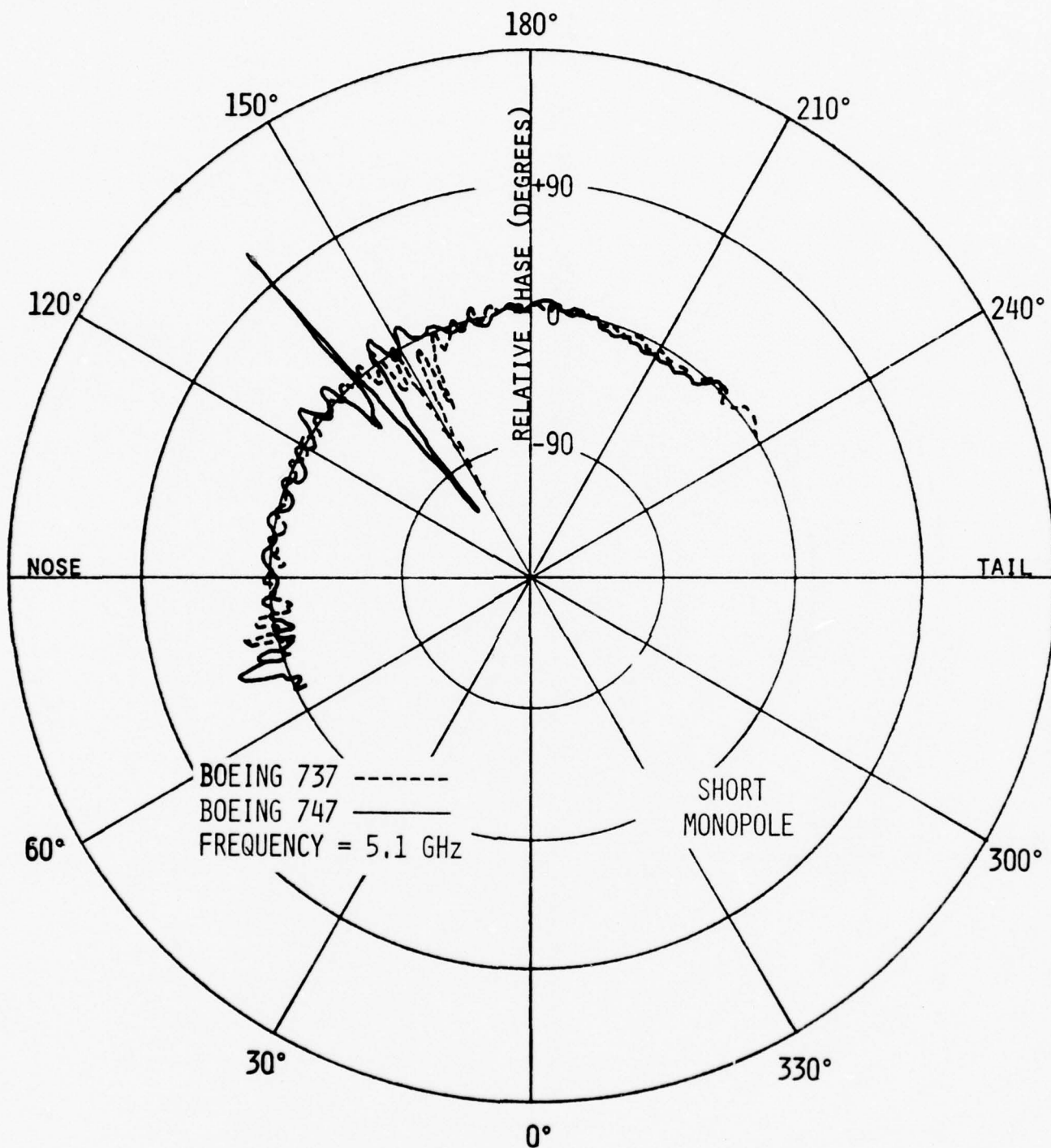


Figure 77. Computed elevation plane relative phase patterns of a short monopole above the cockpit of full scale Boeing 737 (station 220) and full scale Boeing 747 (station 306).

at station 169 was estimated to be about 24° while that of the Boeing 737 at station 222 was estimated to be about 18° . For station 306 the Boeing 747 slant angle was estimated to be 42° while for station 220 the Boeing 737 showed a slant of about 30° .

To examine the coverage variations by a circumferential and an axial aperture as a function of structure profile slant angle at the location of the antenna, elevation plane amplitude patterns were computed where the slant angle was allowed to vary $\pm 5^{\circ}$ for station 169 below the nose and station 306 above the cockpit. The results are shown in Figures 78-81 and a close observation will reveal that the patterns are essentially the same except that they are rotated by $\pm 5^{\circ}$. There are some small differences in the pattern structure but those are very small. So the slope of the structure at the antenna location plays a major role in the coverage provided by the antenna.

At the beginning of this section, elevation plane amplitude patterns of antennas mounted below the nose of a 1/35 scale space shuttle model were presented (Figures 42-44). When those patterns were measured the radome part of the nose (shown dashed in Figure 41) was truncated. Another set of amplitude patterns for a circumferential aperture, an axial aperture, and a quarter wavelength monopole were measured without the truncation of the radome part of the nose of the space shuttle orbiter. The antenna location and configuration of the 1/35 scale space shuttle model are shown in Figure 82 with the amplitude patterns in Figures 83-85. Again a good agreement between theory and experiment is indicated and a comparison between the corresponding patterns of Figures 42-44 with those of Figures 83-85 will reveal that the truncation of the nose allows more energy to be directed toward the upper part of the hemisphere. In the presence of the

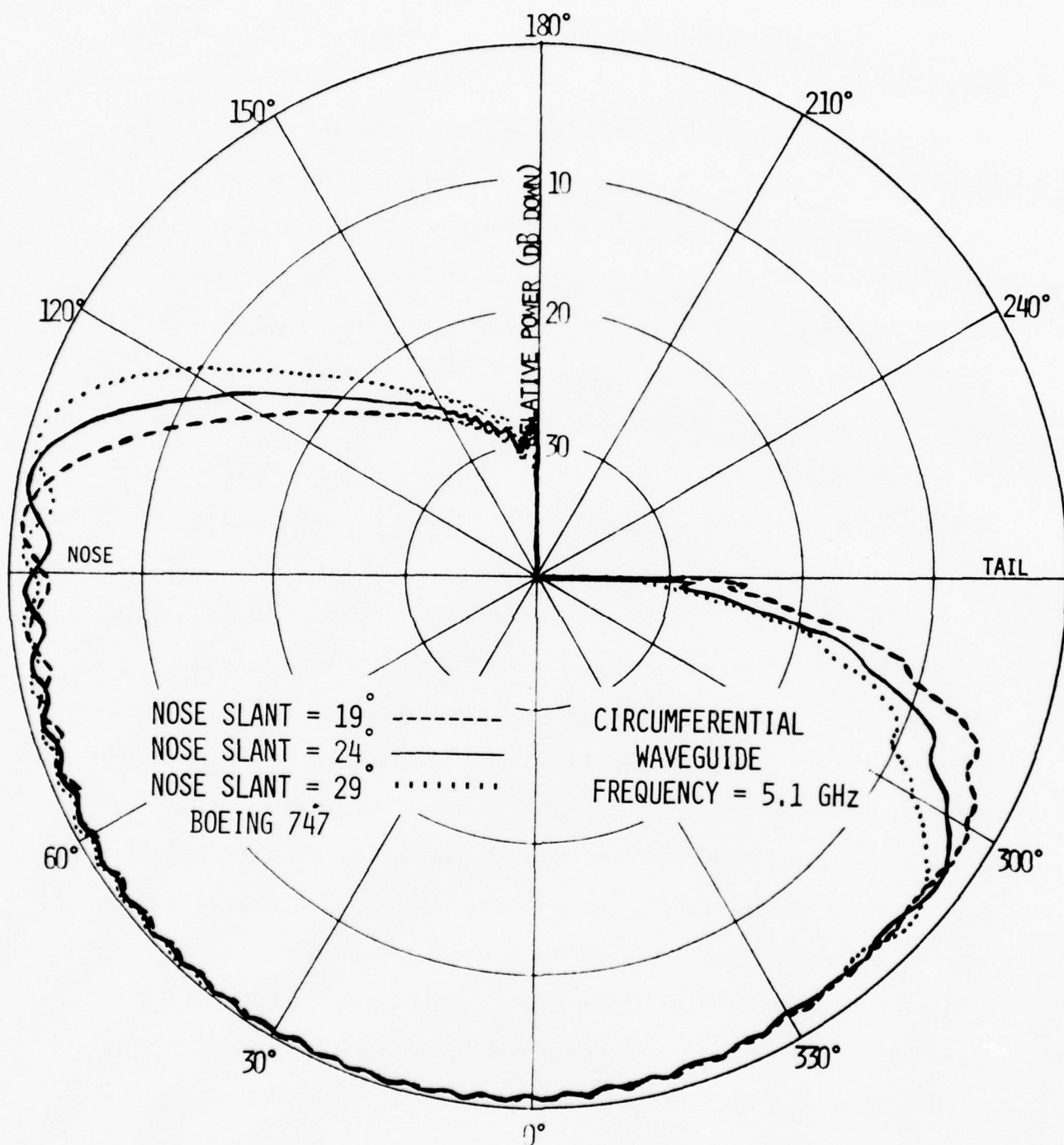


Figure 78. Computed elevation plane amplitude patterns of a circumferential waveguide below the nose (station 169) of a full scale Boeing 747 as a function of slant angle.

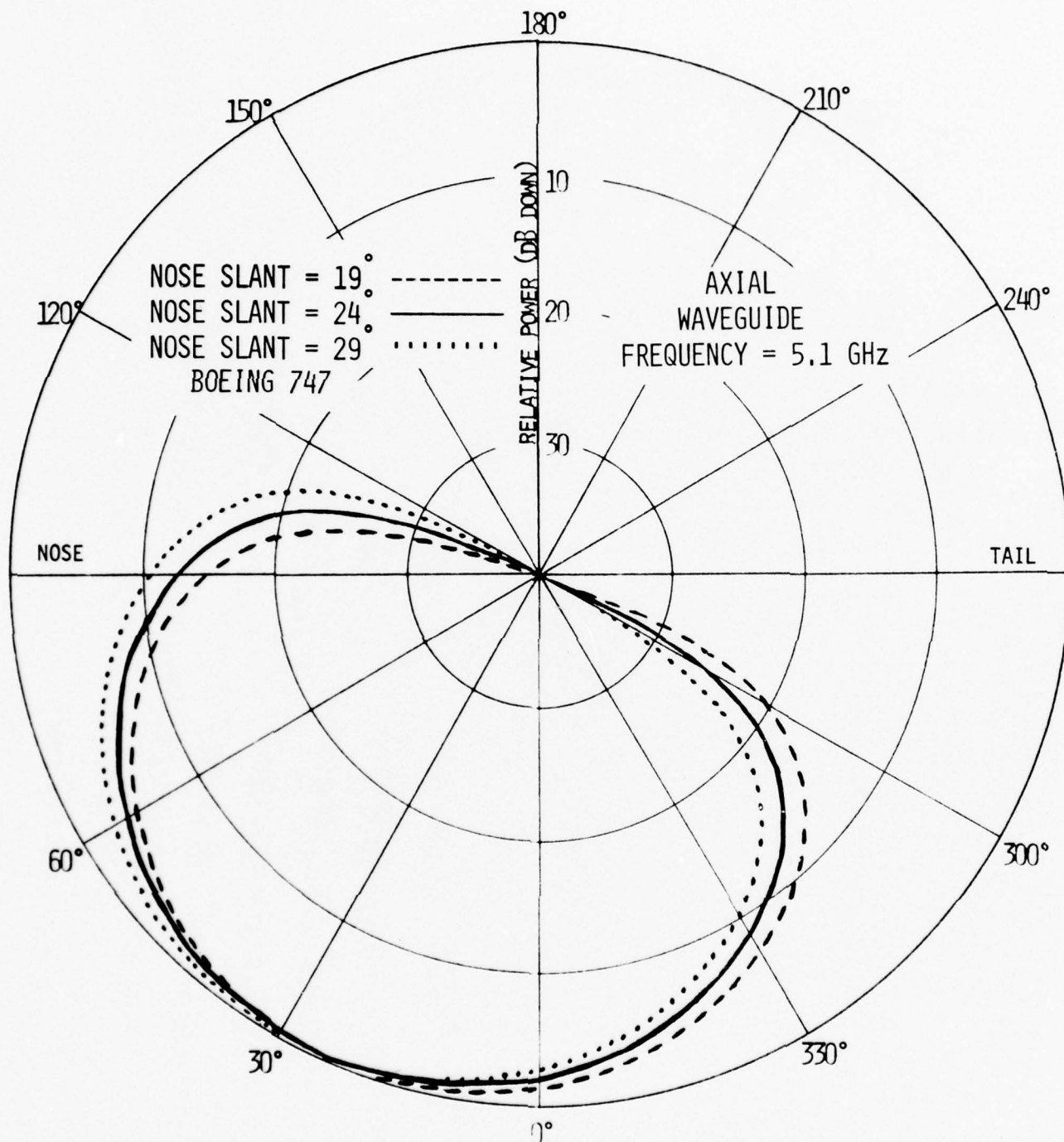


Figure 79. Computed elevation plane amplitude patterns of an axial waveguide below the nose (station 169) of a full scale Boeing 747 as a function of slant angle.

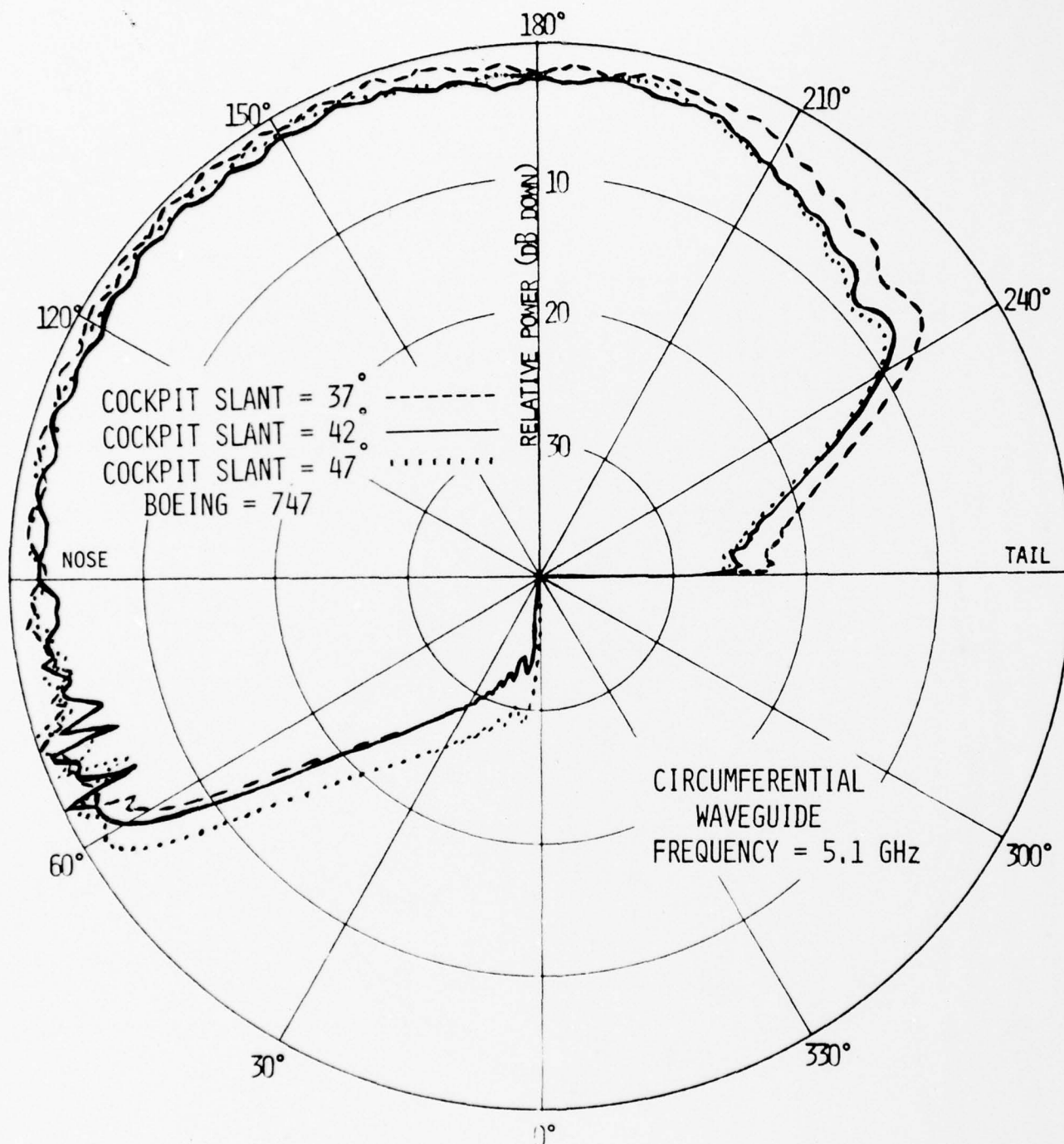


Figure 80. Computed elevation plane amplitude patterns of a circumferential waveguide above the cockpit (station 306) of a full scale Boeing 747 as a function of slant angle.

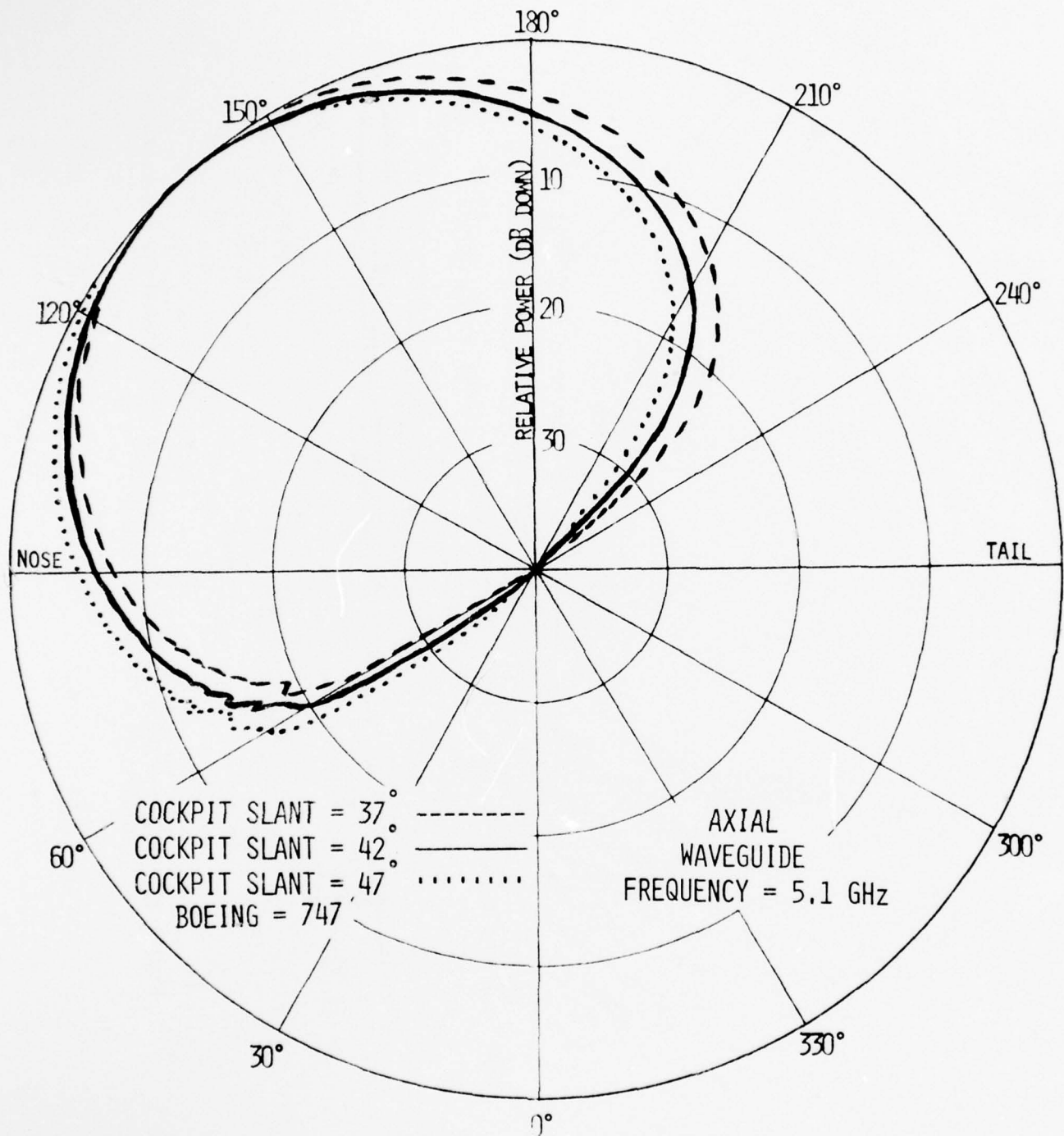


Figure 81. Computed elevation plane amplitude patterns of an axial waveguide above the cockpit (station 306) of a full scale Boeing 747 as a function of slant angle.

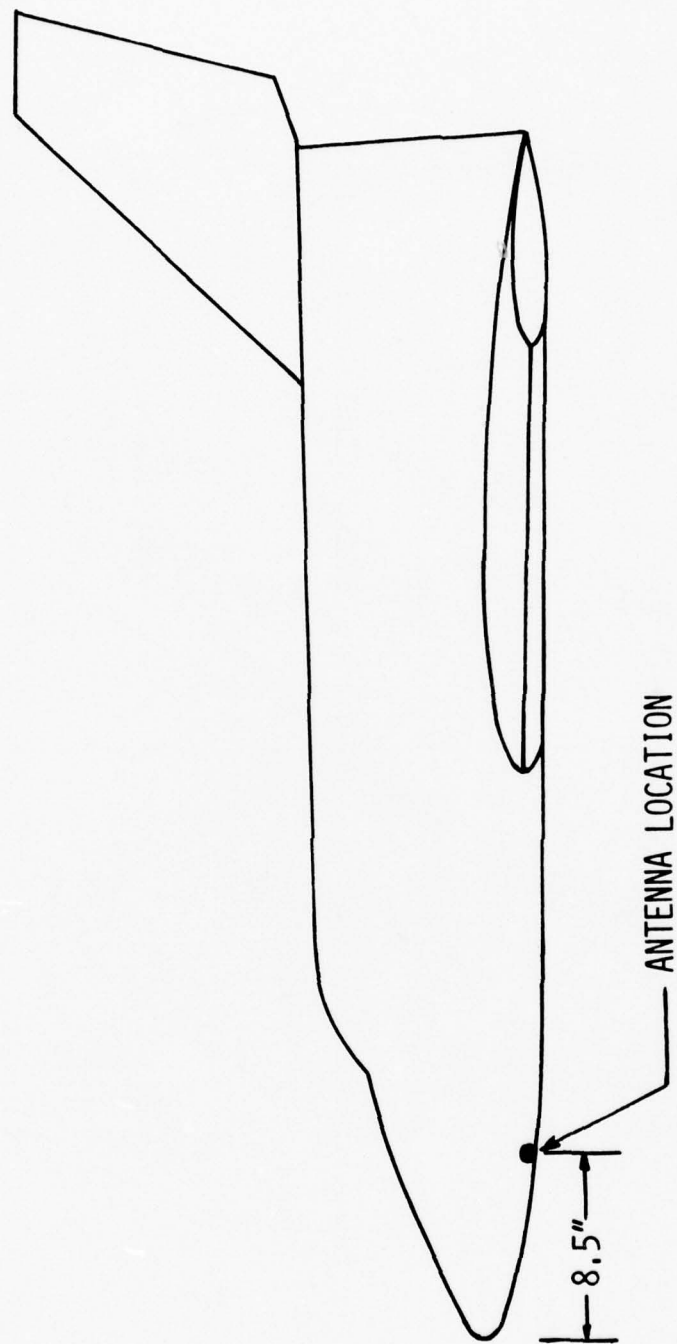


Figure 82, Space shuttle orbiter configuration with dimensions and antenna location on a 1/35 scale model.

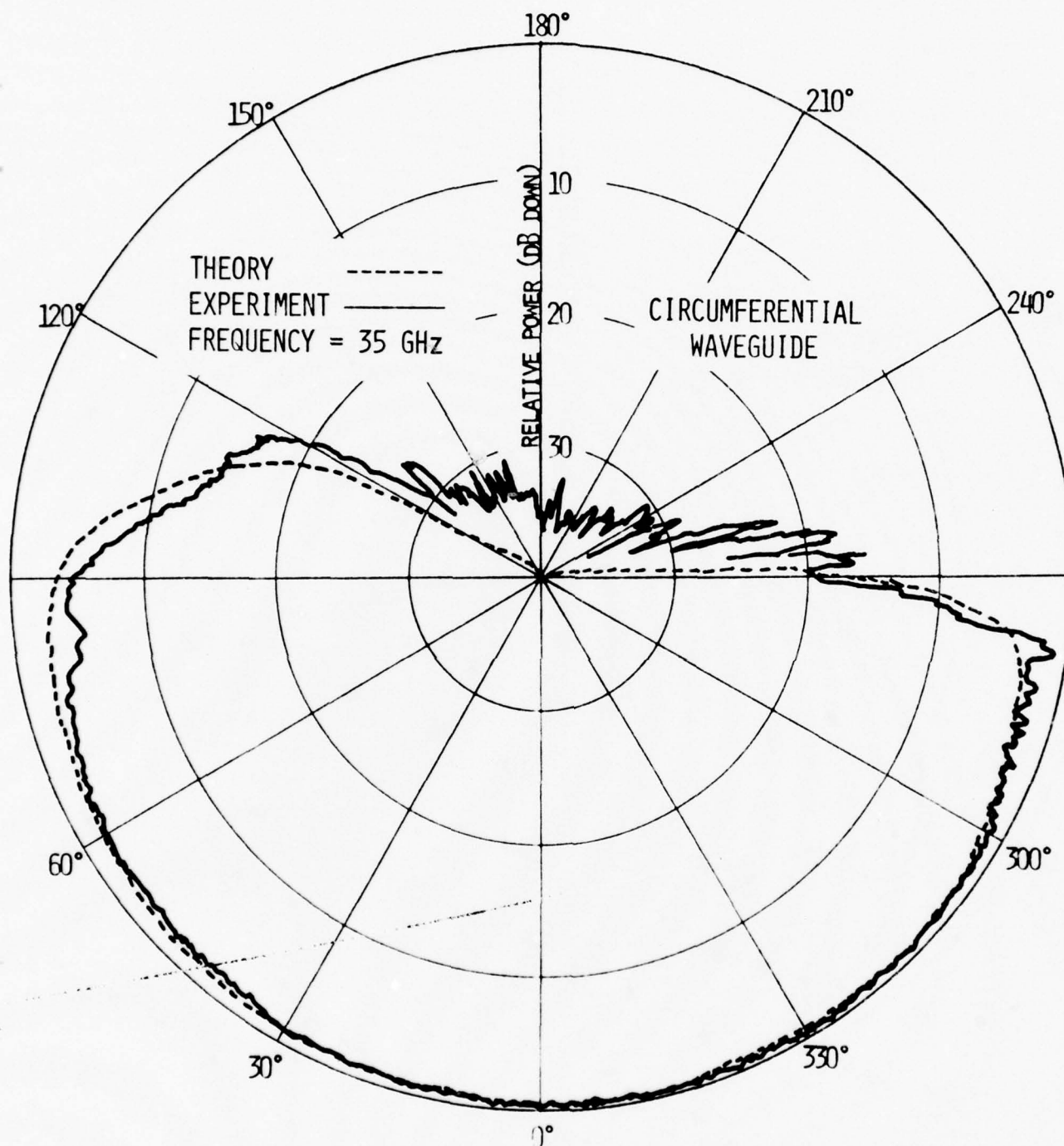


Figure 83. Computed and measured elevation plane amplitude patterns of a circumferential waveguide below the nose of a 1/35 scale space shuttle.

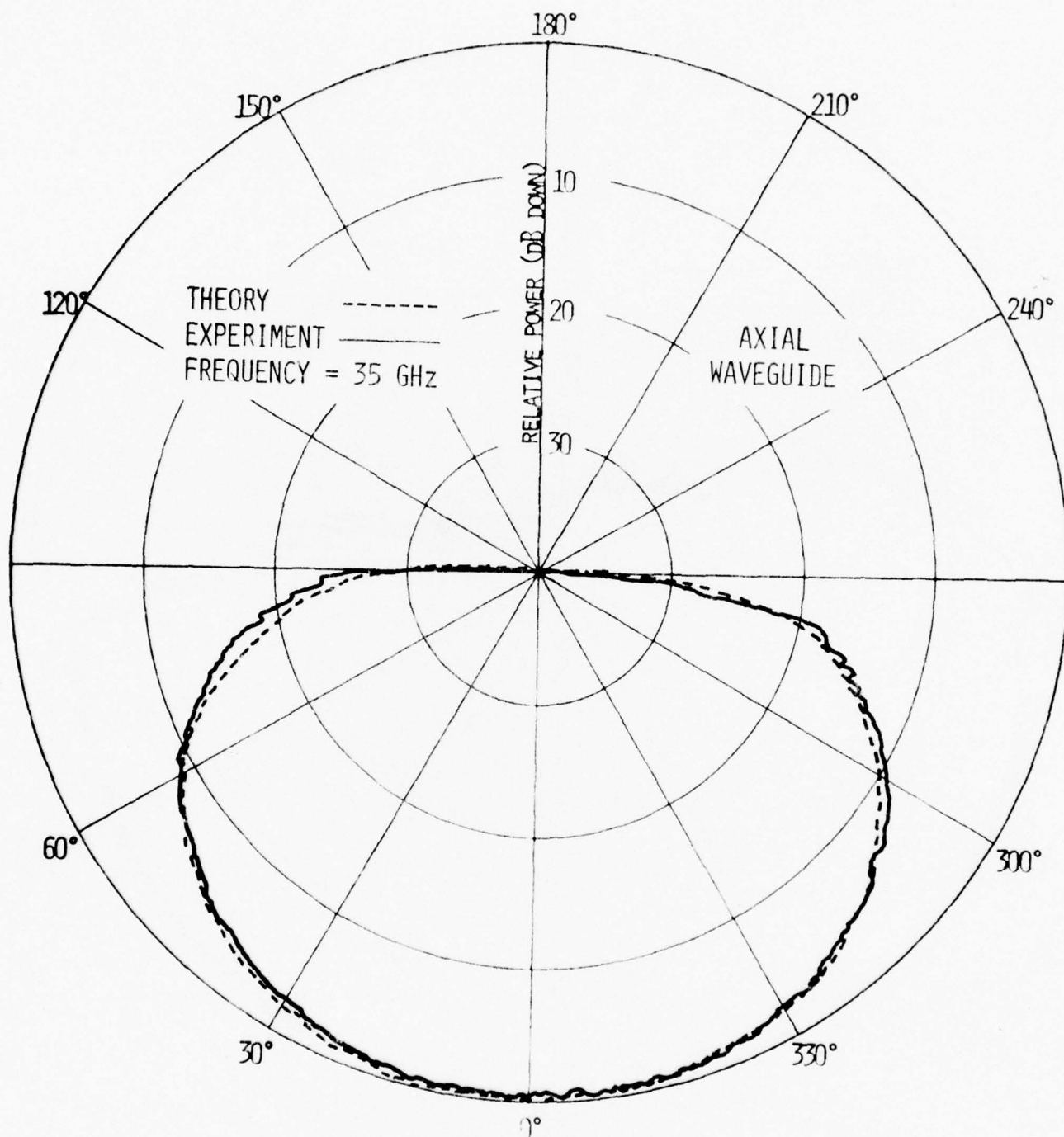


Figure 84. Computed and measured elevation plane amplitude patterns of an axial waveguide below the nose of a 1/35 scale space shuttle.

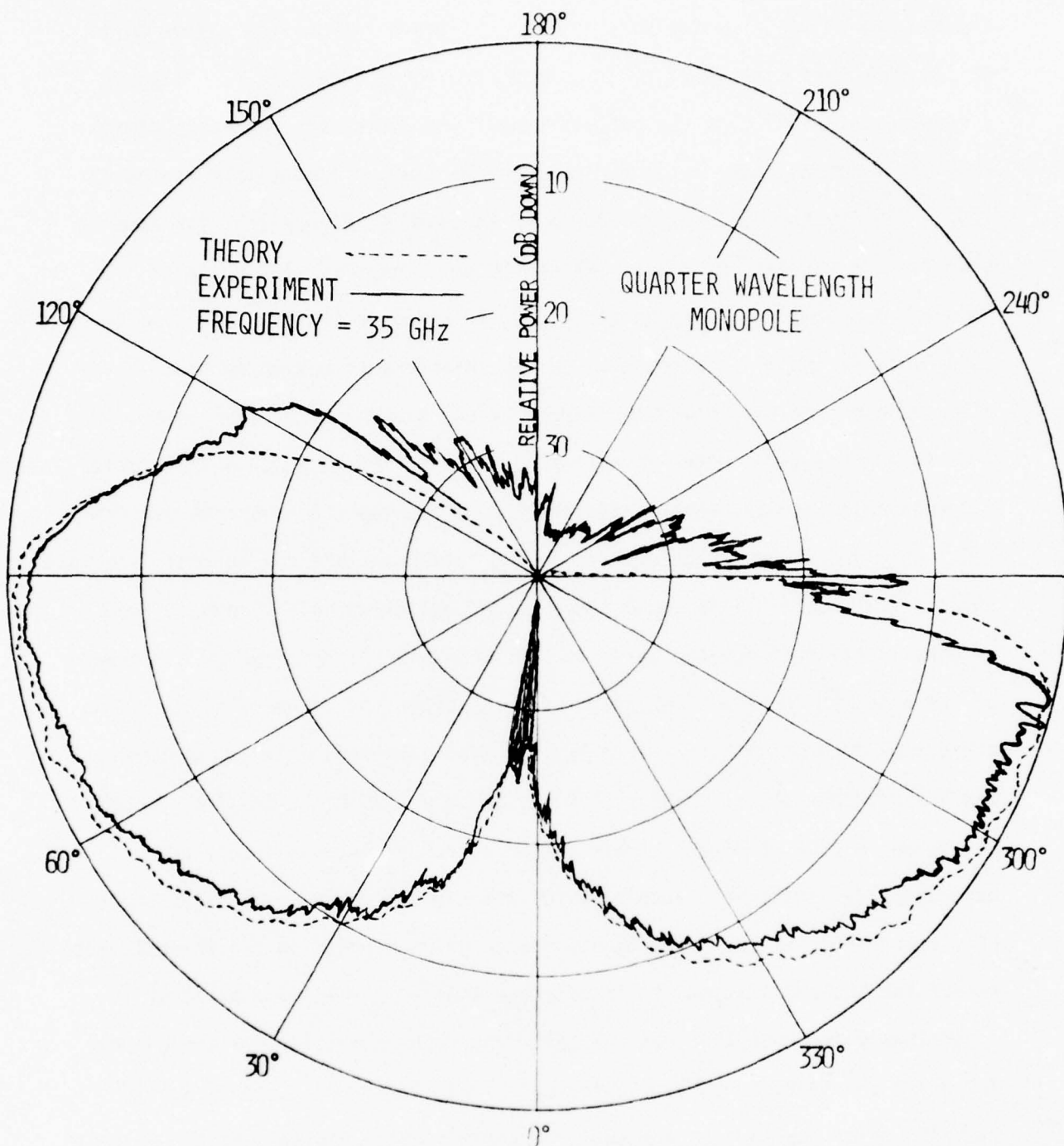


Figure 85. Computed and measured elevation plane amplitude patterns of a quarter wavelength monopole below the nose of a 1/35 scale space shuttle.

radome, the energy from the main source must travel around the curved part of the nose, while reradiating in a tangential direction, and resulting in a reduced intensity. As the path of travel increases, the radiation diminishes as is demonstrated by comparing the coverage provided in the region of $120^{\circ} - 180^{\circ}$ by the patterns of Figure 42 to those of Figure 83. The same is true for the patterns of Figures 43 and 44 when compared with those of Figures 84 and 85. The ripple structure indicated in the $120^{\circ} - 180^{\circ}$ region in Figures 42 and 44 is attributed to the interference caused by the diffractions from the two wedges formed by the truncation of the radome.

Another airplane model investigated was a KC-135 of which a 1/25 scale was available at NASA Langley Research Center and where a number of measurements were undertaken. The overall configuration and the two antenna locations for the 1/25 scale KC-135 model investigated are shown in Figure 86. The antenna location designated as #1 in Figure 86 will be referred to as forward of the wings while #2 will be referred to as above the wings. The elevation plane amplitude patterns for a circumferential aperture, an axial aperture, and a short monopole at locations #2 and #1 on a 1/25 scale model at 35 GHz are shown in Figures 87-92. Again a good agreement between theory and experiment is indicated, especially for the circumferential and axial slots. Even though none of the antennas provides a good coverage in the forward (nose) sector for MLS application, it is observed that as the antenna position is moved toward the nose the coverage below the nose especially for the circumferential and short monopole increases. These locations would be more attractive for positioning antennas for communication and navigation systems. With the availability and versatility of the analytical methods, amplitude patterns for the same type of antennas operating at 5.1 GHz and positioned at the corresponding locations on a full scale KC-135 were computed and are

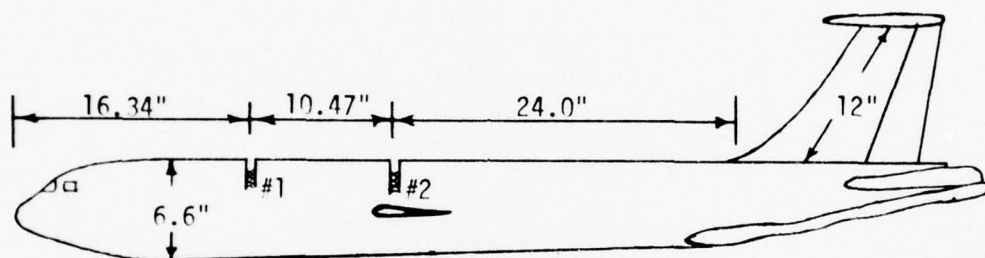


Figure 86, Elevation plane configuration and airplane dimensions of a 1/25 scale KC-135 model.

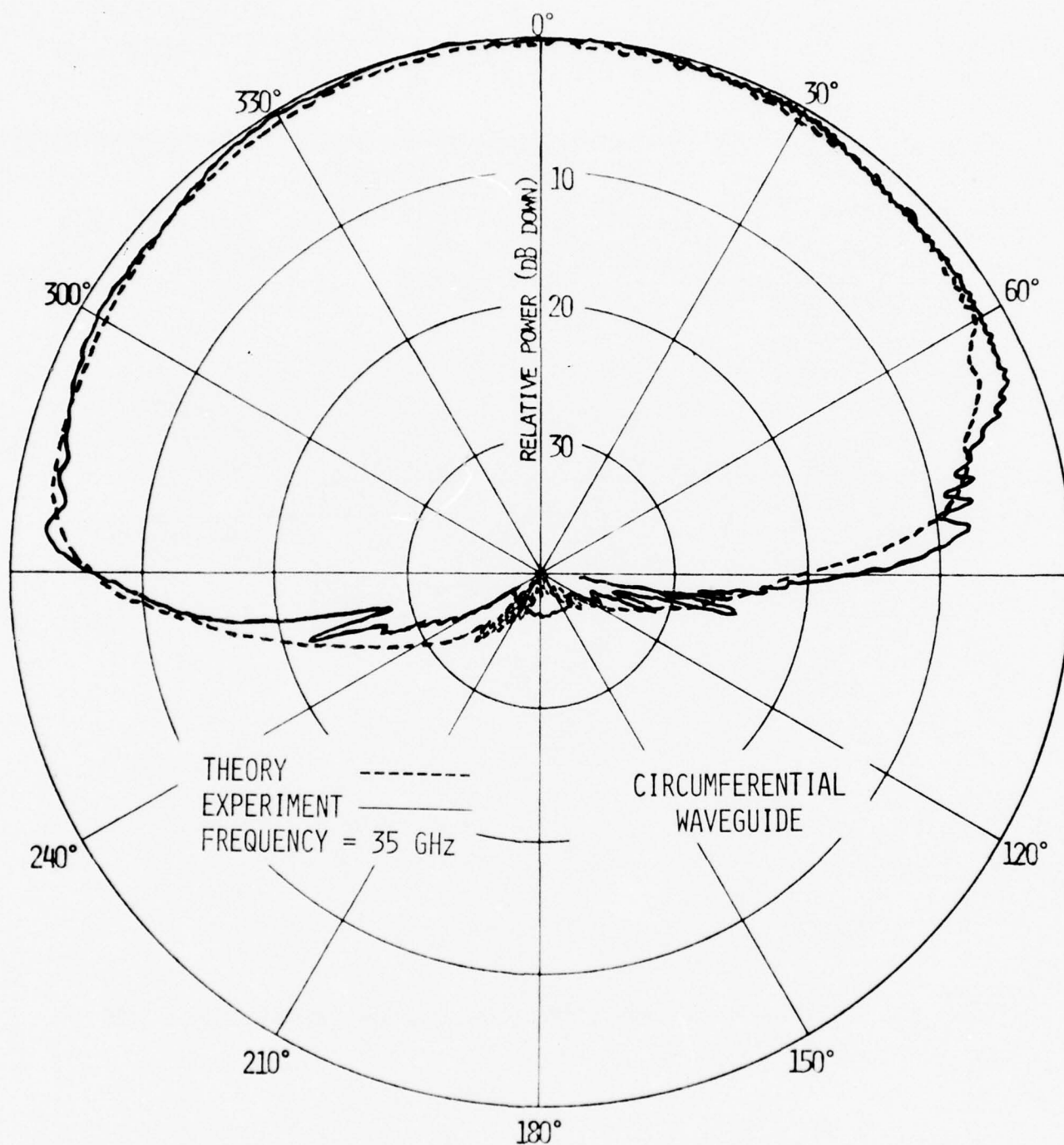


Figure 87. Computed and measured elevation plane amplitude patterns of a circumferential waveguide above wings (location #2) of 1/25 scale KC-135

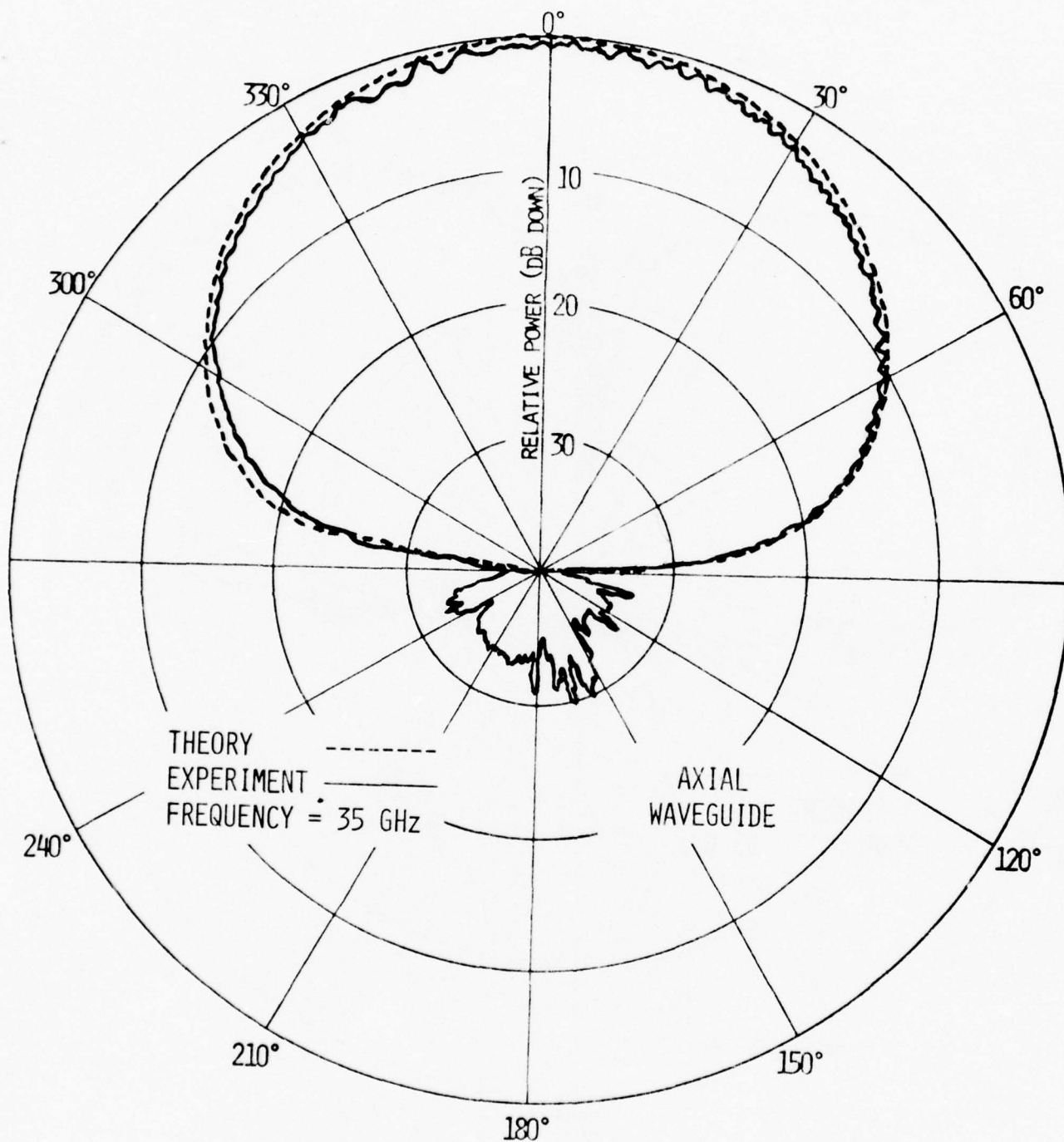


Figure 88. Computed and measured elevation plane amplitude patterns of an axial waveguide above wings (location #2) of 1/25 scale KC-135.

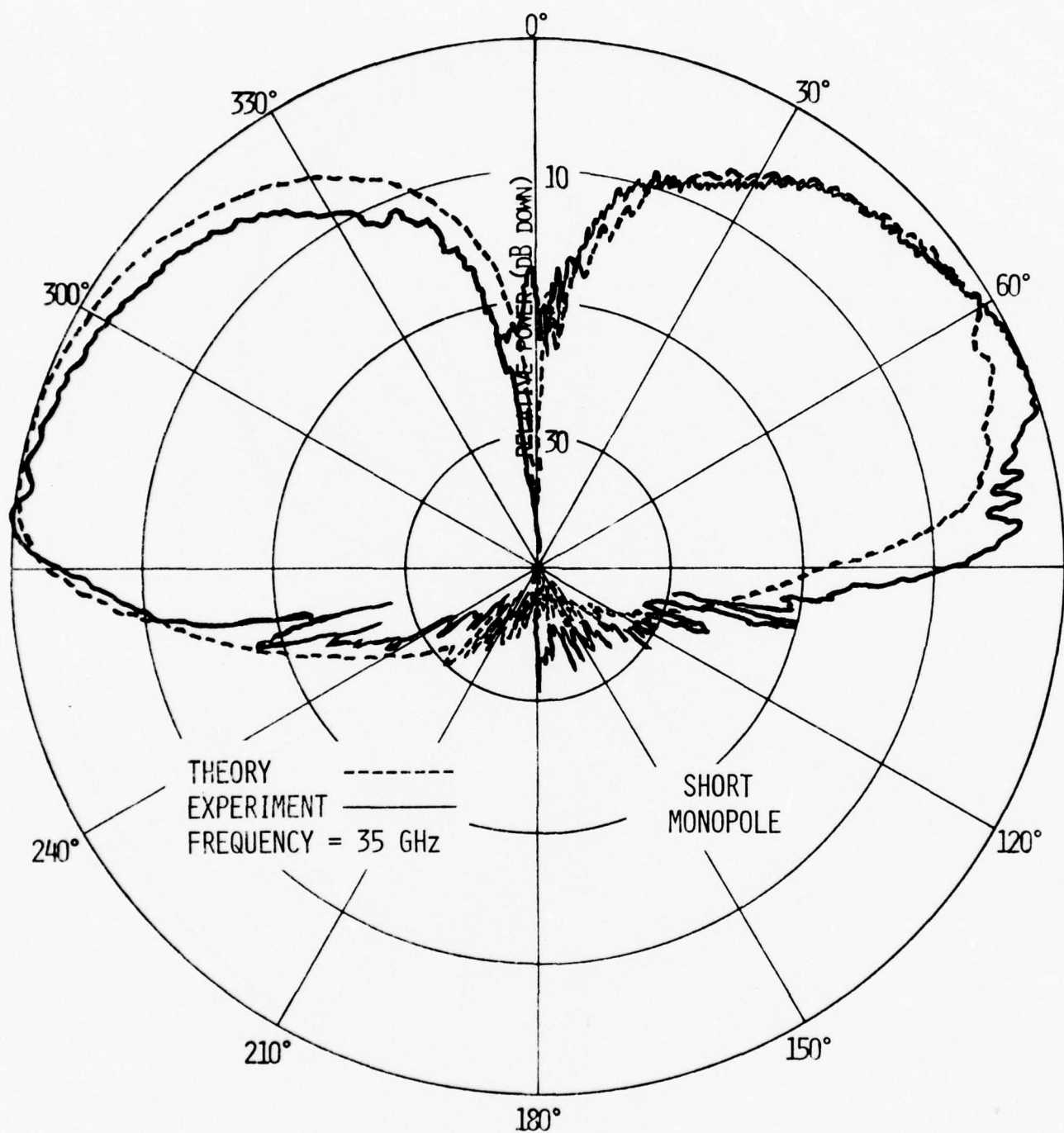


Figure 89. Computed and measured elevation plane amplitude patterns of a short monopole above wings (location #2) of 1/25 scale KC-135.

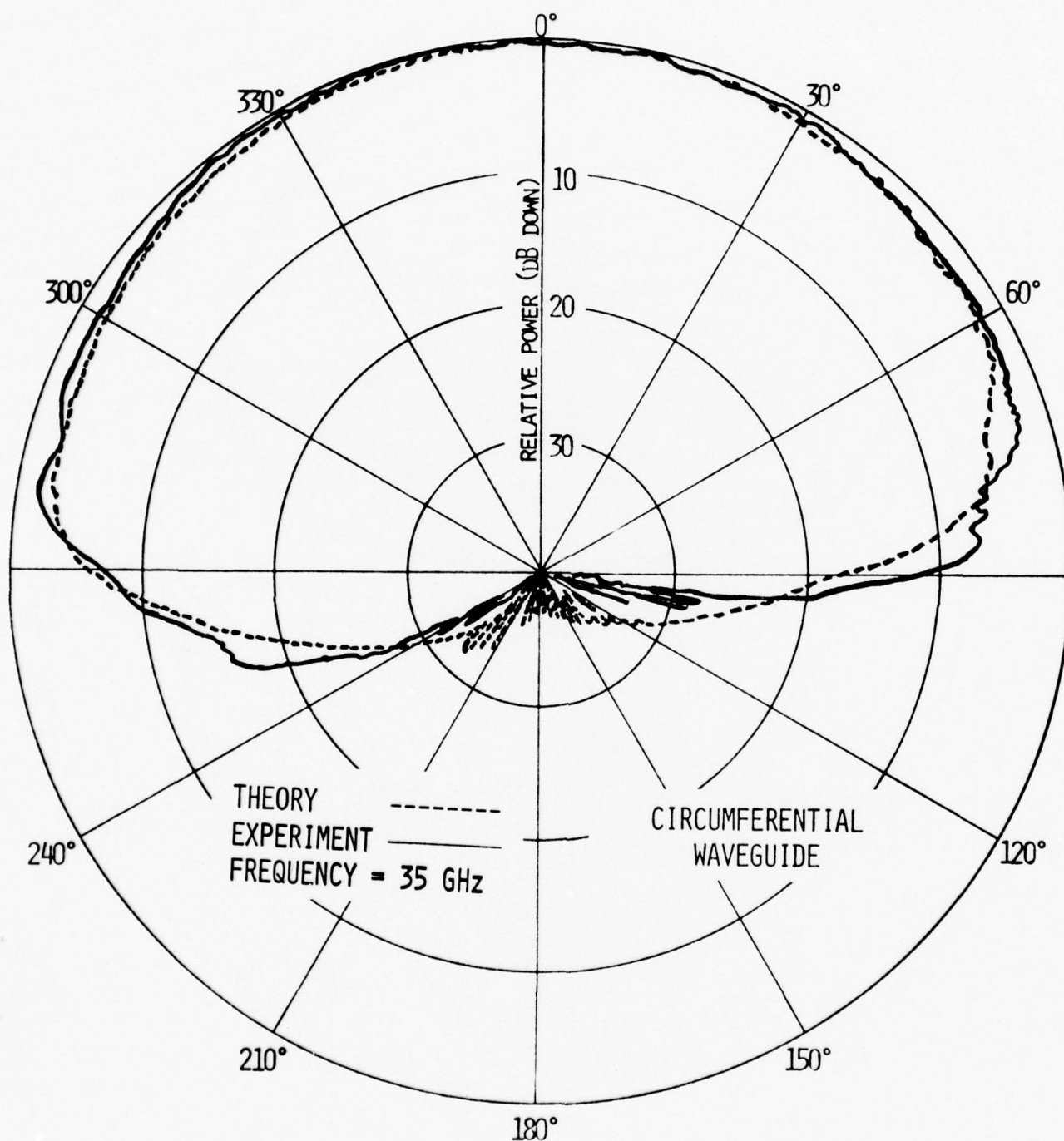


Figure 90. Computed and measured elevation plane amplitude patterns of a circumferential waveguide forward of wings (location #1) of 1/25 scale KC-135.

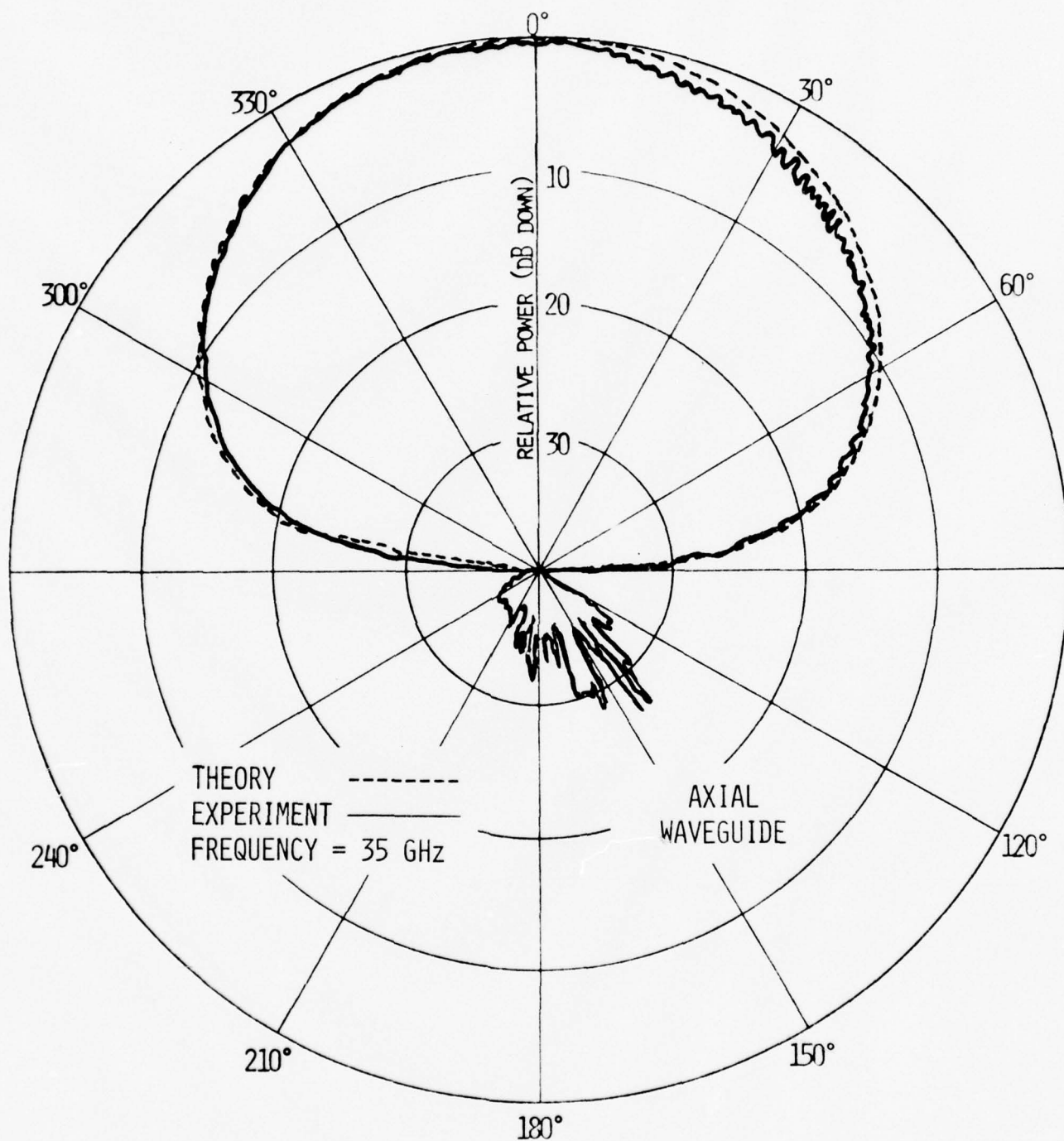


Figure 91. Computed and measured elevation plane amplitude patterns of an axial waveguide forward of wings (location #1) of 1/25 scale KC-135.

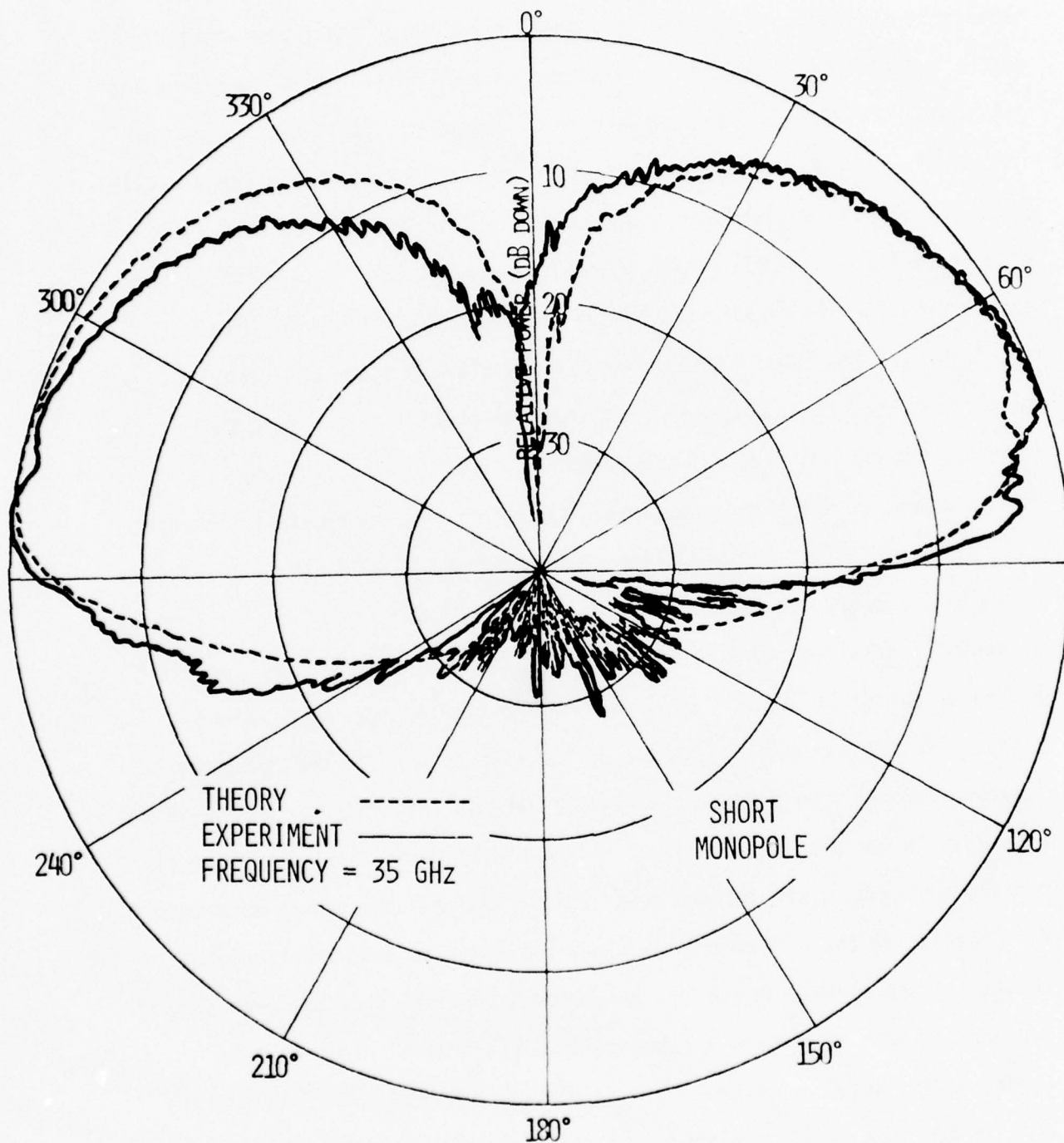


Figure 92. Computed and measured elevation plane amplitude patterns of a short monopole forward of wings (location #1) of 1/25 scale KC-135.

shown in Figures 93-98. When compared to the corresponding 1/25 scale model patterns, it is clear that the overall shape of each corresponding pattern is the same. There are some small differences which are attributed to the nonidentical electrical dimensions of each model. When comparing the computed pattern of Figure 87 with that of Figure 93, it is quite apparent that the overall shape is the same except that the radiation in the direction below the nose is somewhat less intense for the pattern of the full scale because of its larger electrical dimensions which cause larger attenuations in the signal as it travels around the curved path of the nose while reradiating. The same is true for the other corresponding patterns. It can be said again, as was stated before, that the profile of the structure controls the overall shape of the patterns. The electrical dimensions of the structure do influence the pattern shape but in a somewhat less degree.

In Figure 99 the azimuth plane configuration and two antenna locations of an airplane are indicated. Azimuth plane amplitude radiation patterns for a circumferential aperture, axial aperture, and short monopole at locations #1 and #2 on a full scale KC-135 are shown in Figures 100-105. Although the circumferential and axial apertures at location #1 provide the necessary coverage for MLS applications, it must be assumed that this position will not be available for placing an antenna on the radome surface because it will provide blockage to the weather radar which is within the radome structure. For location #2 the circumferential aperture provides the widest coverage in the azimuth plane. It must be remembered, however, that the same antenna does not provide as good of a coverage in the elevation plane as the corresponding axial aperture.

In addition to the amplitude and phase radiation patterns, another parameter that was examined in this investigation was coupling between two

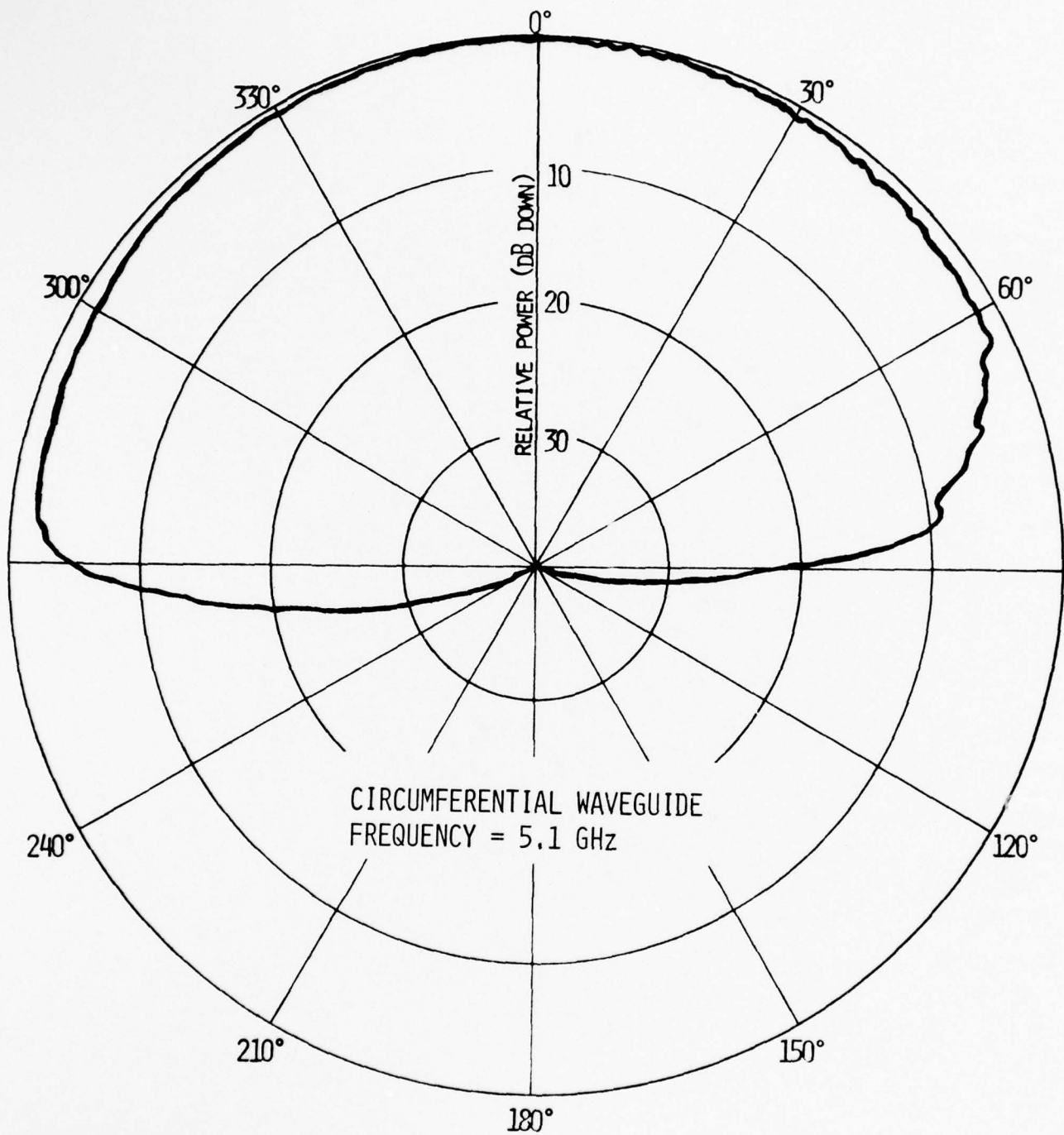


Figure 93. Computed elevation plane amplitude pattern of a circumferential waveguide above wings (location #2) of full scale KC-135.

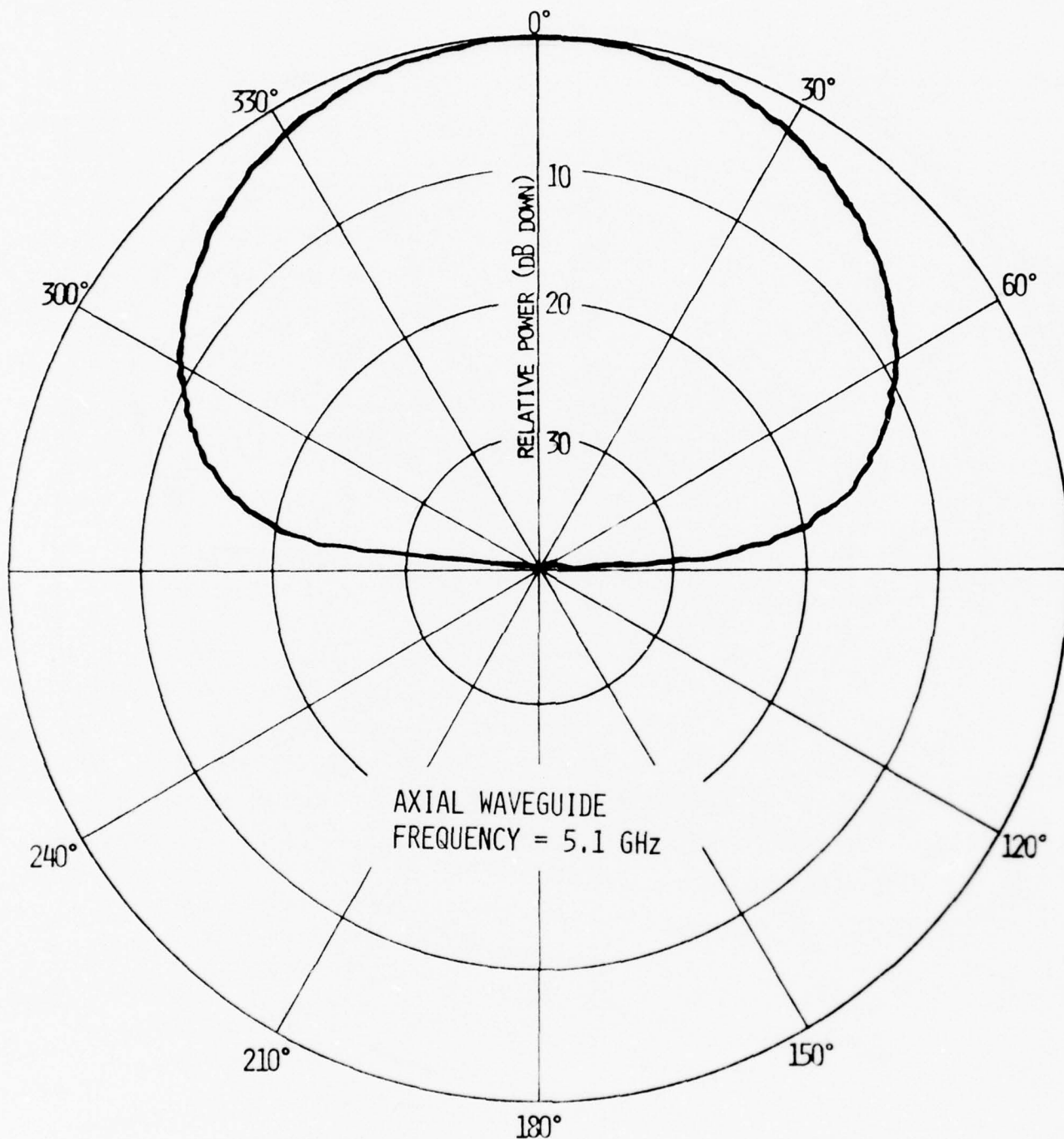


Figure 94. Computed elevation plane amplitude pattern of an axial waveguide above wings (location #2) of full scale KC-135.

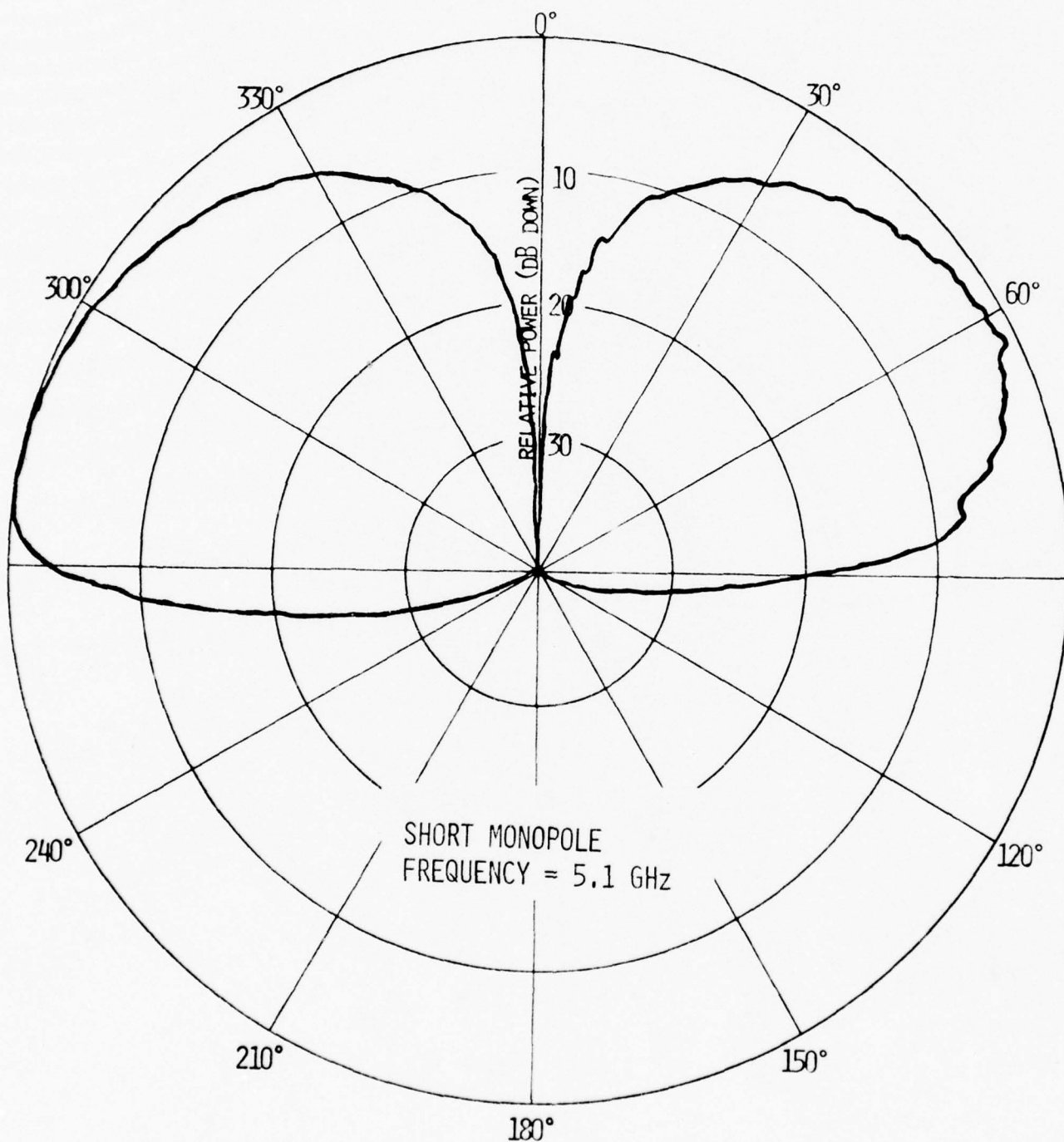


Figure 95. Computed elevation plane amplitude pattern of a short monopole above wings (location #2) of full scale KC-135.

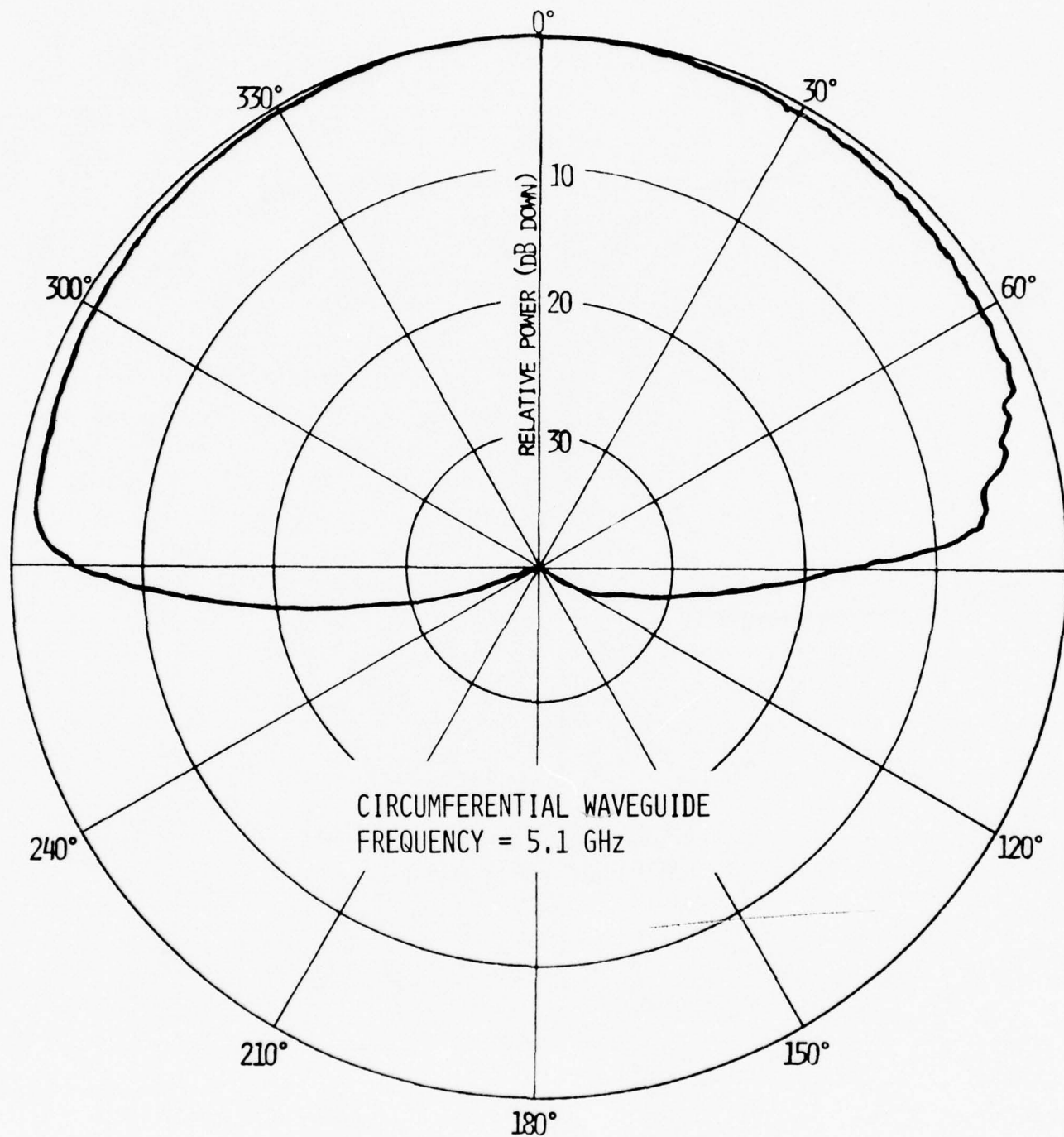


Figure 96. Computed elevation plane amplitude pattern of a circumferential waveguide forward of wings (location #1) of full scale KC-135.

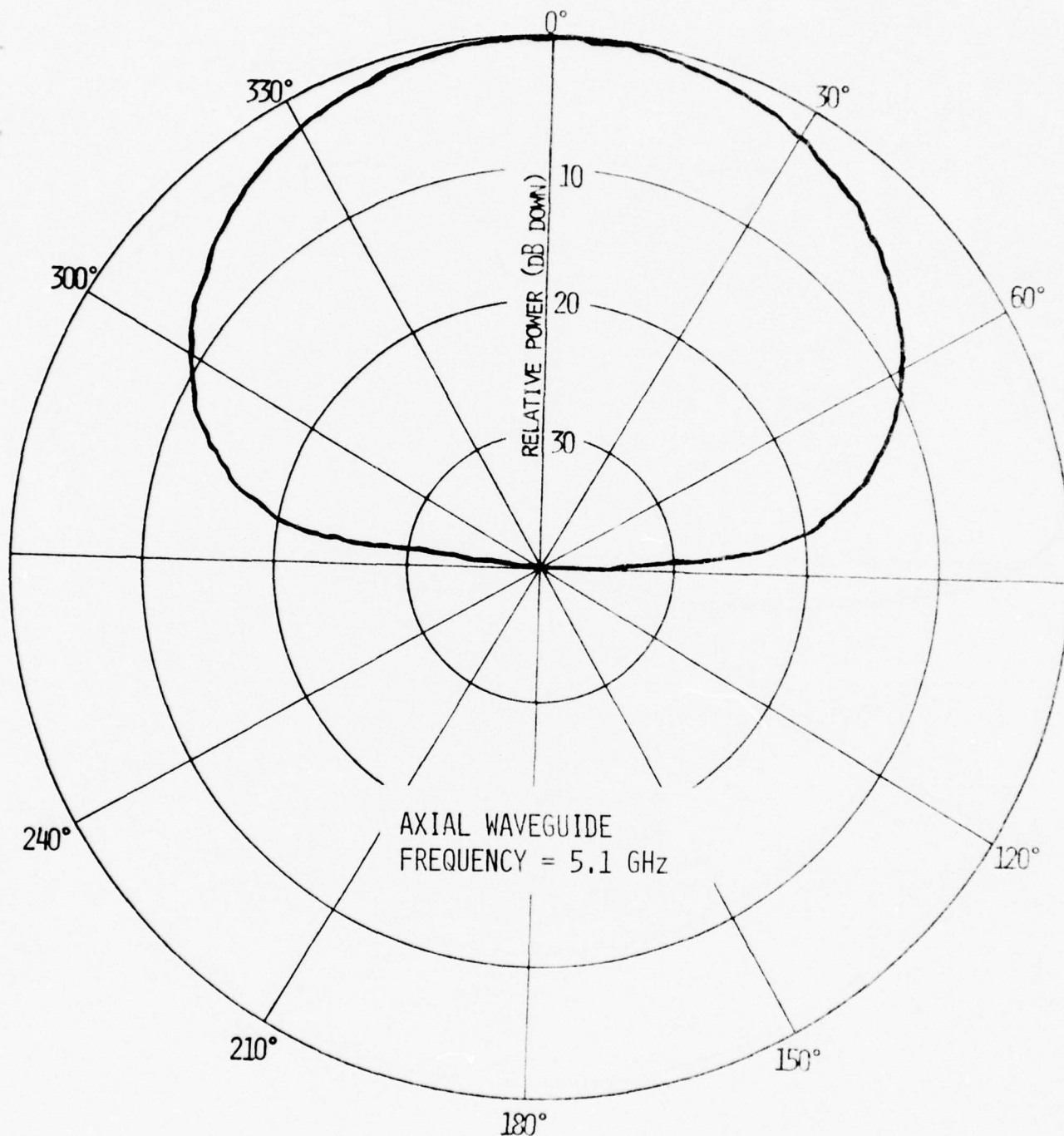


Figure 97. Computed elevation plane amplitude pattern of an axial waveguide forward of wings (location #1) of full scale KC-135

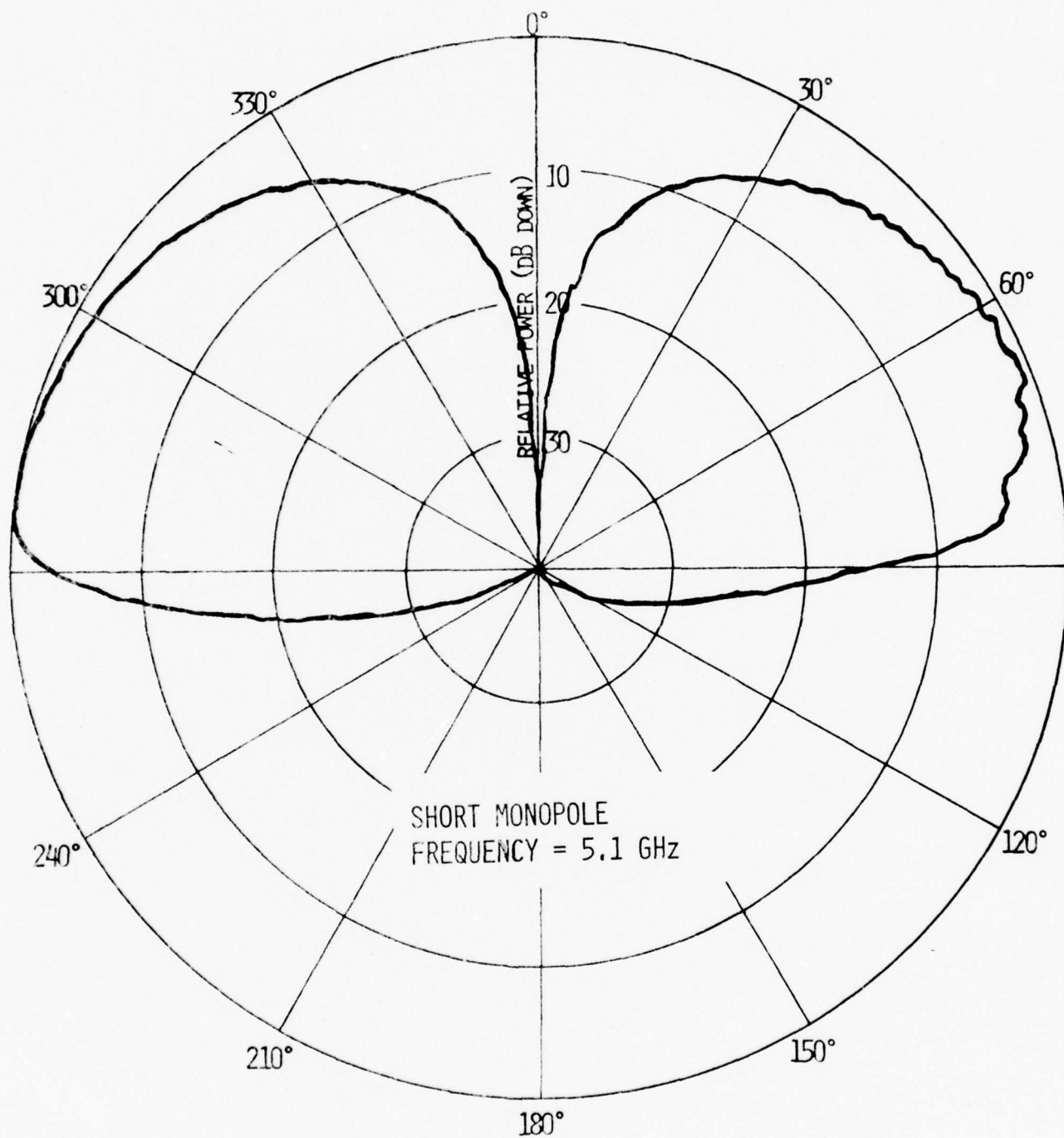


Figure 98. Computed elevation plane amplitude pattern of a short monopole forward of wings (location #1) of full scale KC-135.

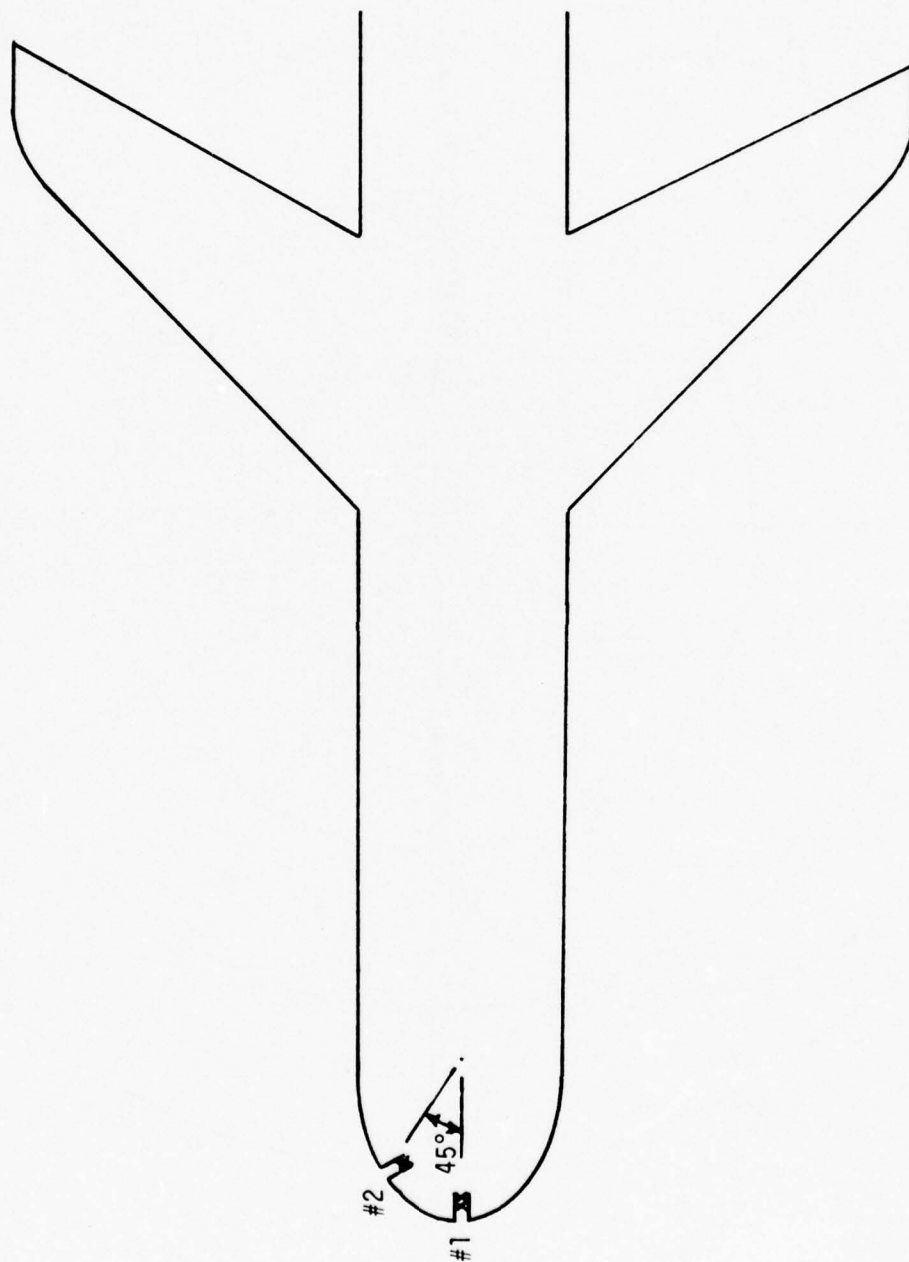


Figure 99. Azimuth plane airplane configuration with two antenna locations on the nose.

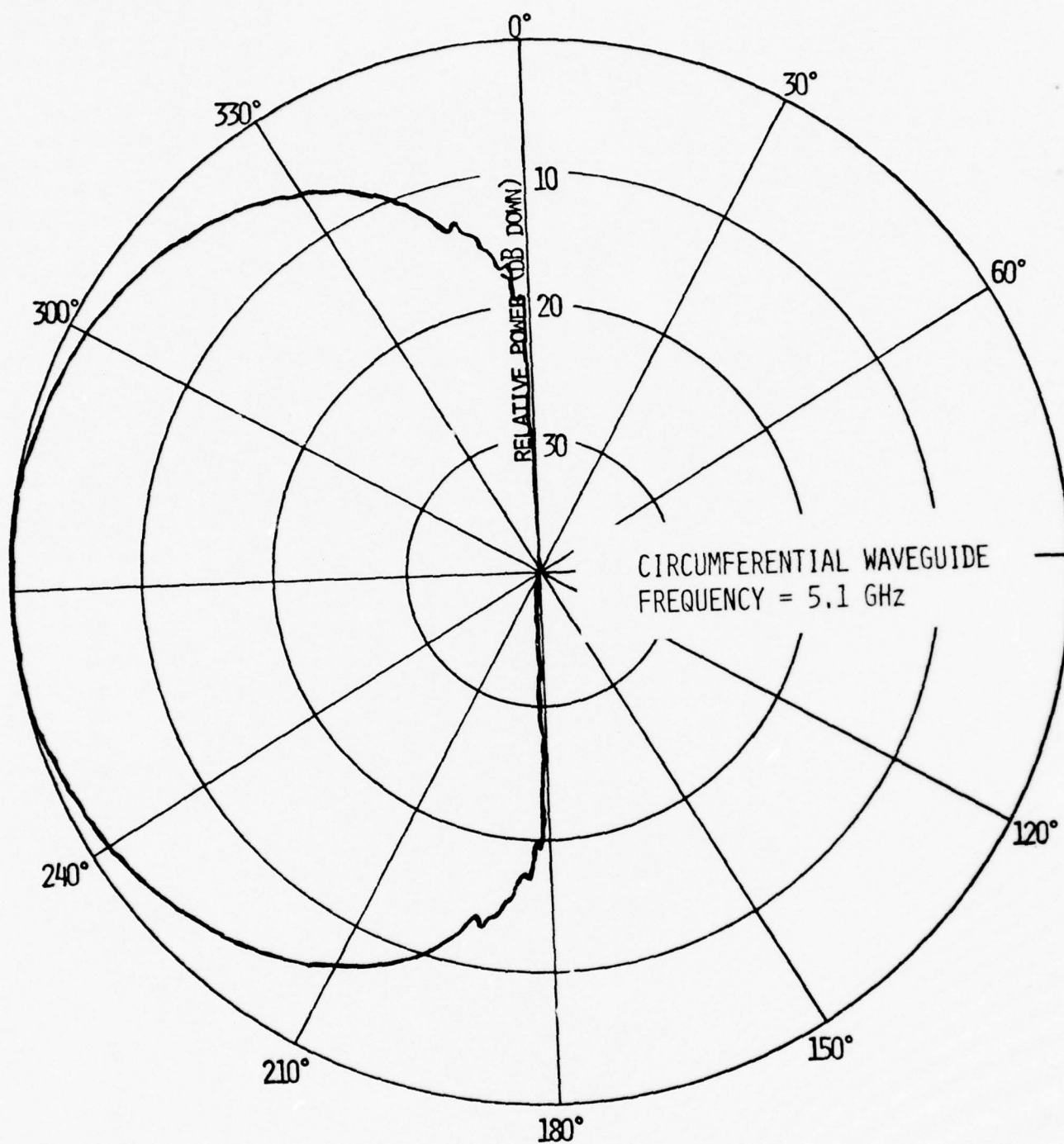


Figure 100. Computed azimuth plane amplitude pattern of a circumferential waveguide on the nose (location #1) of a full scale KC-135.

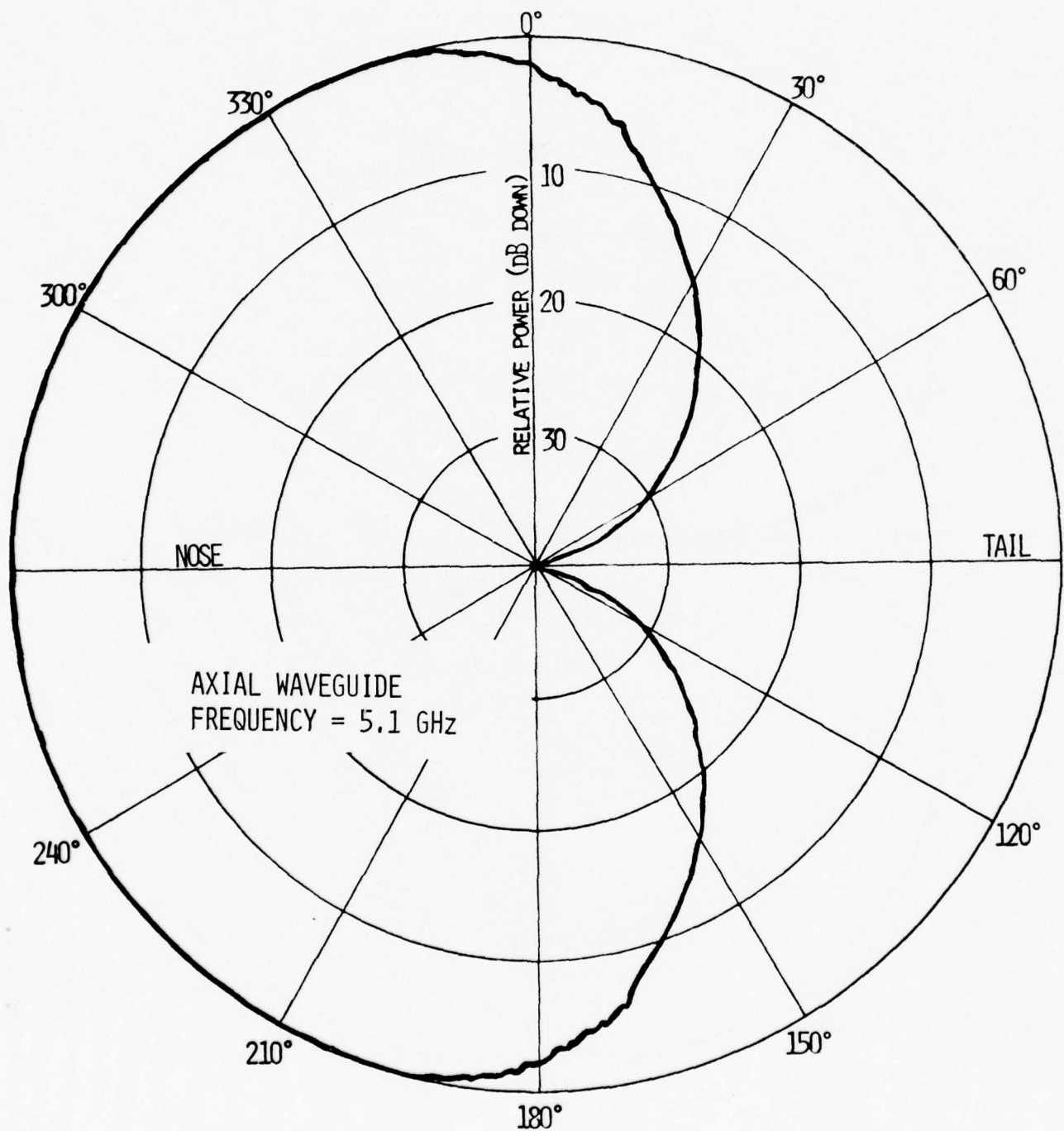


Figure 101. Computed azimuth plane amplitude pattern of an axial waveguide on the nose (location #1) of a full scale KC-135.

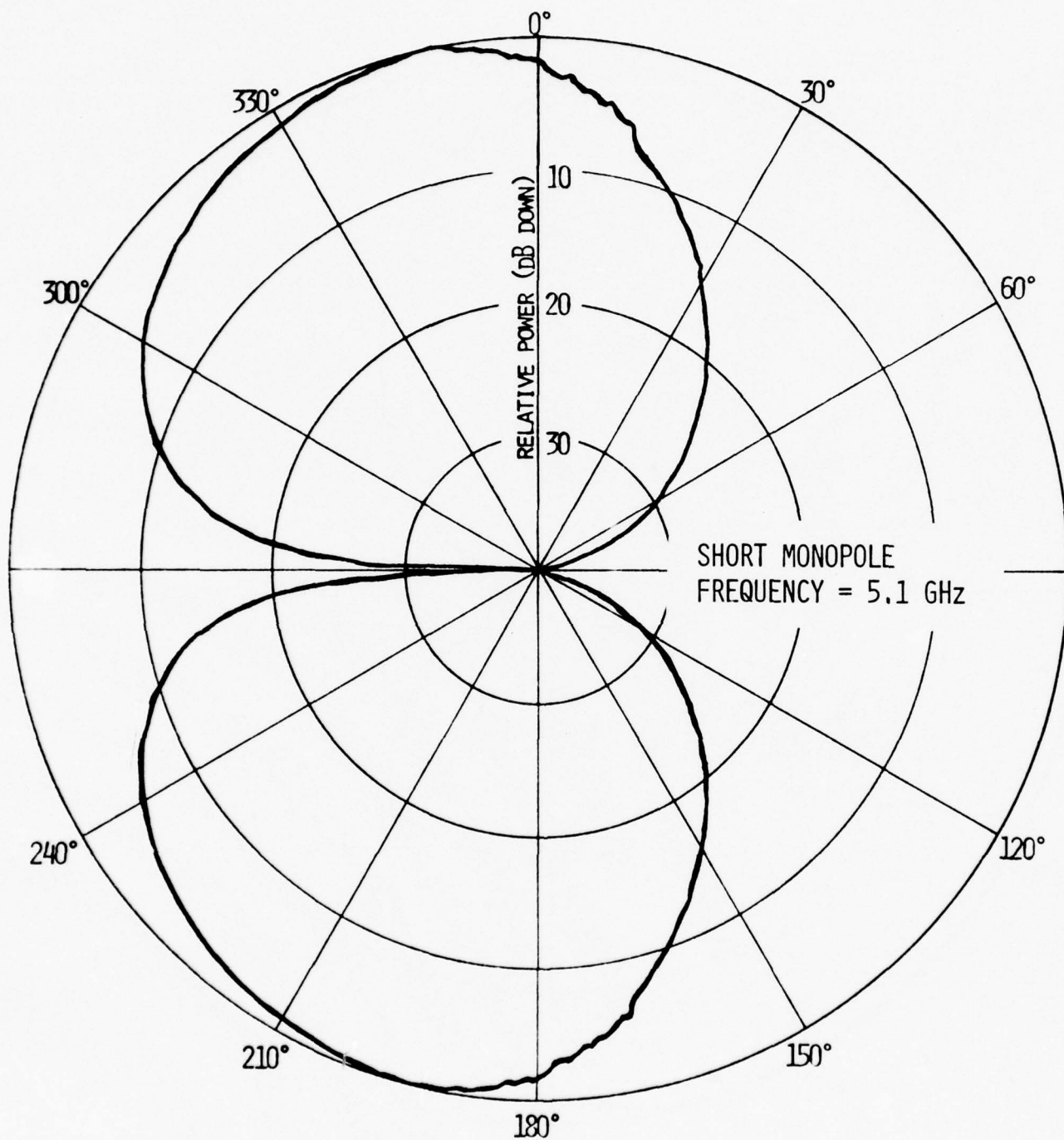


Figure 102. Computed azimuth plane amplitude pattern of a short monopole on the nose (location #1) of a full scale KC-135.

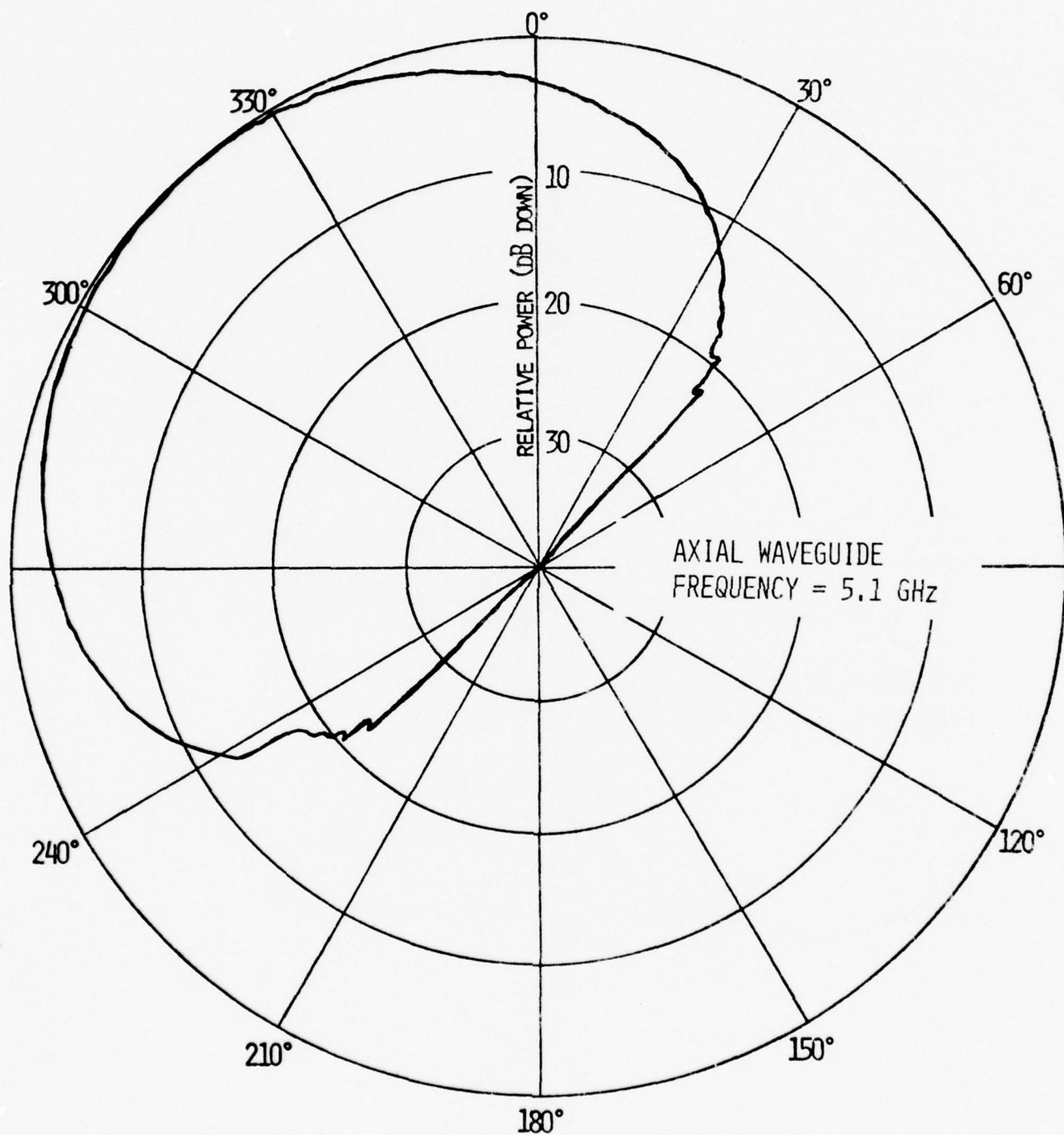


Figure 103. Computed azimuth plane amplitude pattern of an axial waveguide on the nose (location #2) of a full scale KC-135.

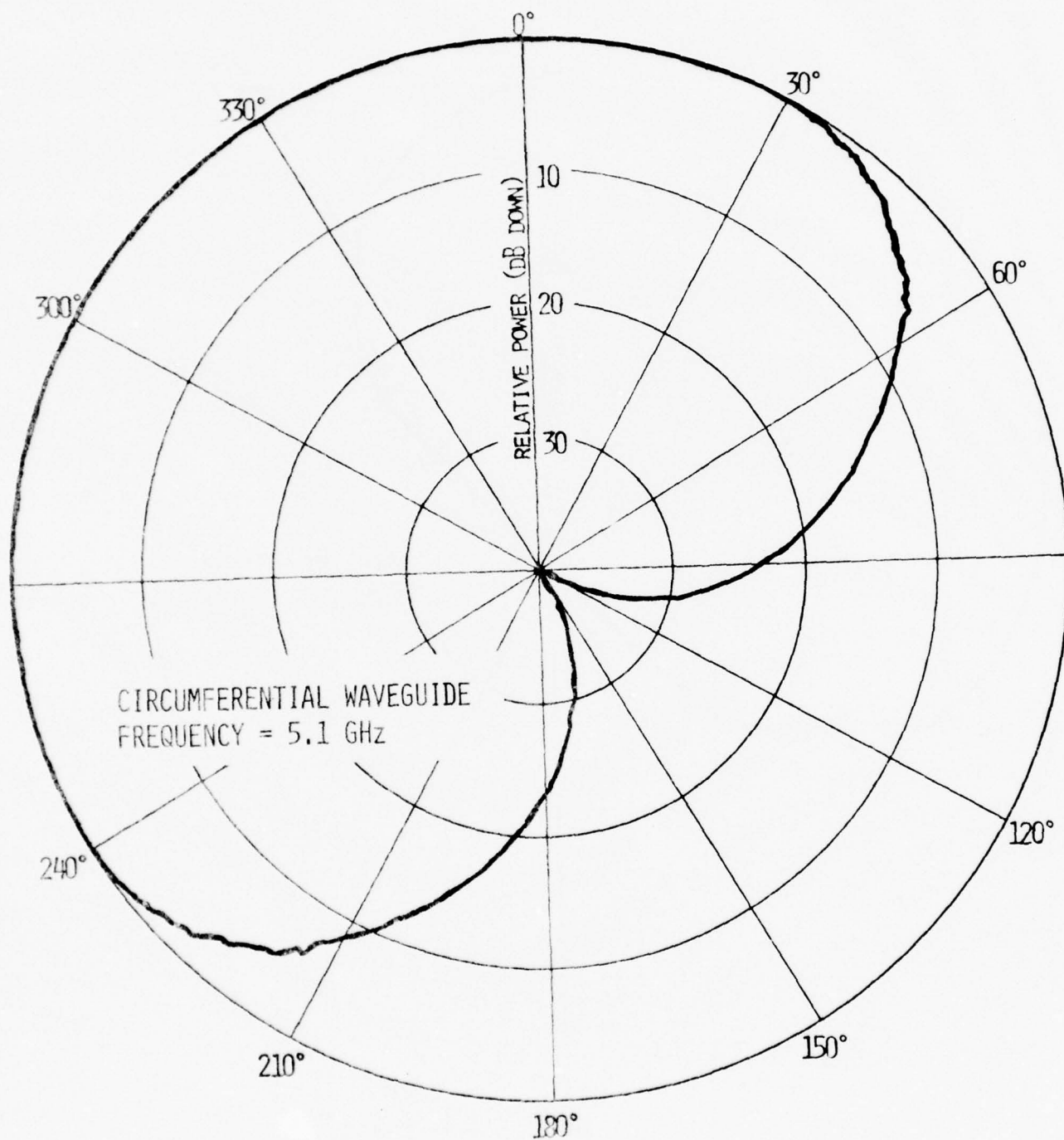


Figure 104. Computed azimuth plane amplitude pattern of a circumferential waveguide on the nose (location #2) of a full scale KC-135.

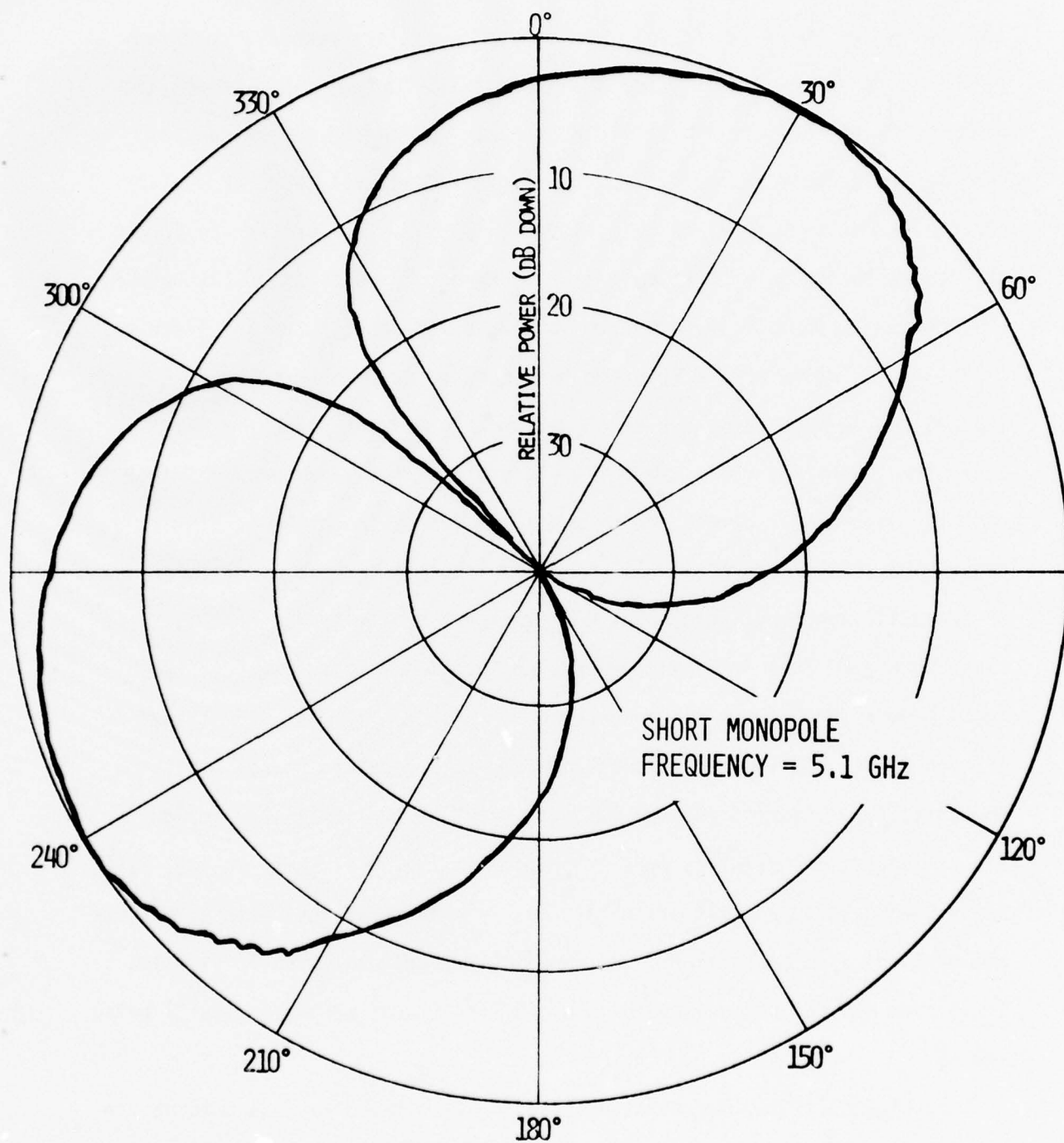


Figure 105. Computed azimuth plane amplitude pattern of a short monopole on the nose (location #2) of a full scale KC-135.

circumferential or between two axial apertures. The analysis for predicting the coupling between two apertures was developed and included in the theory section. In order to verify the analytical methods, computed results were compared with other available data. Shown on the insert in Figures 106 and 107 are two aperture antennas located on elliptical and circular cylinders, respectively. The nose-fuselage structure of the airplane was modeled by half of an elliptical or half of a circular cylinder, and each attached to another cylinder as shown in each figure. The results obtained were compared when the same antennas were mounted on an elliptical or a circular cylinder and reported in reference 32. The results of Figures 106 and 107 compare favorably and place a degree of confidence in the analytical techniques. In Figure 108 two antenna positions are indicated with the separation between the antennas denoted by the angle ψ . In Figures 109-116 the computed values of coupling between two circumferential or two axial apertures when mounted on the nose part of the airplane, as shown in Figure 108, are indicated and are plotted as a function of the angle separation between the antennas. In this case it was assumed that antenna #1 was stationary while antenna #2 was allowed to change position. The initial position of antenna #2 would start at the transition region. The configurations examined were 1/25 scale KC-135, full scale KC-135, full scale Boeing 737, and full scale 747. It is clear that for these structures and the indicated separations, the coupling between apertures is very low (less than -20 dB) especially for the axial apertures which is usually below -40 dB.

In Figure 117 another relative positioning between two antennas on the nose of an aircraft is indicated. For this position it is also assumed that antenna #1 is stationary while #2 is allowed to change position. The

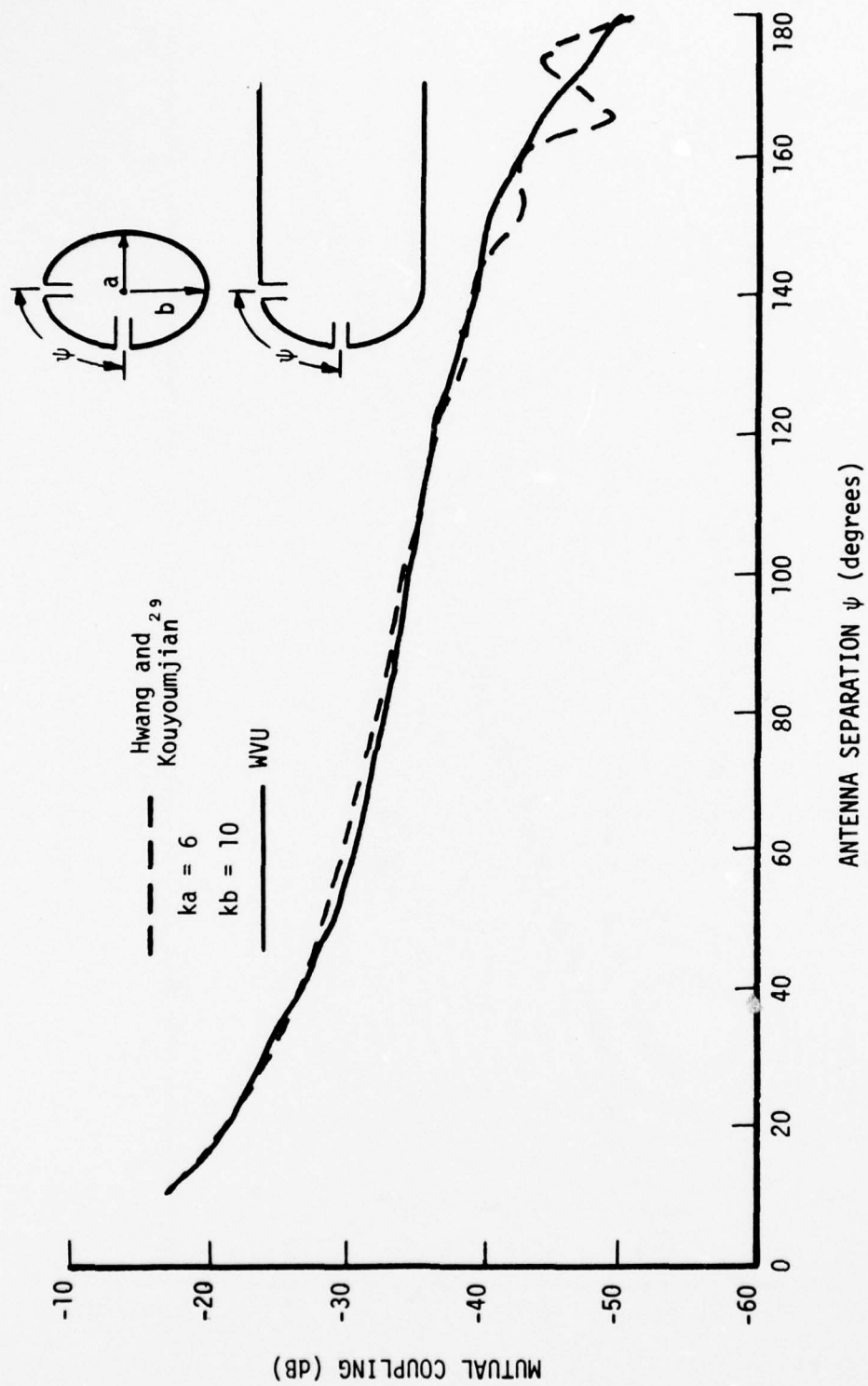


Figure 106. Mutual coupling between two axial apertures computed at West Virginia University (WVU) and compared with that reported in reference 29.

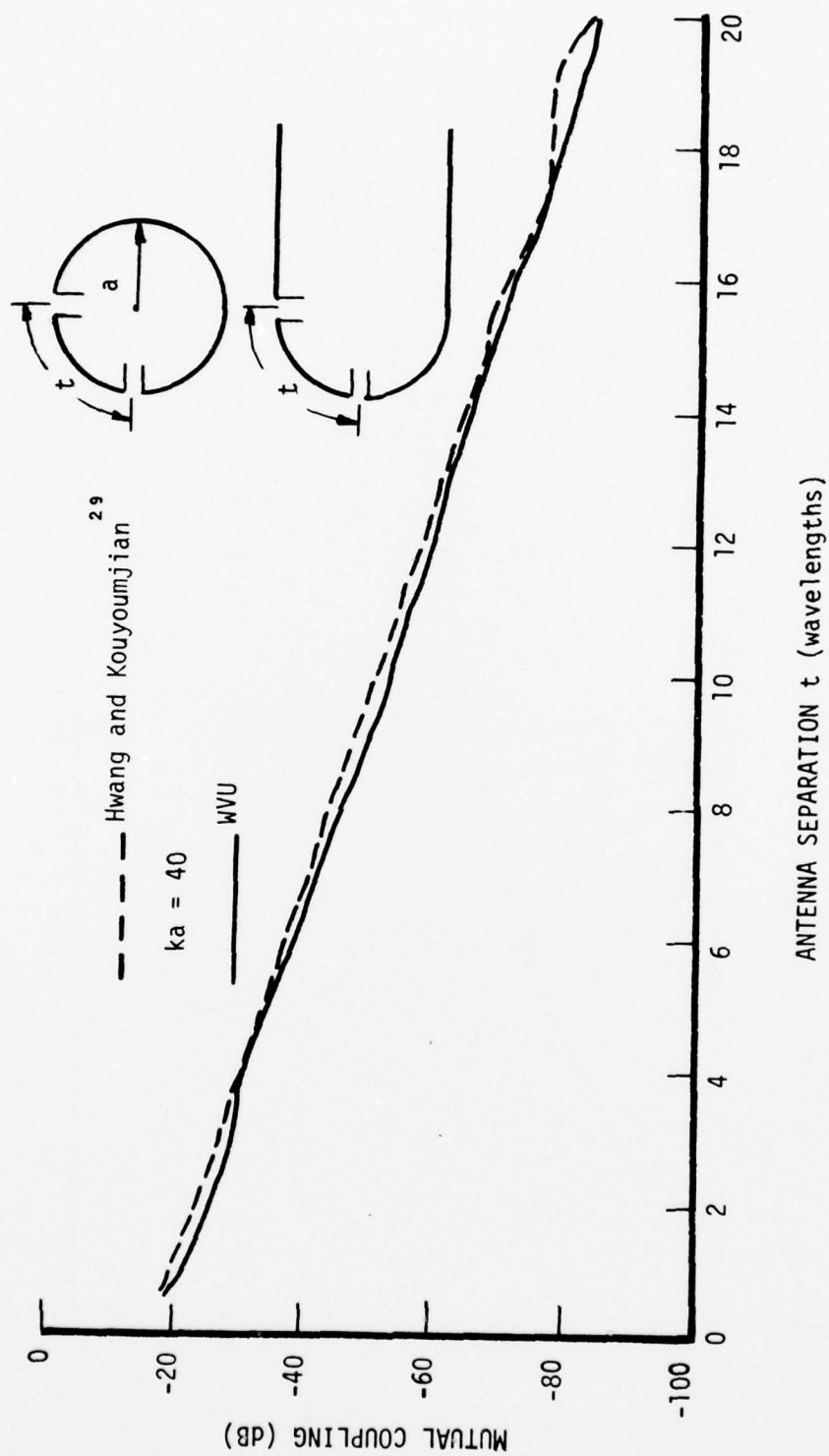


Figure 107. Mutual coupling between two axial apertures computed at West Virginia University (WVU) and compared with that reported in reference 29.

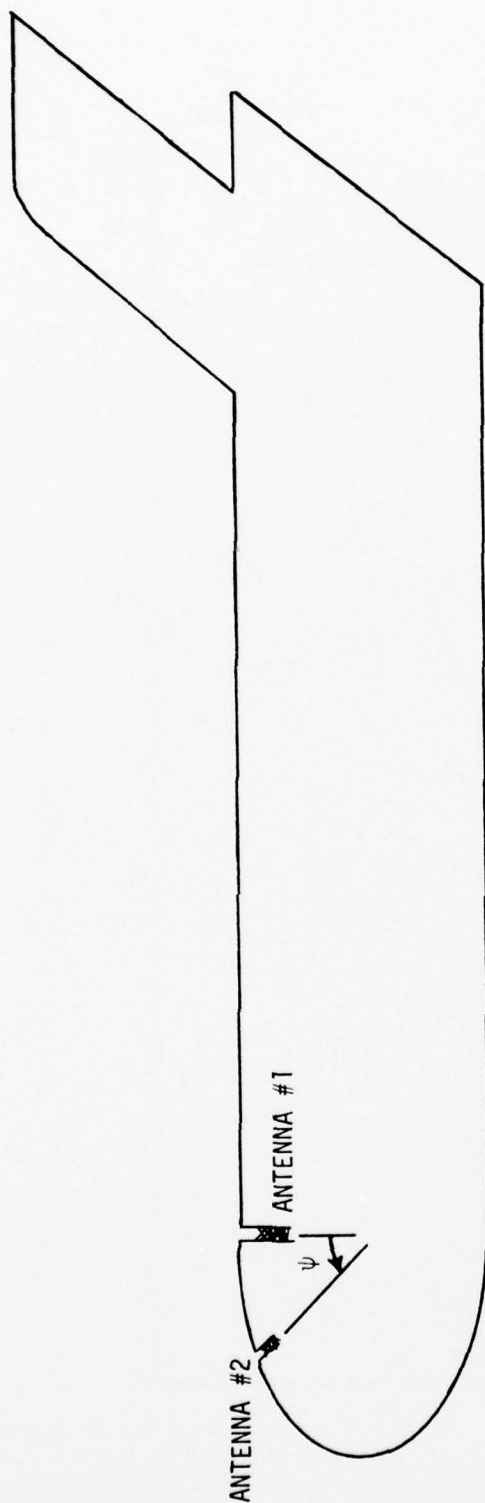


Figure 108. Antenna positioning along the nose of the aircraft.

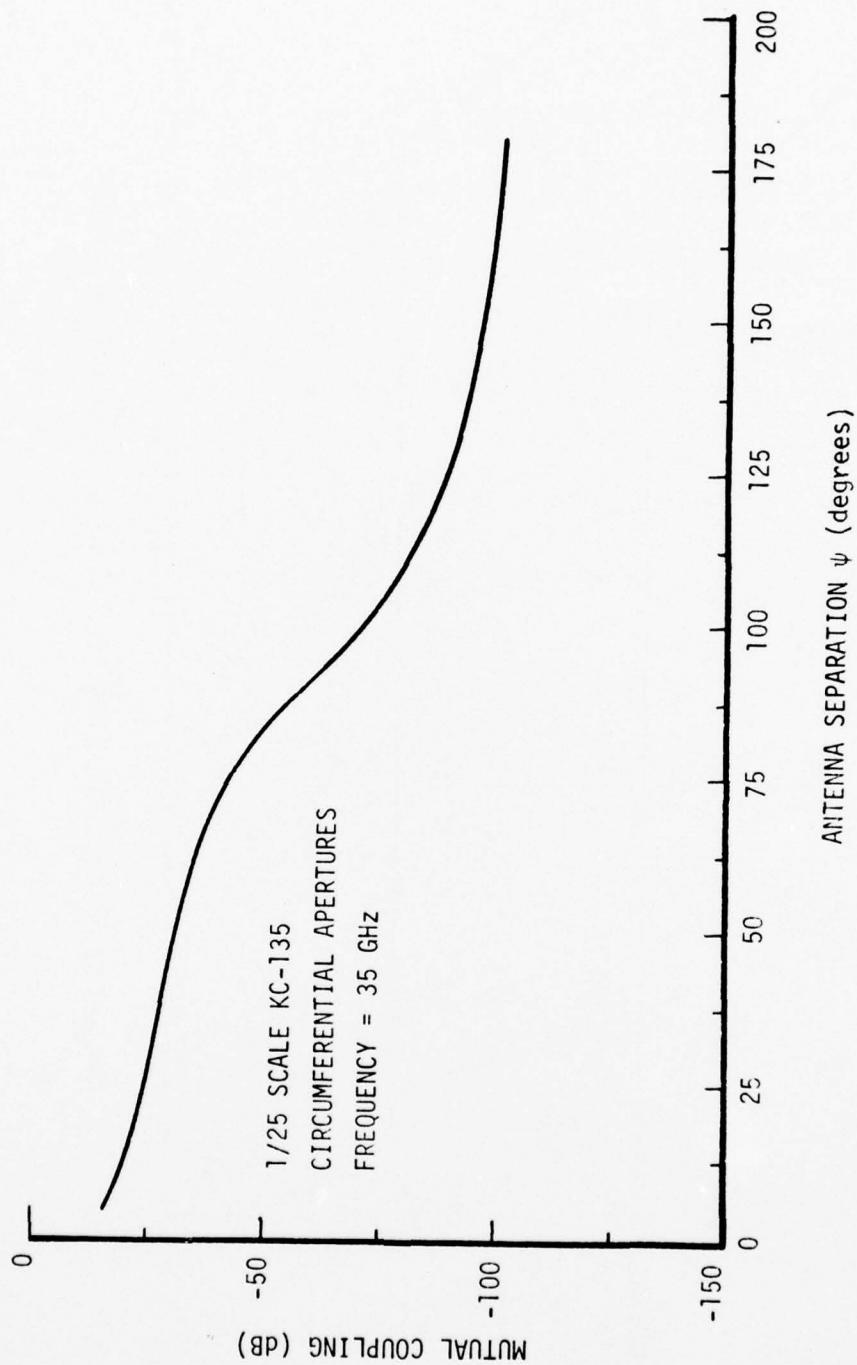


Figure 109. Mutual coupling between two circumferential aperture antennas mounted as shown in Figure 108 (1/25 scale KC-135).

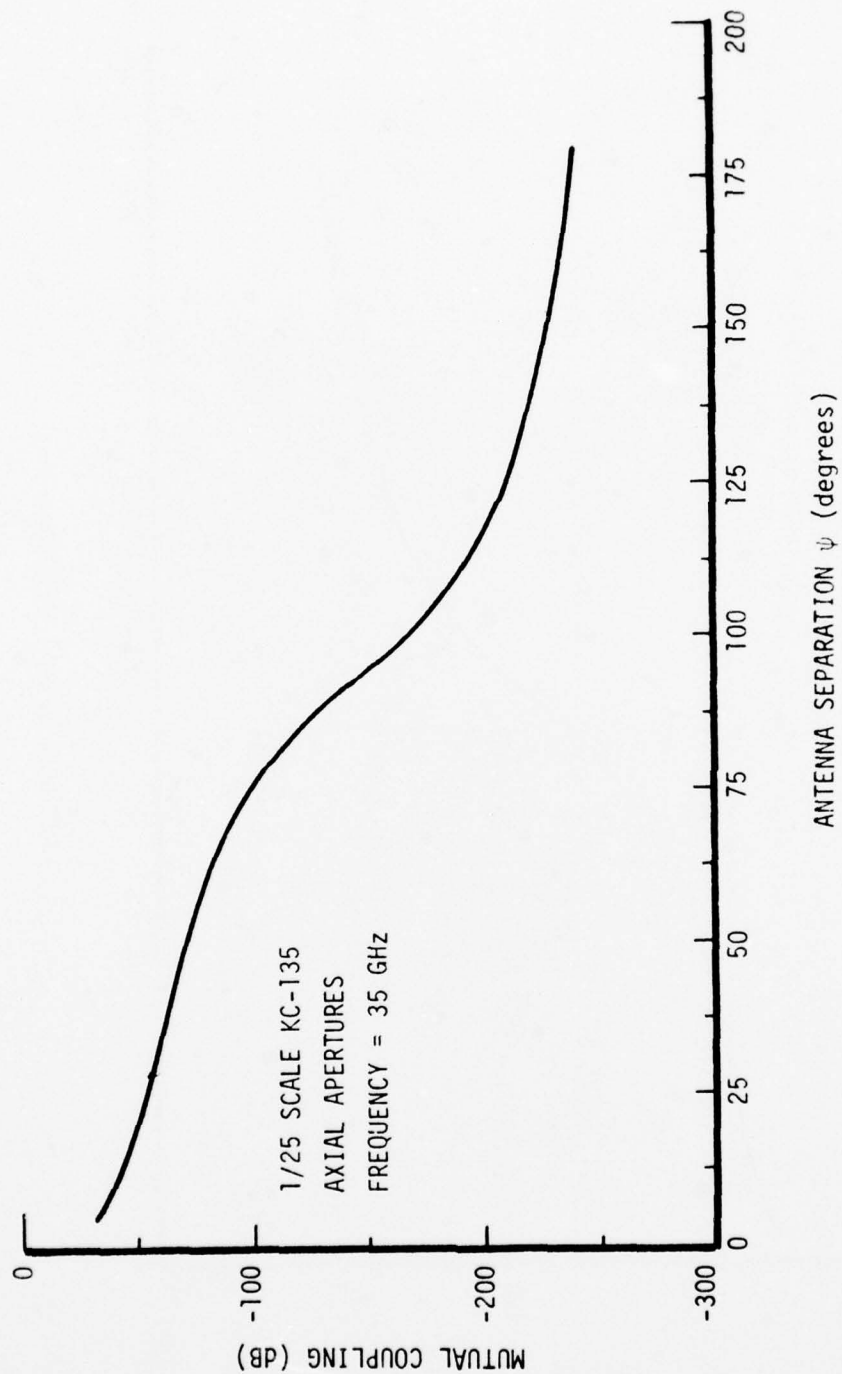


Figure 110. Mutual coupling between two axial aperture antennas mounted as shown in Figure 108 (1/25 scale KC-135).

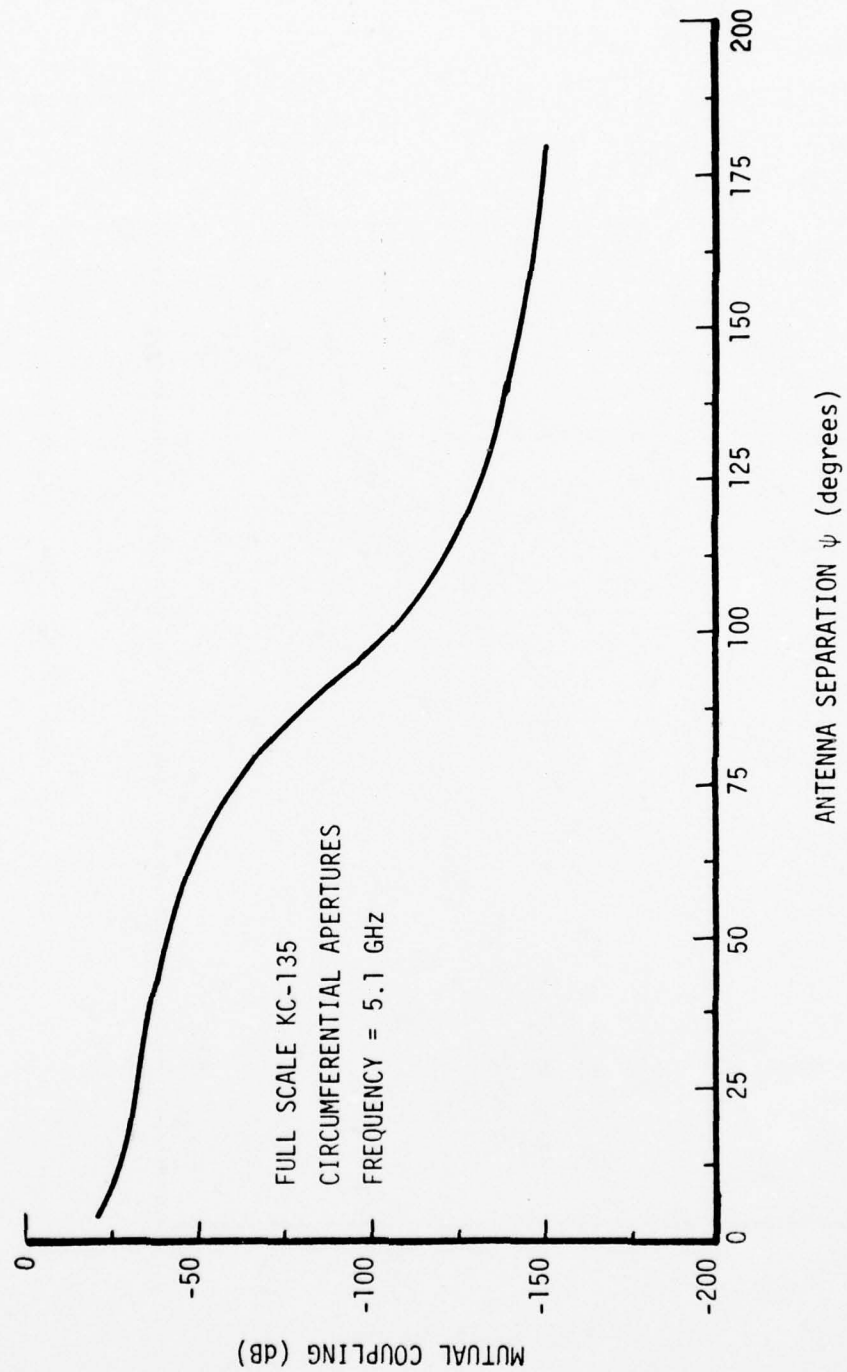


Figure 111. Mutual coupling between two circumferential aperture antennas mounted as shown in Figure 108 (full scale KC-135).

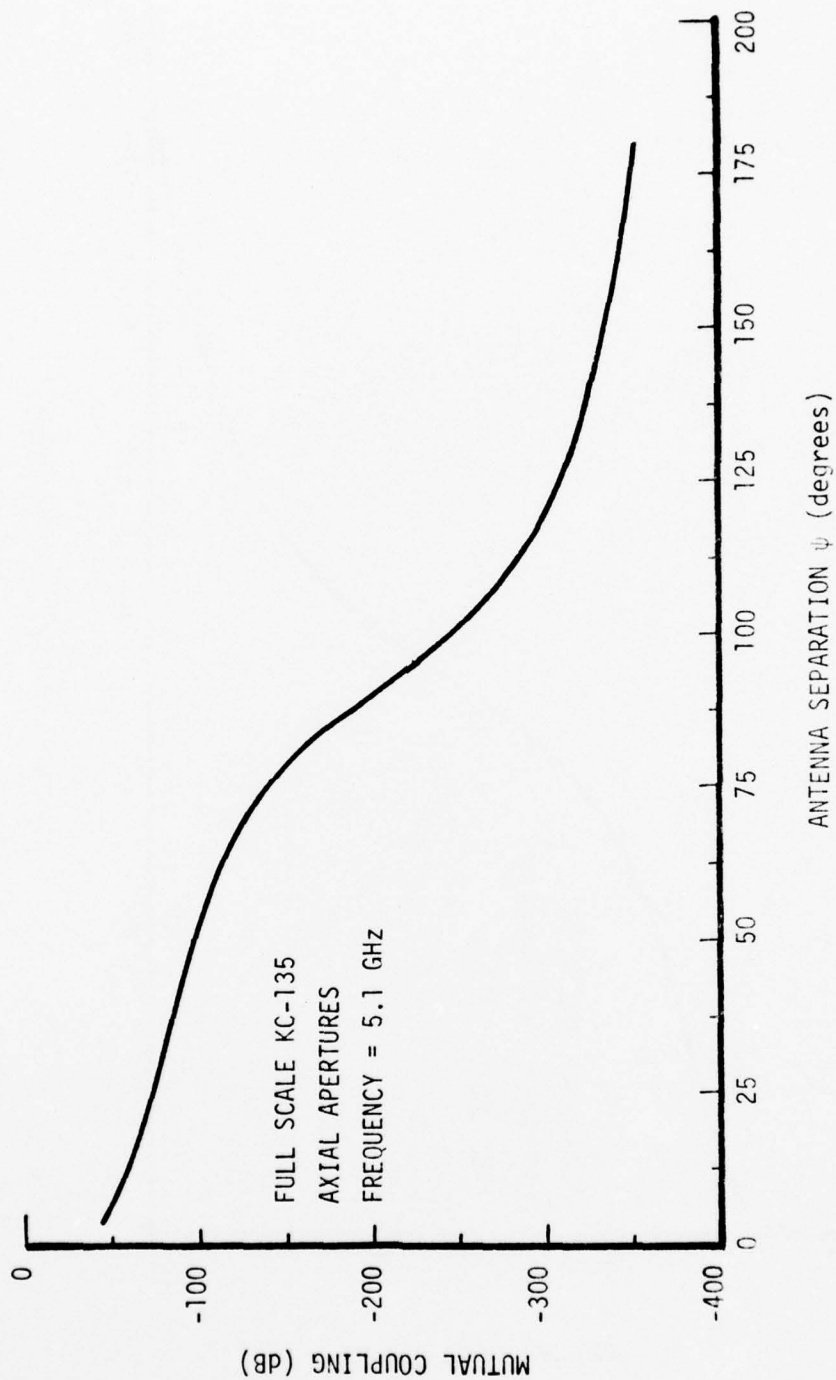


Figure 112. Mutual coupling between two axial aperture antennas mounted as shown in Figure 108 (full scale KC-135).

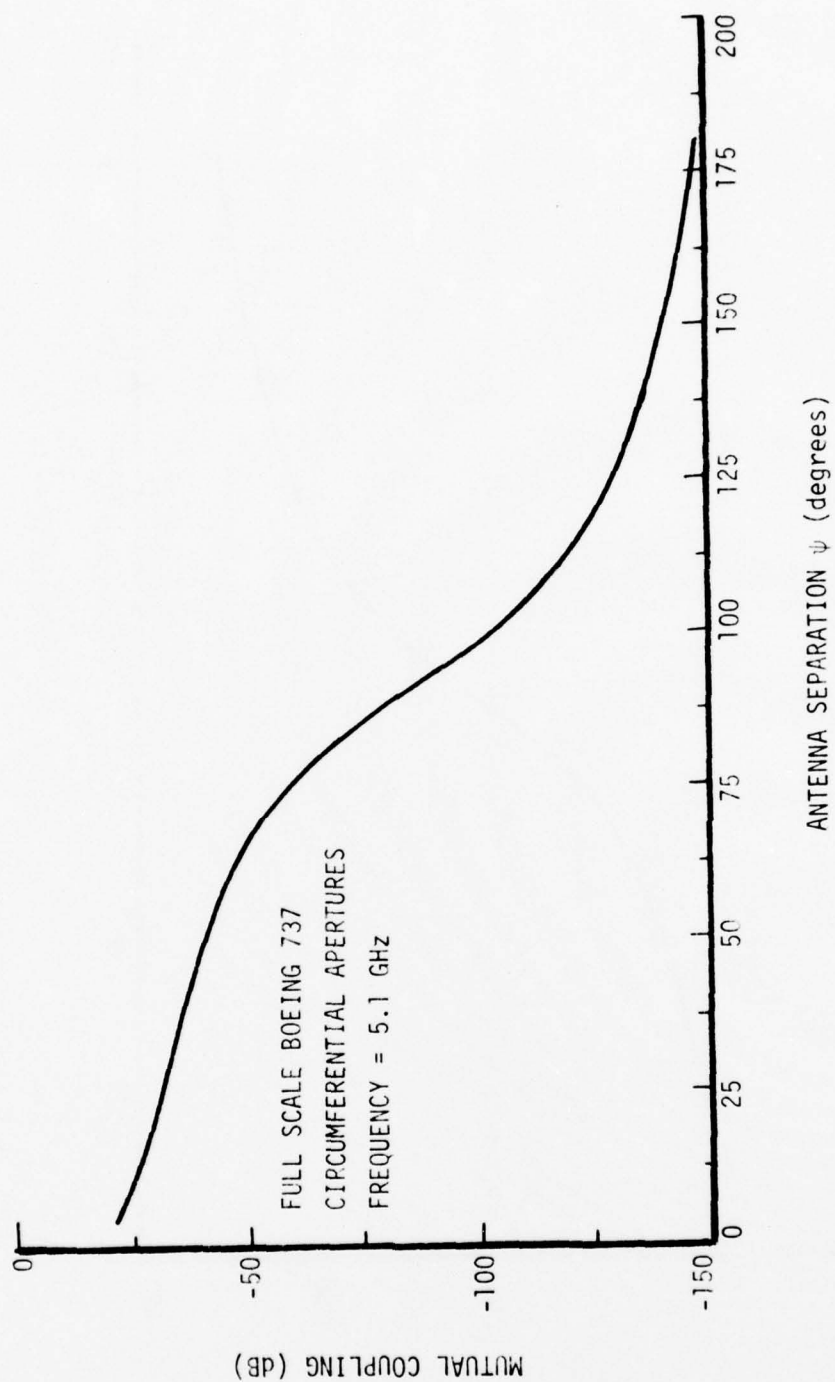


Figure 113. Mutual coupling for two circumferential aperture antennas mounted as shown in Figure 108 (full scale Boeing 737).

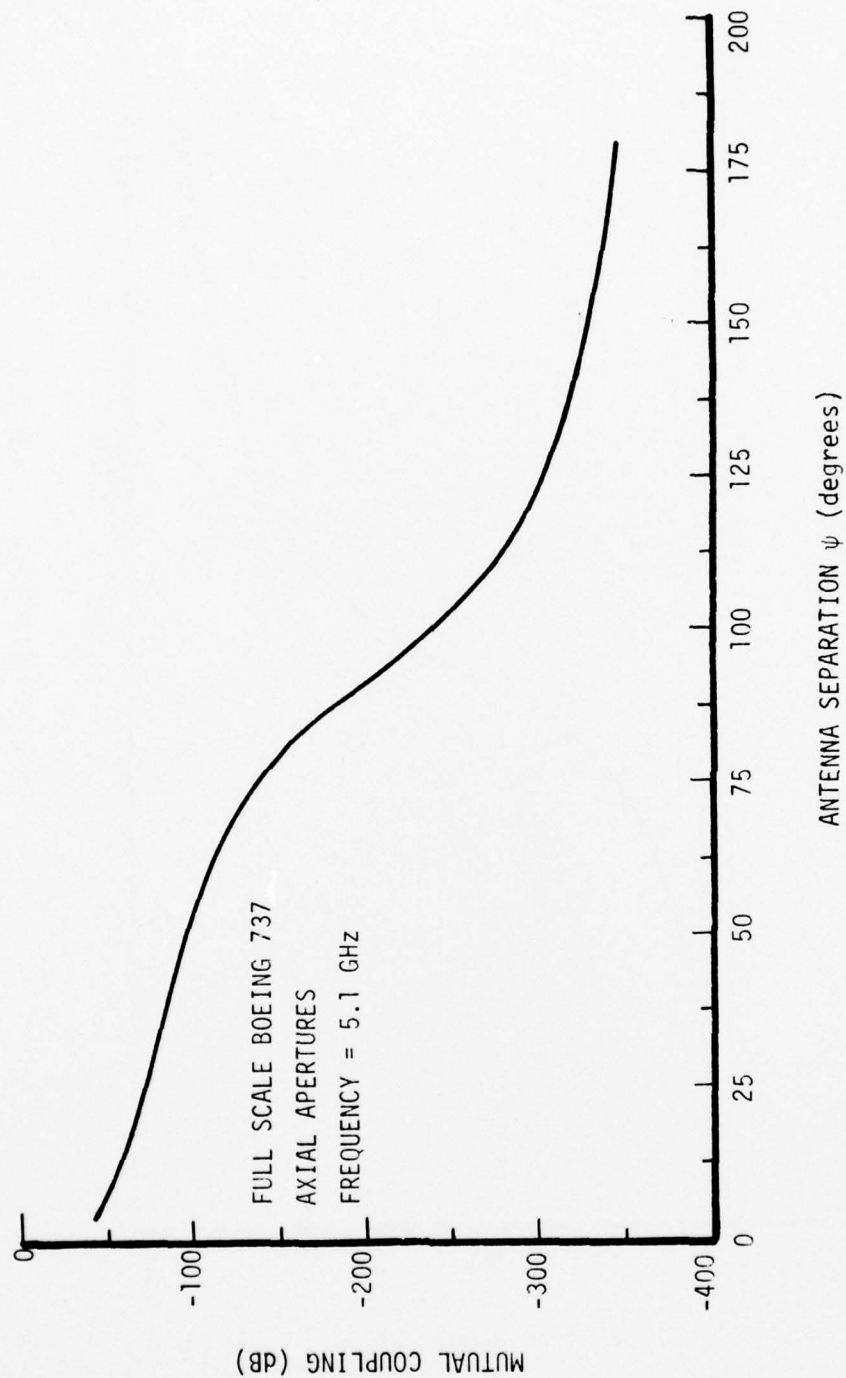


Figure 114. Mutual coupling for two axial aperture antennas mounted as shown in Figure 108 (full scale Boeing 737).

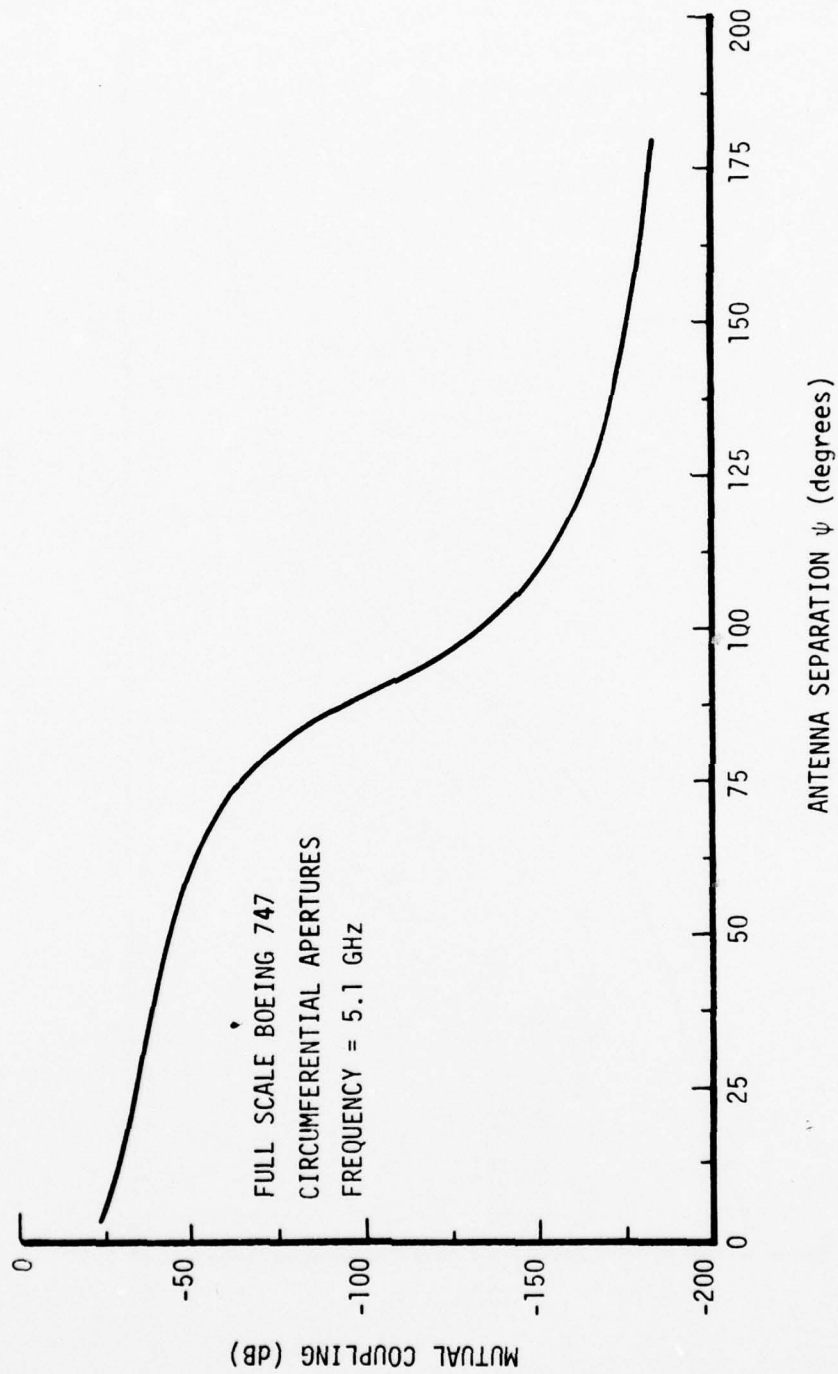


Figure 115. Mutual coupling for two circumferential aperture antennas mounted as shown in Figure 108 (full scale Boeing 747).

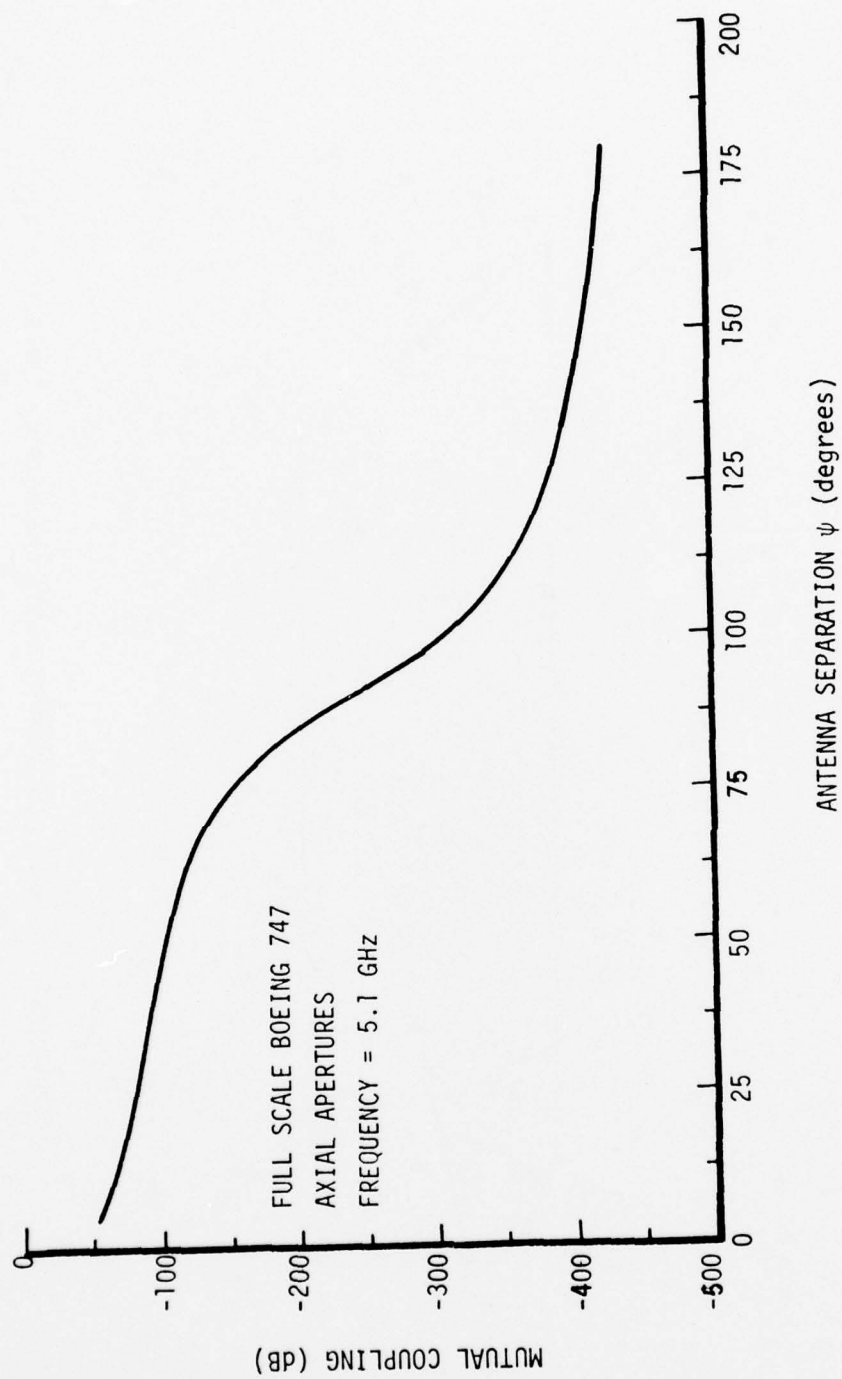


Figure 116. Mutual coupling for two axial aperture antennas mounted as shown in Figure 108 (full scale Boeing 747).

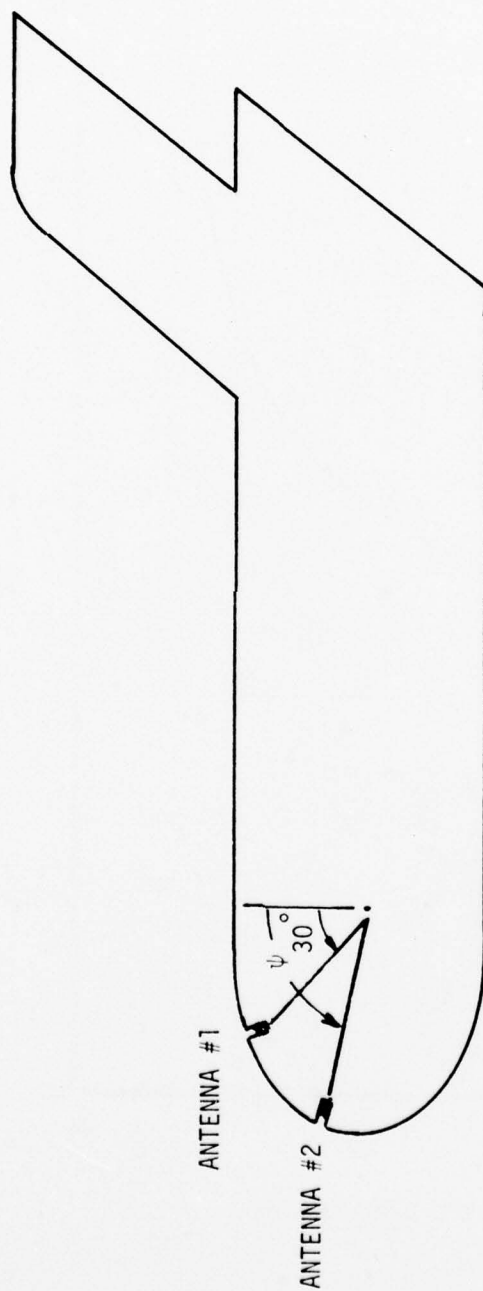


Figure 117. Antenna positioning along the nose of the aircraft.

results for the same airplane configurations, as examined for the other positioning, are shown in Figures 118-125. Again it is clear that coupling between the apertures is very small (below -20 dB) and for axial apertures is usually below -40 dB.

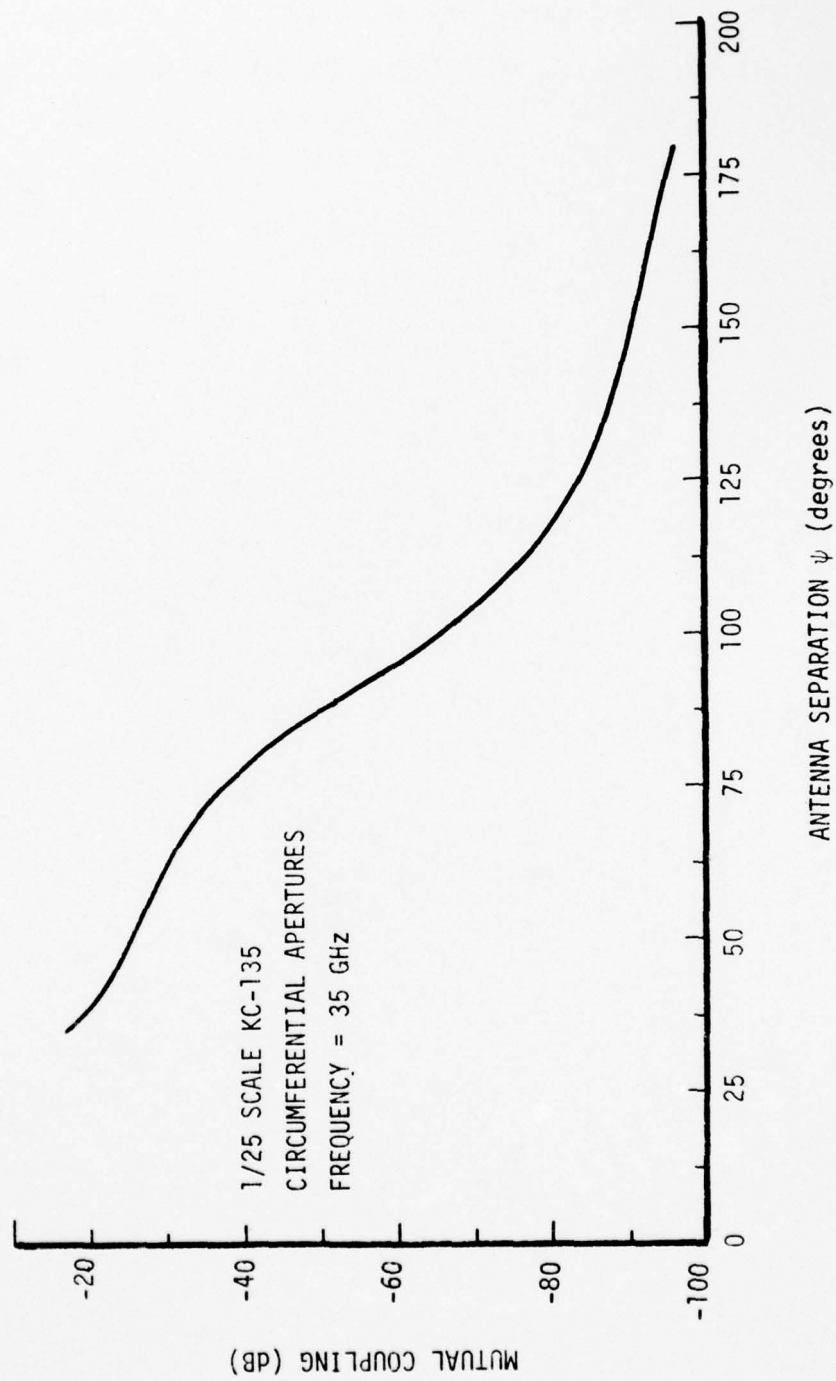


Figure 118. Mutual coupling for two circumferential aperture antennas mounted as shown in Figure 117 (1/25 scale KC-135).

AD-A041 484

WEST VIRGINIA UNIV MORGANTOWN DEPT OF ELECTRICAL ENG--ETC F/G 1/2
AIRCRAFT ANTENNA ANALYSIS AND MICROWAVE LANDING SYSTEM (MLS) AP--ETC(U)
JAN 76 C A BALANIS, Y CHENG DOT-OS-40013

UNCLASSIFIED

FAA-RD-76-37

NL

3 OF 3
ADA
04/484



END

DATE
FILMED
7-77

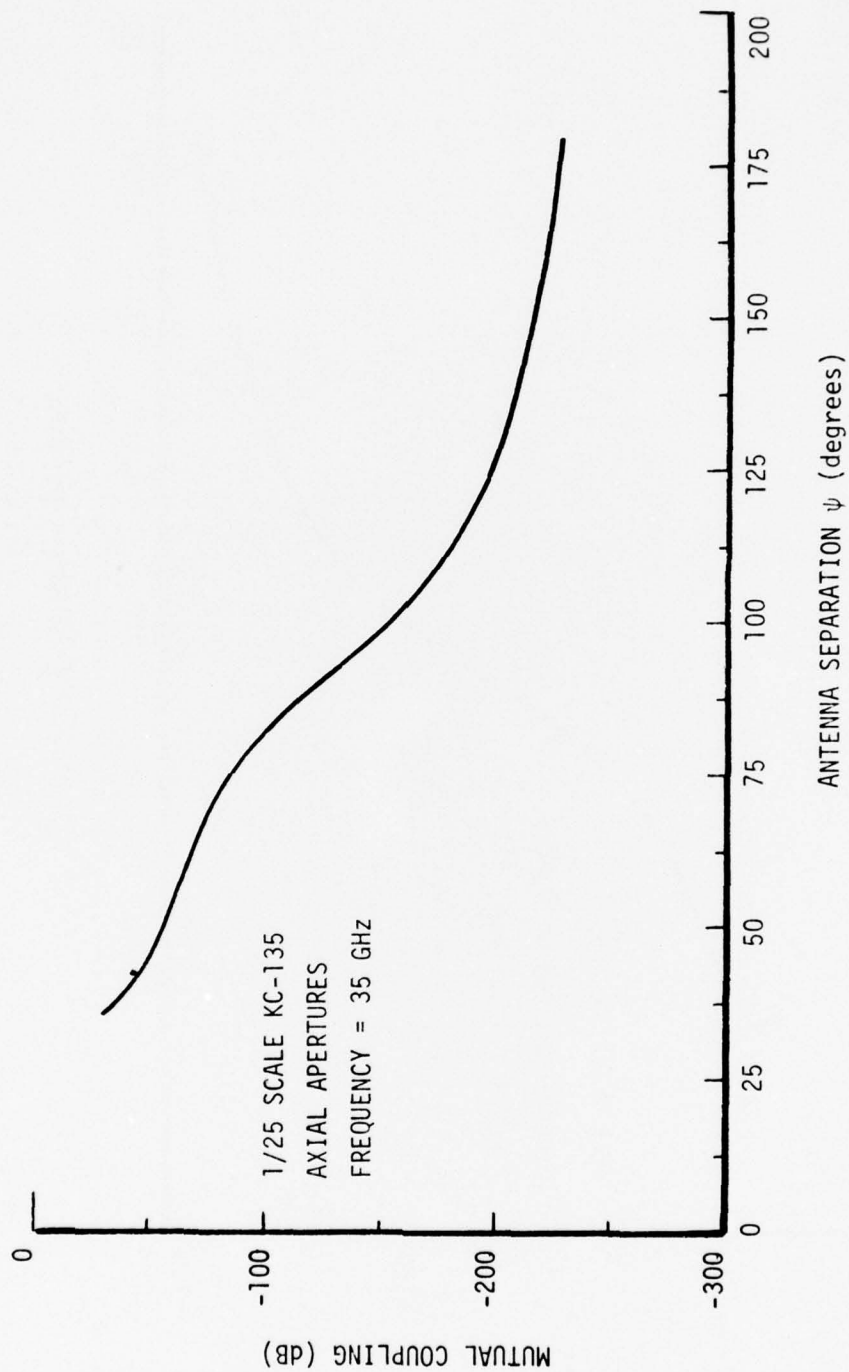


Figure 119. Mutual coupling for two axial aperture antennas mounted as shown in Figure 117(1/25 scale KC-135).

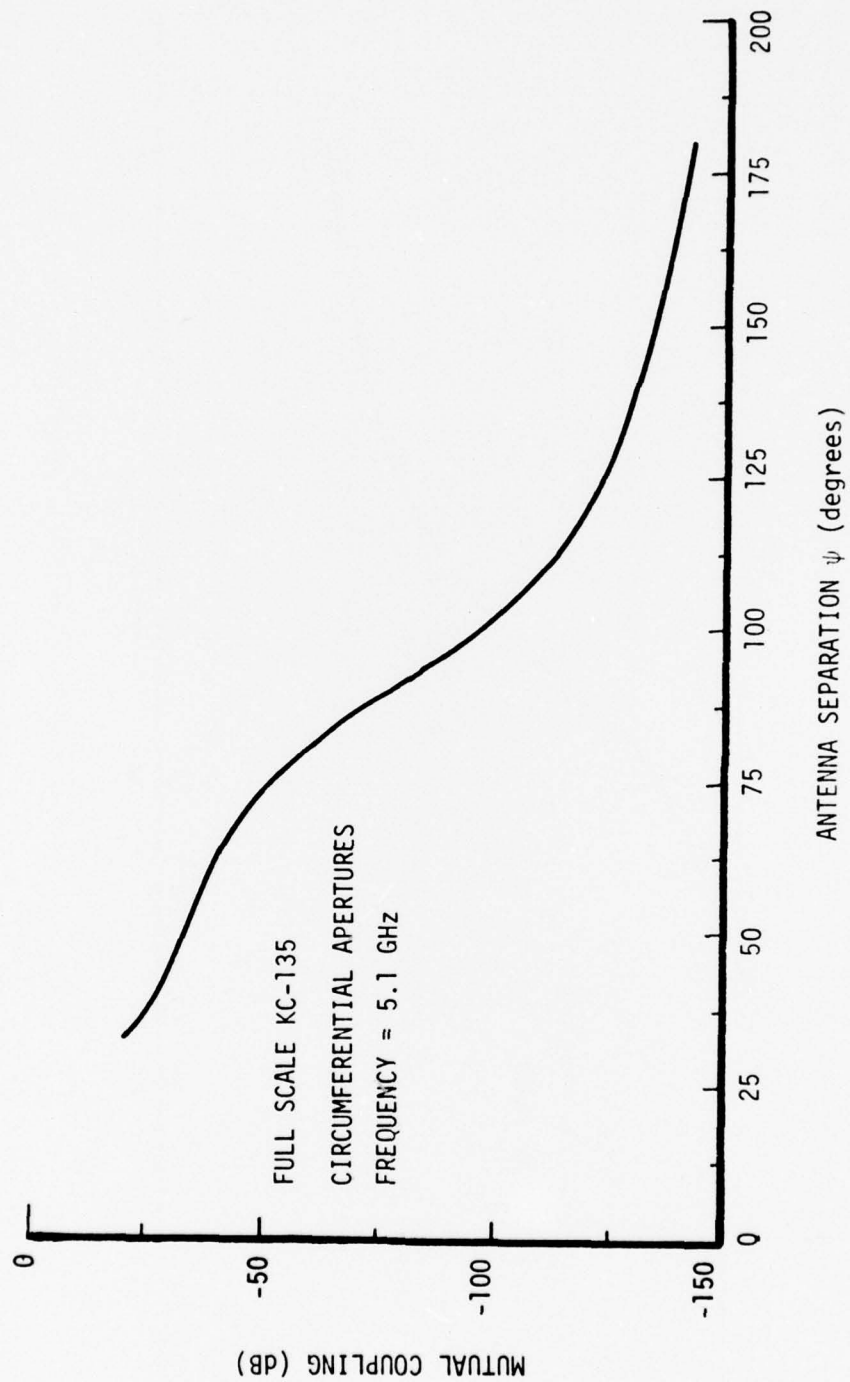


Figure 120. Mutual coupling for two circumferential aperture antennas mounted as shown in Figure 117(full scale KC-135).

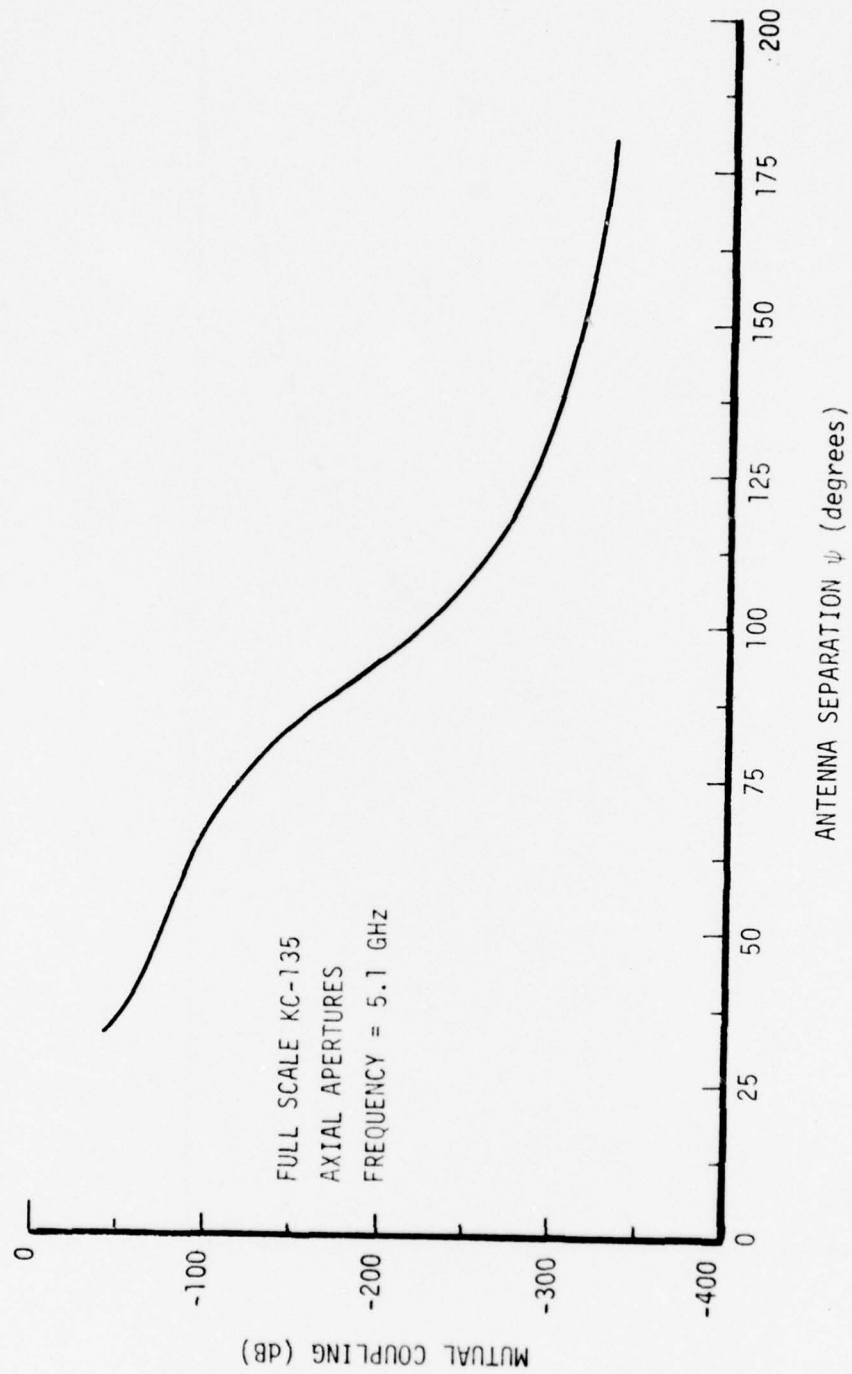


Figure 121. Mutual coupling for two axial aperture antennas mounted as shown in Figure 117(full scale KC-135).

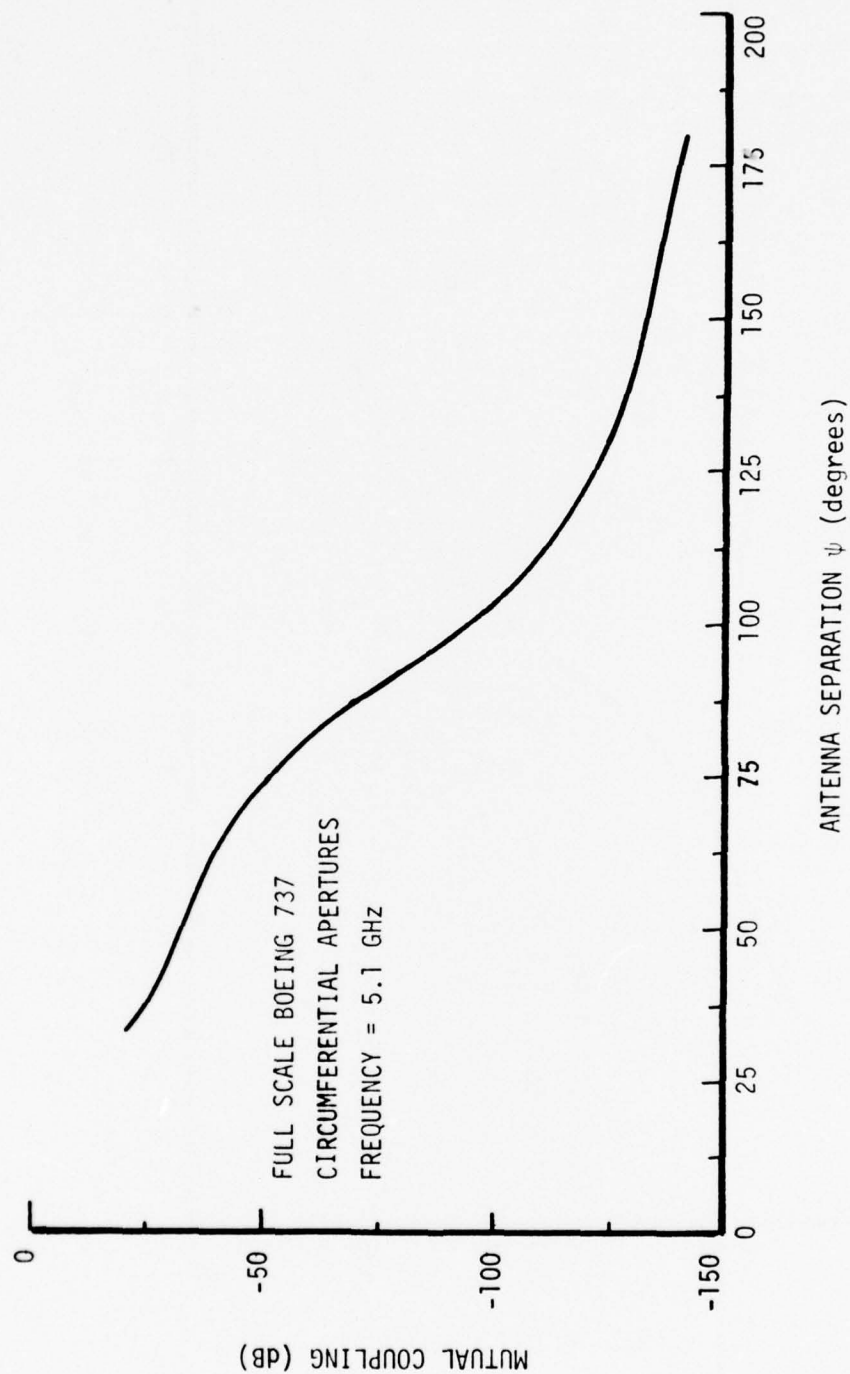


Figure 122. Mutual coupling for two circumferential aperture antennas mounted as shown in Figure 117(full scale Boeing 737).

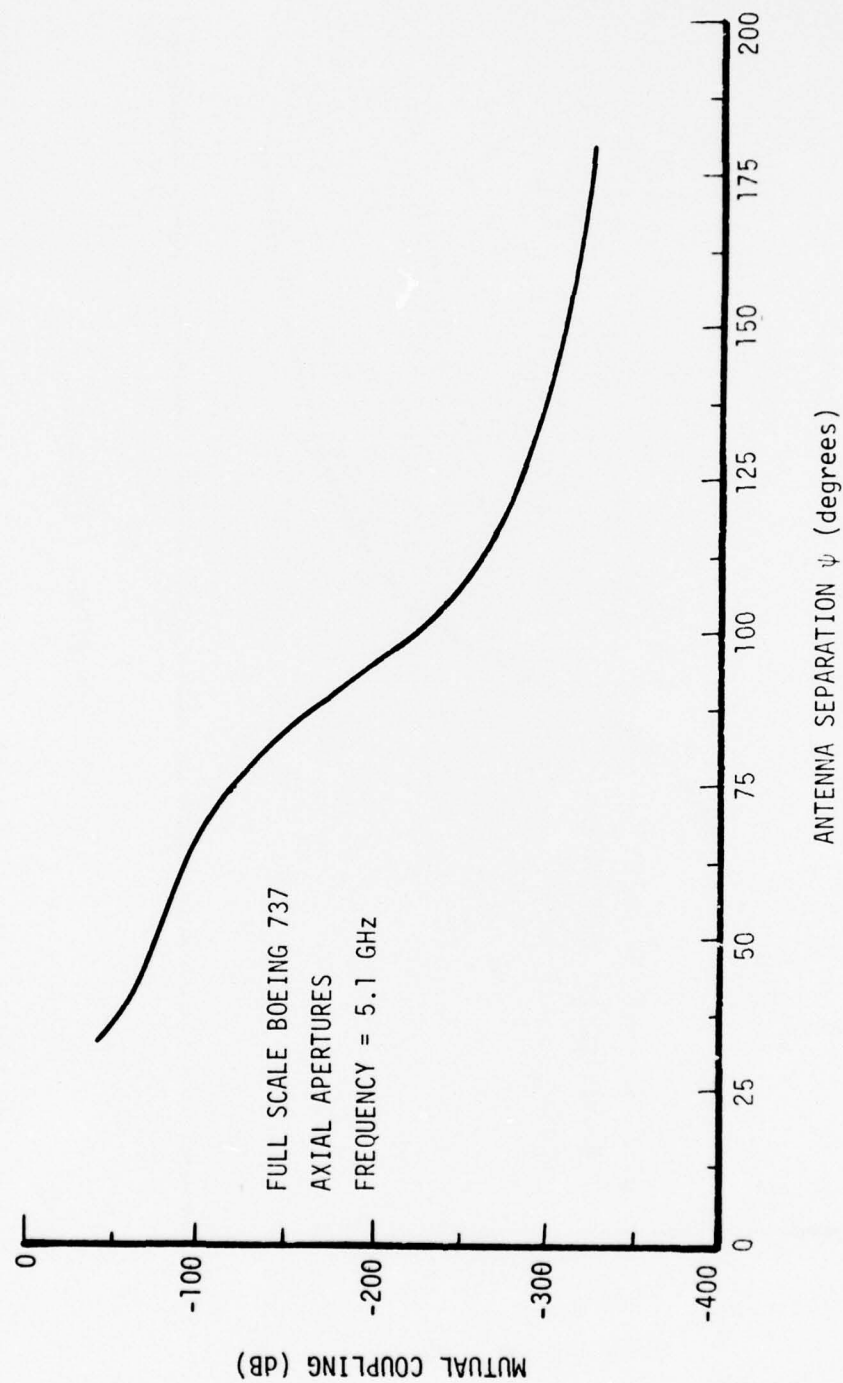


Figure 123. Mutual coupling for two axial aperture antennas mounted as shown in Figure 117 (full scale Boeing 737).

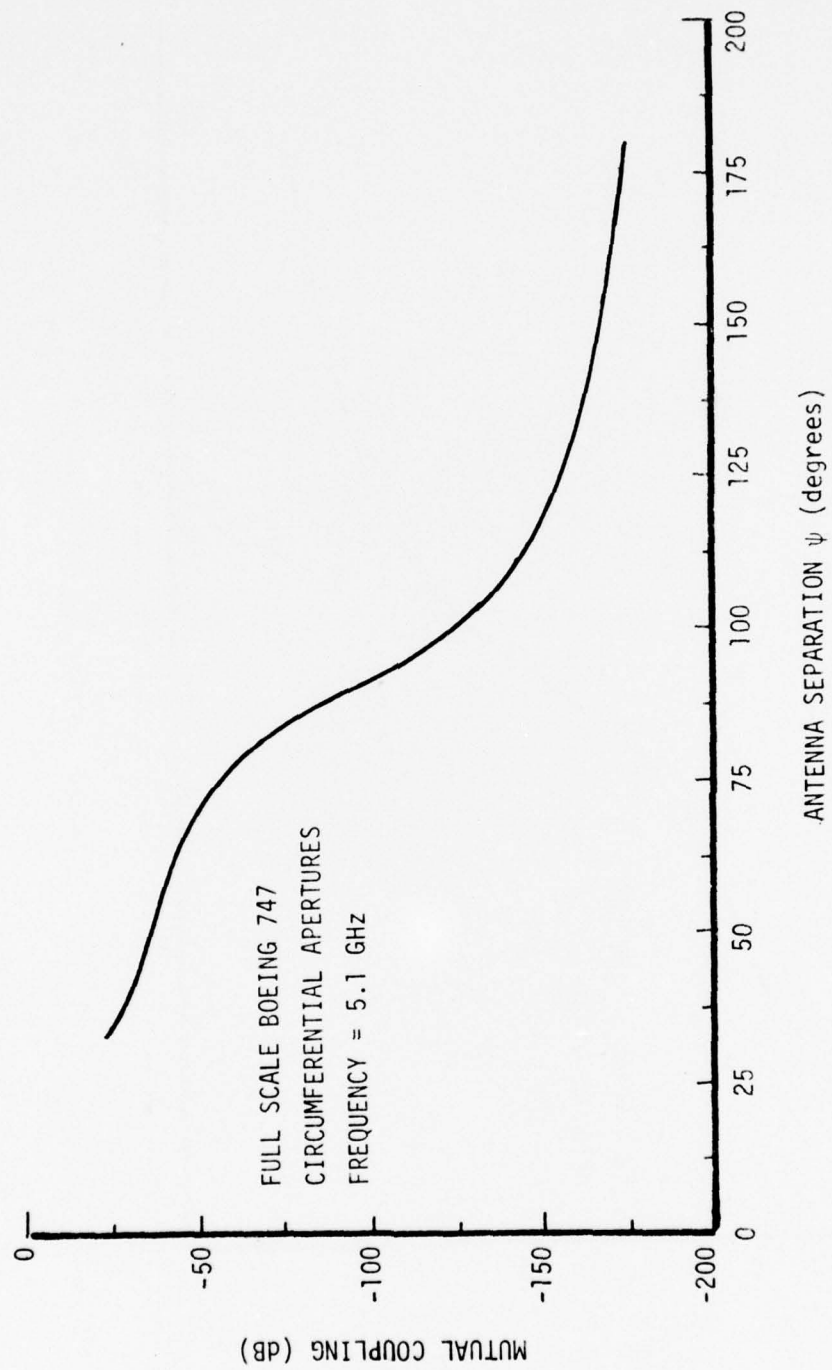


Figure 124. Mutual coupling for two circumferential aperture antennas mounted as shown in Figure 117 (full scale Boeing 747).

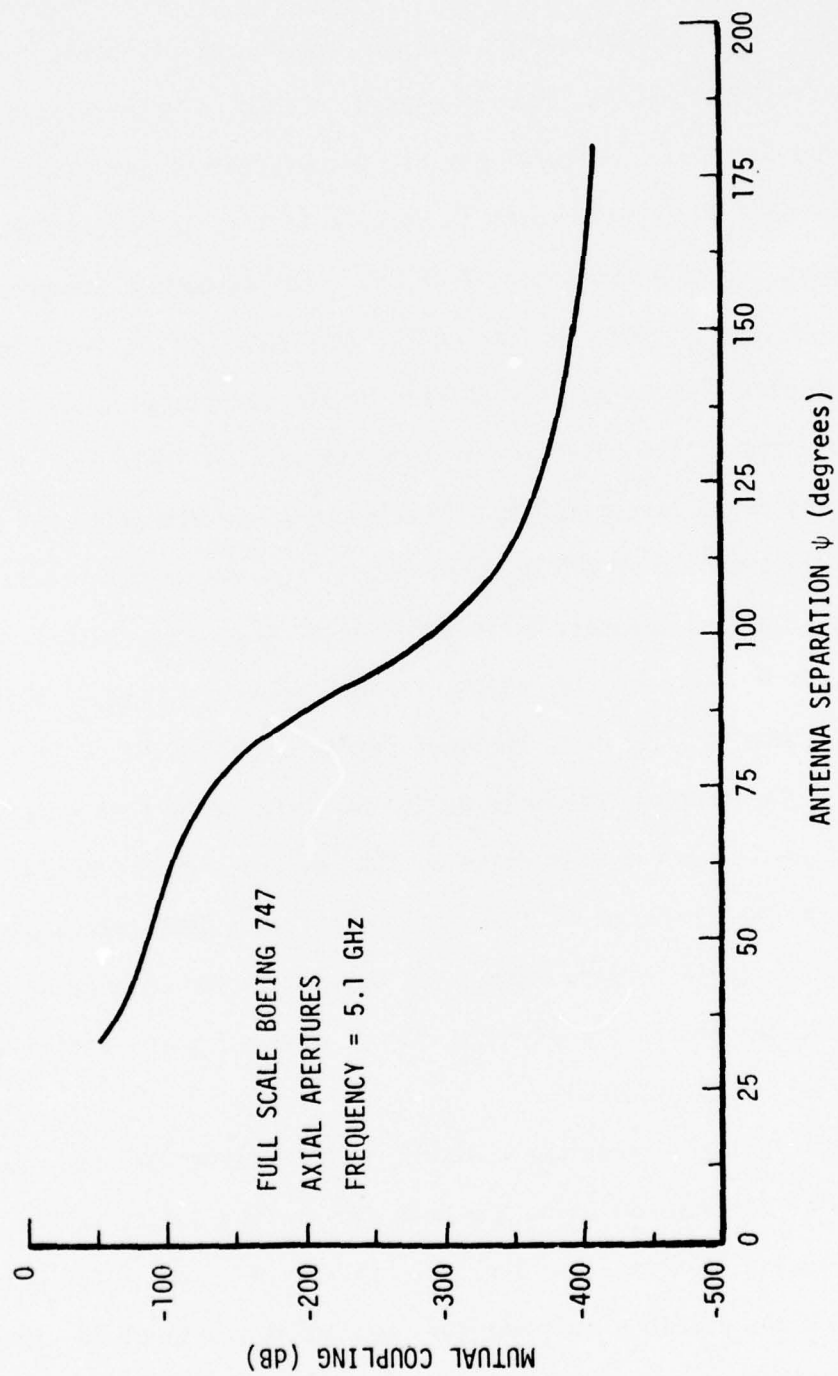


Figure 125. Mutual coupling for two axial aperture antennas mounted as shown in Figure 117 (full scale Boeing 747).

IV. CONCLUSIONS

Analytical radiation models of antennas mounted at different locations on an aircraft structure have been developed. Computed data using these models were compared with measurements of circumferential and axial apertures, and monopoles on a 1/35 scale space shuttle, a 1/11 scale Boeing 737, and a 1/25 scale KC-135 at a frequency of 35 GHz. The agreement between theory and experiment is very good considering the complexity of the problem.

With the availability and versatility of the analytical techniques, radiation coverage of the same type of antennas on full scale Boeing 737, Boeing 747, and KC-135 was examined. The frequency of operation was 5.1 GHz which is within the band of the proposed MLS. From the results it is evident that for flush mounted antennas a circumferential aperture, which is vertically polarized in the elevation plane, located below the nose or above the cockpit of the aircraft exhibits the most promising MLS coverage in the elevation plane. The vertical monopole at the same locations also demonstrates good coverage but is not as attractive as that of the circumferential aperture. From the viewpoint of landing it would seem that antennas mounted above the cockpit would be more attractive because of the absence of any structural features within the airframe during landing, such as landing gear, which would distort the pattern.

Of the aircraft and locations examined in this investigation, placement of an antenna at station 169 below the nose and station 306 above the cockpit on a Boeing 747 exhibited the most attractive coverage for MLS in the elevation plane and it almost met the coverage criteria of 20° above and 30° below the nose. The wider coverage provided by the Boeing 747 is attributed mainly to the steeper slope of the structural profile of the

airplane at the location of the antenna. Further investigation could lead to more attractive locations.

By comparing radiation patterns of antennas mounted on scaled and full scale models, it was concluded that the overall shape of the antenna pattern is mainly controlled by the overall configuration of the airplane and not as much by the electrical dimensions. The overall dimensions do influence the shape of the pattern but to a much lesser degree.

V. ACKNOWLEDGEMENTS

The authors wish to thank Al Stein, Doug Hodgkins, and Still Millington of the MLS Division of FAA for their interest and helpful discussions throughout this project. In addition, the authors would like to express sincere appreciation to M.C.Gilreath and W.F. Croswell of NASA Langley Research Center who made available the measured patterns. Also, we wish to thank Julie Wainstock for her expert typing of the manuscript.

VI. APPENDIX A

DIFFRACTION BY A PERFECTLY CONDUCTING WEDGE

Consider a two-dimensional wedge and a line source to be situated in space as shown in Figure A.1. The faces of the wedge are formed by two semi-infinite intersecting planes. The infinitely long line source is parallel to the edge of the wedge, and its position is described by the coordinate (r_0, θ') . The typical field point is denoted by (r, θ) . The line source is assumed to have unit strength and time dependence of the form $e^{j\omega t}$. The Green's function for this radiating system can be written as³²

$$G = \frac{1}{n} \sum_{m=0}^{\infty} \epsilon_m J_{\frac{m}{n}}(kr) H_{\frac{m}{n}}^{(2)}(kr_0) [\cos \frac{m}{n} (\theta - \theta') \pm \cos \frac{m}{n} (\theta + \theta')] \quad (\text{A-1})$$

if $r_0 > r$. For the case $r_0 < r$, r and r_0 are interchanged. In this expression ϵ_m is the Neumann number which is equal to 1 if m is 0; otherwise it is equal to 2. The plus sign between the two cosine terms is used if the boundary condition is of the homogeneous Neumann type ($\frac{\partial G}{\partial n} = 0$ on both faces of the wedge). For the homogeneous Dirichlet boundary condition ($G = 0$ on both faces of the wedge), the minus sign is used. This convergent series is an exact solution to the time harmonic, inhomogeneous wave equation for the problem of a radiating line source and wedge embedded in a linear, isotropic, homogeneous, lossless medium.

Many times it is necessary to determine the total radiation field when the line source is far removed from the vertex of the wedge. In such cases, Equation (A-1) can be simplified by replacing the Hankel function by the first term of its asymptotic expansion, that is by the relation

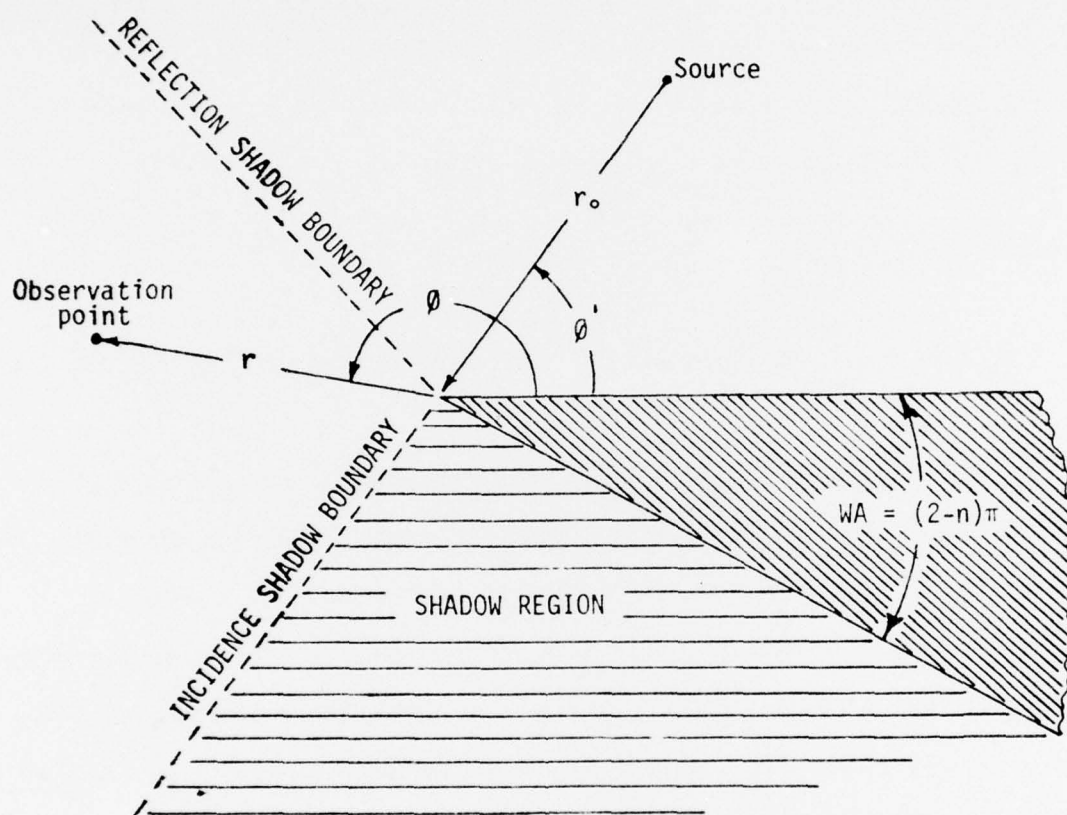


Figure A.1. Two-dimensional wedge and region separation.

$$H_{\frac{m}{n}}^{(2)}(kr_0) \sim \sqrt{\frac{2}{\pi kr_0}} e^{-j(kr_0 - \frac{\pi}{4} - \frac{m}{n} \frac{\pi}{2})} \quad (A-2)$$

This substitution reduces G to the form

$$\begin{aligned} G &= \sqrt{\frac{2}{\pi kr_0}} e^{-j(kr_0 - \frac{\pi}{4})} \frac{1}{n} \sum_{m=0}^{\infty} \epsilon_m J_{\frac{m}{n}}(kr) e^{+j\frac{m}{n} \frac{\pi}{2}} [\cos \frac{m}{n}(\theta - \theta') \pm \cos \frac{m}{n}(\theta + \theta')] \\ &= \sqrt{\frac{2}{\pi kr_0}} e^{-j(kr_0 - \frac{\pi}{4})} E \end{aligned} \quad (A-3)$$

where

$$E = E_D + E_G = \frac{1}{n} \sum_{m=0}^{\infty} \epsilon_m J_{\frac{m}{n}}(kr) e^{j\frac{m}{n} \frac{\pi}{2}} [\cos \frac{m}{n}(\theta - \theta') \pm \cos \frac{m}{n}(\theta + \theta')] \quad (A-4)$$

with E_D and E_G being the total diffracted and geometrical optics fields, respectively, and E , the series form of the Green's function describing the total field created by the diffraction of a plane wave by a wedge.

An asymptotic expansion for E in inverse powers of kr is very useful for computational purposes, because of the slow convergence of Equation (A-4) for large values of kr . In order to derive an asymptotic expression for E by the standard method of steepest descents, it must first be transformed into an integral or integrals of the form

$$\int_c F(z) e^{kr f(z)} dz \quad (A-5)$$

and then evaluated for large kr by means of the method of steepest descents. Such a procedure leads to the expression for the diffracted field for a plane

wave incident on a wedge of included angle $(2 - n)\pi$ to be²¹

$$E_D(r, \theta, \theta', n) = V_B(r, \theta - \theta', n) \pm V_B(r, \theta + \theta', n) \quad (A-6)$$

where the plus sign applies for the polarization of the electric field perpendicular to the edge

$$\left(\frac{\partial E}{\partial n}\right)_{\text{wedge}} = 0 \quad (A-7)$$

and the minus sign applies for polarization parallel to the edge

$$E_{\text{wedge}} = 0 \quad (A-8)$$

The geometrical optics field is given by

$$E_G(\text{g.o.}) = \begin{cases} e^{jkr \cos(\theta - \theta')} \pm e^{jkr \cos(\theta + \theta')} & 0 < \theta < \pi - \theta' \\ e^{jkr \cos(\theta - \theta')} & \pi - \theta' < \theta < \pi + \theta' \\ 0 & \pi + \theta' < \theta < 2\pi - \theta' \end{cases} \quad (A-9)$$

The wedge-diffraction function $V_B(r, \theta \mp \theta', n)$ for a plane wave has also been determined^{19,21} and can be written as

$$V_B(r, \theta \mp \theta', n) = I_{-\pi}(r, \theta \mp \theta', n) + I_{+\pi}(r, \theta \mp \theta', n) \quad (A-10)$$

where

$$I_{\pm\pi}(r, \theta \mp \theta', n) \sim \frac{e^{-j(kr + \frac{\pi}{4})}}{jn\sqrt{2\pi}} \sqrt{g} \cot \frac{\pi \pm (\theta \mp \theta')}{2n} e^{jkr} \int_{\sqrt{kr}g}^{\infty} \frac{e^{-j\tau^2}}{\sqrt{kr}g} d\tau + \text{Higher-order terms} \quad (A-11)$$

$$g = 1 + [\cos(\theta \pm \theta') - 2n\pi N] \quad (\text{A-12})$$

and N is a positive or negative integer or zero which most nearly satisfies the equation

$$\begin{aligned} 2n\pi N - (\theta \pm \theta') &= -\pi & (\text{for } I_{-\pi}) \\ 2n\pi N - (\theta \pm \theta') &= +\pi & (\text{for } I_{+\pi}) \end{aligned} \quad (\text{A-13})$$

Equation (A-11) contains the leading terms plus higher-order terms which are negligible for large values of kr . For large values of kr , Equation (A-10) reduces to the form presented by Pauli¹⁹ and given by

$$v_B(r, \theta \pm \theta', n) = \frac{e^{-j(kr + \frac{\pi}{4})}}{\sqrt{2\pi kr}} \frac{\frac{1}{n} \sin \frac{\pi}{n}}{\cos \frac{\pi}{n} - \cos \frac{\theta \pm \theta'}{n}} + \dots \quad (\text{A-14})$$

The diffracted field of Equation (A-14) is that from which the asymptotic diffraction coefficients of the geometrical theory of diffraction are obtained.⁵ This expression is not valid in the shadow boundary because $g = 0$ there.

VII. APPENDIX B

DYADIC DIFFRACTION FUNCTION BY A CONDUCTING WEDGE

Consider a conducting wedge of included angle $(2-n)\pi$ with a source positioned at a point O. Defining a ray-fixed coordinate system,¹⁶ (s, β_0, θ) for the source point and (s, β_0, θ) for the observation point as shown in Figure B.1, in contrast to the edge-fixed coordinate system $(\rho, \theta, z; \rho, \theta, z)$, the diffracted field observed at point P can be written as¹⁶

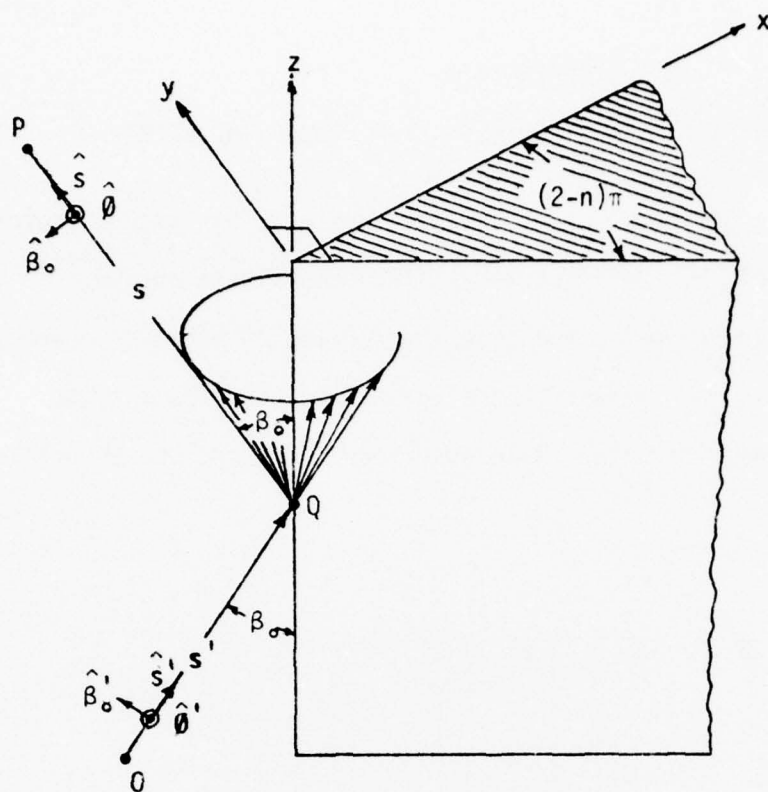
$$\begin{bmatrix} E_{||}^d(s) \\ E_{\perp}^d(s) \end{bmatrix} = - \begin{bmatrix} v_B^S & 0 \\ 0 & v_B^h \end{bmatrix} \begin{bmatrix} E_{||}^i(Q) \\ E_{\perp}^i(Q) \end{bmatrix} \frac{\sqrt{L} e^{+jkl}}{\sin \beta_0} A(s) e^{-jks} \quad (B-1)$$

where $E_{||}^i(\theta)$ is the component of E-field parallel to the plane of incidence and $E_{\perp}^i(Q)$ the perpendicular component and are defined by

$$\begin{aligned} \text{where} \quad E_{||}^i(Q) &= \hat{\beta}_0' \cdot \underline{E}_i \\ E_{\perp}^i(Q) &= \hat{\theta}' \cdot \underline{E}_i \end{aligned} \quad (B-2)$$

The corresponding diffracted components are denoted by $E_{||}^d(s)$ and $E_{\perp}^d(s)$. The diffraction functions v_B^S and v_B^h for soft and hard polarization are related to the diffraction function of (A-10) by

$$\begin{aligned} v_B^S &= v_B(L, \theta - \theta', n) - v_B(L, \theta + \theta', n) \\ v_B^h &= v_B(L, \theta - \theta', n) + v_B(L, \theta + \theta', n) \end{aligned} \quad (B-3)$$



$$\begin{aligned}\hat{s}' &= \hat{\beta}_0' \times \hat{\phi}' \\ \hat{s} &= \hat{\beta}_0 \times \hat{\phi}\end{aligned}$$

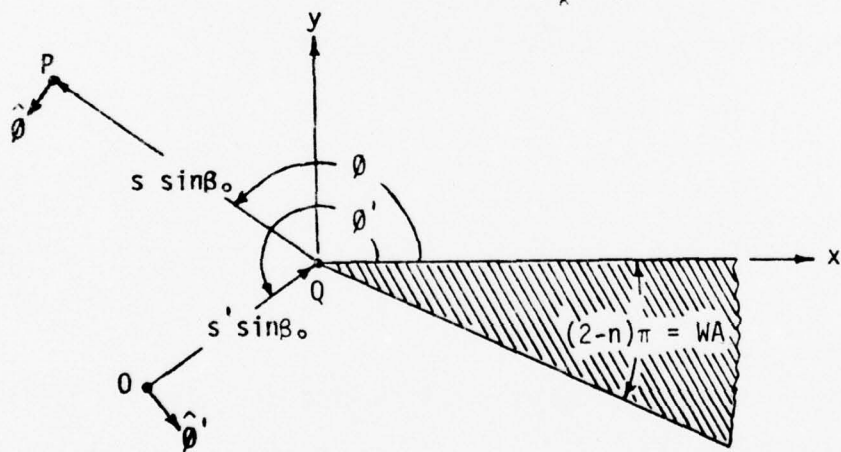


Figure B.1. Oblique wave incidence diffraction by a two-dimensional wedge.

where the distance parameter L is defined by

$$L = \begin{cases} s \sin^2 \beta_0 & \text{plane wave incidence} \\ \frac{\rho \rho'}{\rho + \rho'} & \text{cylindrical wave incidence} \\ \frac{ss' \sin^2 \beta_0}{s + s'} & \text{conical and spherical wave incidence} \end{cases} \quad (\text{B-4})$$

and the spatial attenuation $A(s)$, which describes how the field intensity varies along the diffracted ray, by

$$A(s) = \begin{cases} \frac{1}{\sqrt{s}} & \text{plane, cylindrical, and conical wave incidence} \\ \sqrt{\frac{s'}{s(s' + s)}} & \text{spherical wave incidence} \end{cases} \quad (\text{B-5})$$

If the observations are made in the far-field ($s \gg s'$ and $\rho \gg \rho'$), the distance parameter and spatial attenuation factor reduce to

$$L = \begin{cases} s \sin^2 \beta_0 & \text{plane wave incidence} \\ \rho' & \text{cylindrical wave incidence} \\ s' \sin^2 \beta_0 & \text{conical and spherical wave incidence} \end{cases} \quad (\text{B-6})$$

$$A(s) = \begin{cases} \frac{1}{\sqrt{s}} & \text{plane, cylindrical, and conical wave incidence} \\ \frac{\sqrt{s'}}{s} & \text{spherical wave incidence} \end{cases} \quad (\text{B-7})$$

For normal incidence $\beta_0 = \pi/2$.

If the edge of the wedge is curved, as shown in Figure B.2, the only modification is to redefine the spatial factor of (B-1) as

FOR CURVED EDGE

$$A(s) = \sqrt{\frac{\rho_c}{s(\rho_c + s)}} \quad (\text{B-8})$$

$$\frac{1}{\rho_c} = \frac{1}{\rho_e} - \frac{\hat{n} \cdot (\hat{s}' - \hat{s})}{\rho_g \sin^2 \beta_0} \quad (\text{B-9})$$

where ρ_c = distance between caustic at edge and second caustic of diffracted ray

ρ_e = radius of curvature of incidence wavefront (infinite for plane, cylindrical, and conical waves; $\rho_e = s'$ for spherical waves)

ρ_g = radius of curvature of edge at diffraction point

\hat{n} = unit vector normal to edge

\hat{s}' = unit vector in direction of incidence

\hat{s} = unit vector in direction of diffraction

β_0 = angle between \hat{s}' and tangent to the edge at point of diffraction

For $s \gg \rho_c$ it reduces to

$$A(s) = \frac{\sqrt{\rho_c}}{s} \quad (\text{B-10})$$

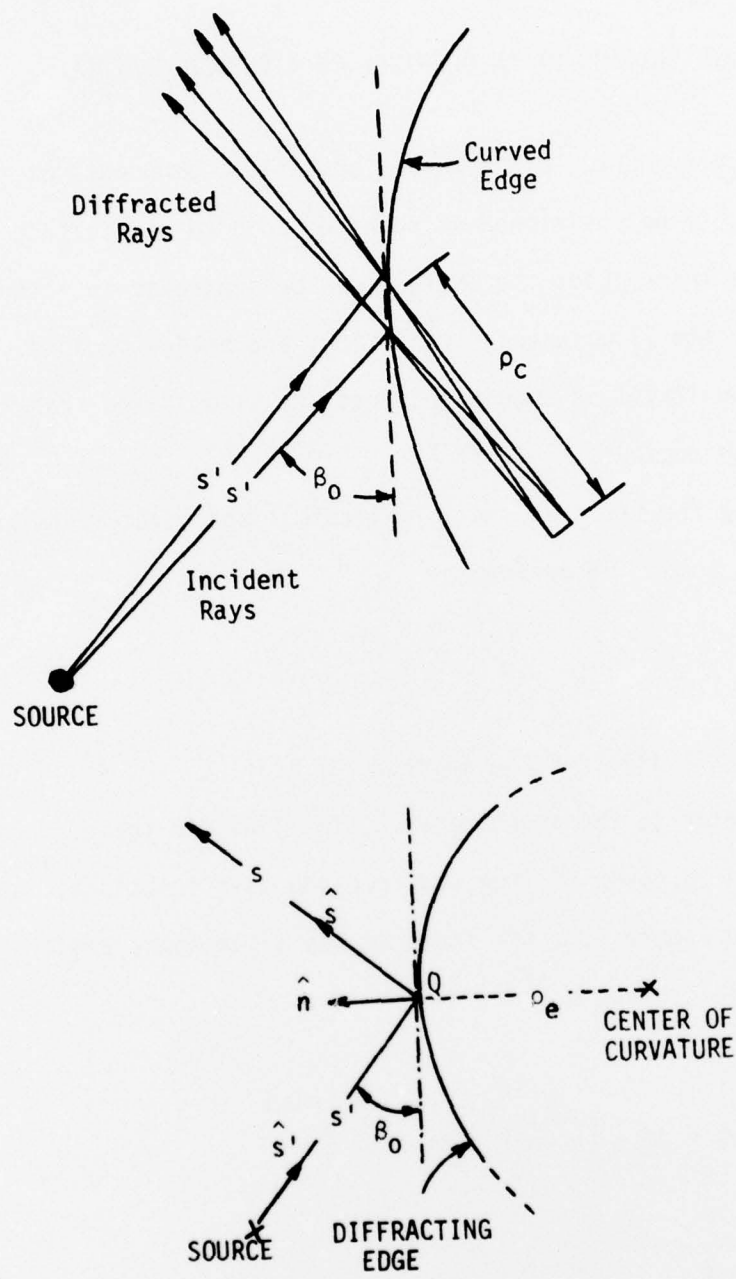


Figure B.2. Oblique wave incidence diffraction by a two-dimensional wedge with curved edge.

VIII. APPENDIX C

DIFFRACTION BY AN APERTURE ON A CURVED SURFACE

Consider a very narrow slot, whose tangential components of the electric field are known, to be positioned at point Q' on a curved surface as shown in Figure C.1. The space about the surface can be separated into three distinct regions; namely, the illuminated, transition, and shadow regions. The transition region itself is subdivided into the illuminated transition and shadow transition regions.

Representing the field at the infinitesimal aperture ds' by an infinitesimal magnetic moment $d\mathbf{M}$ defined by

$$d\mathbf{M}(Q') = \mathbf{M}_s(Q') ds' = -\hat{n}' \times \mathbf{E}(Q') ds' \quad (C-1)$$

where $\mathbf{E}(Q')$ is the E-field of the aperture at point Q' and \hat{n}' is the outward directed unit vector to the aperture at Q' , the field in the different regions can be formulated in terms of Fock and creeping wave functions.¹⁵

Referring to Figure C.2, the field in the illuminated region $[0 < \theta < \pi/2 - \Delta]$ is given by¹⁵

$$\mathbf{E}(p) = d\mathbf{M} \cdot [\hat{b}' \hat{n} F + \hat{t}' \hat{b} G] \frac{e^{-jks}}{s}$$

$$F = 2 \quad (C-2)$$

$$G = 2 \cos \theta$$

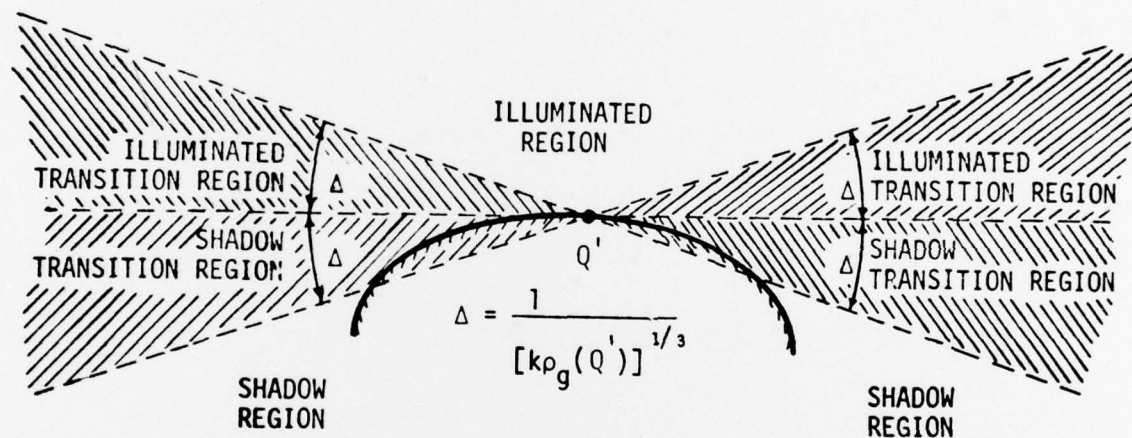


Figure C.1. Region separation for wave diffraction of an aperture on a curved surface.

ILLUMINATED REGION $[0 \leq \theta \leq \frac{\pi}{2} - \Delta]$

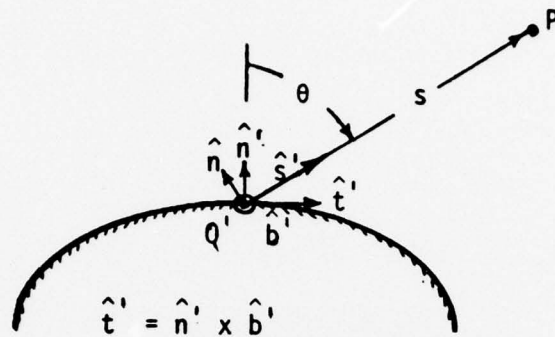


Figure C.2. Geometry for illuminated region radiation by an aperture on a curved surface.

ILLUMINATED TRANSITION REGION $(\frac{\pi}{2} - \Delta \leq \theta < \frac{\pi}{2})$

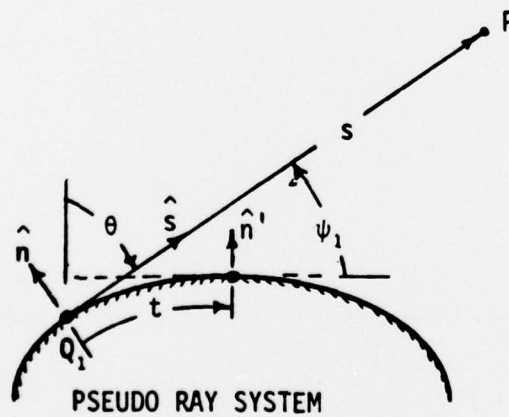


Figure C.3. Geometry for illuminated transition region radiation by an aperture on a curved surface.

where the F function is used to represent an axial slot on a cylindrical surface and the G function a circumferential slot. In the illuminated transition region $[\pi/2 - \Delta \leq \theta \leq \pi/2]$, a pseudo ray system has to be introduced,¹⁵ as shown in Figure C.3, and the fields are given by (C-2) with the F and G functions defined by

$$F = g(\xi) e^{-jkt} \quad \text{where } t, \xi < 0 \quad (C-3)$$

$$G = -j \left[\frac{2}{k \rho_g(Q')} \right]^{1/3} \tilde{g}(\xi) f(t) e^{-jkt}$$

where $f(t)$ is a heuristic function which joins smoothly the field in the illuminated transition region to the geometrical optics field in the illuminated region and it is defined by

$$f(t) = \begin{cases} \frac{-\hat{n}' \cdot \hat{s}}{\xi \left[\frac{2}{k \rho_g(Q')} \right]^{1/3}} & 0 \leq \hat{n}' \cdot \hat{s} < 1 \\ 1 & -1 < \hat{n}' \cdot \hat{s} \leq 0 \end{cases} \quad (C-4)$$

which for a constant radius reduces to

$$f(t) = \begin{cases} \frac{\sin \psi_1}{\psi_1} & -\frac{\pi}{2} \leq \psi_1 < 0 \\ 1 & \psi_1 \geq 0 \end{cases} \quad (C-5)$$

The functions $g(\xi)$ and $\tilde{g}(\xi)$ are the hard and soft Fock functions which are well tabulated^{31,33} and are defined by

$$g(\xi) = \frac{1}{\sqrt{\pi}} \int_{\Gamma_1} \frac{e^{-j\tau\xi}}{w_2'(\tau)} d\tau \quad (C-6)$$

$$\tilde{g}(\xi) = \frac{1}{\sqrt{\pi}} \int_{\Gamma_1} \frac{e^{-j\tau\xi}}{w_2(\tau)} d\tau$$

where $w_2(\tau)$ and $w_2'(\tau)$ are Fock-type Airy functions. The parameter ξ is defined by

$$\xi = \int_0^t \frac{1}{\rho_g} \left[\frac{k\rho_g}{2} \right]^{1/3} dt' \quad (C-7)$$

and the path of integration Γ_1 is shown in Figure C.4.

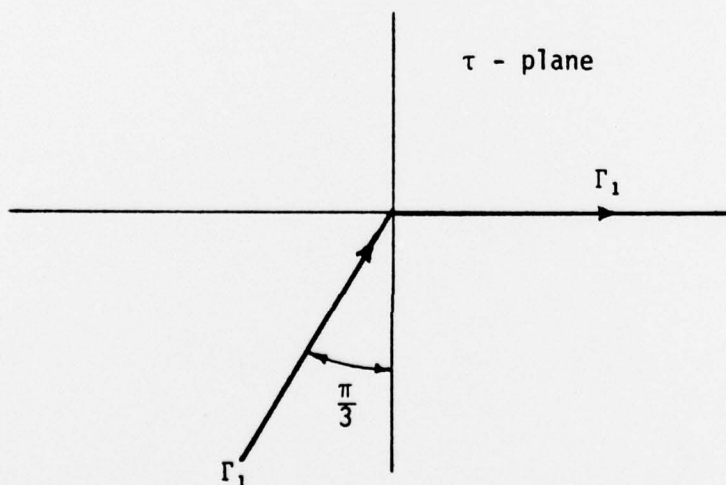


Figure C.4. Path of integration for Fock functions.

The magnitude (modulus) and phase (argument) of the hard $[g(\xi)]$ and soft $[\tilde{g}(\xi)]$ Fock functions are shown plotted in Figures C.5 and C.6, respectively.

Referring to Figure C.7, the field in the shadow transition region $[\pi/2 \leq \theta \leq \pi/2 + \Delta]$ is given by (C-2) with the F and G functions defined by

$$F = \sqrt{\frac{d\psi_0}{d\psi}} g(\xi) e^{-jkt} \left[\frac{\rho_g(Q)}{\rho_g(Q')} \right]^{1/6}$$

where $t, \xi > 0$ (C-8)

$$G = -j \sqrt{\frac{d\psi_0}{d\psi}} \left[\frac{2}{k\rho_g(Q')} \right]^{1/3} \tilde{g}(\xi) e^{-jkt} \left[\frac{\rho_g(Q)}{\rho_g(Q')} \right]^{1/6}$$

where $\sqrt{d\psi_0/d\psi}$ is a spread factor which is related to the spread of the geodesic path.

In the shadow region $[\pi/2 + \Delta \leq \theta]$, the field, according to Figure C.8, are given by (C-2) where the F and G functions are defined by

$$F = \sqrt{\frac{d\psi_0}{d\psi}} \sum_{p=0}^{\infty} L_p^h(Q') D_p^h(Q_2) e^{-jkt} e^{\int_0^t \alpha_p^h(t') dt'}$$

$$G = \sqrt{\frac{d\psi_0}{d\psi}} \sum_{p=0}^{\infty} L_p^s(Q') D_p^s(Q_2) e^{-jkt} e^{\int_0^t \alpha_p^s(t') dt'}$$

(C-9)

$$L_p^h = e^{j\frac{\pi}{12}} \sqrt{2\pi k} \left[\frac{2}{k\rho_g} \right]^{1/3} A_1(-\bar{q}_p) \left[1 + \left(\frac{2}{k\rho_g} \right)^{2/3} \frac{\bar{q}_p}{15} e^{j\frac{2\pi}{3}} \right] D_p^h$$

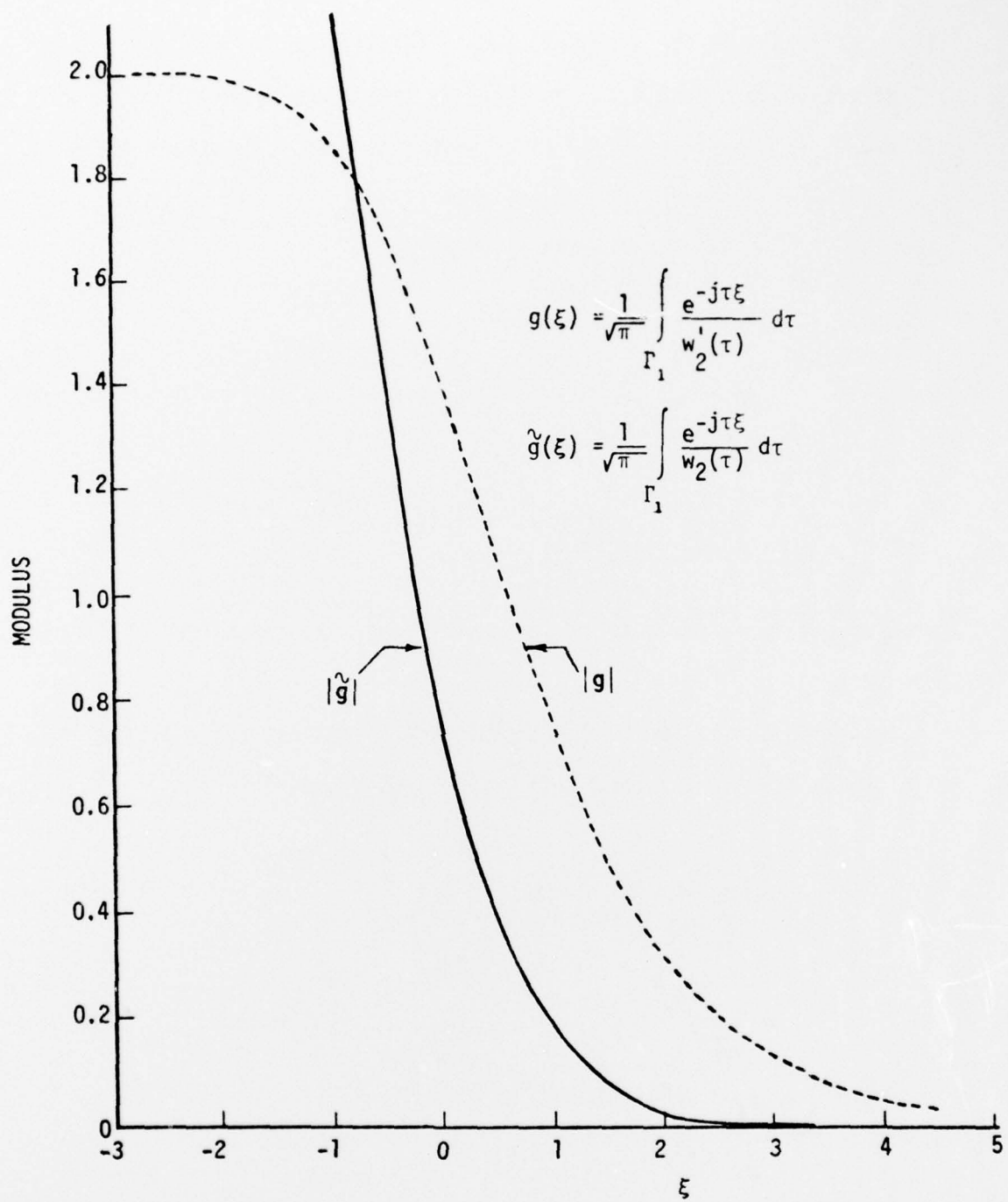


Figure C.5. Magnitude (modulus) distributions of hard $[g(\xi)]$ and soft $[\tilde{g}(\xi)]$ Fock functions.

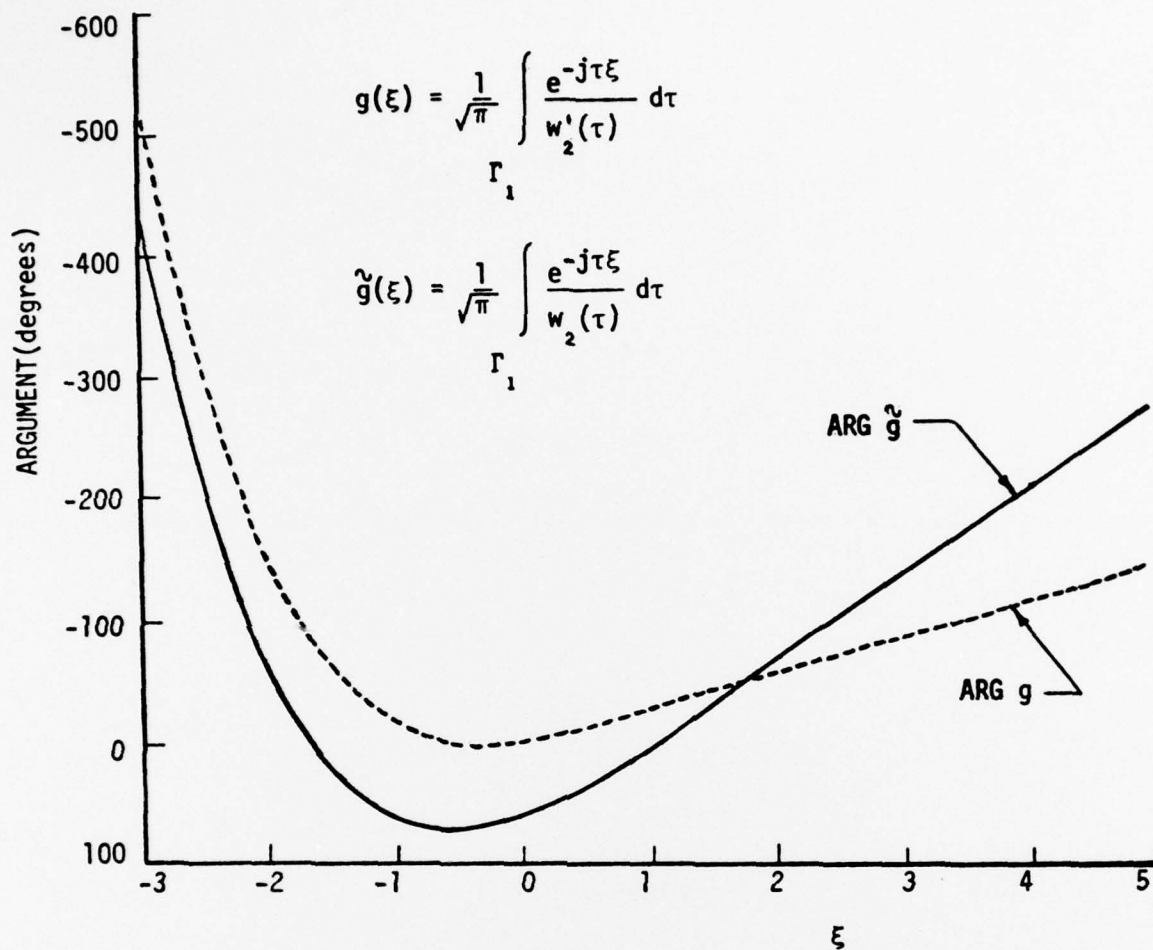


Figure C.6. Phase (argument) distributions of hard [$g(\xi)$] and soft [$\tilde{g}(\xi)$] Fock functions.

SHADOW TRANSITION REGION ($\frac{\pi}{2} \leq \theta \leq \frac{\pi}{2} + \Delta$)

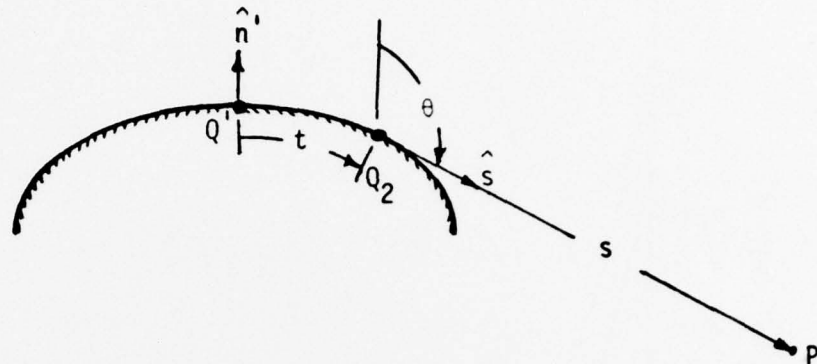


Figure C.7. Geometry for shadow transition region radiation by an aperture on a curved surface.

SHADOW REGION ($\frac{\pi}{2} + \Delta \leq \theta$)

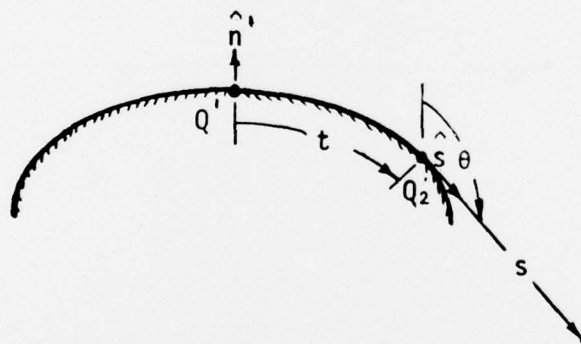


Figure C.8. Geometry for shadow region radiation by an aperture on a curved surface.

$$L_p^S = e^{-j\frac{\pi}{12}} \sqrt{2\pi k} \left[\frac{2}{k\rho_g} \right]^{2/3} A_i'(-q_p) \left[1 - \left(\frac{2}{k\rho_g} \right)^{2/3} \frac{q_p}{15} e^{j\frac{2\pi}{3}} \right] D_p^S \quad (C-10)$$

where L_p^h, L_p^S = launching coefficients for hard, soft boundary conditions
 D_p^h, D_p^S = diffraction coefficients for hard, soft boundary conditions
 α_p^h, α_p^S = attenuation coefficients for hard, soft boundary conditions
 q_p = zeroes of the Airy function $A_i(-x)$
 \bar{q}_p = zeroes of the derivative of the Airy function $A_i(-x)$

The expressions for $D_p^h, D_p^S, \alpha_p^h, \alpha_p^S$ and the values of $q_0, q_1, \bar{q}_0, \bar{q}_1, A_i'(-q_0), A_i'(-q_1), A_i(-\bar{q}_0)$, and $A_i(-\bar{q}_1)$ are shown listed in Tables 3 and 4 shown in the main text.

IX. REFERENCES

1. Shank, R.J., "The Microwave Instrument Landing System," Microwave Journal, Vol. 15, No. 12, pp. 6, 13, January 1972.
2. Sebring, J.R., and Ruth, J.K., "MLS Scanning-Beam Antenna Implementation," Microwave Journal, Vol. 17, No. 1, pp. 41-46, January 1974.
3. Record of "International Microwave Landing System (MLS) Symposium," Report No. FAA - RD - 74-56, April 1974.
4. Leopard, G.W., "The Flight Evaluation of Aircraft Antennas," IRE Transactions on Antennas and Propagation, Vol. AP-4, pp. 158-166, March 1960.
5. Keller, J.B., "Geometrical Theory of Diffraction," Journal of Optical Society of America, Vol. 52, pp. 116-130, February 1962.
6. Balanis, C.A. and Peters, L. (Jr.), "Equatorial Plane Pattern of an Axial-TEM Slot on a Finite Size Ground Plane," IEEE Transactions on Antennas and Propagation, Vol. AP-17, pp. 351-353, May 1969.
7. Balanis, C.A., "Analysis of an Array of Line Sources Above a Finite Ground Plane," IEEE Transactions on Antennas and Propagation, Vol. AP-19, March 1971.
8. Balanis, C.A., "Radiation from Conical Surfaces Used for High-Speed Spacecraft," Radio Science, Vol. 7, pp. 339-343, February 1972.
9. Sengupta, D.L. and Weston, V.H., "Investigation of the Parasitic Loop Counterpoise Antenna," IEEE Transactions on Antennas and Propagation, Vol. AP-17, pp. 180-191, March 1969.
10. Sengupta, D.L. and Ferris, J.E., "On the Radiation Patterns of Parasitic Loop Counterpoise Antennas," IEEE Transactions on Antennas and Propagation, Vol. AP-18, pp. 34-41, January 1970.
11. Balanis, C.A. and Peters, L. (Jr.), "Aperture Radiation from an Axially Slotted Elliptical Conducting Cylinder Using Geometrical Theory of Diffraction," IEEE Transactions on Antennas and Propagation, Vol. AP-17, pp. 507-513, July 1969.
12. Balanis, C.A., "Radiation Characteristics of Current Elements Near a Finite Length Cylinder," IEEE Transactions on Antennas and Propagation, Vol. AP-18, pp. 352-359, May 1970.
13. Ryan, C.E., (Jr.) and Peters, L. (Jr.), "Evaluation of Edge-Diffracted Fields Including Equivalent Currents for the Caustic Regions," IEEE Transactions on Antennas and Propagation, Vol. AP-17, pp. 292-299, May 1969.

14. Burnside, W.D., Marhefka, R.J., and Yu, C.L., "Roll-plane Analysis of On-Aircraft Antennas," IEEE Transactions on Antennas and Propagation, Vol. AP-21, pp. 780-786, November 1970.
15. Pathak, P.H. and Kouyoumjian R.G., "An Analysis of the Radiation from Apertures in Curved Surfaces by the Geometrical Theory of Diffraction," Proceedings of the IEEE, Vol. 62, No. 11, pp. 1438-1447, November 1974.
16. Kouyoumjian, R.G. and Pathak, P.H., "A Uniform Geometrical Theory of Diffraction for an Edge in a Perfectly Conducting Surface," Proceedings of the IEEE, Vol. 62, No. 11, pp. 1448-1461, November 1974.
17. Collin, R.E. and Zucker, F.J., Antenna Theory I, New York: McGraw-Hill, 1969, pp. 71-79.
18. Knop, C.M. and Cohn, G.I., "Radiation from an Aperture in a Coated Plane," Radio Science, Vol. 4, pp. 363-378, April 1964.
19. Pauli, W., "An Asymptotic Series for Functions in the Theory of Diffraction of Light," Physical Review, Vol. 54, pp. 924-931, December 1938.
20. Oberhettinger, F., "On Asymptotic Series for Functions Occuring in the Theory of Diffraction," J. Math. and Phys., Vol. 34, pp. 245-255, April 1955.
21. Hutchins, D.L. and Kouyoumjian, R.G., "A New Asymptotic Solution to the Diffraction by a Wedge," 1967 URSI Spring Meeting, Ottawa, Ontario, Canada, pp. 154-155.
22. Sommerfeld, A., Optics, New York: Academic Press, 1954, pp. 245-255.
23. Rusch, W.V.T. and Potter, P.D., Analysis of Reflector Antennas, New York: Academic Press, 1970, pp. 20-42.
24. Keller, J.B., "A Geometrical Theory of Diffraction" in Calculus of Variations and its Applications, New York: McGraw-Hill, 1958, pp. 27-52.
25. Vainshtein, L.A., The Theory of Diffraction and the Factorization Method (Generalized Wiener-Hopf Technique), Boulder, Colorado: Golem Press, 1969.
26. Kouyoumjian, R.G., "Asymptotic High-Frequency Methods," Proceedings of the IEEE, Vol. 53, No. 8, pp. 864-876, August 1965.
27. Levy, B.R. and Keller, J.B., "Diffraction by a Smooth Object," Communications on Pure and Applied Mathematics, Vol. 12, pp. 159-209, 1959.
28. Keller, J.B., and Levy, B.R., "Decay Exponents and Diffraction Coefficients for Surface Waves on Surfaces of Non-Constant Curvature," IRE Transactions, AP-3, pp. 552-561, December 1959.

29. Hwang, Y., and Kouyoumjian, R.G., "The Mutual Coupling Between Slots on an Arbitrary Convex Cylinder," submitted for publication in the IEEE Transactions on Antennas and Propagation.
30. Galejs, J., "Self and Mutual Admittances of Waveguides Radiating Into Plasma Layer," Radio Science Journal of Research, NBS/USNC-URSI, Vol. 69D, No. 2., pp. 179-189, February 1965.
31. Logan, N.A., "General Research in Diffraction Theory," Missiles and Space Division, Lockheed Aircraft Corp., Vol. 1, Report LMSD-288087 and Vol. 2, Report LMSD-288088, December 1959.
32. Harrington, R.F., Time-Harmonic Electromagnetic Fields, McGraw-Hill Book Company, New York, pp. 238-242, 1961.
33. Fock, V.A., Electromagnetic Diffraction and Propagation Problems, New York: Pergamon Press, 1965.